White Light Filamentation:
Tailoring & Application for Charge Reversal of Ag_3^-

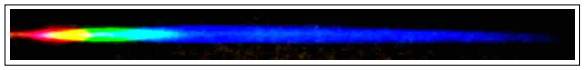

im
Fachbereich Physik
der
Freien Universität Berlin
eingereichte Dissertation
von

Bruno Eugen Schmidt

September 2008

Diese Arbeit wurde in der Zeit von November 2003 bis September 2008 unter der Aufsicht von Herrn Prof. Dr. L. Wöste am Fachbereich Physik der Freien Universität Berlin durchgeführt.

Erstgutachter: Prof. Dr. L. Wöste
Zweitgutachter: Prof. Dr. N. Schwentner
Disputationstermin: 17.11.2008

Picture on title: Spectrum of white light filamentation in air.

Contents

List of Figures

Abbreviations

4WM	Four Wave Mixing
BBO	Beta barium borate, ß-BaB_2O_4
CARS	Coherent anti-Stokes Raman scattering
CCD	Charged coupled device
CM	Chirped mirrors
CPA	Chirped parametric amplifier
cw	Continuous wave
DFG	Difference frequency generation
EA	Evolutionary algorithm
FC	Franck-Condon
FS	Fused silica
FROG	Frequency resolved optical gating
FWHM	Full width at half maximum
fs	femtosecond (10^{-15})s
ITO	Indium tin oxide
IP	Ionization potential
LC	Liquid crystals
NIR	Near infrared spectral region: 730–900 nm
NOPA	Noncollinear optical parametric amplifier
nm	nanometer (10^{-9})m
OCT	Optimal control theory
PCGP	Principal components generalized projections
ps	picosecond $(10^{-12})s$
SC	Supercontinuum
SD	Self diffraction
SPM	Self phase modulation
SFG	Sum frequency generation
SLM	Spatial light modulator
SHG	Second harmonic generation
SPIDER	Spectral phase interferometry for direct electric-field reconstruction
TG	Transient grating
TGC	Telescope-grating compressor
TL	Transform limited
Ti:Sa	Titanium (doped) Sapphire
THG	Third harmonic generation
VIS	Visible spectral region: 400-730 nm
WL	White light

Introduction

Optics is one of the oldest fields of physics and deals with the knowledge of the properties of light and its interaction with matter. From a scientific viewpoint, optics has a twofold meaning. Studying optical effects gained insight into the fundamental physics, for instance the wave - particle duality of light. On the other hand, light serves as an invaluable investigation tool in other natural sciences. One example is the benefit of microscopy to biology and medicine where small objects became visible through optical imaging. The long tradition of gathering knowledge on geometric optics can be dated back to the Assyrians in the ninth century B. C. who used polished spheres as burning glasses. Accordingly, "Archimedes' heat rays", although located in the field of mythology, display a famous consideration of light-matter interaction. It is said that Syracuse's soldiers set fire to Roman warships besieging their home town around 214 B.C. by focusing their polished shields on one spot [1].

A decidedly more peaceful implementation of light-matter interaction was the invention of photography by the two Frenchmen Nicephore Niepce and Louis Daguerre [2][1]. The final process, still valid even today, was published by William Henry Fox Talbot in 1839. From 1844–1846 he edited the first picture book called "The Pencil of Nature" [3], in which he described the photogenic drawing process:

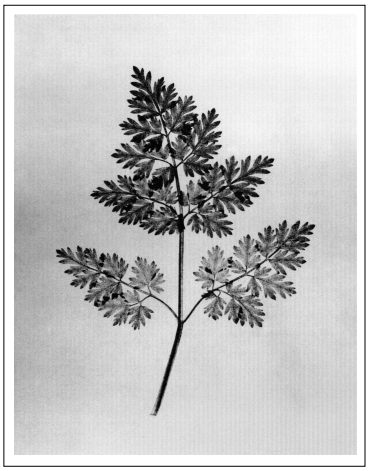

Figure 1: " *The little work presented to the public is the first attempt to publish a series of plates or pictures wholly executed by the new art of Photogenic Drawing, without any aid whatever from the artist's pencil [...] They are the sun-pictures themselves, and not, as some persons have imagined, engravings in imitation.*"
From "The Pencil of Nature" by W. H. F. Talbot [3]

Talbot's photogenic drawings had been created by nothing more than the light itself, acting on light sensitive material. He discovered that a short exposure time triggered an invisible effect in his silver paper. By employing a chemical developer, Talbot turned this latent image into a visible negative. Exposure times, previously ranging from minutes to even hours, shrunk to seconds.

Meanwhile, technical progress allows the size of investigated objects to become smaller and smaller just as the exposure time shortened towards the attossecond (1 as = 10^{-18}s) regime which

[1] Indeed the first realization by Niepce in 1827 was called *Heliographie* and the technique officially introduced by the French Academy of Science in 1839 was named after his inventor *Daguerreotypie*.

enables even the imaging of electronic motions in atoms or molecules [4–6]. On a femtosecond (fs) (1 fs = 10^{-15}s) time scale the slower motion of atoms in molecules can be resolved [7, 8]. The molecules investigated in this work are small sized silver clusters. Aside from their immense role in the elementary photographic process [9], the three atom cluster Ag_3 is an interesting model system exhibiting ultrafast nuclear dynamics like configurational changes followed by internal vibrational relaxation (IVR) [10–12].

Nuclear dynamics in these clusters are investigated via charge reversal spectroscopy (from negative Ag_n^- to neutral Ag_n to positive Ag_n^+ - NeNePo), being an ultrafast pump probe method developed in the Wöste group [10]. This method is extended in this thesis by parametric pulse train excitation of the dimer Ag_2^- whose vibrational period of the neutral Ag_2 was determined by scanning the sub pulse separation in the pump step. To gain insight into the more complex dynamics of the triatomic Ag_3, the universality of the pulse forming tool was expanded by ultra broadband operation.

To come full circle, again the beneficial self-action of light in the form of intense fs laser pulses leads to the formation of plasma filaments [13, 14] which are in turn the light source of choice in the current work. These filaments, providing an octave spanning spectrum, are utilized to reach the first goal, which lies at the improvement of ultra fast spectroscopy techniques by means of arbitrary shaped white light (WL) pulses. After accomplishing this goal, the second step is the application of this universal tool to investigate the quantum nature of small silver clusters Ag_n in a size range n where each atom counts [15].

Providing the basis for this thesis, underlaying principles of WL generation, their measurement as well as their utilization in the framework of coherent quantum control are introduced in Ch. 1. Furthermore, the concept of NeNePo spectroscopy is explained in this chapter. In Ch. 2, the experimental realization of generating, characterizing, and arbitrary manipulating of fs WL is described. Since optical gating of few cycle pulses and especially of octave exceeding spectra is a major task, different setups resting upon Four Wave Mixing (4WM) are presented. Results concerning the steering of filamentation behavior and subsequent fs engineering of the light field is the content of Ch. 3. A very simple setup consisting of 10 standard optical components only, for the generation and measurement of sub 7 fs pulses via filamentation in laboratory air is described. A novel discovery is the ability to perform cross-correlation measurements as a single beam arrangement. This peculiarity arises from combining WL shaping and 4WM. The synthesis of charge reversal spectroscopy on Ag_3 clusters and ultra broadband shaping in a closed loop scenario, in which nature is drawing itself with the "Pencil" of freely optimizing a desired quantum state population with an evolutionary algorithm [16, 17], is presented in Ch. 4. By turning the artists palette from sunlight into coherent WL, ultrashort pulse sequences were found which for the first time exhibit temporal structures far below the time scale observed in previous pump probe experiments on Ag_3 [10, 18, 19].

Chapter 1

Light-Matter Interaction

This chapter recalls fundamental physics connected to the generation of electromagnetic waves, their propagation as intense light pulses and their application in the framework of ultrafast spectroscopy.

General properties of linear and nonlinear fs pulse propagation in dispersive media are presented in Sec. 1.1. White light (WL) filamentation, obtained when high intensity pulses themselves modify the material they are propagating through by inducing an optical Kerr effect and weak ionization, is described in Sec. 1.2. In Sec. 1.3, the utilization of light-matter interaction according to a Four Wave Mixing (4WM) scheme is presented. It provides the basis for the characterization of octave exceeding spectra and few cycle pulse, respectively.

The WL generation was not (only) motivated as end in itself, but rather as an investigation tool for ultrashort dynamics of quantum systems. Basic principles of these systems and their behavior under fs pulse excitation is the content of Sec. 1.4.1. The experimental realization of foregoing theory by means of coherent control methods is discussed in Sec. 1.4.2. The special ultrafast spectroscopy method utilized in this work, namely the charge reversal of small metal clusters in an ion trap is explained in Sec. 1.4.3.

1.1 Ultra short pulse characteristics

An oscillating electric dipole emits a time varying electric field which induces a time varying magnetic field. This magnetic field again induces an electric field an so on. Consequently, an electromagnetic wave[1] can propagate in vacuum over long distances. The spectral region from 400–700 nm of those electromagnetic waves conforms to the visible (VIS) part and is of great relevance for spectroscopic investigations. Special techniques allow the generation of very short time durations, even a countable number of optical cycles is achievable combined with very high field strengths, which become comparable to the binding energies of electrons in atoms. Basic properties of such fields in dielectric matter are subject of this section.

1.1.1 Source of light

The classical description of electromagnetic phenomena is governed by the **Maxwell** equations (A.1)–(A.4), treated in App. A.1, which are a system of coupled differential equations. By combining them, the wave equation (A.7) is obtained, which describes the propagation of light in vacuum. A specific solution is given by periodic wave functions of the form

$$\mathbf{E}(\mathbf{r},t) = \mathbf{E_0} e^{i(k\mathbf{r}-\omega t)} + c.c. \tag{1.1}$$

The function $\mathbf{E}(\mathbf{r},t)$ describes an electric field vector which developes in time t and space $\mathbf{r}$ periodically oscillating with the light frequency ω. E_0 is the maximal amplitude of the electric field

[1] Propagation of a perturbation of the equilibrium whereat energy is transfered without the need of mass transport. Electromagnetic waves are not restricted to propagation in a medium.

and the abbreviation "c.c." denotes the complex conjugate to describe a real valued field, which is dropped in the following for simplicity. The wave vector $\mathbf{k}$ is related to the wavelength λ of the light through $|\mathbf{k}| = 2\pi n/\lambda$ with n being the refractive index of the medium ($n = 1$ for vacuum). For propagation in a dielectric medium the wave equation takes the form

$$\nabla^2\mathbf{E}(\mathbf{r},t) - \frac{1}{c_0^2}\frac{\partial^2\mathbf{E}(\mathbf{r},t)}{\partial t^2} = \mu_0\frac{\partial^2\mathbf{P}(\mathbf{E}(\mathbf{r},t))}{\partial t^2}\,. \tag{1.2}$$

$\mathbf{P}(\mathbf{E}(\mathbf{r},t))$ is the medium polarization which is a complex macroscopic quantity arising from the summation upon all induced dipole moments in the interaction region. In the following, the expression for $\mathbf{E}(\mathbf{r},t)$ is not written in full, only as $\mathbf{E}$ for convenience. The polarization depends on the strength of the incident field $\mathbf{E}$ by

$$\mathbf{P}(\mathbf{E}) = \epsilon_0\chi\mathbf{E} \tag{1.3}$$

where χ is the electronic susceptibility and ϵ_0 the dielectric constant. Throughout the following the response of the dipole moments is assumed to be instantaneous and interactions between individual dipoles are neglected. In case of high field strengths[2] the polarization can be decomposed in a linear $\mathbf{P^{(1)}}(\mathbf{E})$ and a nonlinear $\mathbf{P^{(NL)}}(\mathbf{E})$ term

$$\mathbf{P}(\mathbf{E}) = \mathbf{P^{(1)}}(\mathbf{E}) + \mathbf{P^{(NL)}}(\mathbf{E}) \tag{1.4}$$

whereat $\mathbf{P^{(1)}}(\mathbf{E})$ is proportional to E and causes the linear refractive index n_0. This linear refractive index lowers the speed of light (strictly speaking the phase velocity) in dielectric material if $n_0 > 1$. With Eq.(A.11) in App. A.1 the wave equation can be written as

$$\nabla^2\mathbf{E}(\mathbf{r},t) - \frac{\epsilon}{c_0^2}\frac{\partial^2\mathbf{E}(\mathbf{r},t)}{\partial t^2} = \mu_0\frac{\partial^2\mathbf{P^{(NL)}}(\mathbf{E})}{\partial t^2}\,. \tag{1.5}$$

Equation(1.5) displays the basic equation of nonlinear optics [20]. It describes the operation principle of the coherent WL source (see Sec. 1.2) which is realized by laser induced filamentation. The nonlinear polarization $\mathbf{P^{(NL)}}(\mathbf{E})$ on right hand side of Eq.(1.5) is a source term for the generation of new frequencies. This origin of light is different compared to WL generation from a thermal source or to the direct emission of a laser. In order to emphasize the distinctiveness of WL filamentation, properties of thermal -and laser light sources are briefly recalled.

From the view point of electrodynamics, the wave property of light can be explained but not the particle property of light. Furthermore these particles contain discrete portions of energy. The cornerstone for this knowledge was layed by **Max Planck** in 1900 who turned his attention to black body radiation and derived a description for the dependence of emitted intensity on frequency and temperature. He had to postulate that electromagnetic energy can be emitted only in quantized form, $i.e.$ as multiple of an elementary portion $E = \hbar\omega$, in order to find an exact expression for the entire frequency range. The new fundamental constant $h = \hbar 2\pi$ is named Plancks constant. This continuously emitted heat radiation has a continuous spectrum inversely proportional to temperature T, with a radiation maximum λ_{max} at [21]

$$\lambda_{max} = \frac{2,9\times 10^{-3}\mathrm{K}}{T}\,. \tag{1.6}$$

[2]High field strengths means that the light field is low compared to the binding energy of the outer electrons and thus treated as a small perturbation.

At a temperature of $\approx$ 4000K a continuous WL spectrum with its maximum centered at $\approx$ 725 nm is achieved. This is comparable to maxima out of laser-plasma-filamentation, but requires considerably less effort to generate. Therefore, it is stressed that thermal radiation is spatially and temporally incoherent, unless filtering is applied.It can be used for absorption spectroscopy but not for time resolved experiments of molecular dynamics, as introduced in Sec. 1.4.

In fact, the particle character of light was more specifically stated by **Albert Einstein** five years later with the existence of photons, explaining the photoelectric effect. Later, in 1917 it was also Einstein who derived Plancks law in another way. He described the interaction between light and matter by introducing stimulated emission in addition to spontaneous emission from an excited state in a two level system. The transition probabilities between the excited state $|2\rangle$ to the ground state $|1\rangle$ are given by the Einstein coefficients for spontaneous emission A_1^2 and stimulated emission B_1^2

$$\frac{A_1^2}{B_1^2} = \alpha\omega^3 \tag{1.7}$$

where α is fine structure constant. Equation(1.7) predicts a domination of spontaneous emission against stimulated emission towards higher photon energy. Stimulated emission decreases with the third power to frequency and denotes a fundamental limitation for laser operation at short wavelengths. In contrast, nonlinear propagation during filamentation (see Sec.1.2.2) causes a strong asymmetric broadening towards short wavelengths with spectra spanning the range from 250–1000nm [22, 23].

Another restriction of lasers is the ultra broadband operation which is limited by the gain medium. Even though octave spanning bandwidths directly out of a laser oscillator have been demonstrated recently [24], the operation is restricted to the NIR spectral region due to the gain curve of the laser medium. Furthermore, the octave spanning width is only reached throughout self phase modulation (see Sec. 1.2.1) effects inside the cavity. On the other side spectra form WL filaments can cover more than two octaves [22]. Never the less, the starting point for generation of plasma filaments is an appropriate laser source whose most important characteristics are presented in the following.

The basis for generating coherent radiation is stimulated emission. A technical implementation of induced emission is the light amplification by stimulated emission of radiation (LASER). The operation principle of the Laser lies in a constantly removing of population inversion which has to be provided by an appropriate pumping scheme. If further a specific optical feedback is present, amplification of light can be achieved. Lasing starts with spontaneous emission from an excited state in all directions. The optical feedback is realized through two faced resonator mirrors which reflect a few of these emitted photons back towards their origin and an avalanche process in the previously excited laser medium starts. Besides, a necessary condition is that the life time of the excited states is meta stable, $i.e.$ much longer than the round trip time of light between the cavity mirrors. The distance L of the mirrors defines boundary conditions in between which only those standing waves can stabilize whose half length is a multiple integer m of L

$$L = m\frac{\lambda}{2}\,, \qquad \text{with } m \in N^+\,. \tag{1.8}$$

Corresponding to Fig. 1.1 the frequency spacing $\delta\omega$ of two neighboring standing waves (ω_m and ω_{m+1}), which are also called longitudinal modes, is

$$\delta\nu = \frac{1}{2\pi}\delta\omega = \frac{c}{2L} = f_{rep} = \frac{1}{T} \tag{1.9}$$

where T is the round trip time in the cavity and f_{rep} is the repetition rate of the laser. In the following angular frequency ω and frequency ν are only distinguished by their notation. Another

aspect associated with stimulated emission is, that population inversion cannot be achieved in a two level system by heating the laser material. This works only through out pumping energy in a multi level scheme. Hence the laser operates not in thermal equilibrium and the high degree of coherence results from the fact that stimulated and emitted light have the same frequency, phase and polarization.

1.1.2 Fs linear optics

Henceforth, two classes of lasers are distinguished. Continuous wave (cw) operation aims for reducing the number m of standing waves in the cavity to favor an infinitely long pulse. That means, one tries to reduce the spectral comb structure of Fig. 1.1 to only one line. Opposite to this, short pulse lasers couple as many comb lines as possible which is known as **mode locking** operation. The comb lines are equidistantly spaced by $\delta\omega$ and the m-th frequency component can be written as

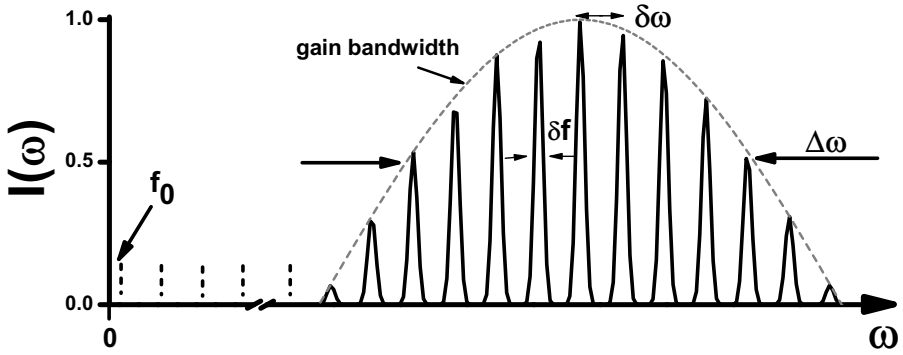

Figure 1.1: Comb spectrum of a pulse laser. $\Delta\omega$ denotes the FWHM of the gain bandwidth, $\delta\omega$ the frequency spacing between two longitudinal modes and δf the line width of a single mode. The offset f_0 of the expanded comb structure to zero frequency is referred to as carrier envelope offset frequency.

$\omega_m = f_0 + m\delta\omega = f_0 + m(f_{rep}/2\pi)$. $\Delta\omega$ is defined as the full width at half maximum (FWHM). For details on different working principles and technical realization of mode locking lasers the reader is referred to the text books [25, 26] and review articles in Refs. [27, 28]. Nowadays, commercial Titanium doped sapphire (Ti:Sa) oscillators provide pulse durations $\leq$ 10 fs with pulse energies in the nJ range at repetition rates f_{rep} which lie in 100MHz regime. Such short pulses are achieved when many individual frequencies ω_m are coupled together, having a constant phase relation to each other. The number of longitudinal modes depends on the supported gain bandwidth of the laser medium, as depicted schematically in Fig. 1.1. A real 10 fs pulse consists of 10^5–10^6 spectral modes which have to be superimposed coherently. Mathematically, this procedure is accomplished by Fourier transformation of the spectral distribution $\widetilde{E}(\omega)$

$$E(t) = \frac{1}{\sqrt{2\pi}} \int_{-\infty}^{\infty} \widetilde{E}(\omega) e^{i\omega t} d\omega \,. \tag{1.10}$$

According to the inversion theorem, the complex temporal electric field can be transformed to its complex spectral representation

$$\widetilde{E}(\omega) = \frac{1}{\sqrt{2\pi}} \int_{-\infty}^{\infty} E(t) e^{-i\omega t} dt \,. \tag{1.11}$$

Both, $\widetilde{E}(\omega)$ and $E(t)$ describe the physical phenomenon completely. Note, that the spectral appearance as comb structure shown in Fig. 1.1 is only given, if the repetition rate is appropriate, so

that many pulses interfere in the detecting spectrometer. In other words, if only one isolated pulse is measured with a spectrometer the comb lines will merge to form a continuous distribution.

The time dependent electric field of ultra short pulses can be represented by three parts. (i) One fast oscillating term containing the carrier frequency ω_0 which stays constant during propagation. (ii) A slowly evolving envelope function $A_E(t)$ which defines the shape of the pulse. (iii) In certain cases a third term containing a time dependent frequency $\omega(t)$ arises

$$E(t) = A_E(t)e^{-i\phi(t)} = A_E(t)e^{-i(\phi_0+\omega_0 t)}e^{-i\omega(t)} \,. \tag{1.12}$$

Equation (1.12) describes the electric field at a fixed point in space, thus the propagation coordinate is omitted. Among others, the Gaussian is the most relevant envelope function used to describe ultra short pulses

$$A_E(t) = e^{-1.385(t/\Delta t)^2} = e^{-(t/\tau_G)^2} \,. \tag{1.13}$$

The subscript E denotes an electric field quantity. Δt is the width of the electric field envelope and τ_G is the sigma width. The conversion between both parameters is given by $\Delta t = \sqrt{2\,ln2}\,\tau_G$. Circumstances for the appearance of a time dependent phase or frequency $\omega(t)$, respectively, are discussed in Secs. 1.1.3 and 1.2.

Recalling the basic rules of Fourier transformation covers the mathematical description of the most relevant features of ultra short pulse propagation properties. For instance, the narrowest feature in frequency domain, δf corresponds to the longest temporal separation that is the distance between two pulses or the repetition rate f_{rep}, respectively. Likewise, the time duration Δt at (FWHM) of the intensity is inversely related to the spectral FWHM of the angular frequency $\Delta\omega$ by [21, 26]

$$\Delta\omega \geq \frac{c_B}{\Delta t} \,. \tag{1.14}$$

The constant c_B depends on the shape of the envelope function and is $c_B = 4\,ln2 = 2.77$ for Gaussian intensity shapes

$$I(t) = e^{-2\times 1.385(t/\Delta t)^2} = e^{-2(t/\tau_G)^2} \,. \tag{1.15}$$

For shapes other than Gaussian, the values are $c_B = 2.77$ for rectangles and $c_B = 1.98$ for $sech^2$ distributions [26]. A pulse, reaching its lower limit when the equality sign in Eq.(1.14) holds, is called bandwidth-limited or transform-limited (TL). It is mentioned, that relation (1.14) holds for the intensity rather than for the electric field whereby they are related to each other by $\Delta t_E \Delta\omega_E = 2(\Delta t_{Int}\Delta\omega_{Int})$ [21]. Unless mentioned otherwise FWHM values are related to intensity rather than to the electric field quantities in the following. The real valued observable that can be measured is the intensity which is related to the electric field by

$$I(t) = \frac{1}{2}\epsilon_0 c\, n\, |E(t)|^2 = \frac{1}{2}\epsilon_0 c\, n A(t)^2 \,. \tag{1.16}$$

Chirp in the frequency domain

According to the theorems of Fourier transformation, the envelope function in one domain is dependent on the phase function in the other domain. This mathematical formalism describes the temporal broadening of ultrashort pulses when traveling through linear responding dielectric media. The physical origin of temporal broadening is dispersion[3]. Dispersion acts on the spectral phase which remains no longer constant but becomes a function of frequency $\phi(\omega)$. This function

[3]Dispersion means that a physical quantity depends on the frequency, like $e.g.$ the refractive index n.

can be approximated in a Taylor series around the carrier frequency ω_0

$$\phi(\omega) = \sum_{j=0}^{\infty} \frac{\phi^{(j)}(\omega_0)}{j!}(\omega - \omega_0)^j \qquad \text{with} \qquad \phi^{(j)}(\omega_0) = \left.\frac{\partial^j \phi(\omega)}{\partial \omega^j}\right|_{\omega_0}, \tag{1.17}$$

whereby the first four terms read as

$$\phi(\omega) = \phi_0(\omega_0) + \phi'(\omega_0)(\omega - \omega_0) + \frac{1}{2}\phi''(\omega_0)(\omega - \omega_0)^2 + \frac{1}{6}\phi'''(\omega_0)(\omega - \omega_0)^3 + ... \tag{1.18}$$

The spectral phase coefficient of zeroth order determines the peak position of the comb lines in Fig. 1.1 with respect to the envelope of the gain curve. In the time domain, this offset defines the relative position of the maximum of the carrier frequency with respect to the pulse envelope $A(t)$ and is called carrier envelope phase (CEP). This value is not of importance unless the pulse durations reaches few cycles. In this case multi photon ionization processes and high harmonic generation sensitively depend on the absolute phase [28]. Another issue is the change of f_0 from pulse to pulse. However, ϕ_0 does not affect the temporal envelope of the pulse and is thus not measurable with pulse correlation techniques used throughout this thesis.

According to the shift theorem, the first order term $j = 1$ in Eq.(1.17) leads to a temporal shift of the time envelope $A(t)$. This resembles the fact that light travels slower in dense media than in vacuum. It gives rise to a group delay of fs pulses which have different center wavelengths. When all $\phi^{(j)} = 0$ for $j \geq 2$ the temporal shape is unchanged and the pulse is called unchirped and $\phi(\omega)$ is constant.

Higher order coefficients give rise to a change of the envelope shape. Even orders cause symmetric distortions like pulse lengthening as a second order phase effect. The quadratic phase function $\phi''(\omega_0)$ is also referred to as linear frequency chirp or group velocity dispersion (GVD). Odd orders lead to an asymmetric temporal pulse shape. The goal of all pulse compression schemes described in Sec. 3.2.2 lies in the recovery of a flat spectral phase function which was previously distorted due to material dispersion. It is pointed out that pulse distortions described by Eq.(1.17) arise from linear propagation of fs pulses, that means that the nonlinear source term in Eq.(1.5) is zero.

For further amplification, these pulses were stretched in time (´´chirped´´) to $\approx$ 100 ps, then amplified through several passes in another Ti:Sa crystal and finally recompressed again in time. The high amplification factors of $\approx 10^6$ require temporal stretching of pulses to prevent damage and is therefore called chirped pulse amplification **CPA** [29]. The repetition rate is reduced to the kHz regime before amplification. Due to the non uniform gain curve of the Ti:Sa crystal the amplified spectrum is narrowed compared to the input spectrum. One should keep in mind, that reduction of repetition rate by factor of 10^5 leads to a narrowing of the comb teeth distance $\delta\omega$ and eventually smears out the sharp comb structure. Hence care has to be taken for ultra high resolution spectroscopy methods with amplified pulses. Now, with these amplified pulses one can enter the fascinating area of nonlinear optics.

1.1.3 Fs nonlinear optics - $\chi^{(3)}$ susceptibility

One year after the invention of laser in 1960 by Theodore Maiman [30], the second harmonic generation by Franken $et.al.$ marked the birth of nonlinear optics [31]. On a fundamental level optical effects like dispersion have their origin in the way the bound electrons respond on the exciting light wave. The strength of induced oscillations is determined by the resonance frequency at which the medium absorbs. When intense laser pulses propagate in isotropic media the motion of bound electrons becomes stronger, and thus anharmonic under the influence of an applied AC-field. The manner on which the material response can lead to a nonlinear dependence of $\mathbf{P}$ on $\mathbf{E}$ is

subject to the field of nonlinear optics. The decomposition in a linear $\mathbf{P^{(1)}}$ and nonlinear part $\mathbf{P^{(NL)}}$ bases on the assumption that $\mathbf{P^{(NL)}}$ is a small perturbation compared to the linear polarization $\mathbf{P^{(1)}}$. According to a perturbative ansatz, Eq.(1.4) can be extended to a power series in the field strength

$$\begin{aligned} \mathbf{P} &= \mathbf{P^{(1)}} + \mathbf{P^{(NL)}} && (1.19) \\ \mathbf{P} &= \epsilon_0 \chi^{(1)} \mathbf{E} + \epsilon_0 \mathbf{E} \left[\chi^{(2)} \mathbf{E} + \chi^{(3)} \mathbf{E}^2 + ... \right] && (1.20) \end{aligned}$$

where ϵ_0 is the vacuum permittivity. The quantity $\chi^{(1)}$ is known as linear electric susceptibility which can be linked to the linear refractive index, see Eq.(A.28). The $\chi^{(m)}$ are the nonlinear optical susceptibilities of order m. In general $\chi^{(m)}$ is a tensor of rank $m+1$. The tensorial properties are simplified to a large extent due to material symmetries. When considering a homogeneous, loss free medium with spatial symmetry and excitation far away from resonances, the tensor can be reduced to a real valued scalar [32]. This holds for all kind of gases, liquids and conventional glass. Assuming linear polarization, the second order susceptibility of Eq.(1.20) takes the form

$$P^{(2)} = \epsilon_0 \chi^{(2)} E^2 \,. \tag{1.21}$$

Equation (1.21) denotes that three fields are coupled. Two incoming fields with their oscillation frequencies (ω_1 and ω_2) induce a polarization oscillating at frequencies equal to the linear combinations of driving fields. According to classical electrodynamics, any motion that is connected with a change of its dipole moment leads to the emission or absorption of radiation. Thus the second order polarization emits light at new frequencies [32]

$$\begin{aligned} P(2\omega_1) = \epsilon_0 \chi^{(2)} E_1^2, P(2\omega_2) &= \epsilon_0 \chi^{(2)} E_2^2 \qquad \text{(SHG)} \\ P(\omega_1 + \omega_2) &= 2\epsilon_0 \chi^{(2)} E_1 E_2 \qquad \text{(SFG)} \\ P(\omega_1 - \omega_2) &= 2\epsilon_0 \chi^{(2)} E_1 E_2^* \qquad \text{DFG} \\ P(0) &= 2\epsilon_0 \chi^{(2)} (E_1 E_1^* + E_2 E_2^*) \qquad \text{(OR)} \end{aligned} \tag{1.22}$$

The abbreviations of the physical processes are second harmonic generation (SHG), sum frequency generation (SFG), difference frequency generation (DFG) and optical rectification (OR). In general, nonlinear process like frequency conversion takes place on individual atoms or molecules, respectively. Efficient conversion, however, requires a coherent superposition of many individual sources. The constructive addition within an ensemble is a contemplation for *phase matching*.

In solids with inversion symmetry as well as for randomly oriented molecules in the gas phase all even order - susceptibilities in Eq.(1.20) vanish due to the fact that polarizations of opposite sign add to zero. Thus the main nonlinear contribution in isotropic media arises from to the $\chi^{(3)}$ susceptibility [4]. Higher order terms are dropped because of their small contributions. The basic effect of the $\chi^{(3)}$ susceptibility is the coupling of four intersecting light waves by the medium. This results in an energy exchange between intersecting light fields which leads $e.g.$ to self-phase modulation (SPM) or four wave mixing (4WM), the two most essential nonlinearities for the observed effects in this thesis. Energy can also be exchanged with the medium and cause phenomena like Brillouin- or stimulated Raman-scattering. However, these interactions were not relevant for effects in this work. Furthermore, the depletion of incoming fields is neglected in the following and the medium response is considered to be instantaneous. The third order polarization of Eq.(1.20) can be written as [32]

$$P^{(3)} = \epsilon_0 \chi^{(3)} E^2 E \tag{1.23}$$

[4] SHG can be observed at glass surfaces and impurities due to a break of symmetry

and denotes an interaction of four waves: Three incoming waves which induce a nonlinear polarization $P^{(3)}$ and one wave generated by this polarization. The total field of four linearly polarized electromagnetic waves propagating in z direction which oscillate at frequencies $\omega_1, \omega_2, \omega_3$, and ω_4 can be described as a linear combination [33]

$$E = \sum_{j=1}^{4} E_j e^{i(k_j z - \omega_j t)} + c.c. \,. \tag{1.24}$$

Substituting Eq.(1.24) in Eq.(1.23) and expressing the oscillations of $P^{(3)}$ as linear combination of plane waves like in Eq.(1.24) writes as

$$P^{(3)} = \sum_{j=1}^{4} P_j e^{i(k_j z - \omega_j t)} + c.c. \,. \tag{1.25}$$

The P_j ($j = 1 - 4$) consists of many terms which involve the products of three electric fields. For example, $P_4^{(3)}$ consists of [33]

$$\begin{aligned} P_4^{(3)} \;=\; & \frac{3\epsilon_0}{8}\chi^{(3)} \left[|E_4|^2 E_4 + 2(|E_1|^2 E_4 + |E_2|^2 E_4 + |E_3|^2 E_4) + \right. \\ & \left. 2(E_1 E_2 E_3) e^{i\theta_+} + 2(E_1^* E_2 E_3) e^{i\theta_-} + ... \right] \end{aligned} \tag{1.26}$$

where θ_+ and θ_- are defined as

$$\theta_+ = (k_1 + k_2 + k_3 - k_4)z - (\omega_1 + \omega_2 + \omega_3 - \omega_4)t \tag{1.27}$$

$$\theta_- = (-k_1 + k_2 + k_3 - k_4)z - (-\omega_1 + \omega_2 + \omega_3 - \omega_4)t \,. \tag{1.28}$$

The first four terms in Eq.(1.26) are responsible for SPM ($\omega_j = const.$) and cross phase modulation (differing ω_j). The terms in the second row in Eq.(1.26) give rise to 4WM. A significant contribution of one of those parametric processes can only occur when the frequencies as well as the wave vectors are matched. There are two types of 4WM terms in Eq.(1.26). Collinear phase matching ($k_4 = k_1 + k_2 + k_3$) pursuant to Eq.(1.28) tend to that three photons transfer their energy to a new photon with frequency $\omega_4 = \omega_1 + \omega_2 + \omega_3$ which is called third harmonic generation (THG). The non collinear phase matching requirement for θ_- in Eq.(1.28) can be written as

$$k_4 = -k_1 + k_2 + k_3 \,. \tag{1.29}$$

It provides the basis for discussing the transient grating arrangement in Sec. 1.3. Looking at Eq.(1.28) in terms of conservation of energy means that two photons at frequencies ω_2 and ω_3 are annihilated in favor of two photons with ω_1 and ω_4

$$\omega_2 + \omega_3 = \omega_1 + \omega_4 \,. \tag{1.30}$$

The phase matching condition Eq.(1.29) considers only monochromatic waves and an extensive investigation on the properties of octave exceeding bandwidths is discussed in Sec. 3.4.

Chirp in the time domain

Other than in case of linear optics where intersecting waves do not influence each other, the induced nonlinear polarization allows the interaction of electromagnetic waves. Interaction means that new frequencies can be generated as superposition of the incoming fields which leads $e.g.$ to

second harmonic generation in a $\chi^{(2)}$ medium. In a $\chi^{(3)}$ medium the temporal phase $\phi(t)$ of a pulse [$cf.$ (Eq.1.12) with $E(t) = A(t)e^{-i\phi(t)}$] can be distorted as a result of nonlinear propagation. Similar to the Taylor expansion in Eq.(1.17) for linear propagation, now $\phi(t)$ can be approximated by

$$\phi(t) = \sum_{j=0}^{\infty} \frac{\phi^{(j)}(t_0)}{j!}(t-t_0)^j \qquad \text{with} \qquad \phi^{(j)}(t_0) = \left.\frac{\partial^j \phi(t)}{\partial t^j}\right|_{t_0} \tag{1.31}$$

whereby the first four terms read as

$$\phi(t) = \phi_0(t_0) + \phi'(t_0)(t-t_0) + \frac{1}{2}\phi''(t_0)(t-t_0)^2 + \frac{1}{6}\phi'''(t_0)(t-t_0)^3 + ... \tag{1.32}$$

The zeroth order coefficient determines the relative position of the oscillations with respect to the pulse envelope and thus corresponds to the carrier envelope phase which was introduced by Eq.(1.18). The first order coefficient gives the carrier frequency of the pulse with $\omega(t) = const.$ The second order term leads to a so called linear chirp in time. It must not be confused that a linear chirp in the time domain has an opposite effect to the pulse as a linear chirp in the frequency domain. The latter broadens the temporal width but keeps the spectrum constant and is an attribute of linear light propagation due to dispersion. Whereas the linear chirp in time, $e.\ g.$ the second order term in Eq.(1.32) results from nonlinear propagation of intense fs laser pulses. The standard example therefore is self-phase modulation (SPM) which will be discussed in Sec. 1.2.1. SPM does not broaden the temporal envelope but the spectral width of the pulse.

1.2 Nonlinear pulse propagation - White light

The self induced changes during filamentation process might be seen as pulse shaping in the time domain different to the pulse shaping in the frequency domain achieved with a 4-f pulse shaper setup of Sec. 2.3. Time domain shaping means on the one hand side a change of temporal phase or on the other hand a change of temporal shape of a propagating pulse. Both types might result in a change of the pulse spectrum which gathers new components if these changes happen sufficiently fast compared to the initial pulse duration. Since no apparatus can operate fast enough compared to the speed of light, the pulse itself has to induce these changes in the nonlinear medium. The temporal phase is affected, $e.\ g.$ when the refractive index varies due to Kerr effect or plasma generation, respectively. The temporal amplitude can be modified by self steepening of one pulse edge (or both edges), self compression or pulse splitting. Above mentioned effects are related to spectral broadening and won't appear strictly separated in real experiments but moreover dependent on each other.

The regime of nonlinear optics as treated in Sec. 1.2.1 looses its validity when the laser field strength becomes comparable to the static atomic Coulomb field which means the perturbative approach for the macroscopic polarization as Taylor series with respect to the electric field (Eq.1.20) is influenced by free electrons ($\gamma \ll 1$). The meaning and definition of γ is given in Sec. 1.2.2 in which plasma generation as the "stormy" counterpart to the Kerr effect is described in its various occurrences. At this stage the regime of *perturbative nonliner optics* [28] described in section 1.2.1 has been left when intensities exceed the 10^{13} W/cm^2 level. Beyond 10^{14} W/cm^2 the *strong field regime of nonlinear optics* is entered and characterized by a γ parameter larger than one.

Before entering the strong field regime the basic principles of nonlinear optics are collected in section 1.2.1. In order to understand these phenomena one has to consider electromagnetic wave propagation in dispersive nonlinear media which is governed by Maxwell's equations, $cf.$ Eq.(A.1)–(A.4). From this staring point the wave equation in vacuum and basic propagation equation in linear dielectric media can be gained which is presented in App. A.1. In case of intense

fs pulses the concept of linear and nonlinear electric susceptibility [32–34] enables explanation of many light-matter interactions which are relevant for this thesis, $e.g.$ Kerr self-focusing and 4WM. Therefore the derived nonlinear envelope equation [35] serves as a theoretical background to explain additional nonlinear propagation effects like pulse splitting and shock waves. Further increase of intensity bridges the way towards the strong field regime [28] which leads to the physics of laser induced plasma filaments [36, 37].

1.2.1 Kerr effect

The current subsection is dedicated to the phenomena which arise from the third order nonlinearity $\chi^{(3)}$. With the relation for the refractive index $n = \sqrt{1+\chi}$ the total refractive index n can be approximated to be

$$\begin{aligned} n(\mathbf{r},t) &\propto n_0 + \frac{1}{2} n_2' \left|\mathbf{E}(\mathbf{r},t)\right|^2 \\ &= n_0 + \frac{1}{2} n_2 \mathbf{I}(\mathbf{r},t) \\ &= n_0 + n_{Kerr}(\mathbf{r},t) \end{aligned} \tag{1.33}$$

and has become intensity dependent in case of nonlinear optics. This time dependent electric field is the earlier mentioned optical Kerr effect. The factor $1/2$ denotes a time average $\langle \mathbf{E} \cdot \mathbf{E} \rangle = 1/2 \left|\mathbf{E}\right|^2$ of the electric field. The nonlinear index is related to the susceptibility via [32]

$$n_2 \approx \frac{1}{n_0^2} Re\left\{\chi^{(3)}\right\} \ . \tag{1.34}$$

Since the emitted laser light is distributed in both time and space $\mathbf{I} = \mathbf{I}(\mathbf{r},\mathbf{t})$, the refractive index $n(\mathbf{r},t)$ is now time and space dependent. The transverse effect leads to self-focusing of the beam and is called Kerr lensing whereas the longitudinal time dependent refractive index causes the pulse to undergo self phase modulation (**SPM**). In the following, these important effects on pulse propagation will be presented successively. A complete description of combined spatio-temporal interaction necessitates the solution of the nonlinear propagation equation which is presented in appendix A.1 and will be used to explain additional phenomena in section 1.2.3.

Kerr lens effect

The transverse Kerr effect was the first type of intensity dependent refractive index, observed in 1964 by Chiao $et\,al.$ [38], as a geometrical "self-trapping of optical beams". The authors explained it as total internal reflection because of the transverse intensity dependent refractive index gradient which prevented from spatial spreading by diffraction. The concept of spatial self-focusing was manifested in further experiments in the late 60s [39]. Figure 1.2 shows the principle of self-focusing when a collimated beam enters a $\chi^{(3)}$ medium. The center of the beam containing the

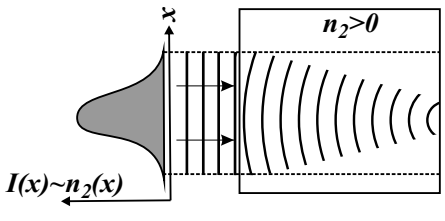

Figure 1.2: Self-focusing or Kerr lensing, respectively, due to the intensity dependent refractive index in Eq.(1.34). The most intense parts in the center of beam are retarded most and a plain wave front of a collimated beam becomes curved like in the case of a focusing optic.

maximum intensity experiences the highest refractive index and is thus retarded to a larger extend as the wings. Hence the plain wave front of the collimated beam is bent as with a focusing optic. Strictly speaking, the focusing gets even tighter as the pulse propagates because the intensity depends on the square of the beam diameter. A certain threshold power value named critical power P_{cr} was found by Marburger and was defined as the starting point from where on a diffraction limited beam starts self-focusing [40]

$$P_{cr} = 0.14\frac{\lambda_0^2}{n_0 n_2} \,. \tag{1.35}$$

Besides its role for self-guiding of plasma channels in air this effect is of prime importance for the operation of self-mode-locked fs oscillators [41]. This operation releis on the fact that stronger focusing due to the Kerr effect reduces intra-cavity losses compared to weaker focusing in cw operation. The self-focusing, however, is halted by pulse lengthening due to GVD in Eq.1.18 and in case of filamentation by plasma creation (Sec.1.2.2). Values for n_2 are given in table 3.1 and additional information about the measurement of n_2 can be found in Ref. [42] for solids and in Ref. [43] for gases. The n_2 value for glasses is roughly three orders of magnitude higher, than for gases.

Self phase modulation

The observation of these spatial effects was followed by earliest frequency broadening experiments in fused silica under ps pulse excitation by Alfano and Shapiro [44] in 1970. For simplicity, a Gaussian temporal envelope function is considered for the description with an intensity profile

$$I(t) = I_0 e^{-(\frac{t}{\tau})^2} \tag{1.36}$$

which is plotted in Fig. 1.3a as solid line. The intensity is related to the electric field with its fast oscillating carrier frequency ω_0 through

$$\begin{aligned} I(t) &= \frac{c\epsilon_0}{2}\left|E_0 e^{i(k(t)z+\omega_0 t)}\right|^2 \\ &= \frac{c\epsilon_0}{2}\left|E_0 e^{i(\phi(t))}\right|^2 \,. \end{aligned} \tag{1.37}$$

A time dependent phase arises from the refractive index defined of Eq. (1.34)

$$\phi(t) = \frac{2\pi n(t)}{\lambda} z + \omega_0 t \qquad \text{with} \qquad n(t) = n_0 + n_2 I(t)/2 \tag{1.38}$$

where c is the speed of light, λ the laser wavelength of the light propagating along the z direction. The temporal characterization of the induced phase modulation $\phi(t)$ is the quantity of the instantaneous frequency $\omega(t)$ which is given by the time derivative of $\phi(t)$

$$\begin{aligned} \omega(t) = \frac{d\phi(t)}{dt} &\propto \omega_0 + \frac{n_2\omega_0 z}{2c}\frac{\partial I(t)}{\partial t} \\ &\propto \omega_0 - \frac{n_2\omega_0 z}{4c}\frac{I_0 t}{\tau^2} e^{-\frac{t^2}{\tau^2}} \,. \end{aligned} \tag{1.39}$$

From Eq.(1.39) it can be seen that SPM increases linearly with propagation distanze z and inversely to the second power of the pulse duration τ which is given as σ-width of the Gaussian in Eq. (1.36). The corresponding evolution of the temporal chirp (instantaneous frequency $\omega(t)$) is visualized in Fig. 1.3b as solid line. In the beginning, $\Delta\omega(t)$ is negative at the pulse front causing a red shift and

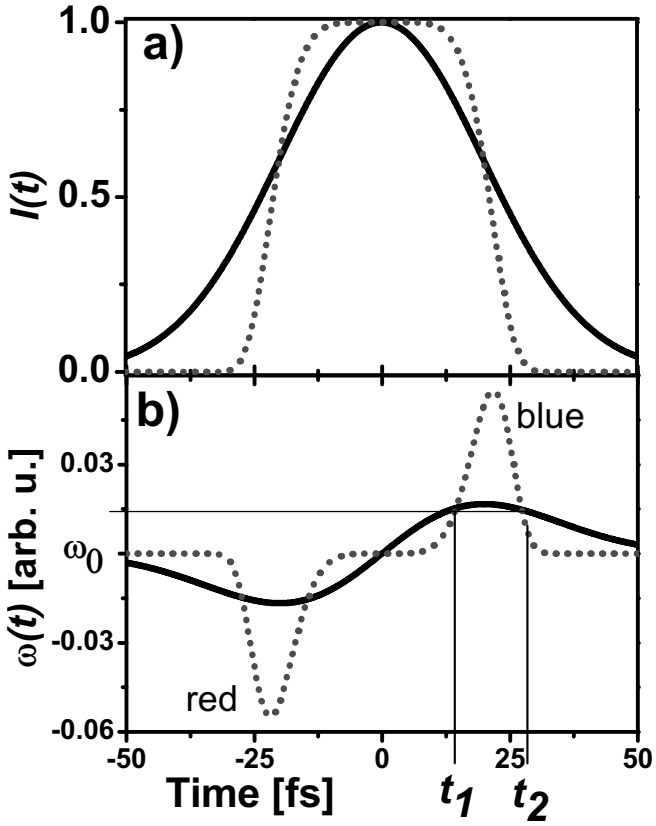

Figure 1.3: Different temporal shapes exhibit a different temporal phase evolution. Pulse envelope for Gaussian (solid line) and super-Gaussian (dotted line) pulses in a). The change of the refractive index is directly proportional to the intensity. Induced phase shift around ω_0 in b). Generally, in the beginning $\Delta\omega(t)$ is negative at the pulse front causing a red shift and becomes positive at the back, where blue wavelengths are generated. Further, the steeper the slope of the pulse envelope, the wider is the generation of new frequencies. Corresponding power spectra are plotted in Fig. 1.4.

becomes positive at the back where blue wavelengths are generated. In the central region of the Gaussian pulse, a linear positive chirp is appearing. On the other hand, for intensity shapes with steeper slopes which can be obtained from super-Gaussian pulses ($I(t) = I_0 e^{-(\frac{t}{\tau})^{2m}}$ with $m = 3$ in this particular case) the center of the pulse remains unchirped. Again, the steeper wings achieve a wider spectral broadening which can be verified in Fig. 1.4 were the power spectral density of both pulse shapes is plotted. The power spectrum $I(\omega)$ is calculated by Fourier transforming the time domain representation of the electric field with its time dependent refractive index $n(t)$

$$I(\omega) = \left| FT \left\{ e^{-(\frac{t}{\tau})^2} E_0 e^{i(z\frac{2\pi}{\lambda} n(t) + \omega_0 t)} \right\} \right|^2 . \tag{1.40}$$

The broadened spectrum is no longer homogeneous but consists of peaks whose number M depends on the maximum phase shift. For Gaussian pulses the phase can be found to be [33]

$$\pm\phi_{max} = \frac{\omega_0 n_2 P_0 z}{c A_{eff}} \tag{1.41}$$

$$\approx (M - \frac{1}{2})\pi \tag{1.42}$$

where P_0 denotes pulse power and $A_{eff} = \pi r_0$ the effective area with r_0 as focus radius. The maximum phase shift, obeying the same function as the intensity, occurs the center of the pulse at $t = 0$. The oscillatory structure in the spectrum of Fig. 1.4 arises from constructive and destructive interference and can be understood in the time domain by referring to Fig. 1.3b. The same frequency component is generated at two different times t_1 and t_2 with their corresponding relative phases. The value of this relative phase determines whether interference is positive or negative. This interference gives rise to the characteristic SPM spectra of Fig. 1.5. Since the SPM broaden-

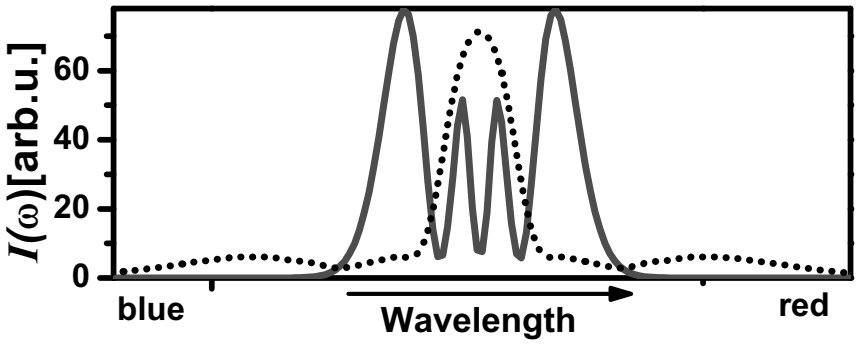

Figure 1.4: Different temporal shapes exhibit a different spectral broadening. The solid (dotted) line displays the broadening due to Kerr effect of Gaussian (super-Gaussian) pulses corresponding to Fig. 1.3 in nonlinear media. The spectral shape depends strongly on the intensity gradient and steeper pulse flanks cause wider broadening.

ing in first approximation is proportional to $n_2 I$, the spectral FWHM increase is proportional to the intensity of the pulse. The broadening is symmetric as long as the input pulse shape is symmetric, the nonlinear response of the medium is instantaneous and dispersion effects are neglected. In a pure SPM process of Gaussian pulses, the temporal width always stays constant with the input temporal width, regardless of spectral shape and phase.

It is further emphasized that, the extension of the broadening increases with increasing initial bandwidth even if the nonlinearity ($n_2 I$) is constant, at what the shape of the envelope and the phase of the broadened spectrum remains the same for all input bandwidths. This means that SPM of more and more shorter pulses does not only benefit from the pulse nonlinearity but also from its spectral width. In other words, reaching a desired output bandwidth by using a larger input bandwidth is advantageous over using a higher intensity because the latter will induce more complicated phase functions and thus more spectral modulations to the spectral shape.

The shape of SPM spectra changes significantly when an initial prechirp is added to the pulse, even if input intensity and bandwidth remain the same. Of course, the plasma generation affects the broadening drastically. For direct comparison between symmetric SPM and with additional plasma blue shift, the frequency axis in Figs. 1.5 and 1.7 have the same scaling increment. An

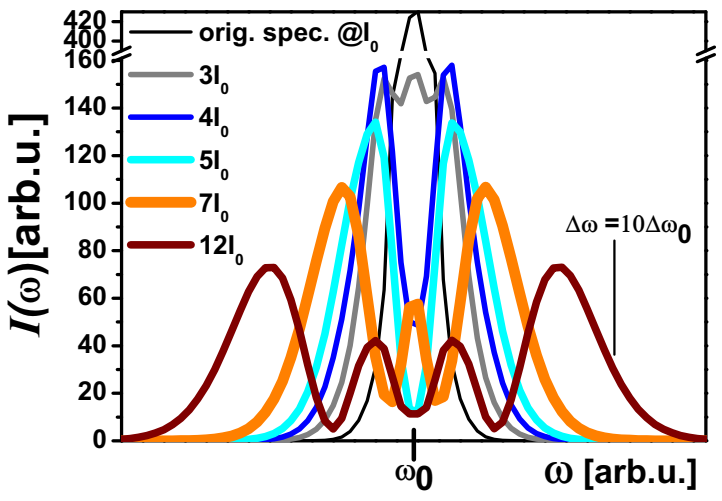

Figure 1.5: Symmetric broadening via SPM as a function of increasing peak intensity. I_0 is the threshold beneath which no broadening occurs (black curve). Increasing peak intensity by a factor of 12 leads to gradual increase of spectral FWHM by a factor 10 (brown curve) which exhibits characteristic amplitude modulations. The temporal shape remains constant for all intensities and spectral shapes, respectively.

introduction on how the plasma properties influence the continuum generation is presented in the next subsection.

1.2.2 Plasma creation

From a physical point of view, a plasma describes a macroscopic many body system of charged particles which is neutral outside. The number of particles is assumed to be sufficient that the system properties[5] depend on electromagnetic interactions of the particles among themselves or on the interaction with an external field, at which heavy ions are treated as a locally fixed positive background. Further it is assumed that in absence of an external field collisions and recombinations on a sub ps time scale are negligible. (The decay time for laser induced plasma was experimentally ascertained to be 130 ns [45].) Furthermore, radiation processes which arise from the interaction of radiation with a free electron gas are not considered as source terms in Eq.(1.5) throughout this work.

A usual plasma characteristic is the Debye length λ_D which ascertains the distance within charge separation occurs

$$\lambda_D = \sqrt{\frac{\epsilon_0 k_B T}{e^2 \rho_e}}\,, \tag{1.43}$$

whereby k_B is the Boltzman constant, T the plasma temperature, e the electron charge and ρ_e is the density of electrons. Typically, for considerations on length scales shorter than λ_D one has to look at individual particles and their mutual interactions. On larger scales than λ_D, the plasma properties can be characterized by collective phenomena. Such a collective phenomenon might arise when an electromagnetic wave is propagating through ionized matter and forces the free electrons to undergo periodic movements with the oscillation period ω_p

$$\omega_p = \sqrt{\frac{e^2 \rho_e}{\epsilon_0 m_e}}\,, \tag{1.44}$$

with m_e being the electron mass whereby ω_p is named plasma frequency. Plasma oscillations arise when an external field breaks the charge neutrality and accelerates the free electrons. $1/\omega_p$ is the characteristic time within which the plasma reacts on this perturbation, $i.\,e.$ the perturbation is shielded [46].

Electromagnetic waves in plasma

Incident light waves are such a perturbation. Concerning plasma and light, it should be clarified that plasma can on the one hand influence an incident field and on the other hand generates new radiation itself. For current work, plasma radiation processes like Bremsstrahlung, recombination radiation and characteristic line radiation are not relevant because they do not contribute to propagating laser field. In general, depletion of the propagating laser field is assumed to be negligible. From the classical equation of motion for free electrons and Maxwell equations in vacuum (A.1-A.4) the wave equation for electromagnetic waves $E(t) = E_0 e^{i(kz-\omega_0 t)}$ in plasma can be derived [47]

$$\left(\frac{\partial^2}{\partial t^2} + \omega_p^2 - c_0^2 \frac{\partial^2}{\partial x^2}\right) E = 0\,. \tag{1.45}$$

The condition $\omega_0 = \omega_p$ defines the critical density ρ_{crit} which follows directly from Eq.(1.44) to be

$$\rho_{crit} = \frac{\epsilon_0 m_e \omega_0^2}{e^2}\,, \tag{1.46}$$

[5] Properties like e.g conductivity, temperature or refractive index

Critical density thereby means that for $\omega_0 < \omega_p$, k is becoming imaginary and the plasma gets opaque for the incident light. According to Eq.(1.46), the experimentally used Ti:Sa wavelength of 800 nm goes around with a critical density ρ_{crit} = 1.7x10^{21} cm^{-3} and is thus of no concern for weakly ionized atmospheric air since plasma densities are much lower. Experimental verifications of the plasma density in fs laser filaments differ from case to case, but a value of 10^{16}-10^{17} cm^{-3} [48] is a reasonable average of different literature data. For $\omega_0 > \omega_p$ the plasma is *underdense* and the electromagnetic wave can propagate with a real refractive index n_p [47]

$$n_p = \sqrt{n_0^2 - \frac{\omega_p^2}{\omega_0^2}} = \sqrt{n_0^2 - \frac{\rho_e}{\rho_{crit}}} \,. \tag{1.47}$$

If further $\rho_e \gg \rho_{crit}$ the square can be developed leading to:

$$n_p = n_0 - \frac{\rho_e}{2n_0\rho_{crit}} \,. \tag{1.48}$$

The second term denotes that free electrons lower the refractive index if its carrier frequency of the laser is larger than plasma frequency ω_p. Therefore, it is supposed to be the "self-defocusing" counter part to Kerr self-focusing of Fig. 1.2. Since ionization recombination takes place on a nanosecond time scale, the decrease of n_p is a monotone function and causes an asymmetric phase shift $\Delta\Phi_e(t)$ of the light pulse by

$$\Delta\Phi_e(t) = -\frac{\rho_e(t)}{\rho_{crit}} \frac{z\pi}{n_0\lambda} \,. \tag{1.49}$$

According to basic relations of Fourier transformation [49], where a phase shift in one plane causes a translation in the Fourier plane, the effect of frequency shifting can be understood. Since the phase shift $\Delta\Phi_e(t)$ is monotonic the corresponding spectral shift is onesided, other than in case of symmetric SPM. The negative sign for the plasma refractive index thus forces the so called *plasma blue shift* which was first observed in gases in 1974 [50] and has at that time been considered as a possible mechanism for generation of few optical cycles [51].

Further on, lowering of refractive index does not only contribute to spatial (self)-defocusing of the laser beam but also modifies dispersive properties of the medium. In this regard, Koprinkov *et. al* discuss plasma generation as a counterpart to normal GVD [52] as well as a reason for self compression and spatio-temporal soliton generation [53]. The macroscopic phenomena like plasma refractive index n_p and plasma frequency ω_p, origin from an ionization process which takes place on individual particles where the released electrons can extract energy from the laser field. The time averaged kinetic energy of free electrons in a periodic field, which is associated with electron oscillations about their equilibrium position (the cycle averaged kinetic energy of the wiggling electron), is referred to as pondoromotive energy U_p or jitter energy [28]:

$$U_p = \frac{e^2E^2}{m_e\omega_0^2} = \frac{e^2\,\langle E_0^2\rangle}{2m_e\omega_0^2} \,. \tag{1.50}$$

Rewriting the previous equation in convenient units yields:

$$U_p[eV] = 9.33 \times 10^{-14} \cdot I[\mathrm{W/cm^2}] \cdot \lambda^2[\mu\mathrm{m}]. \tag{1.51}$$

The amplitude a_e of the wiggling motion of an electron is given by [54]:

$$a_e = \frac{e\,E_0}{m_e\omega_0^2} = \frac{4U_p}{e\,E_0} \,. \tag{1.52}$$

Recombining electrons can emit the energy U_p plus the ionization energy and generate light in the vacuum ultra violet region, a process known as high harmonic generation [54]. Another remarkable observation is, that light induced currents in the plasma lead to coherent radiation of sub THz electromagnetic pulses [55]. This remote generation of Thz pulses is another intrinsic feature of fs filamentation in air.

Absorption in plasma

Among different possible ways of creation, only light induced and non resonant ionization will be addressed herein after. Overviews of multi photon ionization mechanisms can be found in Refs. [56, 57]. This field was pioneered by Keldysh in 1964 who classified the nonlinear process by the adiabaticity -or Keldysh parameter γ which allows distinguishing between the two most important ionization mechanisms: multi photon ionization (**MPI**) and tunnel ionization (**TI**). γ is defined as

$$\gamma = \sqrt{\frac{E_I}{2U_p}} = \frac{\omega}{E_0}\sqrt{\frac{2E_I m_e}{e^2}} \begin{cases} < 1: & \textbf{TI (high intensity)} \\ > 1: & \textbf{MPI (low intensity)} \end{cases} \tag{1.53}$$

and can be interpreted as the ratio of classical round trip time of the bound electron over the characteristic tunneling time through the potential barrier [58]. Keldysh's model was extended by Ammosov, Delone and Krainov for any atoms and atomic ions and is known as ADK theory. Further improvements on Keldysh's theory towards diatomic molecules can be found in Refs. [59, 60]. MPI is explained utilizing the photon picture of light in Fig. 1.6a. Like in parametric

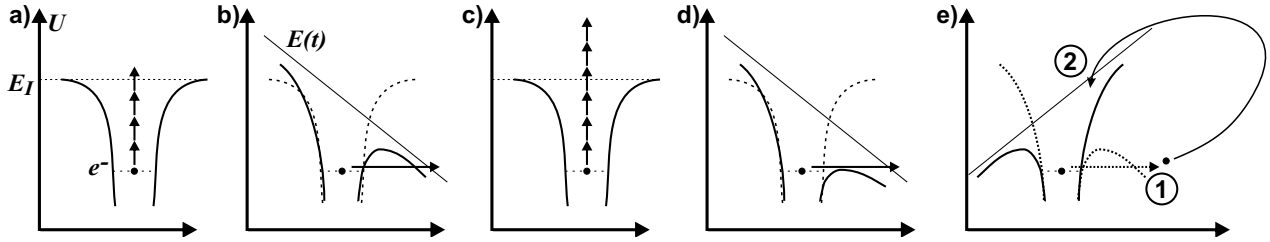

Figure 1.6: Ionization diagrams in intense laser fields in one dimension. a) multi photon ionization (MPI), b) tunnel ionization (TI), c) above threshold ionization (ATI), d) over the barrier ionization (OTBI) and (non)-sequential multiple ionization in e). The pictures are ordered with increasing intensity. For details see text.

processes the simultaneous absorption of a sufficient number of photons enables overcoming the energy gap, necessary for excitation from the bound state into the continuum. Following Keldysh's theory the probability W_{MPI} for MPI in the limit of $\gamma \gg 1$ can be derived [36, 37]

$$W_{MPI}(I) = \sigma^{(K)} I^K \,, \tag{1.54}$$

with K being the minimum number of photons, necessary to bridge the gap between the bound state and the continuum. The factor $\sigma^{(K)}$ denotes an element dependent multi photon cross section which generally increases with frequency ω of the driving laser. That means ionization becomes more probable at shorter wavelengths. A specialty of MPI is above threshold ionization (ATI) where more low energy photons were absorbed than necessary for overcoming the level E_I [61,62], as drawn in Fig. 1.6c. Excess energy is transferred to kinetic energy of the free electrons which eventually collide with other particles. The transitional range from the MPI regime (I $\leq 10^{13}$ W/cm^2 at $\gamma < 1$) to TI (I $\approx 10^{13}$-10^{15} W/cm^2 at $\gamma > 1$) is passed by increasing laser intensity and denotes leaving the validity of nonlinear optics, like described in Sec. 1.2.1. TI becomes dominant over MPI when the tunnel time for outer-shell electrons through the barrier is shorter than the

oscillation period of the laser field [60]. This modified barrier originates from the superposition of the binding Coulomb potential with the external laser field and is depicted in Fig. 1.6b. The width and hight depend on the laser intensity and the tunneling probability increases with wavelength. When the external field strength is comparable to the Coulomb field, the potential wall is bent (Fig. 1.6b) and reduces to a finite thickness through which the electron might tunnel out following an exponential law

$$W_{TI}(I) \cong \sigma_{TI} exp\left[-\frac{\alpha_{TI}}{\sqrt{I}}\right] . \tag{1.55}$$

With the factor α_{TI}

$$\alpha_{TI} = \frac{e^5 m^2}{\hbar^4 (4\pi\epsilon_0)^3} \sqrt[3]{E_I / E_{Hydrogen}} \tag{1.56}$$

in the exponent, where $E_{Hydrogen}$ denotes the ionization energy of the hydrogen atom. A detailed explanation and discussion of the factor of the exponential α_{TI} is given in [37, 60]. In their work Mishima $et\ al.$ [60] state explicitly that the ionization mechanism (TI) for atoms and randomly oriented diatomic molecules is exactly the same besides the prefactor which determines the absolute ion yield. Intensities higher by on order of magnitude lead to a suppression of the Coulomb potential and the former bound electron escapes into the continuum, shown in Fig. 1.6d. This over the Barrier ionization (OTBI) stays in background to earlier inserting TI because $\gamma \gg 1$, meaning it requires more intensity. Nonetheless it becomes more and more relevant for few cycle pulses since the total number of tunneling events is restricted with extremely short pulses [28].

From the different ionization rates $W_{ionization}$ for different mechanisms introduced above, the change of the electron density $\rho_e(t)$ can be calculated as

$$\frac{\partial \rho_e(t)}{\partial t} = W_{ionization}(\rho_0 - \rho_e(t)) , \tag{1.57}$$

with ρ_0 as the initial gas density. Under the assumption of a weakly ionized plasma in atmospheric air, where the density of neutral molecules is much higher compared to the one of free electrons ($\rho_{atm} \gg \rho_e(t)$), the previous equation reduces to

$$\frac{\partial \rho_e(t)}{\partial t} = W_{ionization} \rho_{atm} . \tag{1.58}$$

After the first electron is ejected, it can be accelerated along several trajectories depending on the exact timing of its birth. It might fly away and never come back. If it comes back, it can either recombine leading to high harmonic generation or scatter at the parent ion. In the special case of elastic scattering under an angle of 180°, drift velocities with a kinetic energy up to $10 \times U_p$ can be achieved [63]. Hitherto mentioned ionization mechanisms relay on the single active electron approximation which means that only one electron of the atom is changing its energy during ionization and the remaining electrons are noninvolved. However, inelastic scattering of the recoil electron leads to interaction with the remaining neighbours and causes multiple ionization as shown in Fig. 1.6e. The theoretical description of multiple ionization as sequential process leads to orders of magnitude lower ionization rates than verified experimentally. Multiple ionization experiments for noble gas atoms caused by fs pulses showed a lucidly higher rate, even for intensities in the 10^{14} W/cm^2 regime [64, 65]. Thus non-sequential ionization, meaning that two (or more) electrons escape simultaneously is the main mechanism for higher charged ions. For overview and further reading on non-sequential ionization models see $e.g.$ Refs. [58, 66, 67]. This process is listed here, because intensity regime is close to conditions reached by geometrical focusing. Additional self-focusing still might increase intensity and thereby locally boost the electron density.

Finally, the contribution of avalanche ionization (AI) by electron impact is mentioned here, although its occurrence in fs laser plasmas is controversially discussed in literature. However, if a peak intensity of 10^{15} W/cm^2 and a maximum kinetic energy of $10\times U_p$ is considered, the amplitude for the wiggling electron according to Eq.(1.52) becomes about 30 nm. For comparison, the mean free path in air at atmospheric pressure is about 66 nm [68]. Avalanching leads to a multiplication of electrons in a laser field with a rate

$$W_{AI}(I) = (\sigma_e/E_I)I \; . \tag{1.59}$$

The electron impact ionization cross sections σ_e are listed in Ref. [69] and calculated multi photon cross sections σ_K are summarized in Ref. [37].

The closing concern is dedicated to losses during nonlinear propagation. Losses might influence the time dependent refractive index and thus contribute to spectral and temporal changes during propagation [28]. Such temporal reshaping becomes more important as the number pulse cycles decreases (10 fs) and intensity increases (>10^{15} W/cm^2). However, multi photon absorption was declared to be negligible compared to MPI for filamentation in air [36] at lower intensities. Under current experimental conditions in the lab, distinct losses in terms of energy depletion from the laser beam were not observed. Typically, the total transmission of filamentation in air was found to be about 96%.

1.2.3 Extended description

Before addressing additional nonlinear propagation effects being discussed in literature, the interplay between plasma generation and Kerr Effect and their influence on WL generation is addressed. The basic message is, that spectral broadening $\Delta\omega$ is proportional to the time derivative of the nonlinear temporal phase

$$\Delta\omega \propto \frac{\partial\phi(t)}{\partial t} \propto \frac{\partial n(t)}{\partial t} \; . \tag{1.60}$$

That means, the larger the change of refractive index, the wider the spectral broadening. The total time depending refractive index $n(t)$ constitutes a linear part n_0 and a nonlinear one which splits into Kerr- $n_{Kerr}(t)$ and a plasma $n_p(t)$ contribution:

$$n(t) = n_0 + n_{Kerr}(t) + n_p(t) \; , \tag{1.61}$$

$$n(t) \cong n_0 + n_2 I(t) - \frac{\rho_e(t)}{2n_0\rho_{crit}} \; . \tag{1.62}$$

The time depending phase of the electric field $E(t) = E_0 e^{i\phi(t)}$ varies with the propagation distance z and is given through

$$\phi(t) = k(t)z - \omega_0 t = \frac{2\pi n(t)}{\lambda_0} z - \omega_0 t \; . \tag{1.63}$$

A representation of the light induced phase change in the time domain is the quantity of the instantaneous frequency $\omega(t)$ which is given by the time derivative of $\phi(t)$:

$$\omega(t) = -\frac{d\phi(t)}{dt} \propto \omega_0 + \frac{\omega_0 z}{c}\left(-n_2\frac{\partial I(t)}{\partial t} + \frac{1}{2n_0\rho_{crit}}\frac{\partial\rho_e(t)}{\partial t}\right) \tag{1.64}$$

where the first term in brackets of Eq.(1.64) denotes the Kerr part whose effect on spectral broadening around the fundamental frequency ω_0 was demonstrated in Fig. 1.5. The second term displays the evolution of the plasma density. Both contribute to the creation of new frequencies and are

proportional to z. The evolution of plasma density (last term in Eq.(1.64)) including MPI, TI and AI under the condition of an underdense plasma ($\rho_e \ll \rho_{atm}$) writes as

$$\frac{\partial \rho_e(t)}{\partial t} = \underbrace{\sigma^{(K)} I(t)^K \rho_{atm}}_{\text{MPI for } \gamma \gg 1} + \underbrace{\sigma_{TI} e^{\left[-\frac{\alpha_{TI}}{\sqrt{I}}\right]} \rho_{atm}}_{\text{TI for } \gamma \ll 1} + \frac{\sigma_e}{E_I} I \rho_e(t) \; . \tag{1.65}$$

The Keldysh parameter γ Eq.(1.53) describes the intensity region of validity for different ionization mechanisms. The first term on right hand side in Eq.(1.65) expresses MPI which takes place at intensities $\leq 10^{13}$ W/cm^2. The second term belongs to the strong field regime (10^{14}-10^{15} W/cm^2) where tunneling is the dominant process. The last term accounts for the possibility of AI which multiplies the former generated electron density with laser intensity.

As mentioned in Sec. 1.2.1, SPM exhibits symmetric broadening because the time derivative of the Gaussian envelope changes its sign. In contrast, the refractive index change due to creation of free electrons does not change its sign and thus a spectral blue shift occurs which is simulated in Fig. 1.7. It shows the spectral broadening according to Eq.(1.62) as a function of increasing peak intensity I_0 under the assumption of multi photon ionization as exclusive contribution.

Intensity range and simulation parameters are the same as in Fig. 1.5 where the behavior of pure SPM was calculated. Scaling constants for plasma creation are such that the resulting change of refractive index is on the same order of magnitude like the one of SPM. Figure 1.7a shows the fundamental spectrum in black at a reference intensity I_0 underneath which no broadening occurs, neither for SPM nor for plasma effects. The orange curve at $8 \times I_0$ is almost similar to the pure SPM case (see the brown curve in Fig. 1.5). An intensity of $9 \times I_0$ as black line in Fig. 1.7b unbalances the maxima in the spectrum and further intensity increase towards $11 \times I_0$ exhibits a rapid change of the spectral shape. The drastic change is caused by the fact, that the plasma density increases with the intensity to the Kth power ($cf.$ Eq.(1.54)), whereas SPM grows linearly with intensity. A small step further to $12 \times I_0$ in Fig. 1.7c leads to a complete depletion of the fundamental light and a blue shift that reaches the second harmonic.

The power spectrum $I(\omega)$ is calculated by Fourier transforming the time domain representation of the electric field with the nonlinear plasma contribution $\Delta\Phi_e(t)$ (1.49)

$$I(\omega) = \left| FT \left\{ E_0 e^{i(\frac{2\pi}{\lambda} n_{Kerr}(t)\, z - \omega_0 t + \Delta\Phi_e(t))} \right\} \right|^2 , \tag{1.66}$$

Comparison shows, that onset of plasma blue shift starts at $9 \times I_0$ which connotes $\approx$ five times higher threshold for plasma effects compared to SPM effects. Once started, plasma induced spectral changes evolve much stronger because of the proportionality to K-th power of intensity. For comparison pure SPM at maximum intensity is plotted as black line in Fig. 1.7c. The strong blue shift bridging the region from the laser fundamental to its second harmonic gives rise to almost complete depletion of Stokes wavelengths.

SPM causes a symmetric broadening (see Fig. 1.5) around the laser fundamental with sequential emergence of new frequencies at different positions under the pulse envelope. Red spectral components appear at the beginning of the pulse and blue ones at the trailing edge. On the other hand the ionization front leads to a monotonic drop of plasma refractive index n_p. It reaches its minimum after the intensity maximum of the pulse, forces spectral broadening on the anti Stokes side and additionally a shift as a whole towards short wavelengths (see Fig. 1.7). Detailed discussion of these effects which were used for simulating measured WL spectra is carried out in Sec. 3.5.2.

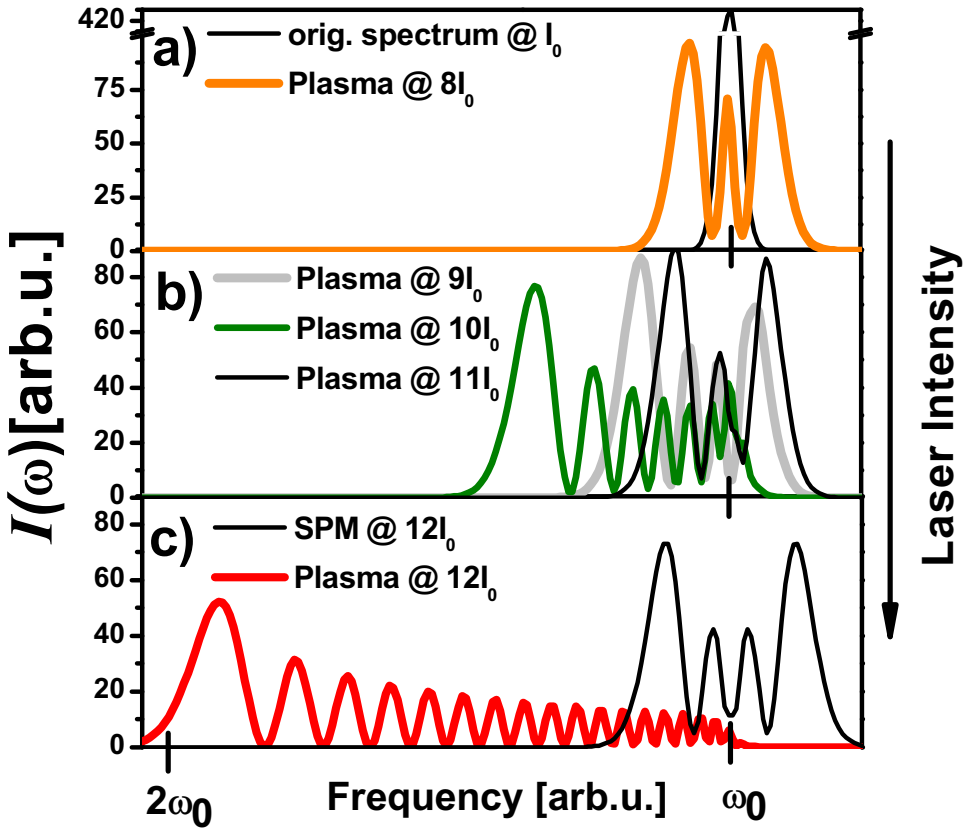

Figure 1.7: Intensity dependence of the plasma contribution leading to a blue shift at high intensities. The spectral changes can be verified as function of increasing peak intensity I_0. Multi photon ionization ($cf.$ Eq.(1.54)) is simulated as underlaying ionization mechanism to calculate the plasma refractive index. Intensity range and normalization is the same as in Fig. 1.5 where pure SPM is simulated. For the given combination of $n_2 I$, the onset of blue shift at $9 \times I_0$ states, that plasma influences on the spectrum occur with five times higher intensity compared to onset of SPM effects. Pure SPM at maximum intensity of Fig. 1.5 is plotted as black line for comparison in c).

Additional effects

Because filamentation is a propagation phenomenon, an isolated treatment depending only on the variable time like in Eqs.(1.64) and (1.65) is not sufficient. In order to achieve a comprehensive simulation of propagation, the starting point for sophisticated 3-D plus time calculations is the *nonlinear envelope equation* (NEE) *of first order in propagation coordinate* [32, 35]:

$$\left[\frac{\alpha_0}{2} + \frac{\partial}{\partial\xi} - \frac{ic}{2\omega_0 n_0}\left(1 + \frac{i}{\omega_0}\frac{\partial}{\partial t'}\right)^{-1}\nabla_\perp^2 - i\widehat{D}\right] A(\mathbf{r}_\perp, \xi, t') = i\frac{2\pi\omega_0}{n_0}\left(1 + \frac{i}{\omega_0}\frac{\partial}{\partial t'}\right) B\,. \quad (1.67)$$

Its derivation is explained in App. A.1 and the main aspects for filamentation are presented here. It allows calculation of a nonlinear polarization, space-time coupling, dispersion and self induced changes. Equation(1.67) is an extension of the vacuum wave equation where last term in square brackets on left hand side $(\widehat{D})$ accounts for dispersion in the material. Nonlinear response of the dielectric medium is included by the nonlinear source term B on the right hand side of Eq.(1.67). The transversal Laplace operator $\nabla_\perp^2 = \frac{\partial^2}{\partial x^2} + \frac{\partial^2}{\partial y^2}$ stands for transverse diffraction. The combined

time and space derivative $\left(1+\frac{i}{\omega_0}\frac{\partial}{\partial t'}\right)^{-1}\nabla_\perp^2$ is responsible for space-time focusing [70]. $\xi = z$ is the propagation direction and t' a retarded time frame moving with the pulse at group velocity v_g. In the above derivation the laser field $\mathbf{E}(\mathbf{r},t)$ and the nonlinear polarization (see Eq.(A.22)) are decomposed in an envelope function and a fast oscillating term in the laboratory reference frame z,t

$$\mathbf{E}(\mathbf{r},t) = A(\mathbf{r}_\perp,z,t)e^{i(k(\omega)z-\omega_0 t+\phi_0)} + c.c.\,. \tag{1.68}$$

For example, an instantaneously responding Kerr medium is represented by a function B [32, 33]

$$B(\mathbf{r}_\perp,z,t,A) = \frac{3}{8n_0}\Re(\tilde{\chi}^{(3)}(\omega))\left|A(\mathbf{r}_\perp,z,t)\right|^2 A(\mathbf{r}_\perp,z,t)\,. \tag{1.69}$$

A further extension of the NEE(1.67) including plasma generation is discussed in [36, 71, 72]. Some nonlinear phenomena arising from $\chi^{(3)}$ susceptibility which are relevant for experimental observations in this thesis are briefly discussed in the following. In particular, the measured WL spectra and the time-frequency structures in the FROG traces are assigned to current standard of knowledge in Chap. 3.

GVD The lowering of the refractive index by plasma generation is not the only counter part to Kerr focusing. In the normal dispersion regime GVD can minder nonlinearity effects such as SPM, self-focusing, self-steepening due to temporal pulse broadening [33, 35]. Additional effects come into play when GVD is included in the propagation by the dispersion operator $\widehat{D}$ in Eq.(A.26). GVD is also discussed to halt catastrophic collapse of beam by generation of pulse splitting, as discussed below [73]. In case of anomalous dispersion (negative GVD) optical solitons can arise.

Self-steepening & shock terms A physically intuitive picture describes self-steepening is an intensity induced amplitude reshaping of the pulse envelope because the velocity for different parts of the pulse becomes intensity dependent ($\Delta n \propto n_2 I$). This means the center travels at lower speed as the tails of the pulse and thus the trailing part catches up with the peak. Mathematically this effect originates from the differential operator $\left(1+\frac{i}{\omega_0}\frac{\partial}{\partial t'}\right)$ on the nonlinear source term B on right hand side of Eq.(1.67) which is also referred to as self-steepening operator T [36]. Self steepening occurs as a result of $\chi^{(3)}$ nonlinearity but not due to plasma creation. If GVD is neglected the intensity dependent amplitude shaping is given by [33, 74]

$$I(t) = I_0\, exp\left[-\left(\frac{t-sI(t)z}{\tau_0}\right)^2\right]\,, \tag{1.70}$$

where the self-steepening parameter s is defined as [74] $s = n_2/\omega_0\tau_0$ and τ_0 is the initial pulse duration. Propagation along the z coordinate leads to an asymmetric shape distortion with energy transfer to the back side of the pulse as simulated in Fig. 1.8. The asymmetry grows with propagation distance and intensity whereby the increasing maximum of the instantaneous frequency is shifted to later and later times. This results in asymmetric broadening towards the blue side. Broadening on the red side is reduced because the intensity slope in the pulse front decreases. All simulation parameters were identical to Figs. 1.7 and 1.5 except of the higher intensity of 18 times I_0. The asymmetric broadening is less blue shifted compared to plasma blue shift through MPI (Fig. 1.7), though the intensity was higher. Further on, without or with only weak dispersion, respectively, self steepening and space-time focusing [70] create an optical shock wave at the rear side of the pulse [35, 71, 75] which means a change of the rear pulse envelope on the order of one oscillation period of the light. Accompanied with the sharp intensity break is a drastic change of temporal phase at the trailing part. Aközbek *et al.* [71] explicitly mention that the sign of the

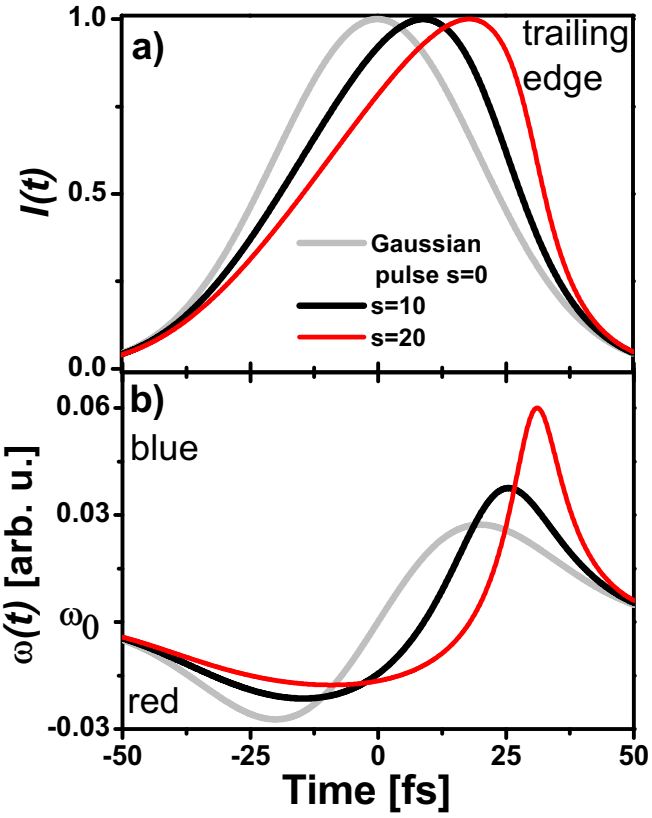

Figure 1.8: Self-steepening is an intensity induced temporal reshaping of the pulse envelope because the peak velocity becomes intensity dependent. Thus the center travels at lower speed and the trailing part catches up with the peak. By that, energy is transferred to the rear side of the pulse. Pulse envelopes a) and instantaneous frequency b) for different self-steepening parameters s. The steeper the trailing edge gets the later and bluer the newly generated frequencies emerge. Corresponding power spectra are plotted in Fig. 1.9.

self-steepening on the Kerr nonlinearity and plasma have the same sign. They expect the plasma generation as support for self-steepening. Other authors assume a decrease of nonlinearity due to defocusing properties of plasma. However, shock waves at the back of the pulse exhibit much more spectral blue shift than self-steepening presented in Fig. 1.9. Experimental observations of these effects were reported in Ref [76].

Pulse splitting One aspect on filamentation is irrevocably, the optical beam does not collapse in an infinitely small focus. Several mechanism are able to arrest the collapse. Among them, there

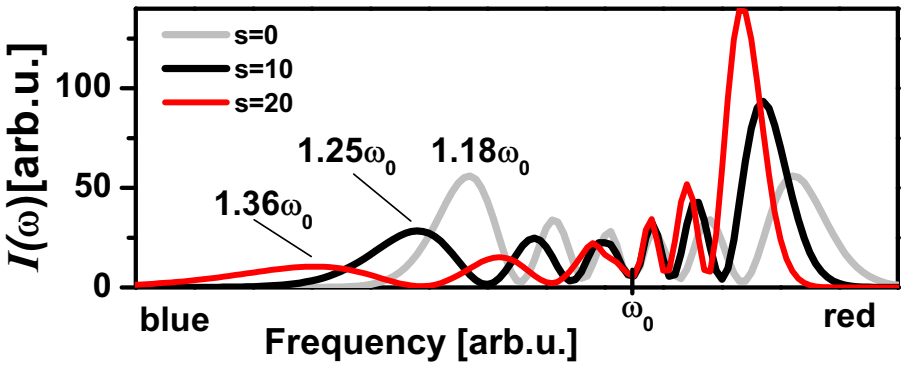

Figure 1.9: Self-steepening spectrum whereby the color coding follows Fig. 1.8. Broadening on the red side shrinks due to a flatter temporal slope in the pulse front. For moderate steepening factors the number of peaks on the blue side remains the same but the spectrum is clearly stretched towards shorter wavelengths. However, plasma blue shift in Fig. 1.7 is much stronger at lower intensities.

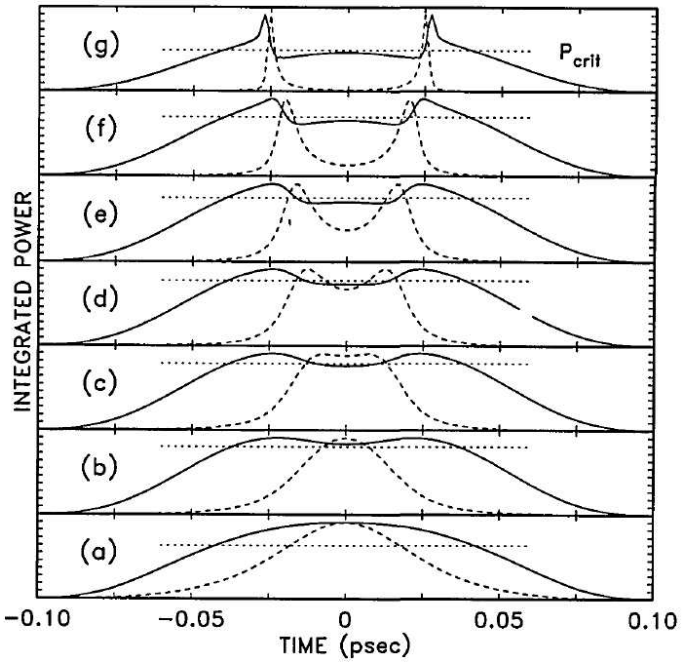

Figure 1.10: Pulse splitting according to Rothenberg [79]. Dashed curves represent the axial intensities whereas solid curves display the spatially integrated power at successive propagation distances: (a) 17.53 cm; (b) 18.6 cm; (c) 18.79 cm; (d) 18.86 cm; (e) 18.92 cm; (f) 18.98 cm; (g) 19.04 cm. The horizontal lines indicate the critical power level. Pulse splitting arises from the competition between the optical Kerr effect and GVD. In the frame of the traveling pulse the red front shifts forward and the blue tail backwards.

are plasma defocusing, GVD [77], saturation of the nonlinear refractive index [78] and pulse splitting as a new option. A Comprehensive understanding of pulse splitting needs the consideration of pulse propagation in three dimensions pulse time with space-time coupling and GVD in the NEE(1.67). From a simple point of view, the process of pulse splitting can be understood as follows. The concentration of energy through space-time focusing enhances SPM which generates a red spectrum in the front of the pulse and a blue part at its back side. Red components travel inherently faster and positive GVD will tend to spread the envelope which means separating the two spectral parts. According to the *moving focus model* [80] where different time slices of the pulse have their own critical power each, these time slices are thus self-focused at different positions along propagation direction. This behaviour is pictured in Fig. 1.10 where the competition between the optical Kerr effect and GVD symmetrically separates the red front and the blue rear side of the pulse as it propagates through the medium. Self-steepening leads to asymmetric energy transfer from the leading to the trailing edge. In contrast, the exclusive action of GVD tends to symmetrically spread the pulse in time. However, the interplay between both effects causes asymmetric temporal splitting of the pulse when power exceeds P_{cr} (Eq.(1.35)) [36, 76]. The symmetry of the split pulses depends further on the ratio of P_{in}/P_{cr}, on the formation of shock dynamics [73] and on the inclusion of higher order dispersion (TOD). Multiple splittings [81–83] are simulated for even higher intensities followed by spatial splittings also referred to as multi filametation.

Self shortening The terminology self-shortening connotes a reduction of pulse duration shorter than the previously incoming one without the requirement of any dispersion compensation. The black box which performs this miracle is the WL filament. In contrast to the normal dispersion regime leading to pulse splitting, for anomalous GVD ($k'' < 0$) power is transferred in the other direction [75]. Recent experimental and theoretical results report on sub 10 fs self-compression which appears at the back side of the pulse [72] in the post-ionization stage of the self-guiding range. In these experiments the red front gives rise to a leading uncompressed pedestal structure. For other experimental evidence for this phenomenon see Refs. [53, 84–86]

Red shift Up to now only the instantaneous response of the dielectric medium was considered. Lehner and Auby [87] modified the propagation equation and included non-instantaneous Kerr effect as a finite time answer for molecular polarization reorientation after excitation by the pulse.

This asymmetry of the time dependent refractive index favors SPM in the red part of the spectrum and is saturating at certain propagation distance. This comparably weak effect is picked up in the discussion of WL broadening in the molecular gas air in Sec 3.5.1

1.3 Nonlinear pulse interaction - Four Wave Mixing

This section is organized in two parts in view of full characterization of the electric field of WL pulses. The first part picks up $\chi^{(3)}$ nonlinearity and its utilization in the framework of the transient grating concept. With this instrument, optical spectrograms (FROG traces) of the fs pulse can be recorded. The second part describes general properties of spectrogram methods [88] which operate in a joint time-frequency domain and their ability for determining the spectral phase of a laser field. The last step, that means solving the inversion problem of retrieving the phase out of the joint time-frequency measurement, is accomplished by Fourier inversion algorithms. Besides its utilization for optical gating, 4WM techniques are used in a wide range of nonlinear optical experiments like $e.g.$ rotational spectroscopy [89], high harmonic generation [90] and nonlinear microscopy [91].

As seen in Sec. 1.1.3, a third order nonlinearity in Eq.(1.23) enables coupling of three input fields $E_j e^{i(k_j z-\omega_j t)}$ with $j = 1, 2, 3$. This leads to, among others, a polarization $P_4^{(3)}$ and the output field $E_4 e^{i(k_4 z-\omega_4 t)}$ is governed by the wave equation

$$\left[\nabla^2 - \frac{\epsilon}{c_0^2}\frac{\partial^2}{\partial t^2}\right] E_4 = \mu_0 \frac{\partial^2 P_4^{(3)}}{\partial t^2} \,. \tag{1.71}$$

The expression for the intensity I_4 of the new radiation[6] reads as [34]

$$I_4 \propto \omega_4^2 \left|\chi^{(3)}\right|^2 |E_1|^2 |E_2|^2 |E_3|^2 \frac{sin^2(1/2\Delta k z)}{(1/2\Delta k z)^2} \,, \tag{1.72}$$

where

$$\begin{aligned} \Delta k &= -k_1 + k_2 + k_3 - k_4 \\ &= \left(-n(\omega_1)\omega_1 + n(\omega_2)\omega_2 + n(\omega_3)\omega_3 - n(\omega_4)\omega_4\right)/c \end{aligned} \tag{1.73}$$

is the phase mismatch accumulated along propagation in z direction. Violation of the phase matching condition will cause a signal decrease according to a $sinc$ function. The take home messages of Eq.(1.72) are: (i) the intensity dependence of the signal (I_4) goes with the third power of the input intensity ($I_1 I_2 I_3$) and (ii) for equal power but different frequencies one expects a quadratic signal increase with frequency if all beams have the same color (degenerate 4WM).

1.3.1 Transient grating (TG) concept

In this chapter the basic concepts of nonlinear optics as introduced previously are used to describe phenomena which origin from multi beam geometries rather than from single beam propagation. The recombination of E_1 and E_2 in Fig.1.11, generated by splitting an incoming beam, allows for interference as long as spatial and temporal coherence [92, 93] in a defined polarization state is given. The picture illustrates intersecting wave fronts as slanted lines which are areas of equal phase separated by 2π. The lines of the induced grating point perpendicular to the drawing plain. In this regard coherence is necessary to enable the superposition of electric fields rather than adding their average intensity. **Gabriel Lippmann** used the periodicity arising from constructive and

[6] Under the assumption of a slowly varying envelope, negligible pump field depletion and in absence of absorption.

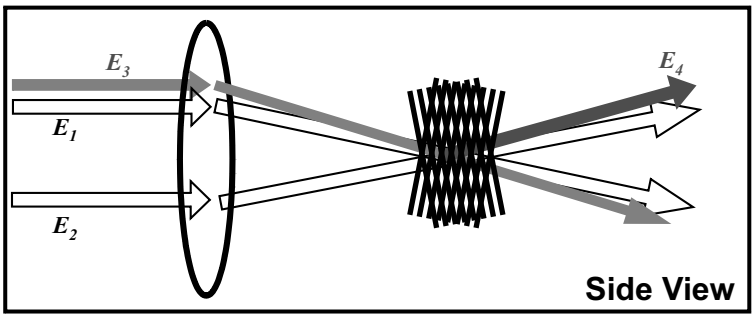

Figure 1.11: Transient grating principle. Two beams (E_1, E_2) induce a transient change of the refractive index which is highest at points of constructive interference. This creates a phase grating, upon which a third beam E_3 is diffracted and creates a new beam E_4.

destructive interference of electric fields in 1891 to record color images and gave the first experimental proof of standing light waves [20]. Along with the invention of laser, the name of **Denis Garbor** is connected to the development of a wide range of holography methods [94] which all base on light induced, permanent diffraction patterns. These kind of interferences were achieved in the regime of linear optics with low intensities and had to be developed after the light exposure to get a permanent structure. In contrast, ultra short pulses with high peak powers are able to induce grating structures only during the short presence of the laser pulse, so called transient gratings, which disappear after irradiation. In this type of experiment a change in population of electronic states is formed corresponding to the spatial interference pattern of the light, as drawn in Fig. 1.12. During this coherent excitation with two beams, a time dependent interference structure with spatial periodicity $\mathbf{\Lambda}$ depending on the beam geometry is induced in the dielectric medium. The spatial period $\mathbf{\Lambda}$ is

$$\mathbf{\Lambda} = \frac{\lambda_0}{sin(\alpha_1) - sin(\alpha_2)} = \frac{\lambda_0}{2sin(\alpha_2)} = \frac{\lambda_0}{sin(\alpha)} \,, \tag{1.74}$$

where λ_0 is the center wavelength. Note that both angles (α_1 and α_2) have opposite signs but same absolute value in case of symmetric intersection with respect to the z axis and hence add to an intersection angle $\alpha = \alpha_1 - \alpha_2$. In vector representation of Fig. 1.13 the corresponding grating vector $\mathbf{k_g}$ is

$$\mathbf{k_g} = \pm(-\mathbf{k_1} + \mathbf{k_2}) \,, \tag{1.75}$$

which can be connected to grating period Λ

$$\mathbf{\Lambda} = \frac{\lambda_0}{sin(\alpha)} = \frac{2\pi}{|\mathbf{k_g}|} \,. \tag{1.76}$$

At this light induced, intensity dependent refractive index (see Sec. 1.1.3), a third beam E_3 can be diffracted and hence creates a new, fourth beam E_4. Those four evoked beams, three initial and one additionally created one, gave name to this parametric interaction: Four Wave Mixing (4WM). The beams E_1 and E_2 are the pump beams and E_3 is the probe beam, respectively. This situation deviates from linear optics where no interaction of light fields takes place, i.e. the principle of undisturbed superposition can no longer be applied and thus some assumptions are made during following discussion unless mentioned otherwise:

- all beams have equal polarization and intensity
- the spatial intensity profile is Gaussian and phase fronts are plane waves
- only the first diffraction order is taken into account
- absorption and depletion of beams during interaction is neglected

- the nonlinear medium is isotropic and shows instantaneous response
- excitation is nonresonant and no electronic dephasing occurs during the pulse duration

Since absorption is excluded, the induced type of gratings are phase gratings rather than amplitude gratings. Moreover, if the diffraction structure in the focal region has a lateral extension d considerably larger than the grating period $\mathbf{\Lambda}$ the grating has to be considered as a volume grating or thick grating and for efficient diffraction the Bragg condition has to be fulfilled

$$\mathbf{k_4} - \mathbf{k_3} = \mathbf{k_g} \, . \tag{1.77}$$

The combination of grating creation (Eq.1.75) and Bragg reflection (1.77) leads to the phase matching condition:

$$\mathbf{k_4} = -\mathbf{k_1} + \mathbf{k_2} + \mathbf{k_3} \, . \tag{1.78}$$

This expression mirrors the law of conservation of momentum of all involved beams and was already presented in Eq.(1.29). The corresponding equation for the conservation of energy for the given geometrical arrangement is

$$\omega_4 = -\omega_1 + \omega_2 + \omega_3 \, , \tag{1.79}$$

which shows one great advantage of 4WM when used as optical gating technique for ultra short pulses. In case of total ($\omega_1 = \omega_2 = \omega_3$) or partial ($\omega_1 = \omega_2 \neq \omega_3$) degeneracy, the frequency ω_4 of the scattered wave E_4 is equal to the frequency ω_3 of the probe beam E_3. That means no frequency conversion like in SHG processes occurs. This is one basis for ultra broadband pulse characterization. Furthermore, there is no restriction on wavelength region unless the dielectric material starts absorbing. Therefore, this optical gating method can be used to characterize laser pulses from 160-5000 nm with a single fused silica glass plate for instance. This enormous physical advantage is associated with a very low procurement costs compared to frequency converting crystals.

Another issue concerning the type of grating is the diffraction efficiency $\eta = I_4/I_3$. In case of thin phase gratings or thin transmission gratings, the maximum diffraction efficiency of the

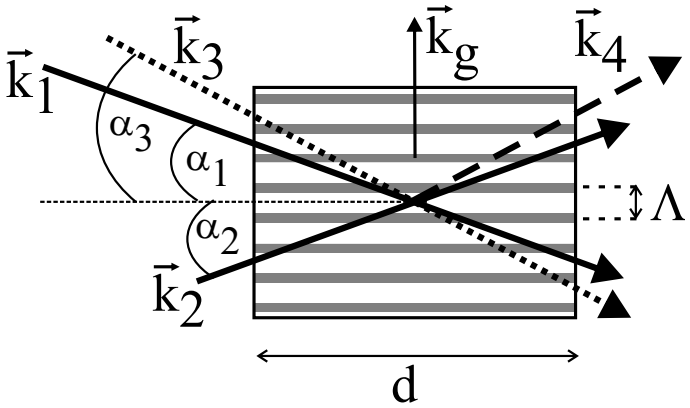

Figure 1.12: Transient volume grating in light ray representation. Interference of pump beams $\mathbf{k_1}$ and $\mathbf{k_2}$ induce intensity modulation $\mathbf{\Lambda}$ with corresponding grating vector $\mathbf{k_g}$. In an extended intersection volume of length d. Bragg condition has to be fulfilled to obtain a high diffraction efficiency of beam $\mathbf{k_4}$.

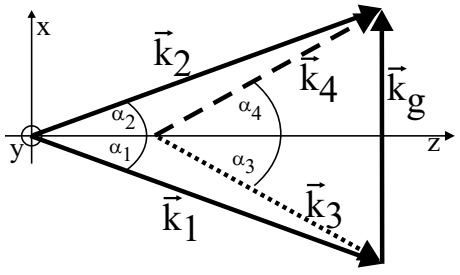

Figure 1.13: Vector representation for symmetric 4WM. Bragg condition (1.77) determines completely the wave vector $\mathbf{k_4}$, not only its x-component. Angels for positive and negative x components have opposite sign.

intensity η is 34% and 6.25%, respectively [95]. Contrary, the theoretical maximum for thick phase gratings (Fig.1.12) satisfying the Bragg condition of Eq.(1.77) is 100%. However, η depends on the grating thickness d [95]

$$\eta = \frac{I_4}{I_3} = exp\left(\frac{-Kd}{cos(\alpha_1)}\right)\left[sin^2\left(\frac{\pi\Delta nd}{\lambda cos(\alpha_1)}\right) + sinh^2\left(\frac{\Delta Kd}{4cos(\alpha_1)}\right)\right] , \tag{1.80}$$

where K is the absorption coefficient, ΔK the change of absorption and Δn the change of refractive index which is related to the pump beam energy by $\Delta n \propto n_2 |E_1| |E_2|$. With negligible absorption, normal incidence and small changes of Δn Eq.(1.80) can be written as

$$\eta = \left(\frac{\pi\Delta nd}{\lambda}\right)^2 = \left(\frac{\pi d}{\lambda 2n}\right)^2 |\Delta\chi|^2 . \tag{1.81}$$

From Eq.(1.81) it is seen that the diffraction efficiency is proportional to the square of the interaction length d and to the second power of the grating intensity, caused by $(\Delta n)^2$. According to Eq.(1.72) the signal intensity I_4 is inversely proportional to the square of the wavelength.

1.3.2 Frequency resolved optical gating (FROG)

Working with ultra short and especially few cycle pulses implies three major complications. The first one is their generation. Therefore one has to provide sufficient bandwidth and an appropriate dispersion management which already introduces the second concern, in particular the handling of the pulses. This means that transmittive optics, large path ways and improper coatings might distort the temporal shape. Thirdly, of chief importance is the characterization of few optical cycles and octave exceeding bandwidths, respectively, which is still a topic of research. Unfortunately, characterization can not be achieved by a direct time domain measurement because electronic devices don't respond on a fs timescale. On the other hand a spectrometer provides only a power spectrum $\propto |E(\omega)E^*(\omega)|$ in which the phase information is lost. In fact there are several spectral interferometry methods [96, 97] which do not rely on nonlinear optical gating processes but require a completely characterized reference pulse covering the same bandwidth as the pulse under investigation [98, 99]. An advancement to this is the spectral phase interferometry for direct electric field reconstruction (SPIDER) because it is a self referencing method and thus does not require a known reference pulse [100, 101]. In contrast to spectral interferometry, SPIDER utilizes a nonlinear optical process which connotes restrictions on the spectral operating range. However, characterization of an octave spanning bandwidth with SPIDER was recently demonstrated [102]. Although it is a direct way for determining the spectral phase, it was not chosen for WL filaments since it is less appropriate to measure arbitrary pulse shapes, which is a desired goal of the current thesis.

The most widespread way of measuring complicated pulses is frequency resolved optical gating (FROG). The key for successful gating lies in the utilization of the right nonlinear process and a suitable geometry. Low signals can be detected most efficiently via two photonic processes whereas third order processes are most suitable for complex structures [99]. In the previous sections the basic physics of $\chi^{(3)}$ optical nonlinearities have been described and now their implementation for determining the electric field will be explained. Since pure time -and frequency domain measurement are not applicable to fs pulses, the way out lies in a measurement device which operates in the combined "time-frequency domain" [88].
It involves both temporal and frequency resolution simultaneously and is referred to as spectrogram $S(\omega, \tau)$ of the pulse. It rests upon the principle of temporally gating the function under

investigation $E(t)$ with a time delayed gate function $G(t-\tau)$

$$S(\omega,\tau) \propto \left|\int_{-\infty}^{\infty} E(t)G(t-\tau)e^{-i\omega t}dt\right|^2 , \tag{1.82}$$

$$\propto \left|\int_{-\infty}^{\infty} E_{sig}(t,\tau)e^{-i\omega t}dt\right|^2 . \tag{1.83}$$

The spectrogram contains a set of power spectra taken at all segments of $E(t)$ as the time delay τ is varied. The transfer of the spectrogram method towards optical pulses is called frequency resolved optical gating (FROG) and was introduced in 1993 by Trebino and Kane [103]. The quantity $S(\omega,\tau)$ of the spectrogram in Eq.(1.82) than turns to the FROG intensity $I_{FROG}(\omega,\tau)$. Because the gate function has to be at least as short as the unknown function $E(t)$, a replica of the pulse itself is commonly used. Optical gating is achieved by utilizing a nonlinear process in an appropriate medium. The measurement result is a two dimensional plot where the time delay τ is drawn along the x-axis and the corresponding power spectrum is given along the y-axis. An example is given Fig. 2.5. Different versions of FROG rely on different beam geometries and nonlinearities, respectively, which were used. As a consequence the signal field $E_{sig}(t,\tau)$ in Eq.(1.83) is defined differently. An overview over various FROG techniques can be found in Ref. [104]. In this review TG-FROG is considered as "best all-round beam geometry for FROG measurements". Indeed this version provides unambiguous traces unlike second harmonic generation (SHG) FROG, does not require special optics as in case of polarization gating (PG) and has no intrinsic phase matching restrictions which arise in self diffraction (SD) geometry. These three aspects will be elucidated briefly.
The most wide spread optical gating mechanism is (SHG) in a beta barium borate (BBO) crystal. Clearly, the main advantage of SHG processes is their operation at energies below the pJ regime. The $\chi^{(2)}$ nonlinearities evoke the interaction of two electric fields E_1, E_2 and the signal for SHG FROG writes as [104]

$$I_{FROG}^{SHG}(\omega,\tau) \propto \left|\int_{\infty}^{-\infty} E_1(t)E_2(t-\tau)e^{-i\omega t}dt\right|^2 . \tag{1.84}$$

The disadvantage is its sign ambiguity in time and the fact that transmission for BBO is restricted to 190 nm [105]. Also, the conversion efficiency limits the SHG method because crystals as thin as currently 5–10 μm have to be used for few cycle pulses [106].

Analogically, the intersection of three electric fields ($E_1(t)$, $E_2(t)$ and $E_3(t)$) in a $\chi^{(3)}$ medium leads to third harmonic generation (THG). All third order correlation methods lead to unsymmetrical signals and thus solve the time ambiguity problem of SHG based methods.

$$I_{FROG}^{THG}(\omega,\tau) \propto \left|\int_{\infty}^{-\infty} E_1(t)E_2(t-\tau)E_3(t)e^{-i\omega t}dt\right|^2 ,$$

$$\propto \left|\int_{\infty}^{-\infty} E^2(t)E_2(t-\tau)e^{-i\omega t}dt\right|^2 . \tag{1.85}$$

One disadvantage of THG FROG is the frequency conversion to the uv spectral range which denotes a disadvantage for ultra broadband gating. Additionally, the group velocity mismatch between third harmonic and fundamental is enormous [105] and decreases the signal strength. In contrast, polarization gating (PG) is a $\chi^{(3)}$ interaction without frequency conversion. In a crossed polarization arrangement for both beams, this technique uses induced birefringence in any transparent media in the presence of the gate pulse. The polarization of the probe pulse $E_1(t)$ can be

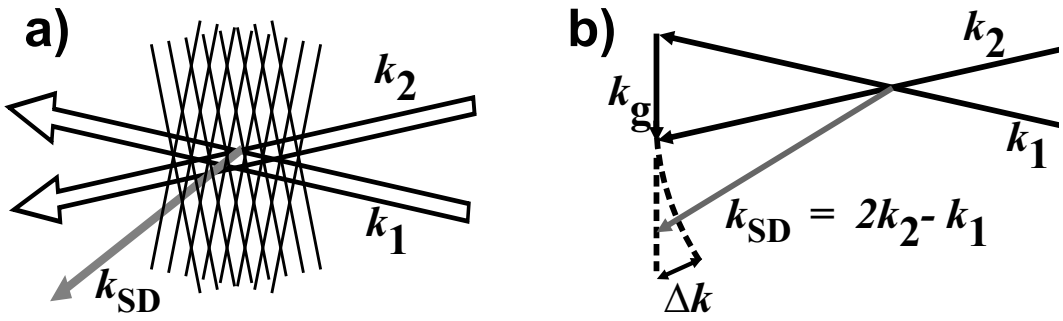

Figure 1.14: Phase mismatch in SD arrangement. Two beam intersection a) and corresponding vector representation b) showing the phase mismatch of $\Delta\mathbf{k}$ between the 4WM signal $\mathbf{k_{SD}}$ and its origin $\mathbf{k_2}$.

rotated due to induced birefringence by the gate pulse $E_2(t)$. Note that the gate function (Eq.1.86) in PG FROG is $|E_2(t-\tau)|^2$. As it is a real intensity function, it thus adds no phase information to the gated slice of $E_1(t)$ whose spectrum is measured. According to Ref. [107] the gating by means of induced birefringence should automatically phase match an infinite bandwidth. However, since the rotated part of $E_1(t)$ gives the FROG signal, this geometry thus necessitates the usage of polarizing optics. The required high extinction ratio for octave spanning spectra denotes a problem for WL gating.

These requirements of polarizers drops out when self diffraction (SD) is used in which two fields $\mathbf{k_1}$ and $\mathbf{k_2}$ in Fig. 1.14a with parallel polarization induce a transient refractive index grating. Upon this grating, one of the beams is diffracted leading to the signal beam $\mathbf{k_{SD}}$ which is sent to the spectrometer.

$$I^{PG}_{FROG}(\omega,\tau) \propto \left|\int_{\infty}^{-\infty} E_1(t)\,|E_2(t-\tau)dt|^2\right|^2 \tag{1.86}$$

$$I^{SD}_{FROG}(\omega,\tau) \propto \left|\int_{\infty}^{-\infty} E^2(t)E_1^*(t-\tau)e^{-i\omega t}dt\right|^2 \tag{1.87}$$

Like PG, SD is a two beam setup without frequency conversion of the signal beam. Its planar geometry causes an intrinsically non-phase matching interaction as depicted in Fig. 1.14b which possess a problem for large bandwidths. The grating vector is given by $\mathbf{k_g} = \mathbf{k_2} - \mathbf{k_1}$ and the vector of the SD signal by

$$\mathbf{k_{SD}} = \mathbf{k_2} + \mathbf{k_g} = 2\mathbf{k_2} - \mathbf{k_1}\ . \tag{1.88}$$

With reference to the vector diagram of Fig. 1.14b it is obvious that the absolute value of the 4WM wave vector $|\mathbf{k_{SD}}|$ in this geometry is larger than the one for $|\mathbf{k_1}|$ or $|\mathbf{k_2}|$ by $\Delta\mathbf{k}$. All FROG geometries discussed that far are realized with two rays. The crucial difference of TG compared to SD is the utilization of a three beam geometry shown in Fig. 1.15. Although SD bases on

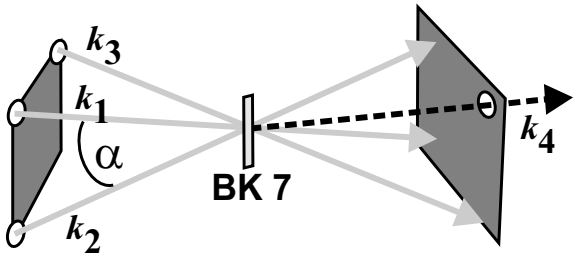

Figure 1.15: Forward box scenario corresponding to the vector description in Figs. 1.12 and 1.13. The three dimensional intersection is automatically phase matched for all wavelengths in a degenerate 4WM process.

a induced transient grating too, only the three beam setup is distinguished as TG in this work simplify matters. Figure 1.15 represents the forward box arrangement [108–110] and corresponds to Figs. 1.12 and 1.13. The three dimensional intersection allows for diffraction at Bragg condition according to Eq.(1.77). In general, 4WM in a forward box configuration constitutes three incoming beams located in three corners of a square. Satisfying the phase-matching condition Eq.(1.78) leads to the 4WM signal pointing to the vacant corner of the rectangle in outgoing direction. In the degenerate case ($\omega_1 = \omega_2 = \omega_3 = \omega_4$) phase matching is automatically achieved for every frequency and one would expect the signal beam to point always in the corner of the square. The TG-FROG trace intensity is given by

$$\begin{aligned} I_{FROG}^{TG}(\omega,\tau) &\propto \left| \int_{\infty}^{-\infty} E_1^*(t) E_2(t) E_3(t-\tau) e^{-i\omega t} dt \right|^2 \\ &\propto \left| \int_{\infty}^{-\infty} E_1^2(t) E_2(t-\tau) e^{-i\omega t} dt \right|^2 . \end{aligned} \tag{1.89}$$

Compared to PG, no extravagant optics are necessary in order to gate a super continuum and the signal strength of TG is nine times higher than for PG [104].

Phase retrieval

A unique advantage of temporal gating with a $\chi^{(3)}$ optical nonlinearity is the ability of generating non-centrosymmetric FROG traces other than in case of SHG. Because $I_{FROG}(\omega,\tau)$ is a real quantity, the phase information is encoded in the total intensity landscape of the trace. Especially PG and TG traces are quite intuitive and directly indicate second -and third order spectral phase distortions as well as double pulses, $cf.$ Ref. [104]. However, quantitative phase information must be obtained using iterative algorithms [103, 111, 112].

While performing the FROG measurement the current signal field $E_{sig}(t,\tau)$ for each time slice is given according to Eq.(1.83) by

$$E_{sig}(t,\tau) = E(t)G(t-\tau) \tag{1.90}$$

with $E(t)$ being the probe pulse which has to be retrieved and a gate function $G(t-\tau)$ depending on the FROG geometry. The herein employed algorithm is laid out for PG geometry Eq.(1.86) which is mathematically equivalent to TG [104]. Writing the signal field as Fourier transform with regard to the time variable t yields

$$\widetilde{E}_{sig}(\Omega,\tau) = \int_{-\infty}^{\infty} E(t)G(t-\tau)e^{-i\Omega\tau} dt \,, \tag{1.91}$$

leading to

$$I_{FROG}(\omega,\tau) \propto \left| \int_{-\infty}^{\infty}\int_{-\infty}^{\infty} \widetilde{E}_{sig}(\Omega,\tau) e^{-i\omega t - i\Omega\tau} dt d\Omega \right|^2 \tag{1.92}$$

which is a two dimensional phase retrieval problem. The goal of any inversion algorithm is to find a solution for the following equation

$$\sqrt{I_{FROG}(\omega,\tau)}\Phi(\omega,\tau) = \left| \int_{-\infty}^{\infty}\int_{-\infty}^{\infty} \widetilde{E}_{sig}(\Omega,\tau) e^{-i\omega t - i\Omega\tau} dt d\Omega \right|^2 \tag{1.93}$$

by determining the phase $\Phi(\omega,\tau)$. Although a large number of possible solutions to solve Eq.(1.93) exist, there is actually only one which simultaneously satisfies Eq.(1.90) and Eq.(1.92). The exact

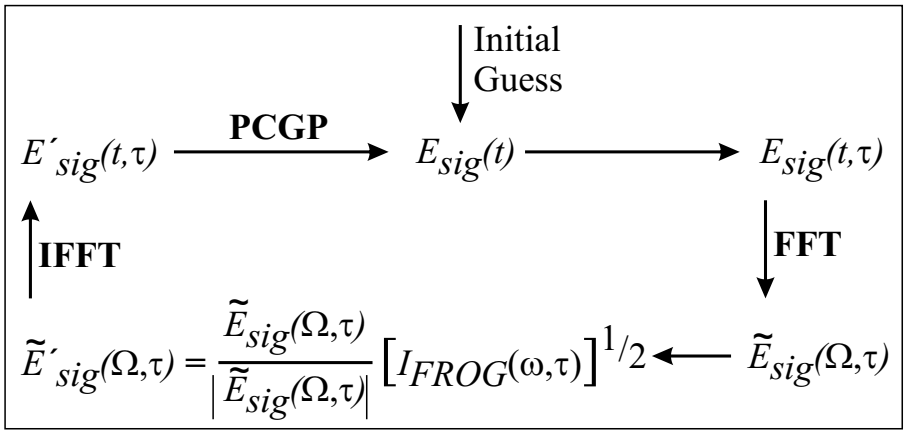

Figure 1.16: Scheme the of retrieval algorithm which has to solve a mathematical inversion problem. FFT indicates a Fourier transform and IFFT its reverse transformation. The inversion step ($E'_{sig}(\Omega,\tau) \rightarrow E_{sig}(t)$) utilizes the principal components generalized projections (PCGP) method for FROG trace inversion including the two constraints $E_{sig}(t,\tau)$ and $I_{FROG}(\omega,\tau)$.

expression for Eq.(1.90) depends on the gating mechanism and is often named physical constraint (or mathematical form constraint). Equation (1.92) is called intensity constraint of the real data. With this mathematical basis, the inversion algorithm according to Fig. 1.16 can be started. It begins with an initial guess for $E_{sig}(t)$ to calculate $E_{sig}(t,\tau)$ by the relation (1.90) which is then Fourier transformed yielding $\widetilde{E}_{sig}(\Omega,\tau)$. Next $\widetilde{E}_{sig}(\Omega,\tau)$ is fitted to the measured FROG trace by replacing the magnitude with the square root of $I_{FROG}(\omega,\tau)$, keeping the phase unchanged. This modified field $\widetilde{E}'_{sig}(\Omega,\tau)$ is transformed back to the time domain. Once a new estimate is obtained for $E_{sig}(t)$ a new spectrogram is calculated. This process is repeated until the intensity FROG trace error ϵ_{I-FROG} converges. The error

$$\epsilon_{I-FROG} = \left[\frac{1}{N^2}\sum_{i,j=1}^{N}\left(I_{FROG}(\omega_i,\tau_j) - \left|\widetilde{E}_{sig}(\Omega_i,\tau_j)\right|^2\right)^2\right] \tag{1.94}$$

represents the root mean square (rms) error per matrix element between the current calculated spectrogram $\left|\widetilde{E}_{sig}(\Omega_i,\tau_j)\right|^2$ and the measured $I_{FROG}(\omega_i,\tau_j)$. N is the array length with respective frequency elements ω_i and delay elements τ_j. The speed and success of the various algorithms mainly depend on the strategy $E_{sig}(t)$ is calculated from $\widetilde{E}'_{sig}(\Omega,\tau)$. The herein used algorithm was invented by Daniel J. Kane and is called principal components generalized projections (PCGP) method. It advantages the commonly used generalized projections (GP) method, since it can retrieve both, an unknown probe pulse and an unknown gate function. Inversion problems such as these with two unknown pulses, where the gate pulse is a function of the probe pulse are called "blind" retrieval. This is important while retrieving traces which are generated with a cross-correlation mechanism, as shown in Sec. 4.2. The formation of this newly invented TG-X-FROG in this work is explained in Sec. 3.4.2. However, GP algorithms have been demonstrated to achieve good convergence for PG FROG traces of very complex pulses, too [99]. For detailed information about PCGP consult with references [112–115].

1.4 Ultrafast spectroscopy

The coherent superposition of vibrational eigenstates of a molecule leads to a nuclear wave function, a so called wave packet (WP). Since the phase of each eigenstate evolves in time, the WP

propagates in between the boundaries of the electronic potential. Some properties of this WP are closer related to classical behavior than those of the eigenstates. For instance the round trip time of the WP of a dimer corresponds to the classical motion of its nuclei around the equilibrium position approximated by an anharmonic oscillator. Ultrafast spectroscopy aims to image $e.\ g.$ the vibrational motion of nuclei, or to select a desired final state to which population is transferred in favor of another one. The following subsections generally describe the quantum mechanical formalism for light-matter interaction in Sec. 1.4.1 and experimental approaches in Sec. 1.4.2. Finally, the method of charge reversal spectroscopy (NeNePo) is explained by introducing previous results on Ag_2 in Sec. 1.4.3.

1.4.1 Laser induced nuclear dynamics

This section briefly summarizes the basic concepts of molecular dynamics and photexcitation.
An isolated molecule consisting of at least two atoms and generally a large number of electrons is described by the time independent Schrödinger equation:

$$H(\mathbf{r},\mathbf{R})|\psi(\mathbf{r},\mathbf{R})\rangle = \epsilon|\psi(\mathbf{r},\mathbf{R})\rangle\ . \tag{1.95}$$

ϵ represents the energy and $|\psi(\mathbf{r},\mathbf{R})\rangle$ the molecular wave function which depends on the coordinates of the electrons $\mathbf{r}$ and nuclei $\mathbf{R}$, respectively. Without external field, the system Hamiltonian $H(\mathbf{r},\mathbf{R})$, which describes the total energy of the system, can be decomposed into:

$$H(\mathbf{r},\mathbf{R}) = \mathbf{T}^e + \mathbf{T}^n + \mathbf{V}^e + \mathbf{V}^n + \mathbf{V}^{en}\ . \tag{1.96}$$

The five terms correspond to the kinetic energy of the electrons $\mathbf{T}^e$, kinetic energy of the nuclei $\mathbf{T}^n$, electron-electron potential energy $\mathbf{V}^e$, nuclear-nuclear potential energy $\mathbf{V}^n$ and electron-nuclear potential energy $\mathbf{V}^{en}$.

Since already the simplest molecule H_2^+ refrains from exact solution of Eq.(1.95), an approximation is introduced. It assumes, that due to their light weight electrons follow the laser field instantaneously. This is different for the about 1880 times heavier nuclei, which react time delayed. Thus electronic motion can be treated separately from nuclear motion and the vibronic ($i.e.$ electronic and vibrational) molecular wave function can be represented as a product of the electronic wave function $|\psi^e(\mathbf{r},\mathbf{R})\rangle$, depending on electronic $\mathbf{r}$ and nuclear $\mathbf{R}$ coordinates, and of a nuclear wave function $\psi^n(\mathbf{R})\rangle$ independent of $\mathbf{r}$[7]:

$$|\psi(\mathbf{r},\mathbf{R})\rangle = |\psi^e(\mathbf{r},\mathbf{R})\rangle\ |\psi^n(\mathbf{R})\rangle\ . \tag{1.97}$$

In this Born-Oppenheimer approximation [116, 117], electronic motion is instantaneously effected by the nuclear motion, and the electronic wave function depends on the position of the nuclei but not on their motion. Since dynamic couplings between nuclei and electrons are neglected, this approximation is called "adiabatic".

A superposition of different time independent nuclear states $|\psi_m^n(\mathbf{R})\rangle$ creates a time dependent nuclear wave packet (WP) $|\Psi^n(\mathbf{R},\mathbf{t})\rangle$:

$$|\Psi^n(\mathbf{R},\mathbf{t})\rangle = \sum_{m=1}^{\infty} c_m|\psi_m^n(\mathbf{R})\rangle e^{-\frac{i}{\hbar}E_m t}\ , \tag{1.98}$$

due to the temporal evolution of the phase term in the exponent. The c_m are the coefficients c_m for the linear combination of eigenfunctions which depend on the excitation condition. With the

[7] Rotational motion are not treated in this summary.

former approximations, molecular dynamics or the evolution of an electronic WP $|\Psi^n(\mathbf{R},\mathbf{t})\rangle$, respectively, can be treated conveniently by using the time dependent Schrödinger equation (TDSE) [117, 118]:

$$i\hbar\frac{\delta|\Psi^n(\mathbf{R},\mathbf{t})\rangle}{\delta t} = H_0|\Psi^n(\mathbf{R},\mathbf{t})\rangle\ , \tag{1.99}$$

with H_0 being the time independent Hamilton operator:

$$H_0 = \mathbf{T}^e + \mathbf{V}^n = -\frac{\hbar^2}{2m}\nabla^2 + \mathbf{V}^n\ . \tag{1.100}$$

However, in the frame work of this thesis light matter interaction by excitation with ultrashort laser pulses is applied for investigation of molecular dynamics. In the dipole approximation, an external laser field $E_L = E_0 e^{i\mathbf{kr}}$ is treated as a weak perturbation $\mathbf{V} = E_L\mu$ in Eq.(1.99). In the dipole approximation, when the light wave exceeds the extension of the molecule by far, the exponential term of the laser field is substituted by 1 [116]. The external field couples to the dipole moment μ of the molecule and enables a change in the population of different molecular states $|\psi(\mathbf{r},\mathbf{R})\rangle$. The dipole moment is described by

$$\mu = -\sum_j e\mathbf{r}_j\ +\ \sum_k eZ_k\mathbf{R}_k \tag{1.101}$$

with e the elementary charge, eZ_k the charge of the nuclei, and the coordinates of the electrons $\mathbf{r}_j$ and nuclei $\mathbf{R}_k$, respectively. With Eq.(1.97), the transition probability from an initial (labeled i) to a final (labeled f) state is proportional to:

$$\mu_{if} = \langle\psi_f|\mu\mathbf{E_L}|\psi_i\rangle = -\sum_j e\langle\psi_f^e|\mathbf{r}_j\mathbf{E_L}|\psi_i^e\rangle\langle\psi_f^n|\psi_i^n\rangle + \sum_k eZ_k\langle\psi^n|\mathbf{R}_k\mathbf{E_L}|\psi^n\rangle\langle\psi_f^e|\psi_i^e\rangle\ . \tag{1.102}$$

Due to the orthogonality of the electronic wave functions $\langle\psi_f^e|\psi_i^e\rangle = 0$, the second term cancels out and Eq.(1.102) reduces to:

$$\mu_{if} = \left(-\sum_j e\langle\psi_f^e|\mathbf{r}_j\mathbf{E_L}|\psi_i^e\rangle\right)\ \langle\psi_f^n|\psi_i^n\rangle\ . \tag{1.103}$$

The first term in brackets displays the electric dipole transition moment, which depends on the displacement of the electrons. The absolute square of the electric dipole transition moment is proportional to the Einstein coefficient of absorption in Sec. 1.1.1. The second term which calculates an overlap integral between the initial and final nuclear (vibrational) wave function, is named Franck-Condon (FC) integral. The absolute square $|\langle\psi_f^n|\psi_i^n\rangle|^2$ of the integration over the internuclear distance is known as FC factor. With Born-Oppenheimer approximation and Franck-Condon principle, the assumption of a perpendicular transition from one potential surface to another is justified.

Since the c_m for each final state m in Eq.(1.98) are proportional to μ_{if} of Eq.(1.103), a WP as superposition of wave functions can be created by an external field. The time dependent probability density is given by the absolute square $|\langle\Psi^n(\mathbf{R},\mathbf{t})|\Psi^n(\mathbf{R},\mathbf{t})\rangle|^2$ of the WP. In a simplified picture, the evolution of the nuclear motion can be described as a motion of the WP along one reaction coordinate along the potential energy surface (PES) being defined by the surrounding electrons. According to Eq.(1.103), transitions between different states are likely to occur at turning points of the PES ($cf.$ Fig. 1.19a), where there is a greater overlap of FC integral. The energetic spectral distribution of the exciting pulse defines which vibrational states are populated and the phase of the light field defines the starting conditions for the temporal evolution. Shaped laser pulses exhibiting phase and amplitude modulations can therefore be employed to selectively induce interference effects in the wavepacket's propagation.

1.4.2 Coherent control

The concept of PES introduced in the previous section is well suited for describing the molecular dynamics introduced by incident light fields. With laser pulses whose duration is much shorter than the vibrational period of the molecule, the evolution of a wave packet can be resolved. Over and above that, it is most desirable to steer the outcome of the light - matter interaction by applying specially designed laser fields. The so called "quantum control" or "coherent control" [119]. This section describes different approaches how to exploit the coherence properties of laser light for the manipulation of quantum pathways in the excitation.

A direct translation of interfering pathways is given by the scheme proposed by **Brumer** and **Shapiro** in 1986 [120]. As depicted in Fig. 1.17a, the excitation combines the ground state potential for a bound molecule (AB) with degenerate final states (A + B and A + B*), accessible with either a photon of energy ω_1 or ω_2 . Differentiation between both excitation paths is achieved when the two cw-frequencies are tuned in their relative phase and ratio of amplitudes. The first experiment realization of this scheme was carried out in 1990 by Chen and coworkers [121].

While the Brumer-Shapiro scheme intuitively works in frequency domain, the idea of **Tanor, Kossloff** and **Rice** is understood best in time domain [122–124]. It requires the picture of wave packets evolving on a PES. Consider a ground state population in a specific configuration, shown as ABC in Fig. 1.17b. An ultrashort (pump) pulse generates a vibrational wave packet by coherent superposition of vibrational eigenstates on an electronically excited PES (ABC^*). After free evolution of the wave packet it is excited a second time which transfers the population to a desired reaction outcome. Control over distinguishable reaction channels (A + BC or AB + C) depends on the time delay between the two pulses. The second pulse is called dump pulse if it transfers population to a lower laying PES and probe pulse if excites a higher electronic state. Since this scheme provides the basis for the charge reversal spectroscopy it is addressed in more detail in the following subsection. Pump probe experiments were extensively used *e.g.* to excite desired electronic states, achieve selectivity in the breaking of chemical bonds [8] or isotope separation [125]. However, the formation of molecular bonds rather than its breaking remains a severe challenge. First examples demonstrate laser induced catalytic surface reactions [126] and first steps towards photo association of Rb atoms in a magneto optical trap were carried out recently [127].

A principal different access to coherent control is stimulated Raman adiabatic passage (STIRAP), depicted in Fig. 1.17c. This scheme, invented by Bergman $et\ .al.$ [128], also utilizes two time delayed excitations to achieve up to 100% population transfer between two levels $|\psi_0\rangle$ and $|\psi_2\rangle$ via

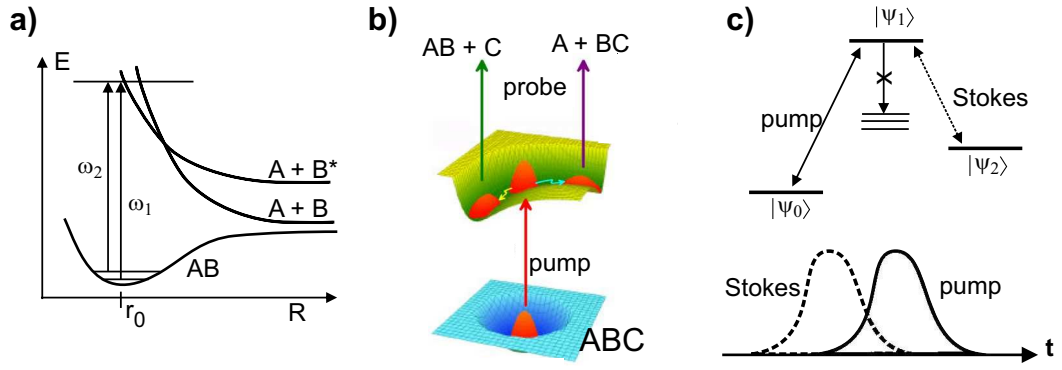

Figure 1.17: Different coherent control schemes according to Brumer-Shapiro a), Tanor, Kossloff and Rice b) and STIRAP c). For details see text.

an intermediate level $|\psi_1\rangle$. The "Stokes" laser couples the intermediate level $|\psi_1\rangle$ and the target level $|\psi_2\rangle$. An efficient transfer from $|\psi_0\rangle$ to $|\psi_2\rangle$ is achieved by counterintuitive pulse ordering: First the Stokes laser opens the passage from $|\psi_1\rangle$ to $|\psi_2\rangle$ and only then the pump laser acts, like sketched in the lower graph of Fig. 1.17c. The efficiency transfer depends on the intensity and timing of the two lasers. Characteristic for this scheme is that the level $|\psi_1\rangle$ remains unpopulated during the transfer and thus does not contribute to a loss of population.

The methods described that far rely on the change of two variables, the amplitude the ratio and phase difference of two cw lasers or the time separation of two pulses, in order to achieve control. However, with increasing complexity of the investigated molecules also the degrees of freedom for the driving field have to raise when selectivity is desired. Methods for predicting experimental laser pulses by help of "optimal control theory" (OCT) were proposed in 1988 [129]. The calculation of laser fields and the experimental verification afterward was named "open loop" procedure.

Adaptive control One difficulty about the prediction of the right excitation fields lies in the calculation of the exact PES. To circumvent this difficulty the "closed loop" scheme can be applied, published with the descriptive title: "Teaching lasers to control molecules" [130]. The idea, to run the experiment without knowledge on the quantum target but to let an optimization algorithm extract physical information, is depicted in Fig. 1.18. The spectral content and temporal shape of an electric field $E(\omega, t)$ is freely adapted in a pulse shaping device [131, 132]. The functionality of such devices is explained in Sec. 2.3. The light-matter interaction on the so called quantum target causes a change of its property. This property can either be fragmentation, change of charge state or even the generation of new products [133]. Next to this interaction step, a detection step follows which measures for instance masses or flight times of the products or fluorescence of electronically excited states. Finally, the observable (or fitness function) is condensed to the form of an integer value. This value is fed into an optimization routine whose objective typically is the maximization of this value. Closing the loop means that the optimization routine steers the shaping device and the result is compared with the former one. The termination criteria for this iterative process is reached by signal convergence. The resulting light field is minted by the properties of the quantum target. Successful optimization depends on the starting point of this closed loop. It might begin with random noise or with an initial guess which already contains knowledge on the system. One disadvantage of those "free optimization" methods is the huge search space within which the solution is embedded. Performing closed loop experiments with a pulse shaper is related the problem of finding a solution in a nearly unimaginably huge search space of about 10^{4151} possibilities[8] [16]. A reduction of the search space can be achieved by: (i) binning of pixels resulting in a reduction

[8] Assuming independent phase and amplitude modulation with $2N = 1280$ pixels with 12-bit resolution.

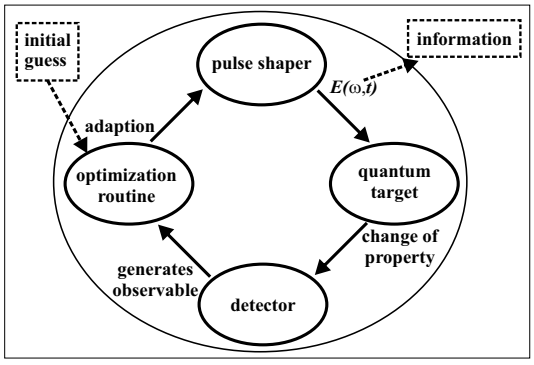

Figure 1.18: Closed loop schema for adaptive coherent control. It consists of a pulse shaper, which designs the electric field according to the settings provided by the evolutionary algorithm. The algorithm aims to optimize a defined property of the quantum system.

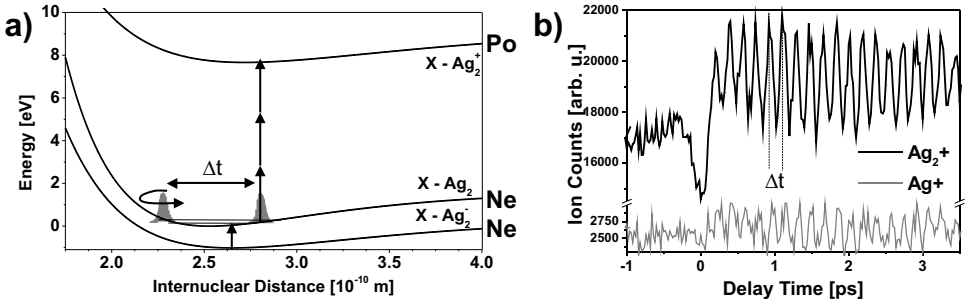

Figure 1.19: NeNePo scheme of Ag_2 in a). Photo detachment from the electronic ground state of the anion XAg_2^- creates a neutral in the electronic ground state XAg_2. Superposition of several vibronic eigenstates lead to the formation of a WP which propagates because the PES of the neutral is shifted with respect to the one of the anion. Ionization in the second step is most probable at maximum overlap of the WPs/wave functions in the neutral and cationic state $XAg_2{}^+$. Both excitations, pump and probe can either be single -or multiphoton transitions. Transient ionization yield in for $Ag_2{}^+$ and its fragment Ag^+ in b). The periodicity of 180 fs is equal to the round trip time of the WP in the XAg_2 state.

of resolution, (ii) performing of binary shaping that means the discrimination to only two settings for the values of transmission (0, 1) and phase (0, π) [134] and (iii) concentration on physically relevant pulse shapes by parametric pulse shaping [135–137].

Irrespective of the mentioned search space reductions, it remains extensive and search strategies are needed to succeed at experimental conditions. The optimization routine employed throughout this work is the so called evolutionary algorithm (EA) because it is well suited for a global search in huge fitness landscapes containing several local maxima (rugged fitness landscape). The terminology like mutation, crossover and survival-of-the-fittest, as well as the basic concepts are borrowed from biological evolution [138]. The implemented algorithm is structured as follows. The initial population contains 30 individuals with the respective variables phase and amplitude. Each variable contains N genes ($e.\ g.$ the transmission value) for the Nth pixel. The population is then probed by evaluating the corresponding feedback signal from experiment. The *survival-of-the-fittest* denotes a selection of the (10) best individuals which turn to parents, procreating 29 new offspring whereby the best individual remains untouched as a survivor. A pair of parents is recombined by *uniform crossover* operation which randomly shuffles (without changing index) their genes with a chance of 50% to originate from either one of its parents. The next step involves *mutation* by adding a random number from a Gaussian distribution of width σ to every gene. In order to achieve convergence, σ has to be adapted during the optimization according to the one-fith rule [138]. This rule states that if 20% of the offspring perform better than their parents, the variance σ is increased by the factor of 1.25 and decreased otherwise. This counterintuitive assessment enables wider steps on the way towards a maximum of the fittnes landscape and a more detailed search arround a reached hill. This procedure is repeated until signal convergence is achieved.

1.4.3 NeNePo spectroscopy

In general, the pump probe technique rests upon light induces property changes by the pump pulse which are probed via a second excitation. In the framework of charge reversal spectroscopy one begins with a beam of mass selected, negatively charged ions which are subject to electron detachment and subsequent photo ionization, carried out under fs laser excitation [10, 18, 19]. Since the clusters change their charge state during the pump-probe procedure from negative-to-neutral-to-positive this technique is abbreviated by the acronym NeNePo.

An ensemble of anionic clusters in the electronic ground state, whose vibrational occupation is given by the Boltzmann distribution, is stored in an ion trap. As is shown on the example of Ag_2 in Fig. 1.19a, the pump pulse photo detaches the excess electron from the anionic ground state ($X - Ag_2^-$) and prepares a neutral species in its electronic ground state ($X - Ag_2$). Due to the pulse shortness its spectral width covers several vibrational eigenstates of the neutral, meaning the coherent superposition of those eigenstate wave functions allows a WP to be formed. According to Eq. (1.98), this WP propagates depending on the boundary conditions defined by the PES. After a certain time the WP can be probed in an ionization step leading to a positively charged cluster. Because the location of the WP determines the ionization probability. Conclusions on the molecular dynamics can be drawn when the ionization yield is plotted versus delay time Δt, like done in Fig. 1.19b which is referred to as NeNePo trace. The black line shows the signal for Ag_2^+ ions and the gray curve gives the transient fragment signal of Ag^+. Before time zero, meaning that pump and probe pulse have the wrong order, only a constant offset signal for the dimer and the fragment is visible. When the pump pulse transfers population from the anion to the cation, the covering of several vibrational eigenstates leads to the formation of a WP, which propagates in time. Always when the WP is located at the outer turning point, population can be further transferred to the cation leading to the periodic modulation in the trace. The time periodicity corresponds to the round trip time of the WP on the electronic ground state of the neutral silver dimer. Further comments and discussion about the signal drop at time zero is given in Sec. 4.3. General particularities of the NeNePo scheme are:
- Mass selection of clusters prior to and after laser irradiation because of their ionic character.
- Due to the Franck-Condon principle, the position of the nuclei does not change during the photo detachment, meaning that the configuration of the neutral is equal to the initial structure of the negatively charged cluster.
- Selection rules for optical excitation does not play a role since an electron is removed during the process. All excited states of the neutral are accessible from the anion.
- Dynamics on the PES of a neutral in the electronic ground state can be investigated.
- Since the probe step is usually multi photonic, it can be resonance enhanced because of intermediate excited states of the neutral.
- The product detection includes the observation of fragmentation (gray line in Fig. 1.19b).
- The scheme can be extended to investigate dynamics in catalytic reactions in the presence of noble metal clusters [139–141].

In general, the conclusion of molecular dynamics from the bare knowledge of the transient time traces is, however, not always as straightforward as in the case of Ag_2. Solely the additional degrees of freedom[9] when adding $e.g.$ another silver atom, makes comparison with theoretical calculations indispensable.

Investigations on metal clusters are mainly motivated by their very different properties compared to bulk material. Especially the small noble metal clusters of silver Ag_n and gold Au_n surprise with their catalytic behavior in the size regime where each atom counts "Shrink it, however, and gold shows a wanton streak" [15]. The subscript n denotes the number of atoms and causes complimentary properties for odd or even numbered clusters when n ranges from 2–10 for instance. The theoretical access is easier compared to other metals since silver and gold are one s-electron systems and numerous theoretical investigations were carried out in the last decade, see for instance Refs. [11, 12, 142, 143]. General reviews on the field are found in Refs. [144, 145]. Because of the one s-electron, even numbered neutral clusters and odd numbered ionic species

[9] A molecule containing m atoms has $3m$-6 vibrational degrees of freedom ($3m$-5 for linear arrangement).

are most stable in thermally excited ensemble. This indicates, that the charge state of the cluster is another important quantity and the different odd/even behavior with regard to the catalysis of molecular oxygen on silver clusters is studied in Ref. [144]. Silver is not only interesting because of its catalytic behavior on O_2 [141, 144]. It is also famous for its role in the elementary photographic process, where Ag_4 clusters are proven to be the critical size for catalyzing the development process [9, 146]. So, one sees that silver is a good confidant when nature is drawing itself - since the birth of photography up to recent closed loop experiments with shaped WL.

Up to now, all NeNePo investigations on Ag_n with $n = 2 - 4$ and mixed silver-gold clusters were carried out following the pump probe scenario of the previous sub section. One aim of the present work is the extension of the NeNePo scheme by implementing excitation with shaped laser pulses. In the case of diatomic Ag_2, parametric pulse forms within the spectral range of the laser fundamental were used to charge reverse Ag_2, which is content of Sec. 4.1. For the more complex case of Ag_3, a new setup for arbitrary phase and amplitude modulation of octave exceeding spectra was developed. The methodology for WL shaping is described in chapter 3 and the results on Ag_3 are discussed in Sec. 4.2.

Chapter 2

Experimental Developments

The motivation to develop a setup for "white light filamentation - tailoring and application", was to extend the coherent control method (Sec. 1.4.2) and to make it applicable for NeNePo spectroscopy (see Sec.4.2). Section 2.1 summarizes the most important historical developments and describes its realization in the laboratory. Inherent with the generation of octave spanning supercontinua are on one hand great opportunities like few cycle pulse generation and a ultra broadband coherent light source. On the other hand the challenges lie in its reliability as well as its characterization in terms of phase and amplitude. For instance, frequency doubling of 800 nm and 400 nm at the same time is not possible with one type of BBO. The modality of how the 4WM process helps to overcome such restrictions is explained in Sec. 2.2. The route towards successful implementation of arbitrary pulse shaping over an entire octave by means of grating based pulse shaper with a liquid crystal mask (LCM) as an active device is addressed in Sec. 2.3. The general capability of the various excitation schemes available for time resolved measurements is presented in Sec. 2.4.

2.1 Octave spanning laser pulses

Strongly related to spectral broadening is the possibility of temporal shortening the pulse duration. Continuous effort in this research field lead to commercial available fs amplifier laser systems delivering several mJ pulse energy and durations as short as 25 fs. For the generation of tunable few cycle pulses through out CPA, physical limitations as for instance gain narrowing and restriction due to Ti:Sa wavelengths have to be overcome [27]. One way is parametric conversion and pulse compression after amplification. In this regard, very competitive noncollinear optical parametric amplifier (NOPA) have been proposed and realized [147]. Pulses as short as 5 fs [148] and assessable wavelength region down to 270 nm [149] have been demonstrated. Besides optical parametric processes, spectral broadening by means of SPM, non resonant four wave mixing have been proven for capability, too. Since the exploration of nonlinear optics started already one year after the invention of the LASER in 1960, a brief summary of phenomena related to WL generation is given in the following subsection.

2.1.1 Towards continuum generation

In 1964, geometrical "self-trapping of optical beams" [38] was explained as total internal reflection in solids because of the transverse intensity dependent refractive index gradient which prevented from spatial spreading by diffraction. This observation of spatial effects was followed by earliest frequency broadening experiments in solids under ps pulse excitation carried out by Alfano and Shapiro [44] in 1970. SPM, non resonant Four-Wave Mixing (4WM) and temporal pulse distortion were the processes most commonly evoked to explain continuum generation with blue shifted spectra in solids and liquids in the following years [74]. Meanwhile, the development of CPA [29] allowed Corkum *et al.* the first realization of plasma filaments in gases [150] in 1986 by irradiating high pressure noble gases with amplified fs pulses (70 fs, 400 μJ).

As nonlinear effects will benefit from both, increase of intensity and interaction length, different approaches - also for weak pulses are capable to provide a large amount of nonlinearity. Various types of nonlinear optical fibers [151, 152] and solids have been utilized for supercontinuum generation with low power pulses in the nJ regime. In contrast, for high peak powers, the use of gaseous media [150] is unbeatable in terms of damage threshold and flexible change of material properties like pressure and gas type. Therefore, extending the interaction length by light confinement when focusing in a gas filled hollow core fiber is extensively used in the few cycle community [153, 154]. Also pump probe like scenarios with gas filled hollow core waveguides were realized for generation of 4 fs pulses at 400 nm center wavelength [155] and very recently 2.6 fs [156]. Despite the excellent results achieved with hollow core fibers, there is room for improvement because the choice of optimal fiber length and diameter, difficult alignment, required pointing stability of laser amplifier, and the risk of fiber damaging due to high powers elaborates experimental handling. An experimental simplification is the self-guiding of laser induced plasma filaments which was first discovered in air by Braun $et\ al.$ in 1995 [13]. A recent comparison between both methods is given in Ref. [157]. Remarkably, not only the ultra broad spectra generated with a spectral range extending from approximately 230 nm to 4.5 μm at altitudes beyond 10 km in the framework of atmospheric research with LIDAR forced the development of new applications like WL LIDAR [14]. In equal measure, the compressibility down to a few cycles with energies ranging to the mJ level and beyond have been demonstrated [84, 158–160]. This in combination together with an excellent spatial beam profile makes the filamentation research important for future high power applications.

2.1.2 White light generation via filamentation

The laser system consists of a cw pumped (*Verdi V5 - Coherent*) Ti:Sa fs oscillator (*Femtosource compact PRO - Femtolasers*) which is Kerr lens mode locked and equipped with chirped mirrors for intra-cavity dispersion management. This oscillator seeds a multi pass amplifier (*Odin C - Quantronix*) operated at 1 kHz repetition rate. The outcome has a typical pulse duration of 40 fs with maximum pulse energy of 1.5 mJ. One finding during this work was, that continuum generation and few cycle pulse generation can be attained simply through out filamentation in atmospheric air by loosely focusing low energy pulses down to 0.65 mJ with a spherical mirror SM1 (ROC = -4 m), shown in upper part of Fig. 2.1. To investigate the properties of different gases like He, Ar, Kr, Xe, O_2, air and mixtures of those, a 1.7 m gas cell was centered around the geometrical focus. The entrance window (right side of tube) is mounted at Brewster angle in order to reduce intensity losses while the exit window is oriented perpendicular to the beam to minimize dispersive material during propagation subsequent to continuum generation. Thus, geometrical

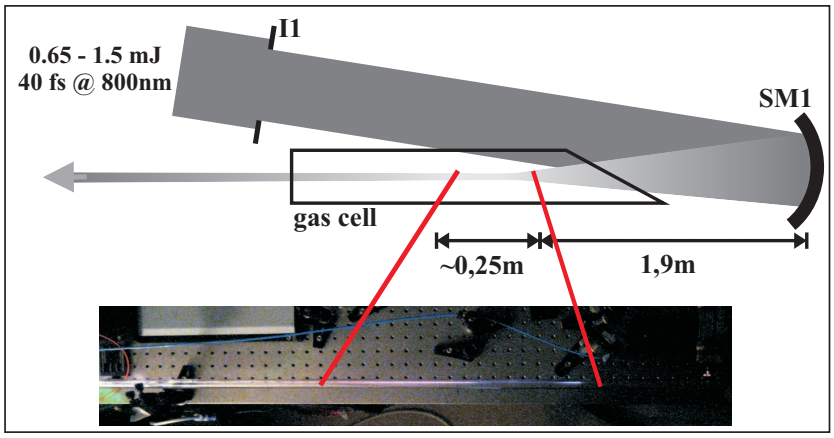

Figure 2.1: Experimental setup for white light generation in a gas cell. The minimum requirement for generation of supercontinua are one focusing mirror and the iris I1 without the gas cell. A picture of white light filament is shown in lower part.

focusing of 40 fs pulses with 1 mJ pulse energy generates an intensity of 6.6×10^{13} W/cm^2 in the focal spot with a radius of 0.1 mm, see Eq.(A.30). The corresponding pulse power of 25 GW is around eight times the critical power for self focusing of about 3 GW in air [37] at atmospheric pressure. Important is the adjustment of the beam diameter through the iris I1, placed 1.5 m ahead of SM1. 10% to 30% reduction of diameter prevents intensity fluctuations and multi filamentation when the full amplifier output (1.5 mJ) is used for white light generation. Plasma creation can be observed roughly 8 cm before the geometrical focus. It lasts for approximately 25 cm which is verified by bluish fluorescence of ionized or excited particles, respectively. Length and onset of filamentation depends on the gas pressure and intensitiy as one would expect, but also significantly on the prechirp out of the amplifier. Collimation of white light is not necessary since its divergence is about 2.5 mrad and therefore much smaller then the previously focused input beam. To prevent from damage the first mirror is placed 1.7 m behind the filament. As described in Sec. 1.2, the pulse undergoes various self induced changes, like change of divergence, spectral broadening and temporal reshaping. Another welcomed effect is the self cleaning of the spatial mode (Fig. 2.2) if appropriate settings of I1, input intensity and pressure are given. This fact in combination with alignement free operation which accepts pointing instabillities of the laser displays the great advantage over beam guiding in hollow fibers. Furthermore, the transmission through the cell is about 85% and increases to 96% when the uncoated FS windows are removed. Results on parameter dependence and further characterization of filamentation is carried out in section 3.1.2. Evacuation was accomplished with a membrane pump and two gas intakes could be steered with needle valves, enabeling the mixing of gas.

Hollow fiber broadening

As mentioned in section 2.1.1 the most wide spread way for broadening amplified fs pulses is focusing in a noble gas filled hollow core fiber in which the beam is guided through grazing incidence of the glass cladding. In the beginning of the thesis, continuum generation was realized with a focusing lens ($f = 1$ m) and FS hollow fibers of various length and inner diameters ranging from 100 μm to 500 μm. The experience made was rather sobering because achieving and keeping of proper alignment through the fiber was extremely difficult. Opposite to plasma filamentation starting with an unclean beam profile caused failure of the whole enterprise. Long term drifts of the beam pointing which took place during first hours of operation lead to burning of the fiber entrance. The latter denoted an exchange of fiber which always brings an experimental uncertainty apart since some fibers simply do not work at all. Having these experiences in mind the supercontinuum generation and pulse compression via filamentation which can be even realized at atmospheric air conditions fully reveals its unbeatable value.

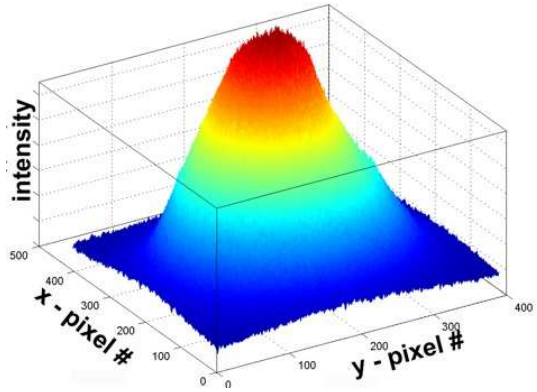

Figure 2.2: Spatial beam profile. False color representation of the intensity profile for filamentation in Ar at 70 kPa. Surprisingly, an imperfect beam profile can clean itself during the nonlinear propagation. However, the generation of few cycle pulses necessitates a good input profile as well as high pulse contrast out of the amplifier.

2.2 TG-FROG in the few-cycle regime

In this section the development of a pulse characterization tool is presented which allows the measurement of few cycle pulses down to 6 fs and furthermore enables optical gating of octave exceeding WL spectra (380–950 nm). Section 2.2.1 explains how the 4WM concept (introduced in 1.3) has been realized as TG-FROG (transient grating - frequency resolved optical gating) with beam splitters in order to provide three incoming fields as schematically depicted in Fig. 2.3. This setup with amplitude splitting was the one used for investigations the on filamentation process as carried out in Sec. 3.2. In Sec. 2.2.2 a dispersion free advancement with geometrical splitting is presented and concluding notes concerning the phase retrieval are given in Sec. 2.2.3. The key point for successful WL gating lies in the utilization of 4WM as nonlinear process which has no optical limitations in terms of broadband phase matching because it does not relay on frequency conversion unlike SHG FROG [161] or SPIDER [100]. Nevertheless, geometrical aspects have to be taken into account as will be shown in the following. Especially the role of the intersection angle α on the temporal blurring during correlation is discussed in Sec. 2.2.2.

The general working principle of TG-FROG is drawn schematically in Fig. 2.3 which corresponds to the theoretical description of 4WM in Sec. 1.3.1. Therefore, one has to focus three parallel beams (E_1, E_2, E_3) in "forward box" configuration. E_1, E_2 induce an intensity grating whereat the intensity pattern is transferred to a phase grating which diffracts the beam E_3. As a result a fourth beam E_4 is generated as 4WM signal and sent towards the spectrometer. E_3 can be retarded with respect to the the fixed grating pulses E_1, E_2 and for each time delay the spectrum of E_4 is recorded in order to generate the FROG traces like $e.g.$ the one in Fig. 2.5. Because different kinds of transient grating setups are discussed in the following the positioning of respective beams is different. Common to all kind of 4WM strategies described below is the utilization of a 1 mm thick BK 7 microscope object plate as the nonlinear medium. Positioning of the glass plate was such that the front surface lies in the focal plane in order to avoid additional travel through dispersive material. When measuring the few cycle pulses, a crosscheck with a 170 μm glass plate was carried out wherein no change of pulse duration was observed, only a decrease of 4WM signal because of thickness dependent efficiency ($cf.$ Eq.1.81). In regard to ultra broadband operation in the short wavelength range the BK 7 material was replaced by FS. The measured FROG trace in the short wavelength range (380 nm) was the same as in case of BK 7, but with lower signal due to lower n_2 of FS.

2.2.1 Amplitude splitting

Besides the nonlinear process and geometrical arrangement it is important that the spectral properties of all optical elements support the whole bandwidth. Thus, the problem of splitting up the

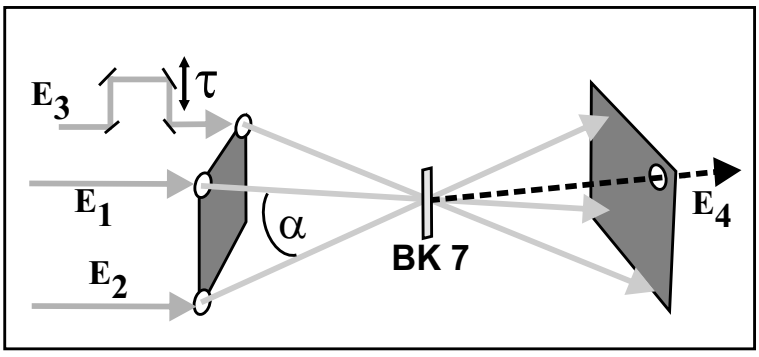

Figure 2.3: 4WM in forward box arrangement. Three parallel, equidistant beams E_1, E_2 and E_3 are focused symmetrically (solid lines) with intersection angle α in the nonlinear medium. The grating beams E_1, E_2 are fixed at time zero and the probe beam E_3 can be temporally scanned across the transient grating where it diffracts and creates a signal beam E_4 (dashed line).

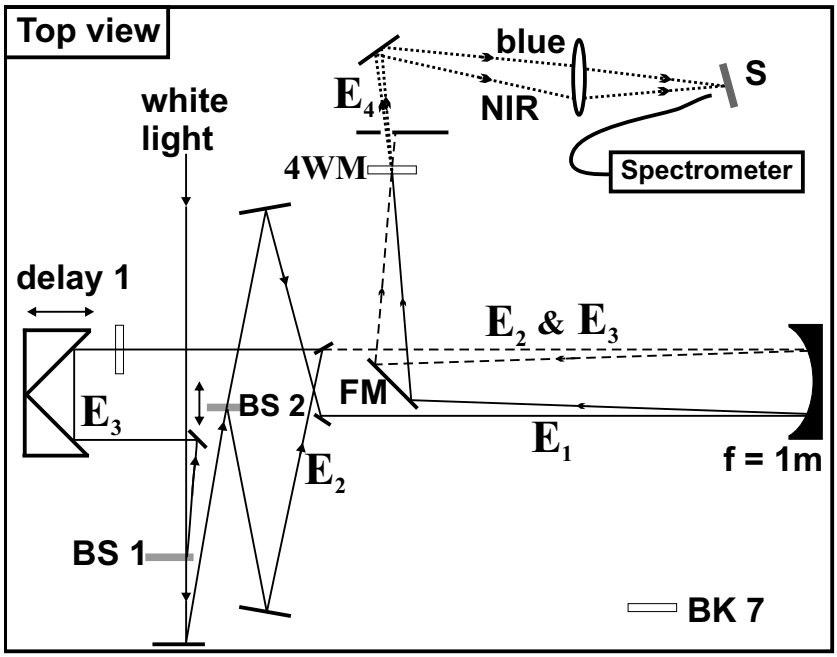

Figure 2.4: TG-FROG with amplitude splitting. The input beam is subsequently split in three equal parts. Probe beam E_3 travels over delay stage and through a compensation plate. The grating pulses E_1 & E_2 are adjusted for zero delay with manual translation stage at BS 2. The three parallel beams are focused ($f = 1$ m) into 1 mm BK 7 glass as the nonlinear medium. The diffracted signal beam E_4 is extracted and focused onto a piece of chalk which acts as a diffuse scatterer. Figure 2.5a shows a FROG trace recorded with this setup.

beam into three equal ones becomes evident. Because conventional multilayer coatings do not support defined partial reflectivity for more than one octave and beam splitter cubes are way to thick for short pulses the choice fell on 1.1 mm thick neutral density plates (Linos) which act as broadband beam splitter. Figure 2.4 shows the TG-FROG setup with amplitude beam splitting. The incoming white light beam firstly hits a R=30% / T=60% beam splitter (BS 1). The reflected part gives the probe beam E_3 which travels over controllable delay 1 towards focusing mirror. The transmitted light of BS 1 is subsequently split in two equal parts E_1 & E_2 on a second splitter (BS 2, R=T=50%) which is mounted on a manual travel stage in order to set zero time delay between both grating pulses. E_3 passes a BK 7 compensation plate to assimilate material dispersion. The three parallel beams have a separation of 18 mm and intersect under an angle α ($cf.$ Fig. 2.3) of 1°. Since E_2 & E_3 travel on top of each other they are drawn as dashed line in the top view. The folding mirror (FM) behind the focus mirror has to reflect the three beams at 90°[1] to guarantee the symmetry of forward box arrangement. In the focal region four wave mixing in a BK 7 glas takes place. After 4WM only the signal beam E_4 is extracted by blocking the other beams with an iris. E_4 is steered to a convex lens and focused onto a piece of chalk which acts as diffuse scatterer (S). The reason therefore was to ensure there is no signal change due to angular changes of E_4 which might pretend spectral efficiency differences of 4WM process[2]. These angular changes are wavelength dependent and represented by two dotted lines labeled "blue" and "NIR" in an overscetched way. Their origin is discussed in Sec. 3.4. The result of a FROG trace recording is given in Fig. 2.5(a) as a representative example in order to explain the main features. Generally the color scale is linear as referenced by the color bar unless mentioned otherwise. In case of few cycle pulses, E_3 can be scanned with an accuracy of 0.5 fs versus fixed grating pulses. The vertical axis contains the gated spectrum for each step motor position. The parameters for filamentation in this case were a laser energy of 1 mJ and tube filling of 80 kPa Ar. In the inset of Fig. 2.5(a) a projection of the 2-d spectrogram onto horizontal axis is displayed which is equivalent to a correlation measurement with spectrally integrating detector. To follow up the spectral efficiency variations

[1] 0° also guarantees the symmetry of the forward box. For 0° reflection one has to set up a Cassegrain reflector as shown in Fig. 2.6

[2] An integrating sphere was used likewise but on cost of signal decrease by three orders of magnitude.

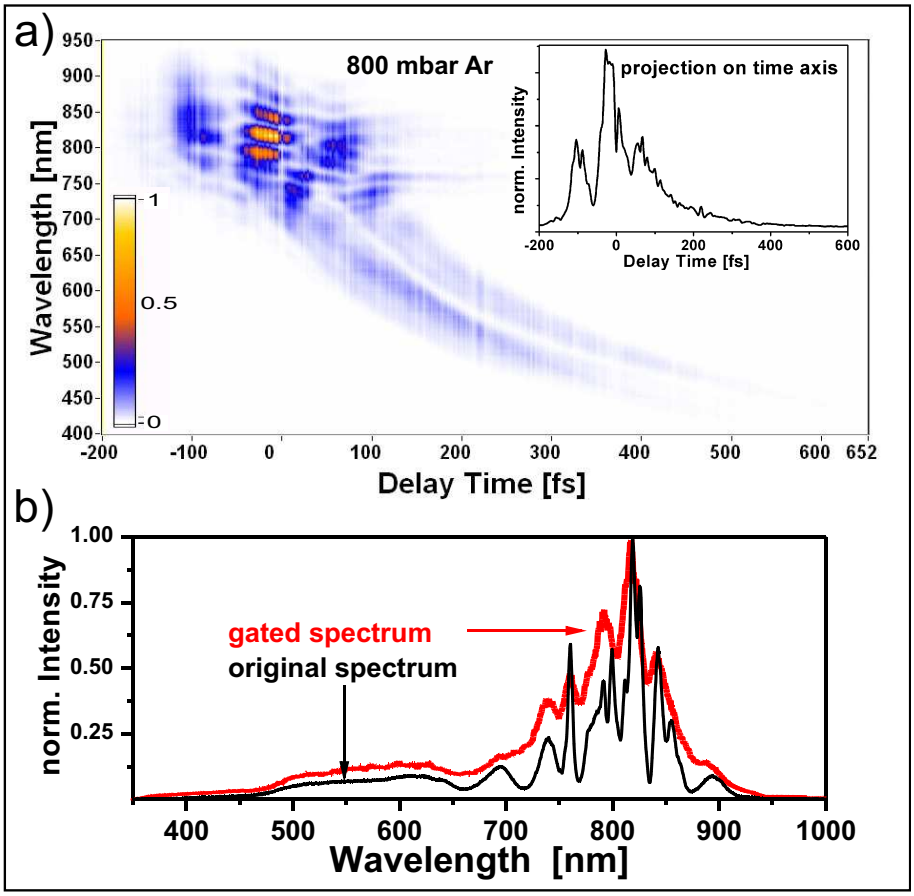

Figure 2.5: TG-FROG trace of WL filamentation in 80kPa Ar with linear color map in the trace of Fig.a). The inset shows a projection of 2-d array onto horizontal axis, corresponding to a correlation measurement. In b) the projection onto the vertical axis (thick, red line) displays the gated bandwidth which is compared to the original bandwidth (thin, black line) of the probe beam E_3. Both curves are directly proportional to each other.

of the 4WM process the original spectrum (thin, blackline in Fig. 2.5b) is compared with the projection of the 2-d spectrogram onto vertical axis (thick, red line). Because the first beam splitter in Fig. 2.4 and subsequent optics might change spectral weighting, the original spectrum was taken directly before focusing in BK 7 sample. The spectrum comparison shows an exact matching of sharp spectral features and a comparable relative hight of spectral bench marks in the present example. Certainly, sharp signatures are convoluted with the (unknown) response function of the TG-FROG. However, Fig. 2.5 clearly demonstrates the capability for white light gating of spectra reaching from 400-950 nm. Further particulars of spectral and temporal structure will be discussed in chapter 3.1.2.

TG- and rhomb arrangement

A 4WM signal can be obtained in different arrangements, TG - & rhomb, respectively, as shown in Fig. 2.6. A transient grating is of course formed in both cases, but since the left geometry of Fig. 2.6 is the typical arrangement for FROG it is referred to as TG geometry without further ado. Now a description of two different arrangements under which a 4WM signal is obtainable shall be given in regard to their capability of gating the entire supercontinuum. It is mentioned, that the important difference between the both cases lies in the fact which of the three beams is delayed $vs.$ the other two grating beams, rather than in the orientation of the square in the drawing of

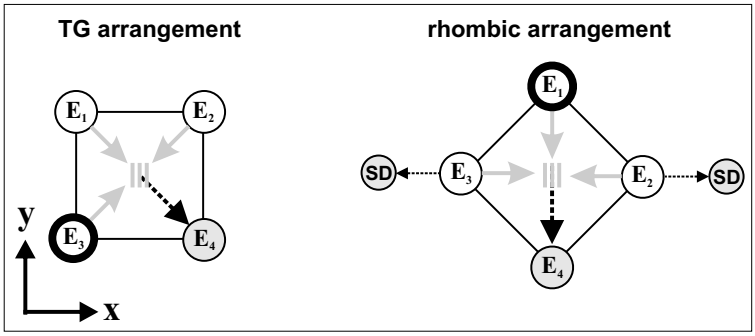

Figure 2.6: Different beam arrangements for 4WM. In this front view, the beams are propagating out of plain towards the reader. Left part of Fig. 2.6 corresponds to a front view of Fig. 2.3. Both cases differ by the utilization of the probe beam which is indicated by a bold circle in the corresponding arrangements.Circles named SD indicate self diffraction of beams E_3 & E_2. For more information see text.

Fig. 2.6. The orientation of both versions is different in order to draw an induced grating (vertical gray lines) which is oriented along the y axis in both cases. By this, the different incident angel of the corresponding scan beam onto the induced grating can be seen. Different geometries thereby mean different ways of phase matching conditions, in case of ultra broadband operation, for the three intersecting beams (E_1, E_2 & E_3) as will be discussed in Sec. 3.5.3. Figure 2.6 shows the two most common arrangements for time resolved experiments where the left part corresponds to a two dimensional front view of Fig. 2.3. Both arrangements have in common that all four beams are located in the corners of a rectangle and are focused to a point in the center. They differ by the beam which chosen for the time delay with respect to the grating pulses. The propagation direction of the beams is perpendicular to the drawing plain. Results on white light gating and further analysis for both 4WM types is presented in result section 3.4.1 and the corresponding discussion in Sec. 3.5.3, respectively.

TG arrangement TG geometry is drawn on left side of Fig. 2.6 where both grating beams E_1 & E_2 inhabit one edge of the square and the probe beam E_3 is placed on a perpendicular axis. Each of the four wave vectors has a component in x and y direction. In the vector description $\mathbf{E_1}$ is subtracted (see Eq.(1.78) $\mathbf{k_4} = -\mathbf{k_1} + \mathbf{k_2} + \mathbf{k_3}$) and hence becomes complex conjugated in Eq.(2.1)

$$E_{4\_TG}(t,\tau) = E_1^*(t)E_2(t)E_3(t-\tau)\ . \tag{2.1}$$

The gray parallel lines in the center of the square at the position of the focus, indicate the grating induced by E_1 & E_2.

Rhomb arrangement The arrangement on right side of Fig. 2.6 is referred to the rhombic geometry for better differentiation. In principle the setup is the same as for TG but another beam is delayed. Here, both grating beams E_3 & E_2 appear in opposite corners of the rectangle and the delayed beam E_1 is located at the obtuse angle of a triangle. In this drawing, rotated with respect to the TG case, the orientation of the induced grating (gray parallel lines) is equal to the left picture. By comparing both, the difference incidence of the corresponding probe beams onto the induced grating becomes recognizable. Now each of the four wave vectors have a component in only one direction, x or y. The circles named SD indicate self diffraction [95] of beams E_2 and E_3. SD can also occur between other beams along the connection line of the two intersecting beams. At higher energies, more and more spots line up next to each other. Unreasonable high intensities (25 μJ) lead to cascaded wave mixing, leading to the colorful diffraction pattern of Fig. 2.7. Two SD spots corresponding to the ones of Fig. 2.6 are marked in the image of Fig. 2.7. The mathematical

expression for this type of 4WM signal E_4 reads as

$$E_{4\_Rhomb}(t,\tau) = E_1^*(t-\tau)E_2(t)E_3(t)\ . \tag{2.2}$$

Figure 2.7 shows a variant of 4WM according to a Cassegrain telescope consisting of a concave and a convex mirror, where the latter is placed in between the three beams. A hole is drilled in the center of the focusing mirror to avoid abberations.

2.2.2 Geometrical splitting

The difficulties in generating one-digit pulse durations raised the question on the usability of our amplitude beam splitters which are not specified for ultra short applications at all. The ultimate circumvention of dispersive beam splitting is a geometrical separation[3]. It is achieved by slicing out three beams with a mask consisting of three holes in the corner of an rectangle corresponding to schematic view in the inset on right bottom of Fig. 2.8. Fortunately, spatial coherence and absence of spatial chirp of the white light enable this way of separation. The geometry for measuring the few cycle pulses accorded the TG arrangement in Fig. 2.6. The complete few cycle TG-FROG setup is depicted in Fig. 2.8 and contains a minimum number of seven optics only. The center part of the filament output is selected with iris I2 which stands 4 m ahead of FROG apparatus. Closing I2 to 1 mm reduces intensity and provides a spot diameter of 6 mm on I3. The divergence sketched behind iris I2 is overstated for better visualization. Beam separation was done by drilling three holes into the metal plate I3 with 4 mm separation d_i and diameter of 2 mm as shown in the inset. In Fig. 2.8 the dashed line stands for the two grating beams E_1 & E_2 spaced one above the other. They are reflected from a single flat mirror FM onto the focusing mirror SM2 (f = 250 mm). E_3, represented by the upper solid line in Fig. 2.8, is reflected via delay mirror towards SM2. Now, the three parallel beams are focused to a spot size of 30 μm in BK 7 glass as the nonlinear medium. At this point two geometrical aspects concerning falsification of measurement have to be discussed. First, the movement of delay mirror (along the bisector of β) causes a parallel shift of E_3 on the surface of SM2. In order to minimize this shift, the incident angle $\frac{\beta}{2}$ on delay mirror is only 1° which introduces a parallel shift of 2 μm for a scan range of 200 fs. Since parallel shift does not change focus position in first approximation, the shift of 2 μm is negligible. More important is to consider temporal resolution for the non collinear interaction of three beams. The intersection angle α inside the medium between two **k** vectors introduces a geometrical time smearing $\Delta\tau$. The angle α is kept small (0.6°) by use of relatively long focal length f combined with small beam

[3]Geometrical separation was recently demonstrated for SHG FROG [162] and TG-FROG [163]

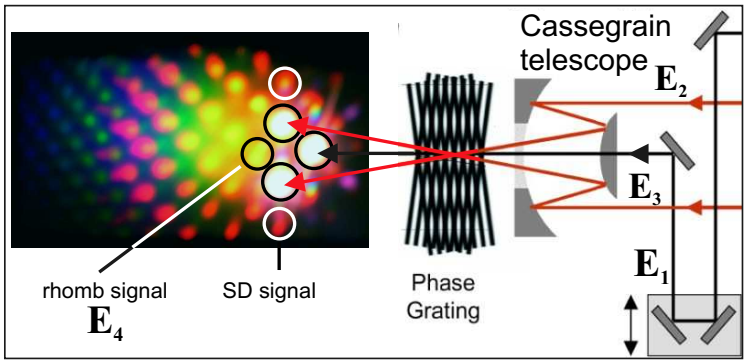

Figure 2.7: Rhomb configuration. Grating beams E_2 & E_3 and the delayed probe beam E_1 are focused via the Cassegrain telescope with f = 1m. Apart from signal beam E_4 this configuration lead to clearly visible SD spots and higher order cascading processes. They lead to extremely nice looking diffraction patterns, but at given experimental conditions, E_4 does not represent the whole octave of frequencies of E_1, the beam under investigation.

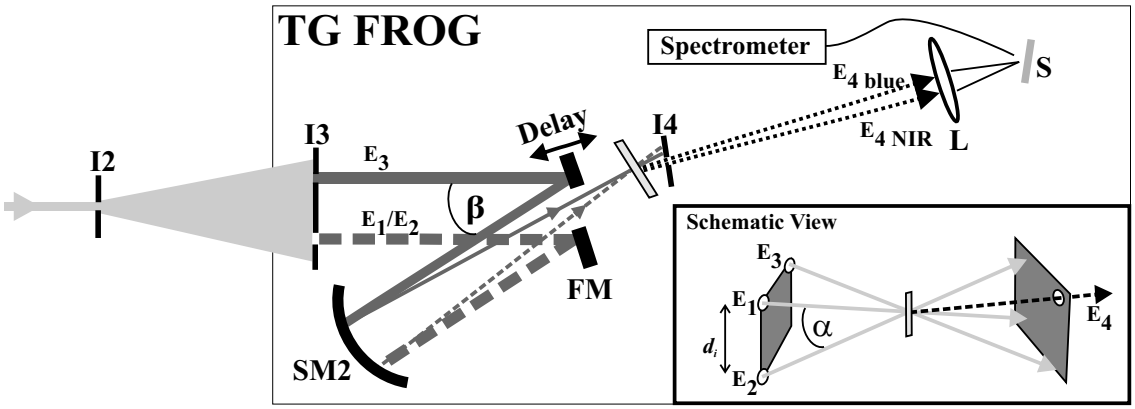

Figure 2.8: Top view of TG-FROG with geometrical beam splitting. This setup is free of dispersion and consists of seven optics only. It enables gating of few cycle pulses and octave exceeding spectra. Important features are the small deflection angle β and small intersection angle α as well as the automatically aligned grating pulses E_1 & E_2 (dashed line). The spatially dispersed signal beam E_4 is represented by two dotted lines. An explanation is given in Sec. 3.4.1.

separation d_i. Assuming Gaussian beams, the temporal smear $\Delta\tau$ can thus be calculated according to [161] by

$$\Delta\tau = \frac{f\alpha\lambda}{d_i\pi c}\,, \tag{2.3}$$

where c is the speed of light and λ denotes the laser wavelength. For the present TG-FROG setup $\Delta\tau$ is maximum 0.63 fs assuming a wavelength of 900 nm as upper limit. $\Delta\tau$ blurs the physical pulse duration τ_0 and gives a measured value τ_{meas}, with

$$\tau_{meas}^2 = \tau_0^2 + \xi\Delta\tau^2\,. \tag{2.4}$$

The scaling constant ξ depends on beam geometry. For three intersecting beams in forward box configuration $\xi \approx 5/3$. Based on above equations the blurring of a 6 fs pulse results in a pulse lengthening of less than 6% during measurement. A further aspect in nonlinear processes is the conservation of energy and momentum which has to be fulfilled for all participating wave vectors. In this regard conservation of momentum is connected to phase matching which practically means spatial and temporal overlap of the evoked electric fields in a small focal volume. The common way to increase phase matching bandwidth in $\chi^{(2)}$ nonlinear processes, is decreasing the length of nonlinear crystal down to currently 5-10 μm. This is necessary in order to guarantee co-propagation of fundamental and frequency converted light. Thus, SHG based methods reach their physical limitation when octave spanning spectra have to be gated. Since TG-FROG exhibits no frequency conversion, this method is usable for large bandwidths in the whole transparency range of glassy material. Another essential role of intersection angels is their influence on phase matching properties. The question of how the conservation of momentum is influenced by geometrical arrangement of 4WM schemes is discussed in Sec. 3.4.1. An explanation why the signal beam is spatially dispersed (E_{4blue} and E_{4NIR}) is also given in Sec. 3.4.1.

2.2.3 Phase retrieval

The measurement output of the setup described above is a two dimensional spectrogram or FROG trace, respectively, see Fig. 2.5a. It shows the frequency resolved intensity of the temporally sliced signal field ($\widetilde{E}_{sig}(\Omega,\tau)$ given in Eq.(1.91) versus delay τ. In the transform limited case, each power spectral distribution corresponds to a unique FROG trace and the spectral phase is known to be constant. Deviations from this constant phase function are coded in an intensity distribution different

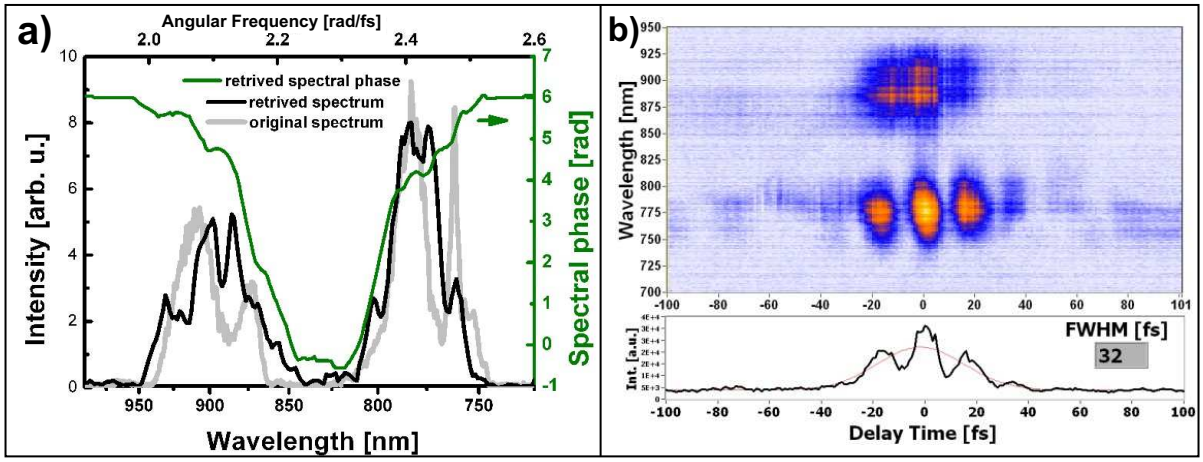

Figure 2.9: Spectral double pulse. Retrieve results and original spectrum are plotted in a). The corresponding time modulation can be seen in the TG-FROG trace in b).

to the transform limited case and the aim of the phase retrieval is the calculation of this unknown phase function. Besides the unique opportunities of the FROG method to measure very complicated pulses, the bottle neck is its need for retrieval of spectral phase which is an iterative process. Again, the retrieval greatly depends on programming skills that means on the implemented way of calculating the guess of the electric field for the next iteration ($cf.$ Sec. 1.3.2). Fortunately, the basic MATLAB code for the retrieval was courtesy of Dr. D. J. Kane which is greatly appreciated. It was extended for calculating the spectral intensity and phase out of the time retrievals. With the purpose of calibrating the wavelength axis of retrieval output, a spectral double pulse was tested. Figure 2.9b shows the TG-FROG trace and its projection onto time axis. It was generated trough amplitude filtering in the Fourier plain of the pulse shaper after broadening via filamentation. Prior to the filtering, the continuum was compressed to a short pulse by adaptive pulse compression in a closed loop scheme as will be explained later in Sec. 3.3. The retrieved spectral intensity and phase as well as the original spectrum are given in Fig. 2.9a. Since the agreement of the spectral intensity of original and retrieved data seems improvable, following corrections to the experimental raw data turned out to be necessary in order to achieve reasonable retrieval results for even more complicated pulses:
(i) Background subtraction. Ideally, the FROG trace should be an island in a sea with very little noise. Surprisingly, embedding the trace in a sea of zeros lead to a worse reconstruction of the spectral phase in some cases.
(ii) The maximum of the trace or the gating NIR structure, respectively, should be centered in the middle of the array.
(iii) Important are the array size and the increment. Complex pulse structures should be measured with appropriate scan range and step width to ensure spectral resolution. The grid size was rescaled to $N \times N$ pixel where N is an integer to the power of two.

2.3 Octave spanning pulse shaping

Throughout this work shaping of electric field means manipulation of spectral amplitude and phase rather than varying the polarization state or any means of spatial beam shaping. Amongst various types of pulse shaping devices, a review on this subject is found in [132]. The most wide spread

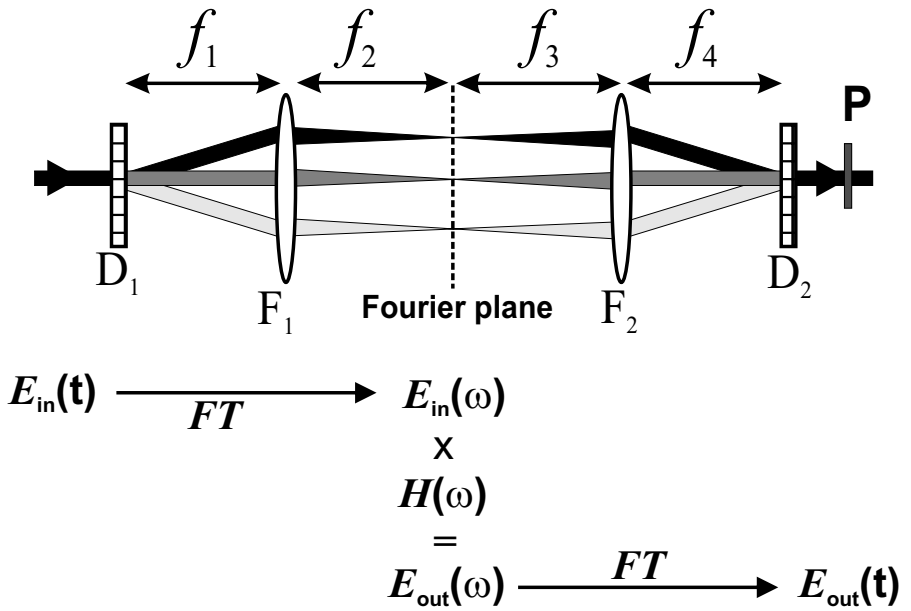

Figure 2.10: Pulse shaping setup. A collimated beam is spectrally dispersed at D_1 and individual frequencies remain collimated. They are focused by F_1 to sharp spots in the Fourier plane. If the second part of the setup is symmetric ($f_1 = f_2 = f_3 = f_4$) and material dispersion of optics is neglected, the pulse duration is not changed during passage (zero dispersion alignment). Lower part sketches the mathematical description. The time varying input $E_{in}(t)$ is Fourier transformed to the spectral domain and multiplied with transfer function $H(\omega)$ which can be steered by the SLM. The second transformation yields shaped output, again in time domain.

configuration is a $4-f$ [4] setup with a spatial light modulator (SLM) located in the Fourier plane. In Fig. 2.10 a collimated fs input pulse enters from left side. The containing frequencies are dispersed on D_1 which could be, $e.g.$, a grating. Subsequently, the still collimated spectral components are then focused by F_1 in order to generate sharp frequency spots in the Fourier plane. If F_1 is separated for a distance equal to the focal length the Fourier plane on the other side of F_1 has the same distance. If further on the second part of the setup is a mirror image to the first one, the Fourier plane displays a symmetry axis. The mathematical description for the given experimental setup corresponds a two times forward, continuous Fourier transformation (at the speed of light) as sketched in the lower part of Fig. 2.10. A time varying electric field $E_{in}(t)$ is transformed into the frequency domain $E_{in}(\omega)$ where it is multiplied with shaper the function $H(\omega)$ and yields $E_{out}(\omega)$

$$E_{out}(\omega) = E_{in}(\omega)H(\omega)\ . \tag{2.5}$$

The second transformation creates $E_{out}(t)$ which is equal to $E_{in}(t)$ if $H(\omega) = 1$. $H(\omega)$ is also called transfer function of a linear system [49] and its Fourier transformation yields the impulse response function $H(t)$. For detailed description of SLM itself the reader is referred to chapter 2.3.2. A symmetric setup ($f_1 = f_2 = f_3 = f_4$) without active shaper, causes no change in pulse duration of incoming and outgoing pulse when dispersion of optics is neglected. The configuration of the two imaging optics (F_1,F_2) represent a 1:1 telescope. If the grating distance f_1 or f_4 is larger (smaller) than the focal length f_2, the transmitted pulses are negatively (positively) chirped in frequency domain. This deviation, however, introduces a spatial chirp on the beam which becomes

[4] $4-f$ means that all optics have the same distance from their respective conjugated optical planes. This distance is equal to the focal length of the focusing optic.

troubling for large shifts. For high power applications, the focusing optics are cylindric ones in order to enlarge the spot size and reduce the peak intensity on the SLM which is located at the Fourier plane. The SLM in combination with an optional polarizer (P) enables independent attenuation and relative phase shifts of individual frequencies. The base for successful management of octave exceeding WL lies in the use of reflective optics instead of lenses, to meet the requirements for ultra short pulses and avoid chromatic aberration. Thereby ray separation was carried out with low vertical tilt in stead of horizontal tilts to avoid off-axis illumination of the mirror.

Universalities for planing the octave spanning pulse shaper are emphasized throughout the current break. The all-dominant parameter is the pixel height of the liquid crystals. It determines the entrance diameter of the input beam, because the beam is not affected in height by any optics in the shaper setup. Next, beam diameter and focal length of the cylindric mirror define the width of cylindric focus on the modulator (*CRI*) which should be smaller than the pixel width (97 μm). Knowing the focal length permits choice of the dispersive element, which is, in turn, the first optics in the setup. Spatial dispersion is maximized in order to illuminate most of the 640 pixels to achieve maximum spectral resolution. Again, the spectral resolution defines the fidelity for writing steep phase functions on the mask. The best compromize for all the above mentioned parameters (including pricing and delivery time) was found for 250 mm focal length with silver coating (*Hellma Optik*), brewstered SF 11 prisms (*EKSPLA*) and later silver gratings blazed @600 nm with a groove density of 300 lines/mm (*HORIBA Jobin Yvon*), respectively. Improvement of ultra broadband operating and reduction of material chirp was achieved by removing the two ex-works assembled polarizers and replacing them by a single, thin broadband polarizer (*CODIXX*, 200 μm) behind the setup.

2.3.1 Prism $vs.$ grating based setup

The basic operation principle of a pulse shaping setup does not depend on the type of dispersive element (D_1, D_2) used to spread and combine frequencies and can either be a grating or a prism. However, handling of octave exceeding spectra is a challenging task. Therefore the two configurations were tested.

Prism layout

The motivation for setting up the shaper with prisms was maximization of transmission in the VIS spectral range and the successful demonstration of sub 4 fs pulses for NIR spectrum out of an fs oscillator with subsequent pulse shaping for compression [164]. Fig. 2.11 shows the setup with SF 11 Brewster prisms which are adjusted for minimum deviation. The reason for choosing high refractive index ($n_{SF11} = 1.77$ @ 706 nm) glass was to spread the beam as wide as possible. The prism distance of $f = 250$ mm to the cylindric mirror comes in for a spatial frequency spread of nearly 40 mm in the Fourier plane. Finally, this setup was not satisfying in our case. The combined glass material dispersion, which is getting even stronger the shorter the wavelengths are, and an intrinsically strong positive chirp of the white light (see Fig. 2.5) in the spectral range from 400–

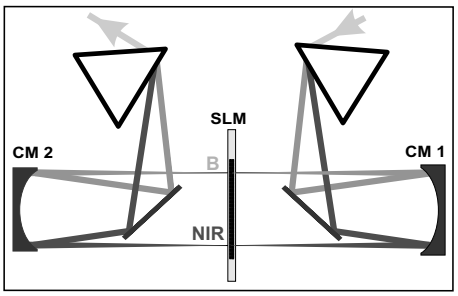

Figure 2.11: Prism shaper. The prism material is SF 11 in order to achieve high spatial dispersion on cost of accompanied temporal pulse dispersion, which could be hardly compressed by an additional prism compressor consisting of FS prisms (not shown here). The Brewster prisms are adjusted for minimum deviation and beams intersect at prism tips in order to reduce material in the path.

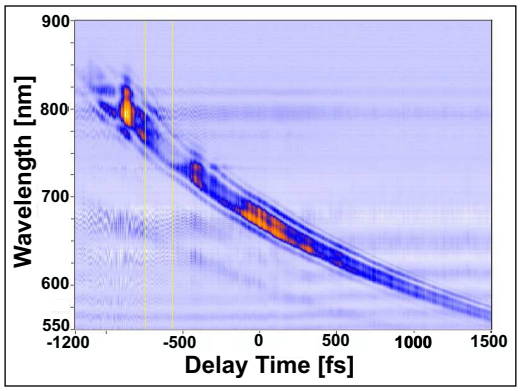

Figure 2.12: FROG trace behind prism shaper setup. Compression of this strongly chirped white light by external prism compressor failed because of insufficient negative dispersion from a single compression stage.

700 nm added up to a huge dispersion as can be seen in Fig. 2.12. The whole WL was spread for more than 3 ps and thus impossible to be compensated. Further positive and negative criteria for refractive dispersive elements are listed below.

Pros for prisms:

- High total transmission of setup is 70%.
- No spectrally dependent efficiency has to be considered despite of glass absorption in the UV range.
- No overlapping orders in the Fourier plain as is the case for dispersion with diffraction gratings.

Cons for prisms:

- Very strong material dispersion because of high dispersive material (SF 11).
- High refractive index leads to increased absorption at 400 nm (19% absorption @ 400 nm for 1 mm SF 11) which is no drawback for desired operating bandwidth (480–950 nm) but causes damage of first prism.
- Non-uniform wavelength spreading per pixel in Fourier plane (4 nm @ 900 nm; 1 nm @ 500 nm)
- Difficult to compensate total amount of dispersion with additional simple prism compressor because it introduces new dispersion itself and requires very large prisms and multiple passings. The huge positive chirp leads to a pulse duration of more than 3 ps.

Introducing an additional prism compressor for compensation caused new problems because the prism size limits the spectral bandwidth and requires additional telescoping of beam. Moreover, the spatial beam quality is becoming worse. At this point the decision was not to spent more effort on multi pass prism compressors with huge prisms but to try an arrangement with gratings.

Grating layout

In this layout, the prisms are replaced by ruled blazed gratings in Littrow configuration[5], see Fig. 2.13. In this picture the light enters from right hand side and is reflected onto the first grating (G1) via a folding mirror. The mayor drawback of gratings is their strong wavelength dependent diffraction efficiency which can be quite high (up to 90%), but only in a narrow spectral region. Due to the fact that our supercontinuum contains most of the energy in the spectral range from

[5]Littrow configuration means that the first order diffraction is reflected back to its origin.

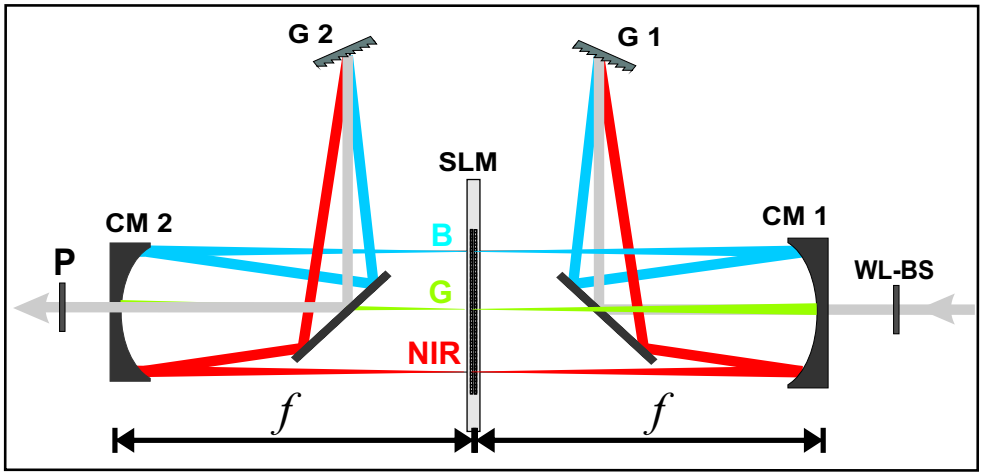

Figure 2.13: Grating shaper setup. The entrance beam from right side is already slanted in height in order to minimize the vertical tilt on each optic. Entrance and exit beam run parallel to the path of rays in the telescope for avoiding spherical aberrations. Folding mirror is oriented for 90° reflection and enables on-axis illumination of the cylindric mirror (CM1). The wavelength region from 430–1000 nm illuminates 440 pixel on the SLM. Without inserted SLM this setup enables flexible white light compression down to 7.1 fs without spatial chirp, see Fig. 3.26.

700–900 nm (see Fig. 2.5) the blaze wavelength (maximum efficiency) of the grating was chosen to be at 600 nm. A second concern are the higher orders of diffraction which overlap in case of very broad spectra. This means that due to second order diffraction, blue wavelengths which should pass the Fourier plain (position of SLM) only in their corresponding part, labeled with B in Fig. 2.13, also pass in the area corresponding to NIR spectrum. This problem is inherently reducing itself since the recombining grating (G2) has to be used in second order diffraction again in order to diffract the second order of blue wavelengths along the original beam path. The original beam is diffracted two times at first order with a high efficiency. The region in which overlapping spectra are relevant reaches from 500 nm down to 430 nm and the unwanted intensity is about 0.2%. "Second order" wavelengths above 500 nm are filtered out with an appropriate mask.

Although the wide spectral region is impressive, the spectral inhomogeneity is improvable.

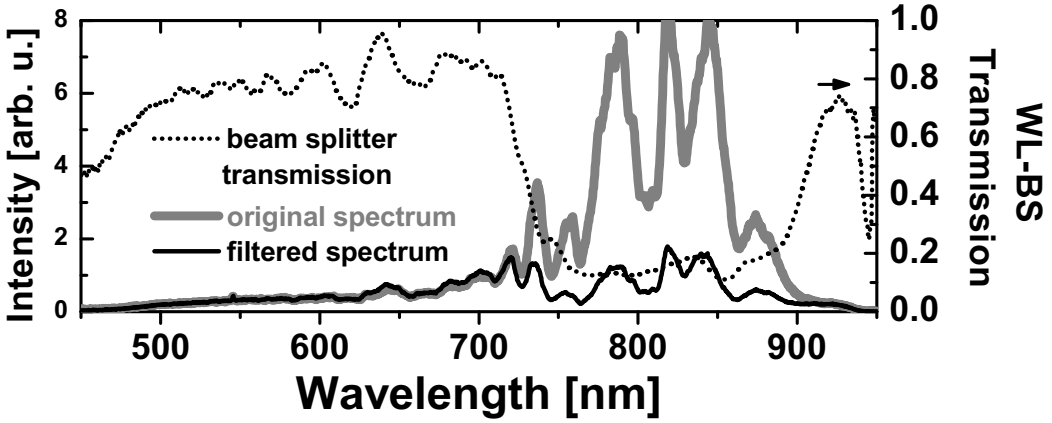

Figure 2.14: White light beam separator WL-BS. Its transmission is given on right hand side and is plotted as dotted curve. The original spectrum (thick, gray line) and the filtered spectrum (thin, black line) are plotted for comparison. Advantages are: (i) homogenizing octave spanning spectra; (ii) protection of SLM mask from damage through NIR light; (iii) reflex could be used as additional ultrashort pump beam.

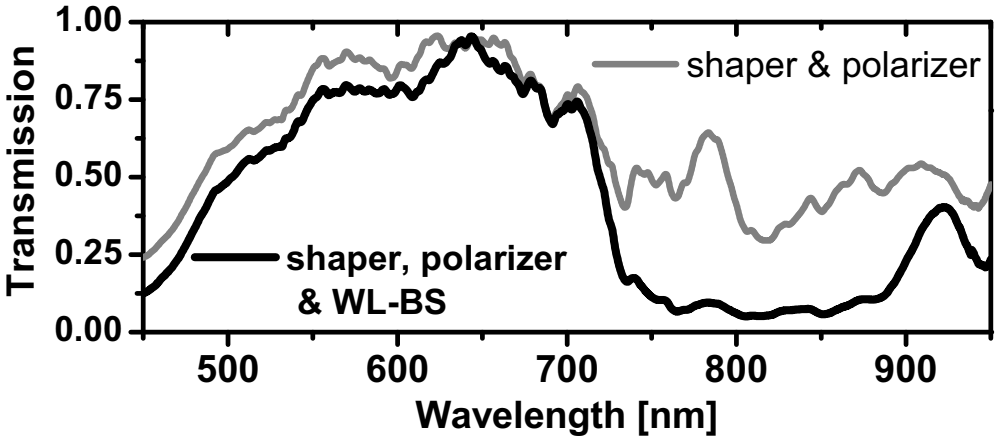

Figure 2.15: Full shaper transmission efficiency. The gray line displays the transmission of the setup in Fig. 2.13 without WL-BS whereas the black line includes the filter. The overall transmission is designed to counter act the asymmetric spectral distribution of the WL filament as shown $e.g.$ in Fig. 3.19.

Indeed, the VIS part can be increased by serving more energy for filamentation, but this brings along reduction of spatial beam quality if a certain intensity level is exceeded. The loss of spatial beam quality is tolerable to some extend for the shaping process and interaction in gas phase experiments, respectively. But it prevents from using the FROG with geometrical beam splitting. To equalize the intense NIR and the weak VIS part, a special white light beam separator (WL-BS) was designed on request by *LAYERTEC*. It reflects 80% of the broadened fundamental and transmits more than 95% in the range from 450–700 nm and above 900 nm. Furthermore, it exhibits minimized dispersion for transmitted as well as for reflected light. Small tilts of $\pm$ 10° tune the region of partial reflectivity @ 800$\pm$70 nm.

The in-sito measured filter transmission curve is shown in Fig. 2.14 as dotted line and for comparison spectra before (thick, gray line) and after filtering (black line) are given. The transmitted spectrum is clearly more homogenous and has a second advantage: It protects the SLM from damage through the NIR part which contains couple of 100 μJ pulse energy. Further on, the reflected portion can be compressed with chirp mirrors and serve as ultrashort pump for experiments, $e.g.$ it could be sent to the second pulse shaper on the table, see Fig. 2.20. Typical energies are 700 μJ for filamented beam, 200 μJ after filtering with (WL-BS) and 60 μJ subsequent to the polarizer (P). Thus the transmission of the whole WL shaper setup is about 28%. While planning the grating setup emphasis was set to the point of minimizing vertical tilt on each optic. Therefore the incoming WL beam (grey ray Fig. 2.13) enters underneath the cylindric mirror (CM1) on the right and is already slanted by steering mirror in front of the setup. This way of hight separation is followed consequently and the beam exits on the left side above cylindric mirror (CM2). With this arrangement a superb spatial beam quality was achieved and the possibility for flexible pulse compression covering 400–1000 nm in a single device is provided. Without SLM in the setup pulses as short as 7 fs were generated by slightly changing the distance of the second grating (G2), $cf.$ Fig. 3.26.

Pros for gratings:

- No additional dispersion introduced.
- Small translation of second grating is sufficient to compress the filament output to few optical cycles.

Cons for gratings:

- Diffraction efficiency is 60% at best for a broad spectral region and is eventually modulated more or less strongly over the entire octave.
- Low groove density is required to keep the spatial dispersion small which causes lower efficiency.
- Higher diffraction order have to be considered.

Figure 2.15 displays the spectral efficiency of the pulse shaper setup consisting of one polarizer, the SLM, two gratings (blaze @ 600 nm), two plane -and two cylindrical Ag mirrors as the light curve. The black curve conforms to overall transmission including WL-BS and is a good counterpart on experimental filament spectrum (see $e.g.$ gray plot in Fig. 3.19).

2.3.2 Single pixel calibration

Another aspect when utilizing a SLM based octave spanning pulse shaper is the wavelength dependent refractive index of the liquid crystals (LC). In the current section the functionality of the SLM is briefly explained with Fig. 2.16 and consequences for WL shaping are discussed. The core component of such a SLM are two arrays (A & B) wich contain nematic molecules whose orientation depends on an external electric DC field. The response time of the SLM is 35 ms for

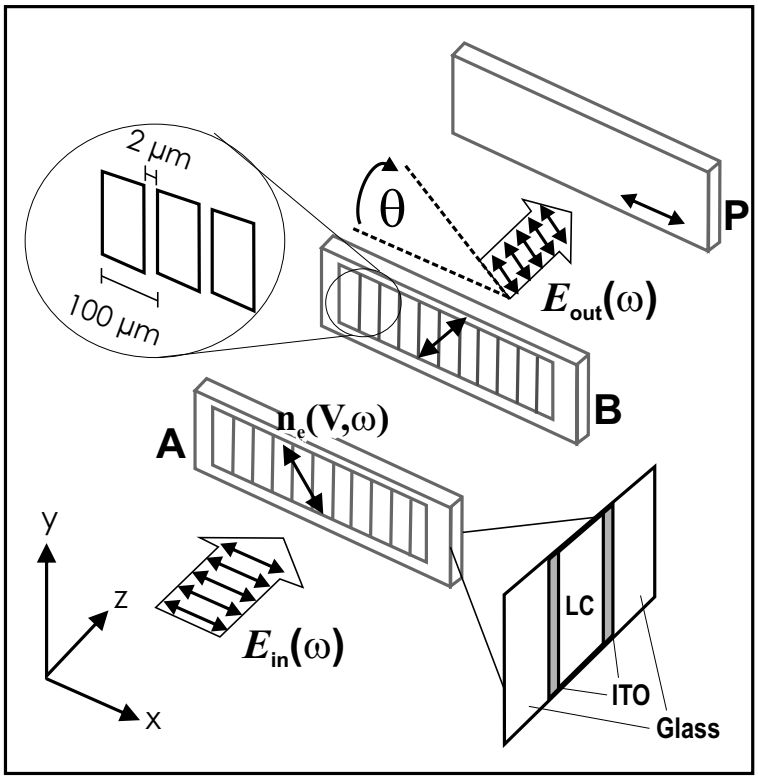

Figure 2.16: Working principle of SLM. One mask consists of liquid crystals (LC) between transparent electrodes (ITO) embedded in glass housing. Each pixel is 98 μm in width and 500 μm in hight with inter pixel gap of 2 μm. Voltage dependent orientation of LC changes birefringence and thus incoming, polarized light $E_{in}(\omega)$ undergoes phase retardation and rotation of polarization (angle θ). Rotated light is blocked at the polarizer (P). Independent modulation of phase and amplitude requires two arrays (A,B) whereby their pre-aligned LC have to orientated perpendicular to each other.

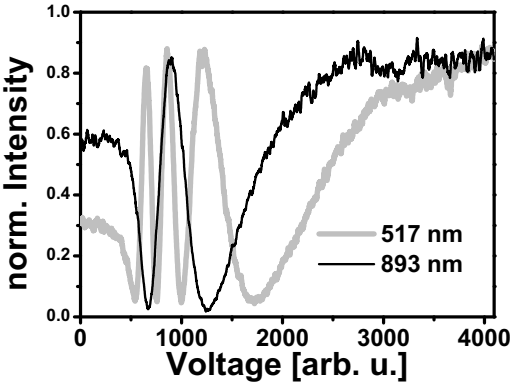

Figure 2.17: Shaper calibration curves @ 517 nm and 893 nm. Both curves differ in the number of peaks and their position. The calibration routine saves voltage dependence transmission of all wavelengths as 3d matrix for each of two arrays A and B. Inverse of eqations (2.8) and (2.10) calculates the desired phase and amplitude value for each voltage. The last step is assignment of pixel number on the SLM to its corresponding wavelength.

2π modulation @ 900 nm. The LC are birefringent because they have two optical axes. One optically active axis along the long molecular axis of the LC with the extraordinary refractive index $n_e(V,\omega)$ and one axis perpendicular to it with the ordinary refractive index $n_o(\omega)$. The pre-aligned molecules[6] of the first array (A) are oriented under 45° with respect to incident light polarization $E_{in}(\omega)$. Thus, the incoming light is decomposed along the ordinary and the extraordinary axis in the x - y plane. Changing the extraordinary refractive index $n_e(V,\omega)$ by changing the molecule orientation is achieved by applying a voltage V through the transparent indium tin oxide (ITO) electrodes. This changes $n_e(V,\omega)$ but not $n_o(\omega)$ and causes a phase retardation and rotation of polarization, by the angle θ in Fig. 2.16. With the refractive index difference $\delta n(V,\omega)$ on a single array A

$$\delta n(V,\omega) = n_e(V,\omega) - n_o(\omega)\,, \tag{2.6}$$

the phase retardation $\delta\Phi_A(V,\omega)$ for a single array is given by [165]

$$\delta\Phi_A(V,\omega) = \omega\frac{\delta n(V,\omega)d}{c}\,, \tag{2.7}$$

where d is the thickness (z-extension) of the array which is around 10 μm. Amplitude attenuation is accomplished when an auxiliary polarizer (P) blocks the turned polarization direction of the outgoing field $E_{out}(\omega)$. Independent modulation of phase and amplitude requires two arrays (A and B) in a row where the extraordinary axis of array B is oriented under -45° with respect to incident light polarization $E_{in}(\omega)$. It means the orientation of molecules in A and B is perpendicular and the total optical phase shift $\phi(V,\omega)$ for one particular point in the Fourier plain is given by the averaged phase retardation of both arrays

$$\phi(V,\omega) = \frac{\delta\Phi_A(V,\omega) + \delta\Phi_B(V,\omega)}{2}\,. \tag{2.8}$$

In contrast, the change in polarization and therewith the possibility for attenuation is equal to the difference of individual phase retardations $\delta\Phi(V,\omega) = (\delta\Phi_A(V,\omega)/2 - \delta\Phi_B(V,\omega)/2)$. After passing both arrays and polarizer the electric field is given by [166, 167]

$$E_{out}(\omega) = E_{in}(\omega)\cdot\underbrace{\underbrace{cos\left((\delta\Phi_A(V,\omega)/2 - \delta\Phi_B(V,\omega)/2\right)}_{amplitude\ modulation}\cdot\underbrace{exp\left((\delta\Phi_A(V,\omega)/2 + \delta\Phi_A(V,\omega)/2\right)}_{phase\ modulation}}_{H(\omega)} \tag{2.9}$$

[6]Pre-alignment is achieved by brushed electrodes which force automatic orientation.

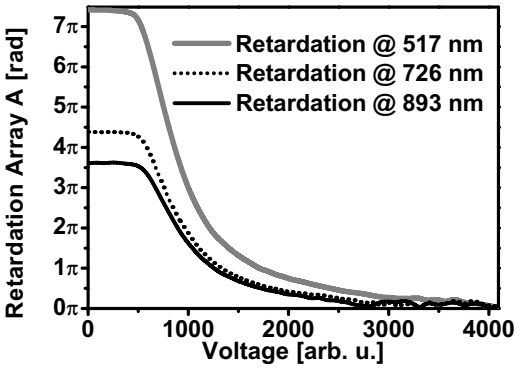

Figure 2.18: Shaper retardation curves @ 517 nm (grey line), @ 726 nm (dotted line) and 893 nm (black line). The difference in total height of stroke for phase shifts corresponds directly to numbers of extrema in Fig. 2.17. Retardation @ 500 nm is twice the retardation @ 900 nm. After calibration, every SLM pixel is associated with its appropriate retardation curve.

The physical origin for the cosine term is the same as in the case of two beam interference $e.g.$ in a Michelson interferometer. Minimum and maximum of the interferometer output depend on the cosine of the relative time delay of one arm with respect to the other. In case of amplitude shaping with both arrays and a polarizer, the (intensity) transmission T can be formulated as

$$T(V,\omega) = cos^2\left((\delta\Phi_A(V,\omega)/2 - \delta\Phi_B(V,\omega)/2\right) \ . \tag{2.10}$$

It was found that amplitude modulation is possible in range from 450–950 nm although spectral range according to *CRI* manual is 488-900 nm [168].

Because the total optical phase shift $\phi(V,\omega)$ is a function of voltage and frequency, a calibration had to be carried out for each pixel or wavelength, respectively. Two exemplary calibration curves are plotted in Fig. 2.17, where transmission of a single array is plotted as function of applied voltage V. The voltage is computer controlled via LabView in the range from 0-10 V within 4096 steps. Minimum and maximum transmission arise from the optical path difference of ordinary and extraordinary ray, depending on the voltage according to Eq.(2.7). Both curves differ in the number of peaks which denotes that total height of stroke for phase shifts is larger for blue wavelengths. A step from one extremum to the next one is equal to a phase shift of π. Further on, the curves also exhibit different peak positions or even interchanged min-max behavior, respectively. The translation from the voltage dependent intensity to phase retardation is achieved by smoothing and

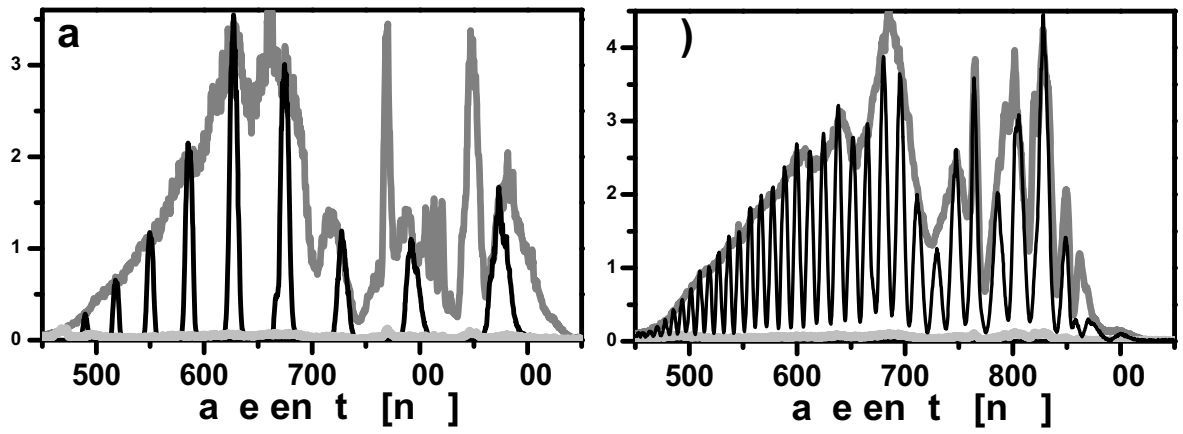

Figure 2.19: Sinusoidal amplitude transmission after successful calibration. Gray plots show minimum and maximum transmission of the WL shaper. The modulation frequency is equidistant on energy axis. A sin^8 function with large modulation period was written in a), whereas a higher frequency was used in b).

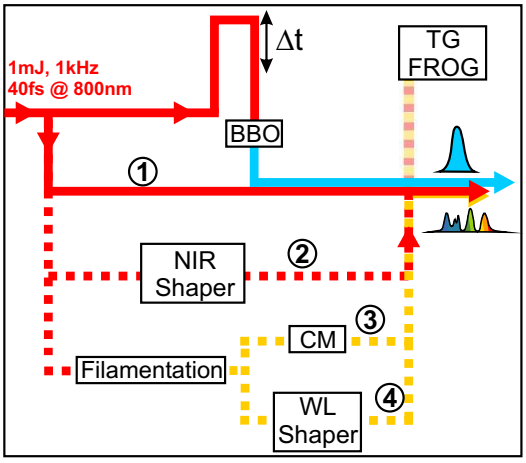

Figure 2.20: Ultrafast spectroscopy setup. It sketches the four different pump probe configurations for NeNePo spectroscopy. Part of the fundamental beam is send via delay line to 1 mm BBO which served as pump beam in most experiments. Pumping was carried out with either (1) unshaped NIR, (2) shaped NIR light, (3) compressed WL and a fourth option (4), where the shaped WL did the complete charge reversal as single beam experiment. For pulse characterization a the home built TG-FROG and a commercial autocorrelator were available. Some pump probe specifications are listed in table 2.1.

unwrapping the plots of Fig. 2.17 which gives the result shown in Fig. 2.18. Here, the different hight of stroke becomes clearly visible.

Obviously, one calibration for the entire octave won't work out and the pixel wise calibration was as follows. One array was set to maximal voltage which guarantees a maximal transmission contribution from this array. On the second array the voltage scan was performed while recording all corresponding transmission spectra. Then the roles of both arrays were interchanged and the procedure repeated. The last step is the assignment of pixel number on the SLM to its corresponding wavelength wherefore only one pixel was set to maximum transmission and scanned across the mask. This precise scan was necessary especially for the prism setup because the spatial spread of frequencies was highly nonlinear. At the end of day, every shaper pixel is associated with an individual retardation curve as shown in Fig. 2.18 for three wavelengths. Successful amplitude modulation of the octave spanning WL pulse shaper is presented in Fig. 2.19. If the transmission modulation frequency is not too high (Fig. 2.19a) a extinction rate of 50:1 is achieved. Smaller modulation period in b) causes a reduction of the extinction contrast. These measurements were performed with the WL-BS (Fig. 2.14) prior to the pulse shaper.

2.4 Time resolved spectroscopy

For time resolved spectroscopy, a pump probe setup was build up and the two pulses were sent to the ion trap which is located in the neighbouring room. For the coherent control experiments the pump probe setup was extended by the WL shaper and a second "conventional" shaper. General specifications of these excitation schemes are presented in this section. Figure 2.20 comprises all possibilities of different pump probe configurations. The design on the optic table allows for

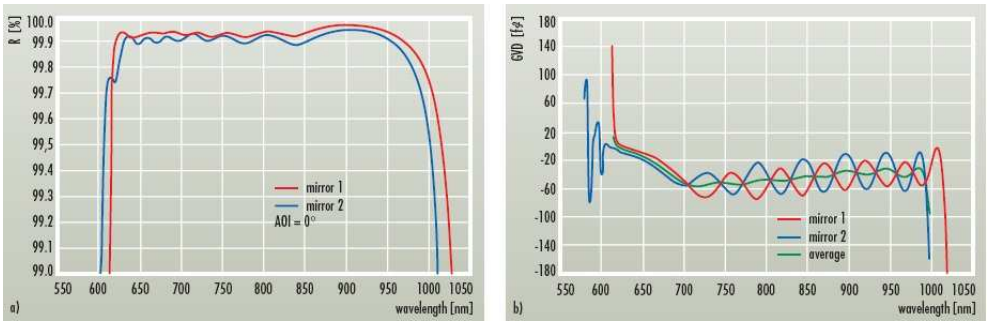

Figure 2.21: Chirp mirror pair with GVD oscillation compensation. Reflectivity curves in a) and negative GVD in b) support the generation of 5 fs pulses. Graphic taken from Ref. [169].

flexible switching between different paths by flipping mirrors. The target, a hexadecapol ion trap, is not displayed here. A brief description of the cluster machine is given at the beginning of Chap. 4.

Four different realizations of pump probe methods were used for NeNePo spectroscopy (Chap. 4) on mass selected Ag_n clusters. Therefore, the amplified laser output was split and the remaining part of the laser fundamental served as pump beam. It is send via a delay line to a frequency doubling stage consisting of 1 mm BBO with 30% conversion efficiency and subsequent separator optics which reflect only 400 nm wavelengths. The main portion (50–80%) of the laser fundamental is sent to one of four possible pump beam paths, numbers (1)-(4). Absolute intensity values are different in the respective experiments and are thus labeled in corresponding sections. Path No. (1) denotes a standard pump beam which could also be frequency doubled if necessary. The second option for the pump step consists of a reflective grating shaper setup which was used for the pulse train excitation described in Sec. 4.1. The basic layout of this setup compares to Fig. 2.13 and is designed to enable amplitude and phase modulation at the laser fundamental with a smaller SLM, consisting of 2×128 pixel. The filamentation output could be either used directly as an ultra broadband excitation or with subsequent compression by chirped mirrors (CM) to generate high energy (0.6-1.2 mJ) few cycle pulses. Dispersion management is achieved by four bounces on commercial available chirped mirror pair CM1 & CM2, (*Layertec*) with GVD oscillation compensation as illustrated in Fig. 2.21, taken from Ref. [169]. The oscillations arise from interferences of the multilayer structure and are small for standard bandwidths. However, ultra broadband negative dispersion mirrors exhibit strong GVD oscillations. In order to flatten these oscillations mirror pairs consisting with slightly shifted GVD oscillations are used which compensate each other. Average negative GVD is approximately -60 fs^2 per bounce in wavelength range from 700–900 nm. Total reflectivity is $> 99.8\%$ from 650–1000 nm at incident angle of 0°. They basically compensate for the GVD arising from 8.5 m beam travel in air behind the filamentation which accounts to $\approx$ +200 fs^2. Ultimate excitation, path (4), by means of arbitrary shaped ultra broad pulses is achieved with the WL shaper. The working principle was explained in previous section and the full capability is presented in Sec. 3.3. It is mentioned here, that WL generation and subsequent octave spanning shaping opens the possibility for performing a pump probe experiment as single beam setup, $cf.$ Fig. 3.39a–d). Single beam pump probe can be achieved with the pulse shaper by applying linear phase ramps $H(\omega)$ for different wavelength regions on the SLM. This causes a

Path	Pump	Probe
1	402 nm $\Delta\lambda = \pm$ 5 nm	805 nm $\Delta\lambda = \pm$ 20 nm; $\Delta t = 40$ fs
2	402 nm $\Delta\lambda = \pm$ 5 nm	shaped 805 nm $\Delta\lambda = \pm$ 20 nm $\Delta t = 40$ fs; $\Delta T = 1000$ fs
3	402 nm $\Delta\lambda = \pm$ 5 nm	white light & chirped mirrors 700-900 nm $\Delta t = 6.5$ fs
4	shaped white light 450-750 nm $\Delta t = 15$ fs; $\Delta T = 600$ fs	shaped white light 750-950 nm $\Delta t = 7$ fs; $\Delta T = 800$ fs

Table 2.1: Pump probe schemes used for NeNePo on Ag_2 and Ag_3. Numbers in first row correspond to optical paths in Fig. 2.20. $\Delta\lambda$ labels available spectral range, Δt the shortest FWHM duration and ΔT the largest separation of two neighbouring pulses of a pulse train.

shift in time but keeps pulse envelope unchanged, see Sec. 3.3. Characterization was carried out with a fiber spectrometer (*Ocean Optics, USB 2000*), a commercial SHG auto correlator (*APE, Pulse Check*) and the home build TG-FROG. In the particular case of Ag_3 excitation (Sec. 4.2), the TG-FROG technique was extended to a single beam cross correlation variant (TG-X-FROG) which is described in detail in Sec. 3.4.2.

Table 2.1 assorts pulse specifications of the different pump probe schemes. The path numbers corresponds to the ones drawn in Fig. 2.20. The two expressions for time duration correspond to the shortest FWHM (Δt) and to the largest separation of two neighbouring pulses of a pulse train (ΔT), respectively. The mentioned pulse trains were produced by writing sinusoidal phase functions on the mask rather than amplitude modulation. Of course, the quality of the pulse trains is reduced for huge and small inter pulse distances, respectively.

Chapter 3

The White Light Toolbox

A famous statement by *Wayne Knox* says:

" *If you haven't measured it, you haven't made it.*"

Thats of course right and one can raise the question: "If you measure something, what does it mean?"
The latter is equivalent to the question if something is true just because your instrument displays certain values. To ensure the truth one can either repeat the measurement many times or perform a crosscheck to achieve a certain degree of confidence.
This chapter contains **optical results** related to to the generation and utilization of WL. On the experimental side, the steering of the desired filamentation behavior by varying initial conditions (Sec. 3.2) as well as subsequent applications like pulse compression (Sec. 3.2.2) and computer controlled pulse shaping (Sec. 3.3) are described. Furthermore, intensive analysis of octave spanning phase matching in the 4WM process leads to the development of a single beam cross-correlation method named single beam TG-X-FROG, which is described in Sec. 3.4.2. This new invention actually enabled the characterization of the coherent control results of chapter 4. Experimental observations of filamentation broadening and 4WM are supplemented by numerical calculations and discussed in Secs. 3.5.2 and 3.5.3, respectively. It will be shown that: (i) The asymmetry of WL spectrum can be numerically steered by different timing of Kerr- and plasma onset. (ii) Octave exceeding gating of those asymmetric WL spectra is a non degenerate process where the intense NIR serves as a gating structure on which the weak VIS part is correlated.

3.1 Characterizing filamentation

As a consequence of the high nonlinearity of the filamentation process, the Kerr effect is a three photon process and the multi photon ionization (MPI) requires eight or ten photons in case of O_2 or N_2, respectively. The role of following parameters was investigated in view of filamentation:

- Input beam profile
- Input energy
- Prechirp of laser amplifier
- Gas pressure
- Gas type

As characterization tools conduced a fiber spectrometer (*Ocean Optics USB 2000*) operating from 350–1024 nm, a power meter (*Coherent FieldMaster GS*) and the TG-FROG with amplitude splitting (Sec. 2.2.1). This TG-FROG version was used because of its better acceptance on inhomogeneous beam profiles and simply because it was invented first. The predominant part of the

investigation presented in this subsection was carried out in the Diploma thesis of Waldemar Unrau [170]. Analysis was achieved by comparing FROG traces and power spectra for different conditions. Investigated gases on the same subject are: He, Ar, Kr, Xe, Air, O_2

3.1.1 Influence of the optical path

Before analyzing the filamentation process, one has to check at which point spectral or temporal changes of the octave might occur, which do not belong to the generation process itself but to propagation elsewhere. The spectral efficiency of the shaper setup has been characterized in Sec. 2.3.1 and effects accompanied with pulse compression will be presented in Sec. 3.2.2. It is mentioned that temporal dispersion during propagation even in atmospheric air has to be considered, when dealing with few cycle pulses. The quadratic chirp (GVD) is about 23 fs^2 per meter and broadens a transform limited 6 fs pulse ($\Delta\lambda$ =160 nm@800 nm) to 12 fs. Thus, only reflective optics were used to avoid material dispersion (mostly special silver mirrors for fs application from *LAYERTEC*), having minor reflectivity changes between 85%-95% over the entire octave. Significant spectral filtering effects from steering mirrors were not observed.

A significant contribution arose from the entrance and exit window of the gas cell because they add GVD and SPM. The GVD of 1mm FS amounts 31 fs^2 and thus broadens the same 6 fs pulse to 18 fs. The spectral change arising from both FS windows, which are roughly 85 cm off the focal point, are evaluated in Fig. 3.1. Laser pulses with varying energy according to the legend were passed through the evacuated cell. A slight positive prechirp of 400 fs^2 was used in Fig. 3.1a since it causes the strongest broadening and allows an estimation for the minimum energy below which the spectrum remains unchanged. Significant changes already occur at low energy of 125 μJ whereby the spectrum broadens with increasing energy and the mean wavelength shifts slightly towards the red side in a). The laser fundamental (FWHM: 785–820 nm) is plotted as thin black line. Sidebands, marked with arrows, arise at 765 nm and 855 nm which are untypical for SPM ($cf.$ Fig. 1.5). The red shift at higher energies is investigated in b), where the energy reaches from 0.5–1.4 mJ which is equal to the range within which the following parameter dependences were investigated. Other than in a) no prechirp was set in order to have a general reference. The curve at 0.6 mJ (open squares) obeys a kind of symmetric, three peaked structure. Increasing the energy to 0.7 mJ (solid red line) causes a sudden change in the spectral shape compared to 0.6 mJ. A further energy increase shifts the spectrum by 15 nm to the red side with a rising flank above 840 nm. This while, the cut-off at the short wavelength side stays constant at 765 nm. In general, the spectral shape at a given input intensity depends strongly on the prechirp of the laser, as can be

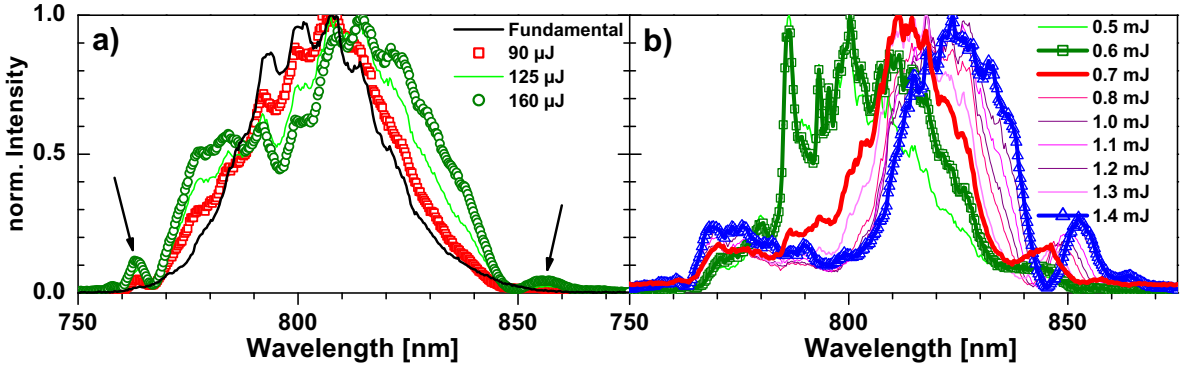

Figure 3.1: SPM in FS windows as a function of laser energy with evacuated cell. A slight positive prechirp of 400 fs^2 causes the strongest changes in a). No prechirp in b) for comparability with the following measurements. A clear red shift of the spectrum occurs at higher energies.

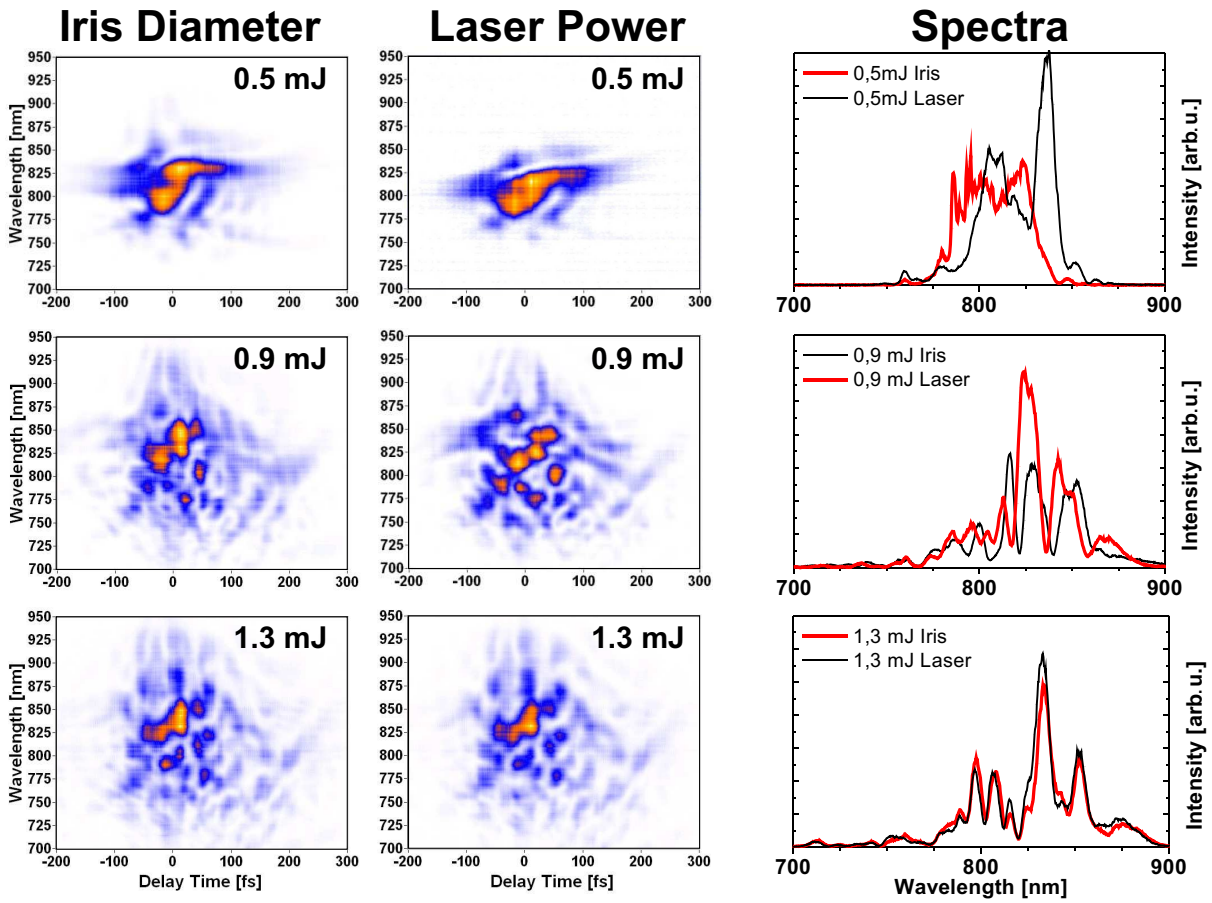

Figure 3.2: Spectral broadening depending on the input beam profile. TG-FROG traces and power spectra for three different pulse energies. Spectral broadening took place in atmospheric air with disassembled FS windows. The difference between energy reduction by closing an iris (left column) and fluence reduction out of the amplifier (middle column) becomes stronger, the more the iris is closed in order to transmit the same amount of energy. The corresponding spectra are given in the right column.

verified in in Fig. 3.8. Interestingly, the spectral side bands marked with arrows in Fig. 3.1a have a different origin than SPM and were also observed in Ref. [42].

All spectra presented herein after display an integration over the entire beam profile by measuring diffuse reflection from a piece of chalk with the fiber spectrometer. This way of spatial integrating was cross-checked by comparison with an integrating sphere, which showed no difference but much weaker signal.

3.1.2 Parameter dependence

Input beam profile At first, a parameter dependence compares the difference between changing the input energy by reduction of laser output or by closing iris I1 in Fig. 2.1 while the laser power is kept constantly at maximum. Fluence adjustment out of the amplifier is achieved by regulating the lamp current of the pump laser. The FS windows were removed for this measurement, thus spectral broadening was achieved in atmospheric air. Starting with transform limited 1.43 mJ pulses, the energy was reduced to 1.3 mJ (third row), 0.9 mJ (second row) and 0.5 mJ (first row) in Fig. 3.2. Closing the iris leads to a radial symmetric near field diffraction pattern. The left column contains TG-FROG traces for reduction of the iris diameter, the middle one for amplifier tuning and the right one shows the corresponding spectra. For small energy reductions from 1.43

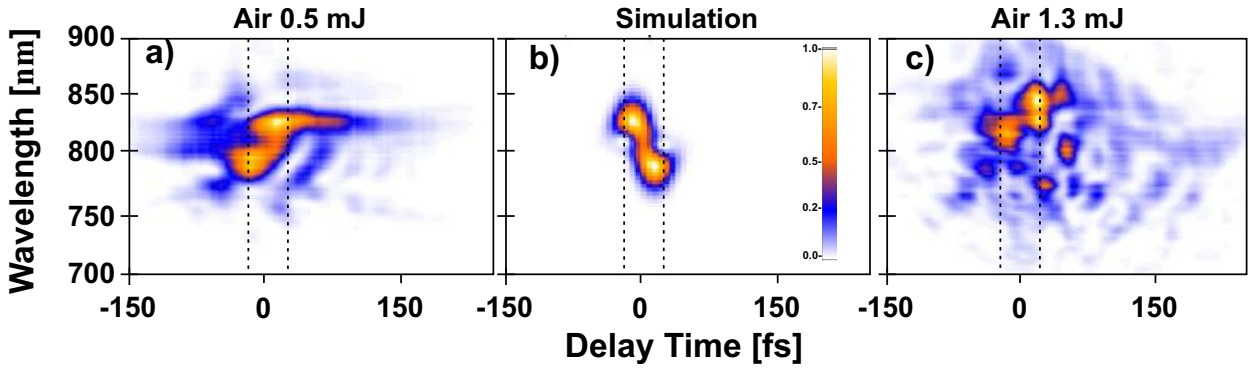

Figure 3.3: Comparison of measured traces a) and c) with theory b). Calculations were performed for a 50 fs pulse centered at 805 nm which conforms to the real situation.

to 1.3 mJ in the third row, TG-FROG traces and spectra look almost identical. This is reasonable since sparse iris closing has a minor effect on the beam profile. At 0.9 mJ, details of the traces and spectral peaks clearly exhibit differences, whereas the overall temporal as well as spectral shape is similar. The differences become most conspicuous at 0.5 mJ, especially in the spectrum in the right column. The temporal envelope for both conditions is rather same, like in all three energy pairs. All spectral pairs of the right column are measured at identical conditions for comparability. One immediately recognizes that filamentation at 0.9 mJ (second row) provides a larger FWHM when focusing a radial symmetric diffraction pattern compared to the broadening with the direct laser output at the same energy. Some discussion about the pattern in the TG-FROG traces is anticipated here, because it provides a basis for the interpretation of the following measurements. Therefore, Fig. 3.3 compares measured SPM traces in air at 0.5 mJ (a) and 1.3 mJ (c) with a calculated trace in b). The spectra corresponding to Fig. 3.3a and c) are given in Fig. 3.2 in the first and last row as red lines.

The simulation of pure SPM in Fig. 3.3b was carried out with commercial software [171] and calculates pure SPM for a 50 fs input pulse centered at 800 nm. The vertical dashed lines indicate the FWHM duration in the images. As expected from theory of Sec. 1.2.1, red frequencies are generated prior to the blue ones and a dip occurs between both maxima. The first difference lies in the temporal broadening which does not occur in the simulation in which dispersion and space time coupling (Sec. 1.2.3) are neglected. The measurement of case c) shows a FWHM increase for about 15% with respect to the input pulse. Moreover the temporal width in the pulse flankes is much broader. The amount of spectral broadening for the low energy case of Fig. 3.3a agrees with the simulation. However, the measured trace of Fig. 3.3a seems to be time inverted to the simulation in b), when comparing the intense parts of the trace. Indeed, the measured pulse in a) also contains red components in the beginning, but they are only about 30% as intense as the maximum.

Spectral broadening in the high energy (1.3 mJ) case in c) has a definitely different origin than pure SPM. The same holds when comparing the corresponding spectra of the second and third row of Fig. 3.2 with theoretical SPM spectra like in Fig. 1.5. Also a shift of the mean wavelength towards NIR side is conspicuous, while SPM should cause only symmetric broadening.

In Fig. 3.2 the influence of the iris was investigated in the NIR regime, but its effects also become recognizable in the VIS part. The furthest extension towards the short wavelengths was usually reached by closing the iris for about 20% at simultaneous observation with the spectrometer. However, all the following parameter dependences were measured with opened iris unless

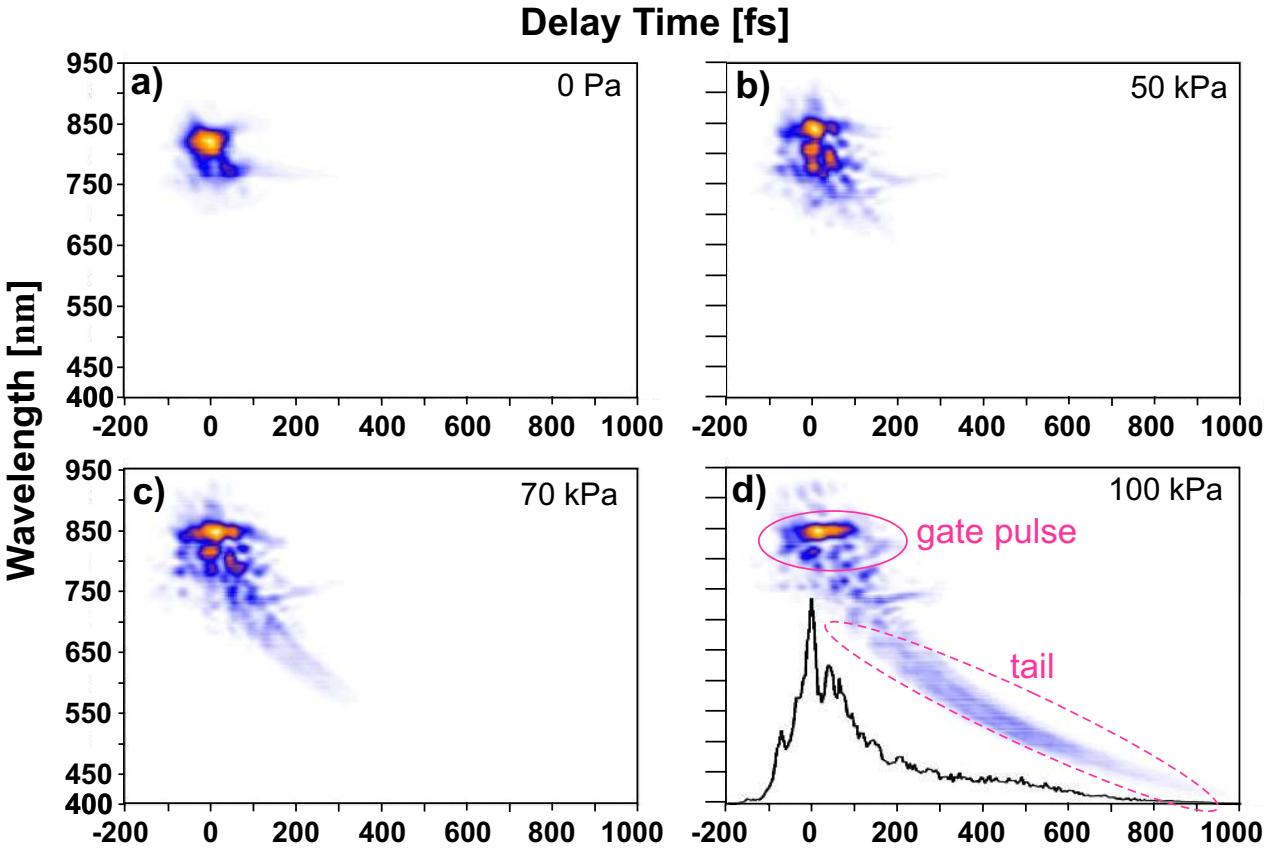

Figure 3.4: Filamentation in air: pressure dependence. TG-FROG traces of WL for an unchirped input pulse with 1.43 mJ and 0/50/70/100 kPa in Figures a)/b)/c)/d). A projection onto the time axis given as black line in d) which shows the temporal dispersion of the strongly chirped VIS part. Two areas are distinguishable in d). An NIR part named "gate pulse" and VIS part referred to as "tail".

mentioned otherwise. This decision was made in order to have reproducible conditions for the successive investigations.

Pressure dependence in Air All pressure dependences were carried out with both FS windows mounted onto the gas cell, as drawn in Fig. 2.1. The first parameter variation in Fig. 3.4 shows TG-FROG traces for broadening of TL pulses in air at a constant energy of 1.4 mJ and different pressures. Generally, the value for n_2 is proportional to the pressure over the range from 10–1000 kPa [172, 173]. Separately measured spectra are given in Fig. 3.5. Clearly, neither the traces nor the spectra conform exclusively to SPM. Indeed the spectral extension increases with pressure, however, not uniformly but with a strong asymmetry, pronouncing the blue side (seen best in the traces of Fig. 3.4c and d)). The center wavelength of the amplifier is 805 nm. From the gray plot in Fig. 3.5a it is seen, that already the broadening in the evacuated cell is asymmetric which can be assigned to a slight residual prechirp although the pulse is called unchirped.

For that, some general remarks concerning the prechirp of the fs amplifier are made. The filamentation, or more precise the spectral fingerprint in the NIR region as well as the cut-off at the blue side and especially the generation of few cycle pulses turned out to be very sensitive on the prechirp. Fine adjustments on the order of $\pm$ 100 fs^2 lead to noticeable change of the output. All given values for the prechirp are calculated from reading off the scale on the linear travel stage of the compressor grating in the amplifier. Finding the shortest pulse ($i.\,e.$ the zero chirp position) was performed with the commercial auto correlator whose accuracy is 40 $\pm$ 2 fs for the used scan

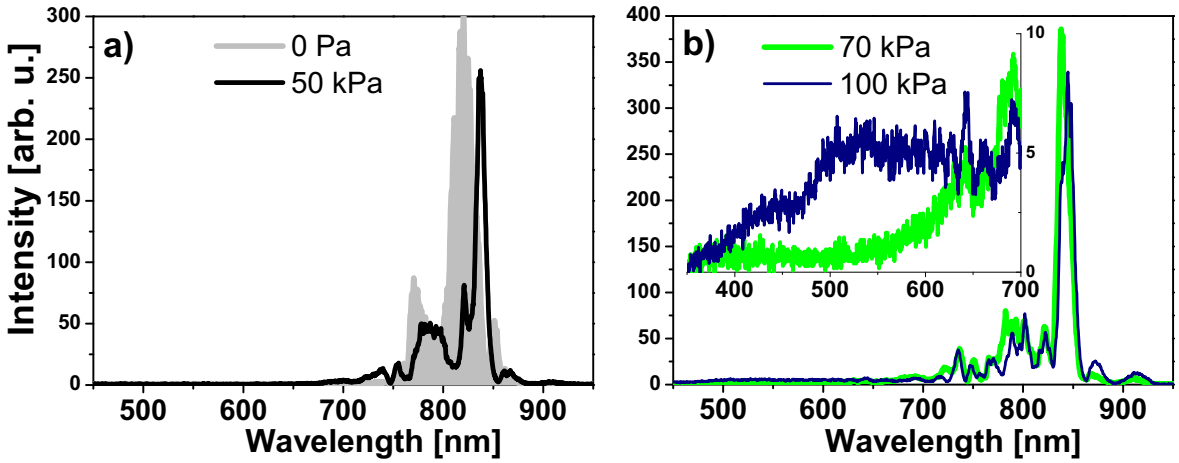

Figure 3.5: Power spectra corresponding to the pressure dependence in air corresponding to Fig. 3.4. A red shift becomes visible for a low pressure of 50 kPa (black) in Fig. 3.5a, where the vacuum broadening due to the FS windows is plotted in gray. High pressures in b) cause asymmetric broadening to the blue side, as is visible best in the inlet of b). Once the broadening beyond 400 nm is achieved, the blue spectral side exhibits a characteristic plateau like appearance (blue). Shorter extensions generally show a continuous decay, as shown for 70 kPa in green.

range. This, in combination with the repeatability of the travel stage, corresponds to an uncertainty of about $\pm$ 300 fs^2 in reproducing the zero chirp position.

Besides the spectral asymmetry in Fig. 3.5a for the evacuated cell, a red shift of the spectrum becomes visible, when 50 kPa air is inserted, as shown by the black curve. The pronounced peak does not shift further to the red side for higher pressures of Fig. 3.5b merely the asymmetric towards the blue side rises. From the inlet, an extension down to 400 nm is seen. Since the corresponding trace in Fig. 3.4d represents a general appearance of the WL filamentation, some expressions shall be clarified by means of this trace. The intense NIR part is also referred to as gate pulse, for reasons which will be discussed in Sec. 3.4. The temporal and spectral details of this gate pulse vary noticeably for different parameters, but its temporal extent is mostly constant amounting to about 200 fs. The highly modulated part of the spectrum ranges from 730–950 nm for all types of filaments in this work. On the other hand, the VIS tail generally appears similar in all cases, except for the case of few cycle pulse generation. If present at all, the tail always shows a strong positive chirp which is almost linear, $cf.$ Fig. 3.20. This distinction of two spectral ranges can be seen in the spectrum of the high pressure filamentation (blue line in Fig. 3.5b). The inlet shows the weaker VIS part reaching from 400–700 nm in this case. The intense gating structure has a narrow peak at 840 nm and a broad pedestal around. The high peak most likely originates from SPM in the glass window because this structure is also present with an evacuated cell (gray plot in Fig. 3.5a). This measurement reveals the influence of the glass windows on the shape of the WL spectrum, especially in the NIR.

Filamentation in noble gases

Up to now, the nonlinearity of the medium was changed by varying its density. Another option is to exchange the medium and to compare different ones among each other. In order to verify the influence of the gas type, pressure-, energy- and prechirp dependencies were carried out with the available noble gases He, Ar, Kr and Xe [170]. The question was, how the different IPs and nonlinear indices n_2 ($cf.$ Table 3.1) contribute to the WL generation. The second point of interest was to see if there is a principal difference when switching from an atomic gas to a molecular

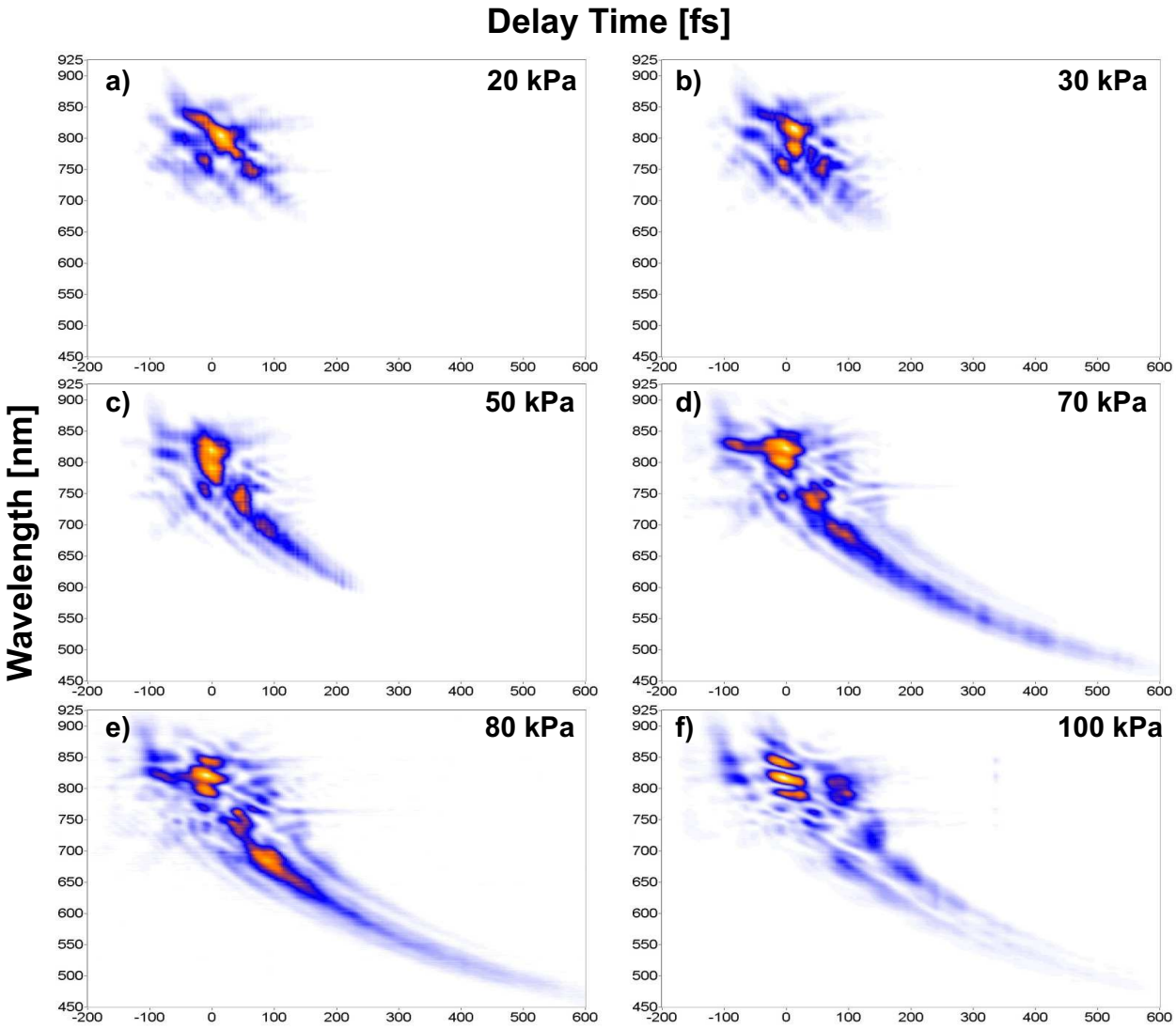

Figure 3.6: Filamentation in Ar: pressure dependence. TG-FROG traces of filamentation with unchirped input at 1.4 mJ for 20/30/50/70/80/90 kPa in Figures a)/b)/c)/d)/e)f).

gas like air or pure O_2. Concerning the noble gases, it is anticipated that He on its own did not exhibit any broadening up to a pressure of 250 kPa which is the upper limit for the cell assembly. A spectrum for 200 kPa He is depicted in Fig. 3.21.

Pressure dependence in Ar Thus, the first discussed candidate is Ar. Ar is of particular interest since it has the same IP but different n_2 compared to N_2 whereby air consists of roughly 79% N_2 (and 21% O_2). The six TG-FROG traces in Fig. 3.6 show the pressure dependence for WL generation with an unchirped input pulse at 1.4 mJ. At 20 kPa Ar in a) the continuum spans from 700–900 nm, the pulse extends temporally over 200 fs and exhibits already an unclean structure. This diffuse gate pulse becomes more and more cohering when increasing the pressure for 10 KPa in b), and up to 50 kPa in c). Simultaneously, the VIS tail begins to evolve and further rises with increasing pressure from d) to e). Although the VIS part from 700–450 nm remains smooth up to 80 kPa in e), a temporal splitting emerges in the NIR part ($cf.$ Sec. 3.1.3). The temporal extension of the tail spreads out to 600 fs. The NIR splitting is fully developed at a pressure of 100 kPa in f) while the tail undergoes slight spectral modulations and appears as a double feature. These VIS modulations can be seen as black curve in the spectrum of Fig. 3.7a. The temporally split NIR

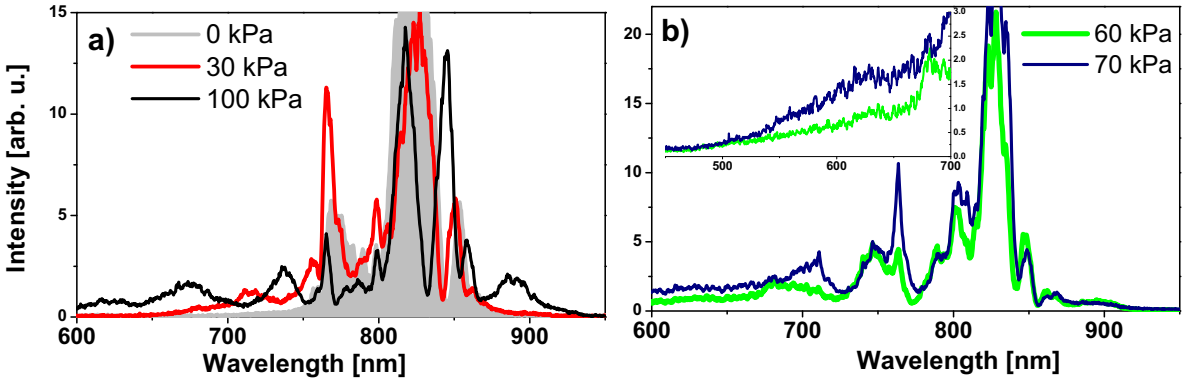

Figure 3.7: Power spectra corresponding to the pressure dependence in Ar of Fig. 3.6.

structure at 100 kPa finds its spectral counterpart in the double peak of the spectrum given as black line.

Like in air, spectral broadening becomes more and more asymmetric towards the blue side but it always exhibits a predominantly smooth VIS tail. Several peaks in the NIR rise and fall when varying the density of the nonlinear medium, but the determinant structure origins from the windows, which can be seen by comparison to the gray filling in Fig. 3.7a. Different compared to air, is the lower pressure required for the onset of WL generation. At 70 kPa of air, the broadening is lucidly narrower ($cf.$ Fig. 3.4). Above 70 kPa Ar in Fig. 3.6d, broadening saturates at an extension from 450–930 nm. The efficiency for generating WL at wavelengths of 500 nm and below reaches its maximum at 70 kPa. In the case of the atomic gas Ar, an initial red shift is not observed when comparing the low pressure spectrum in red in Fig. 3.7a to the gray curve for vacuum.

Chirp dependence in Ar The strong impact of the prechirp on the WL generation manifests not only by the amount of broadening, but also because it leads to an asymmetry of the spectrum [33, 42]. To begin this chirp series in 70 kPa Ar at 1.5 mJ, the grating separation in the amplifier compressor was successively enlarged to reach positive chirp values, until no noticeable spectral changes occurred compared to the broadening in vacuum. The given chirp parameters are calculated from reading the scale on the linear stage. Seven representative TG-FROG traces are selected in Fig. 3.8, beginning at a positive prechirp of 2150 fs^2 in a) and ending at -1000 fs^2 in g). These two positions denote the complete termination of filamentation, although in both traces the chirped NIR pulse look different. This is due to the nonlinearity in the windows, which is still present at these chirp parameters.

During the parameter variation, the gate pulse takes very different appearances. Though having a similar absolute chirp value, the NIR traces for positive and negative sign are completely different in Fig. 3.8c and f), respectively. In contrast, the form of the tail (wavelengths beneath 700 nm) is equal in all pictures. The occurrence of a split NIR structure is accompanied by corresponding manifold VIS tails (images c–f). For these traces one cannot fully distinguish whether the manifold origins from the filamentation process, which is most likely for the present case, or from the gating mechanism in the TG-FROG. Concerning the latter argument, the reader is referred to Sec. 3.4.1.

The spectral evolution depending on the prechirp is presented in Fig. 3.8h in ascending order, $i.\,e.$, a change from positive to negative prechirp. The spectra for the selected images are named with corresponding letters on the right side. One recognizes that drastic changes take place from 750–900 nm whereas the VIS spectra remain smooth.

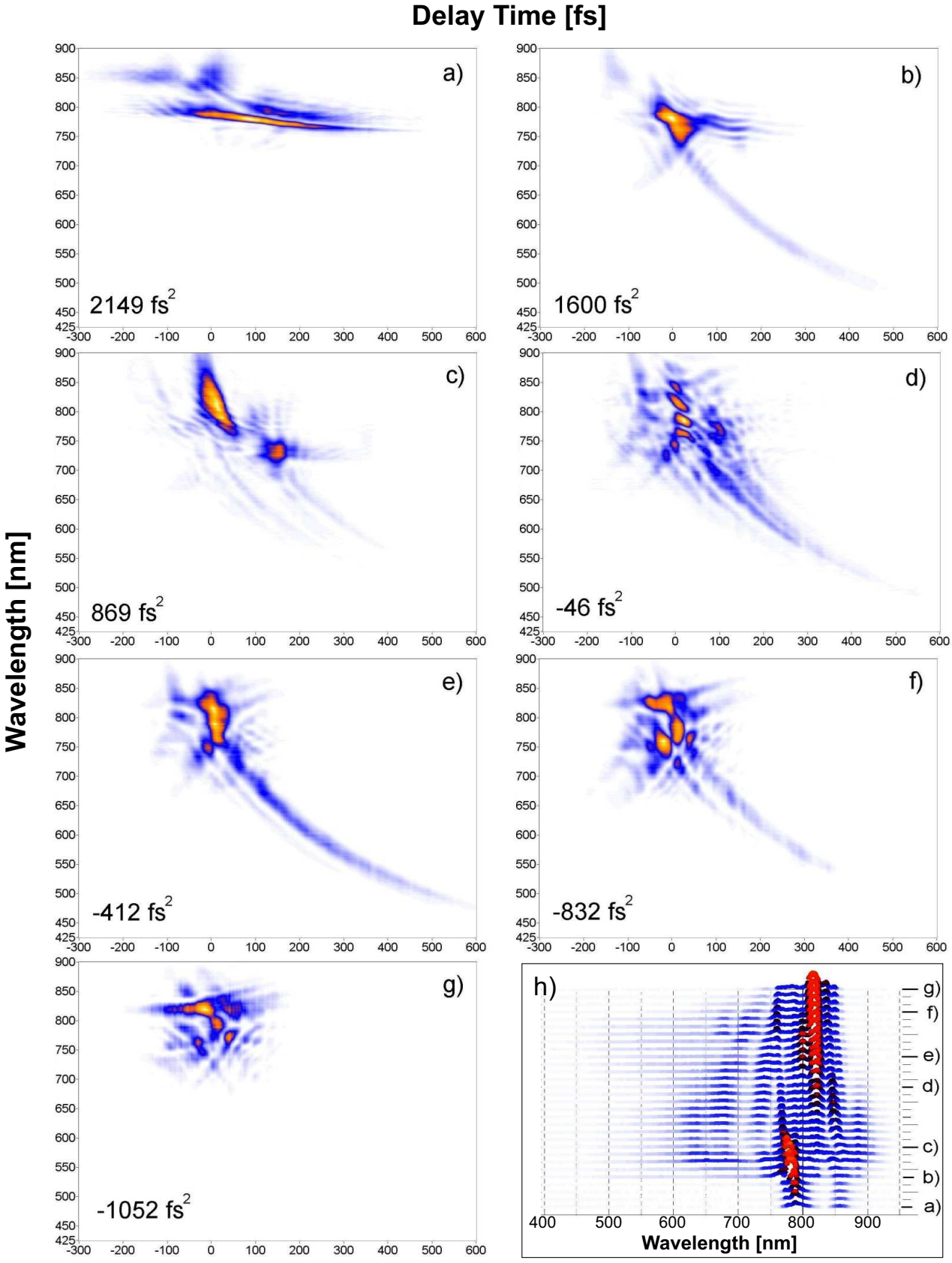

Figure 3.8: Filamentation in Ar: chirp dependence. TG-FROG traces of filamentation with constant energy of 1.5 mJ in Ar@70 kPa. The spectral evolution for the different prechirps in Fig. a)-g) can be followed up in Fig. h).

From the directly measured spectra in Fig. 3.8h, it is seen that a positive prechirp in graph a) exhibits one NIR peak below 800 nm which switches to 825 nm for negative prechirps in graphs e)–g). At the zero chirp position in graph d), the NIR spectrum is entirely modulated and the lower signal indicates a spatial beam break up. Since the prechirp does not only change the spectral phase of the input pulse but also reduces its peak intensity or peak energy, respectively, an estimation is made in order to compare the chirp dependence versus the energy dependence with regard to maximum pulse energy. Chirping the pulse reduces the peak energy while keeping the integral energy constant. Assuming a Gaussian shape, the prechirp of $\pm$ 1000 fs^2 denotes a doubling of the FWHM duration compared to a transform limited 40 fs pulse. Thus, the peak energy is reduced to half. Accordingly, a prechirp of $\pm$ 1600 fs^2 causes an increase to almost three times the TL duration (118 fs) and a decrease the peak energy to one third.

Energy dependence in Ar TG-FROG traces for the outstanding parameter variation in Ar, the pulse energy, are presented in Fig. 3.9. The constant parameters for the Ar filling were 70 kPa for the pressure and -380 fs^2 for the prechirp because these values prevent from breaking up of the spatial mode as well as the formation of colored islands in the beam profile. The series starts at 0.7 mJ in Fig. 3.9a. At this energy, changes occur which are already caused by filamentation process itself and not only due to the FS windows. The total investigated energy range from 0.5 to 1.5 mJ corresponds to a change of the peak energy by a factor of three, similar to the chirp variation of Fig. 3.8. However, during the energy variation in Fig. 3.9, the changes are weaker than for the previous chirp variation in Fig. 3.8. The broadening is still asymmetric in Fig. 3.9 and also evolves continuously towards the blue side down to 400 nm. The gating structure does not undergo changes with increasing energy which are as dramatic as with the prechirp variation in Fig. 3.8. This reflects in the independently measured spectra of Fig. 3.10 which exhibit less changes in the NIR region than in Fig. 3.8h for the chirp variation. The broadening around the fundamental in Fig. 3.10 from 750–875 nm basically grows from the seeding structure of the window nonlinearity (gray filling in a). At 0.8 mJ, the onset of the spectral VIS shoulder is developing. The NIR spectral shape from 750–875 nm undergoes minor changes from 0.8 up to 1.5 mJ. The lower signal for 1.5 mJ compared to 1.1 mJ indicates spatial beam break up, leading to an overall signal decrease.

One should note the difference in the generation of VIS light when reducing the peak energy to one third by positive chirping Fig. 3.8b and reducing the amplifier output in Fig. 3.10a (gray filling for 0.5 mJ). Energy reduction by positive prechirping still generates a WL continuum down to 500 nm, whereas direct energy reduction completely terminates the broadening.

Energy dependence in Kr The energy dependence was repeated with the remaining noble gases Kr and Xe. A consecutive study of many different parameter combinations can be found in [170]. To summarize, all noble gases (except of He) behave similar to the initial parameters except of the pressure regime. Heavier atoms with a higher polarizability and thus higher n_2 require lower pressure for a comparable broadening. It turned out, that Kr and Xe exhibit the best efficiency for transferring energy from the fundamental towards the VIS range (450–750 nm). Unfortunately, the high nonlinearity corrupted the spatial beam quality to an extend that it could not be used for subsequent applications like pulse shaping. Since broadening for positive prechirps is always stronger, 30 kPa Kr with a prechirp of +500 fs^2 is presented exemplarily in Fig. 3.11. At 0.5 mJ pulse energy in Fig. 3.11a, a continuum is generated reaching from 700–900 nm whose spectrum is also shown as gray filling in Fig. 3.12a. This energy is sufficient to cause broadening different to the one arising from the cell windows only. However, already 0.6 mJ in Fig. 3.11b cause pulse splitting, even before maximal broadening is achieved. With increasing pulse energy in c) and d), one sees a redistribution of energy towards the back side where the blue frequencies are generated ($cf.$ Sec. 3.5.2). The corresponding spectra in Fig. 3.12b show the impressively uniform spectrum

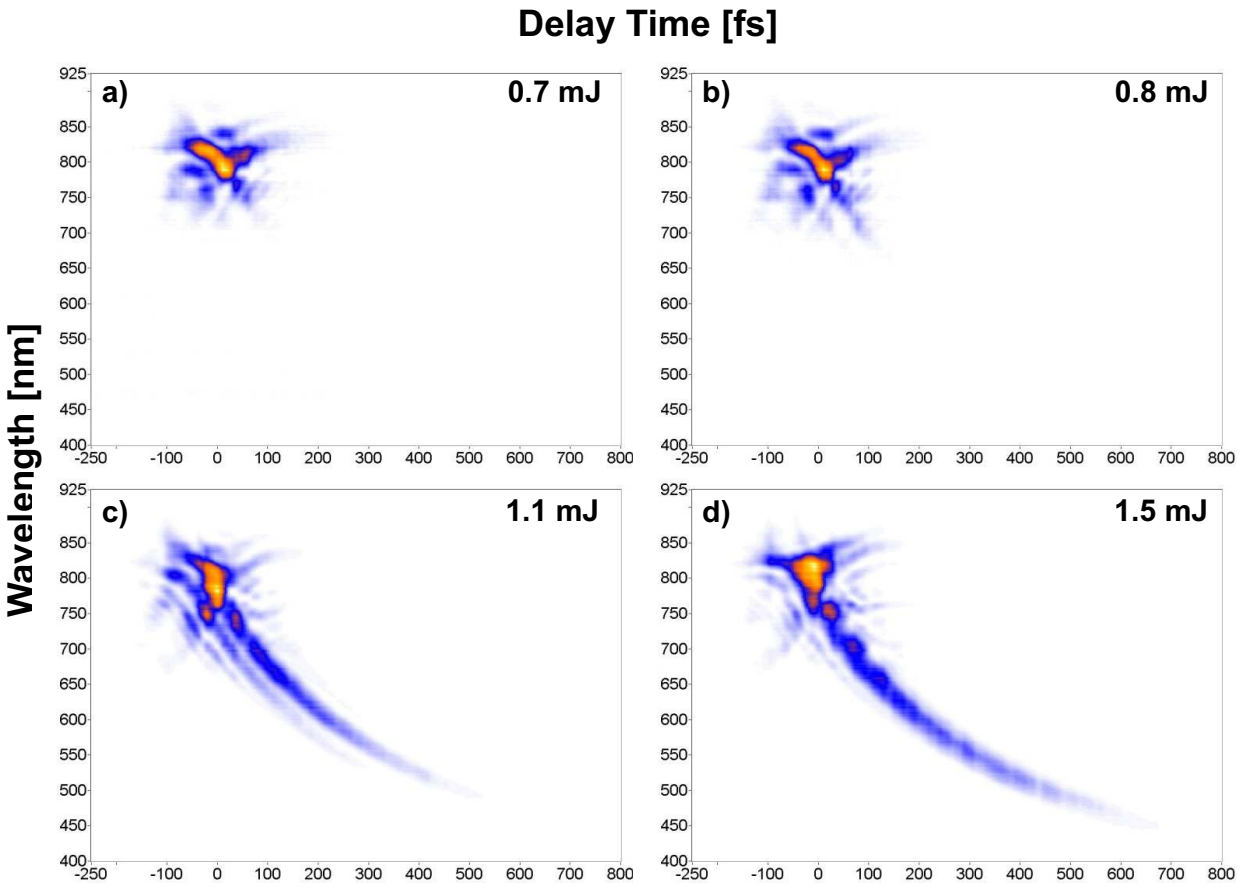

Figure 3.9: Filamentation in Ar: energy dependence. TG-FROG traces of filamentation in Ar@70 kPa with a slight negative prechirp of -380 fs^2. The energies of 0.7/0.8/1.1/1.5 mJ in Figures a)/b)/c)/d) cause less drastic changes than the tuning of the prechirp in Fig. 3.8 although the change of the maximum pulse energy is on the same order of magnitude in both cases.

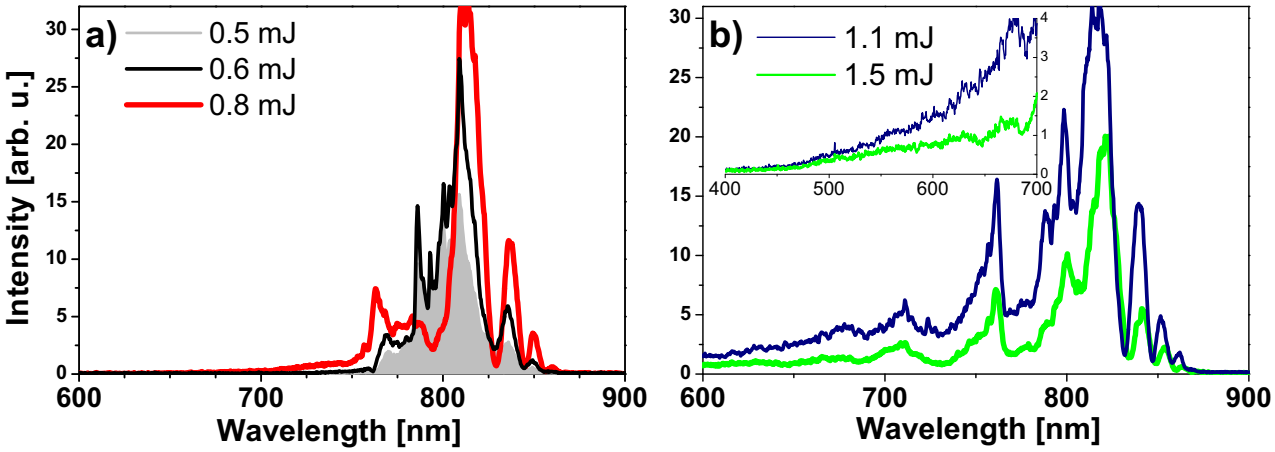

Figure 3.10: Power spectra for the energy dependence in Ar@70 kPa with additional energy ranges compared to Fig. 3.9.

for the high energy filaments covering 450–950 nm. Unfortunately, this multiple temporal splitting goes along with spatial impurities and multi filamentation beyond 0.9 mJ. Nevertheless, despite the

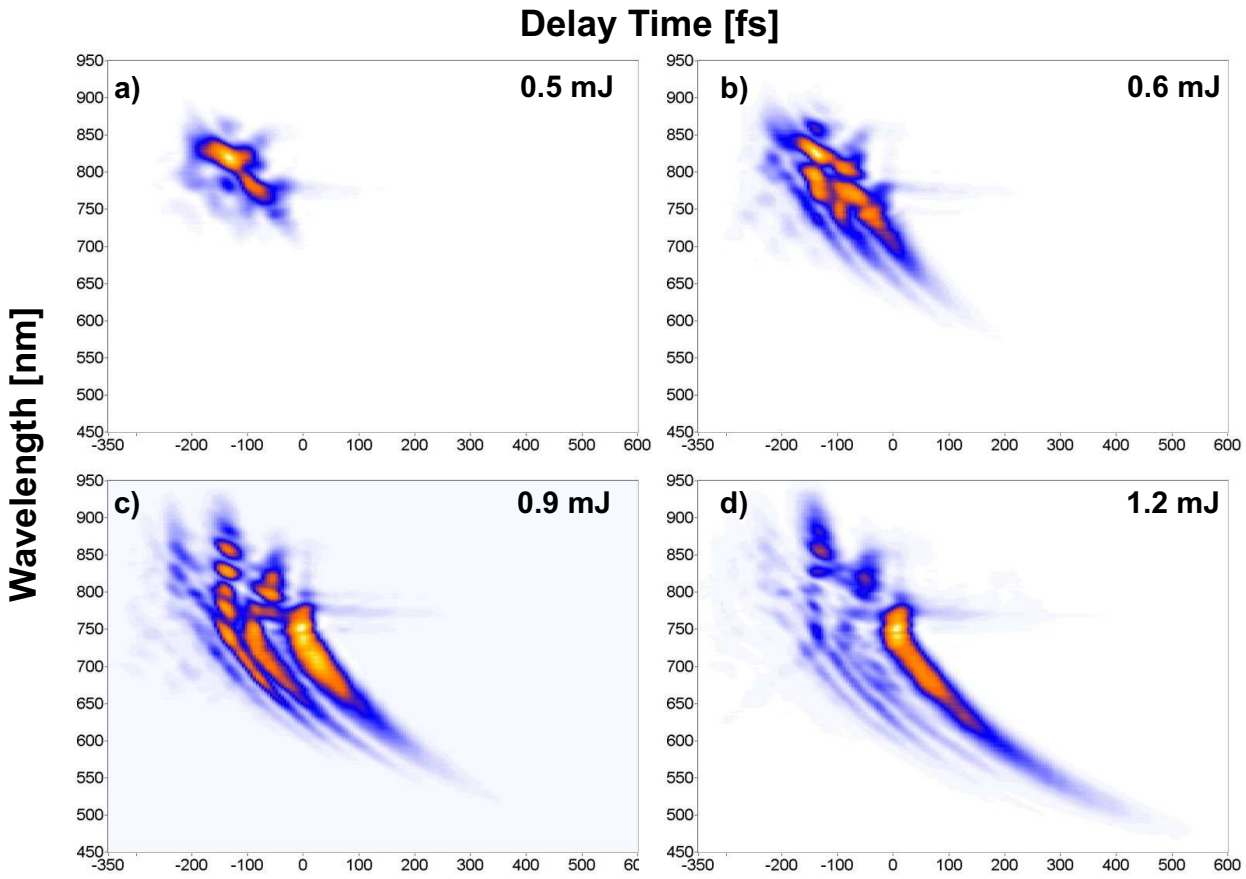

Figure 3.11: Filamentation in Kr: energy dependence. TG-FROG traces of filamentation in Kr@30 kPa with a slight positive prechirp of 500 fs^2. The energies are 0.5/0.6/0.9/1.2 mJ in Figures a)/b)/c)/d).

worse spatial beam quality and an expected complicated spectral phase, this spectrum provides the bandwidth for an isolated single cycle optical pulses with a TL of about 3.3 fs.

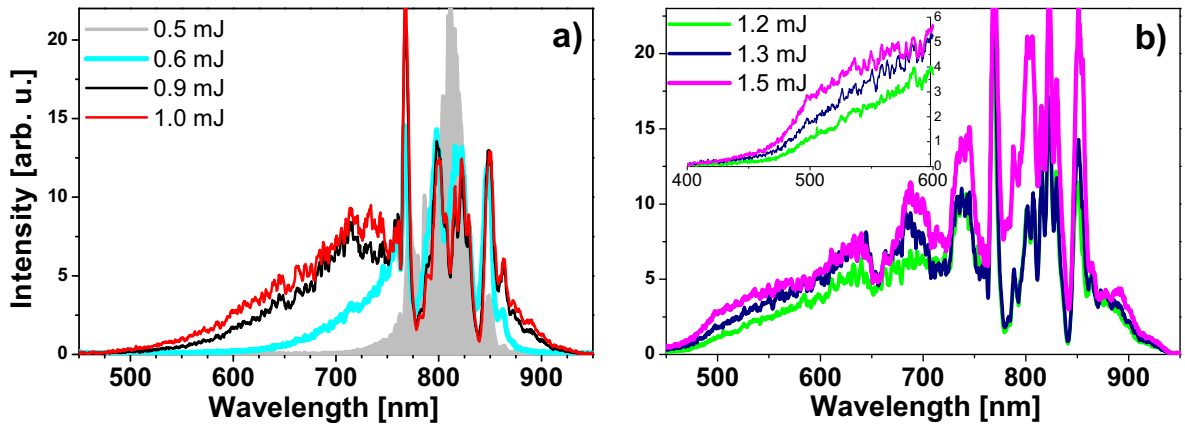

Figure 3.12: Power spectra for the energy dependence in Kr@30 kPa with additional energies compared to Fig. 3.11.

Comparison of gases Table 3.1 gives a survey of different material properties for the investigated gases and water for comparison. As already mentioned, the basic characteristics of the investigated

Medium	n_2 [$10\times^{-23}$m^2/W]	Ip [eV]	K	σ_{MPI} [cm^{2K}/s W^K]
He	0.06^a	24.59	16	2.6×10^{-215}
Ne	0.12^a	21.56	14	1.5×10^{-185}
Ar	1.4	15.76	11	5.1×10^{-140}
Kr	3.3^a	14.00	10	4.3×10^{-125}
Xe	8.1	12.13	8	2.4×10^{-96}
O_2	5.1	12.06	8	2.8×10^{-96}
N_2	2.3	15.58	11	6.3×10^{-140}
Air	2.9	14.8	10	
water	2700^b			$1.1 \times 10^{-28\,b}$

Table 3.1: Material parameters related to WL filamentation. The values for n_2 are valid for about 100 fs pulses at a center wavelength of 800 nm according to [43]. σ_{MPI} are taken from Ref. [37] for 120 fs pulses at 800 nm. n_2 values with index ^{a} are measured with 5 ps pulses at 1.055 μm according to Ref. [174]. The values for water are found in Ref. [36]

noble gases are congruent, as long as for instance the pressure is reduced for those gases with higher n_2. This statement is verified by generating distinctive TG-FROG traces, by choosing combinations of very different settings for the input parameter. Therefore, the reproducibility of characteristic pulses is shown in Fig. 3.13, where each column contains a very distinctive pulse shape. Similar input parameter for the measurements in the corresponding row (except of the pressure) lead to virtually identical TG-FROG traces for the investigated gases. The left column shows a three peaked structure with a single pulse above 800 nm and a double structure between 800 and 700 nm, each attended by a VIS tail. This series also finds an equivalent example for filamentation in air (Fig. 3.13g). The reproducibility constrain in the right column contains a splitting signature at NIR wavelengths, escorted by a double VIS tail. For all noble gases, a certain combination of pressure and intensity brought apart almost identical results. As expected, a lower IP and higher n_2, respectively, requires lower pressure at equal energy for the corresponding noble gases. This graphical summary states that no fundamental behavior difference was observed for the used noble gases.

Further on, no principle difference exists when switching from atomic gases to a mixture of molecular gases like air. An exception is the absent picture for air at bottom right in Fig. 3.13. It is missing because filaments in air were not generated under identical conditions. However, generally the traces for NIR pulse splitting in air differ from those of the noble gases. Two typical traces for splitting in air are given in Fig. 3.4 and in Fig. 3.20. One minor difference occurring at lower nonlinearities is the previously mentioned initial red shift, as became visible in Fig. 3.5a.

Since filamentation requires the action of a $\chi^{(3)}$ susceptibility in combination with plasma generation via multi photon ionization (the most likely process according to [36, 37]), it is interesting to compare gases with the same IP but different n_2. This comparison is carried out for the combination of Xe / O_2 and Ar / N_2. Figure 3.14 shows Xe spectra obtained at 20 kPa (gray filled curve) as well as O_2 at 100 kPa (black line) and 30 kPa (pink line), all at an energy of 1.0 mJ. The energy was reduced by closing the iris prior to the filament and the prechirp was tuned in the positive regime in both cases in order to achieve the broadest spectra. Filamentation in Xe (gray filling) is maximal at low pressure of 23 kPa, whereas 30 kPa O_2 show no significant broadening at all (bright, pink line in Fig. 3.14). Xe generates a much more intense spectrum in the VIS range,

certainly on cost of spatial beam quality. A comparable amount of broadening in O_2 could be obtained only for a high pressure of 100 kPa (black line). The spectral shape at the cut-off region is similar, although O_2 truncates about 60 nm earlier, as seen in the inset of Fig. 3.14.

Comparing the second gas pair of Ar and air in Fig. 3.15 confirms the former observation. Here, air is approximated as representative for N_2, since the natural ratio is 79% N_2 and 21% O_2. Pulse energy (1.5 mJ) and prechirp (0 fs^2) were equal in both gases. At 70 kPa, Ar beats air in terms of generating VIS light. Air needs to be increased up to atmospheric presure to obtain the same cut-off wavelength of 400 nm as for Ar at 70 kPa. Due to the high energy, the spatial mode was no longer clean and symmetric in both cases. From the inset of Fig. 3.15 the typical step like spectra at the UV range for air can be seen. A pronounced step appears at about 480 nm and one below 400 nm.

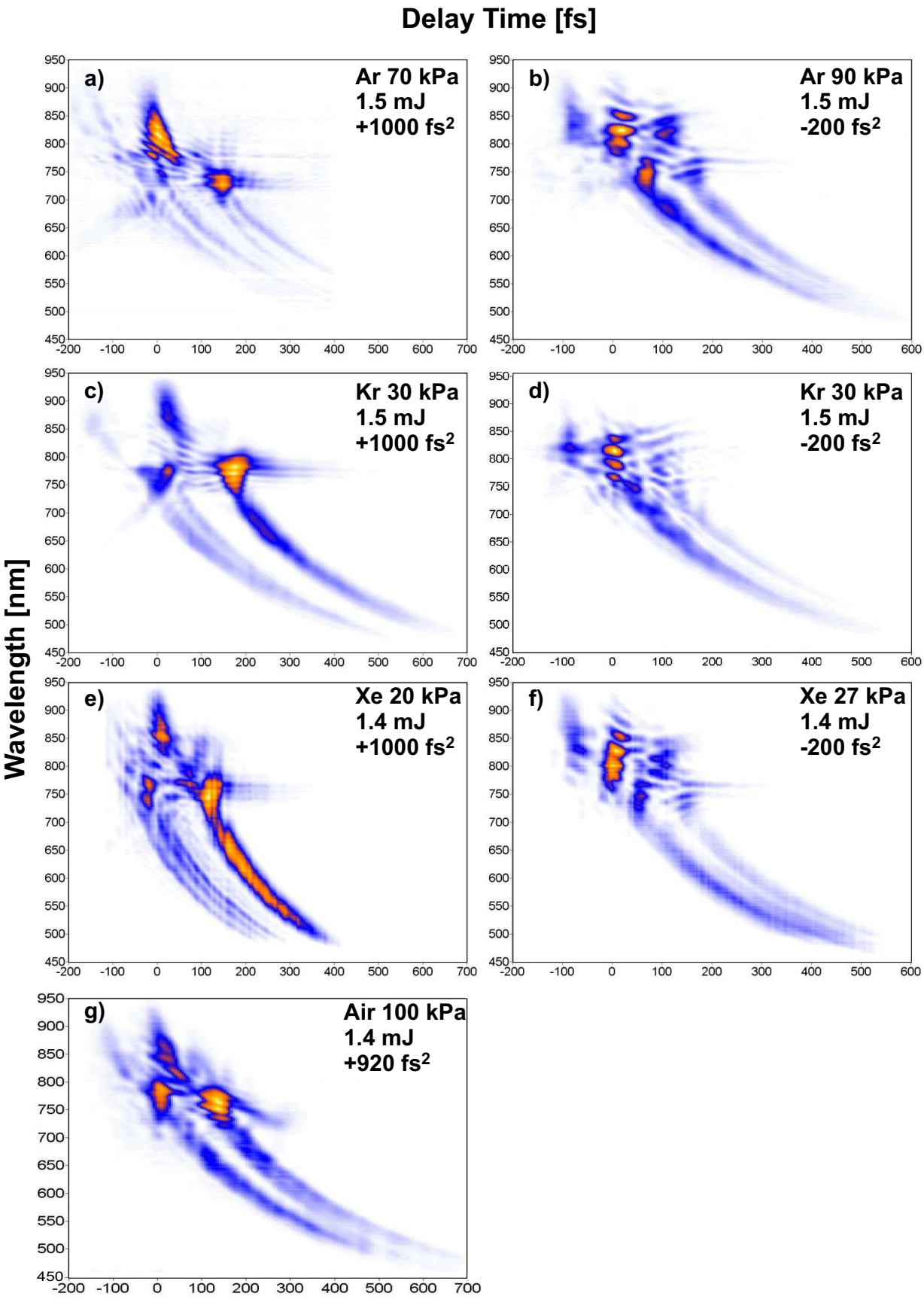

Figure 3.13: Comparison of WL filamentation by playing with the parameter toolbox. Different gases under similar conditions exhibit the same pulse characteristics. For details see text.

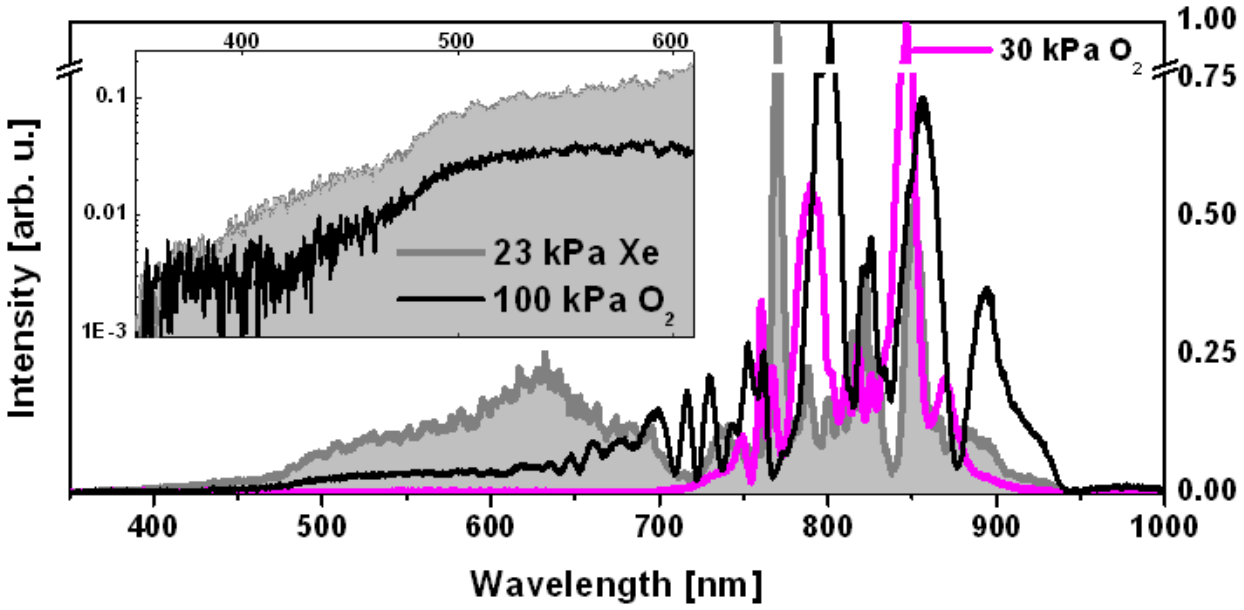

Figure 3.14: Comparison between Xe and O_2. Xe at 23 kPa is given as filled gray curve. 30 and 100 kPa O_2 spectra are plotted in pink and black, respectively.

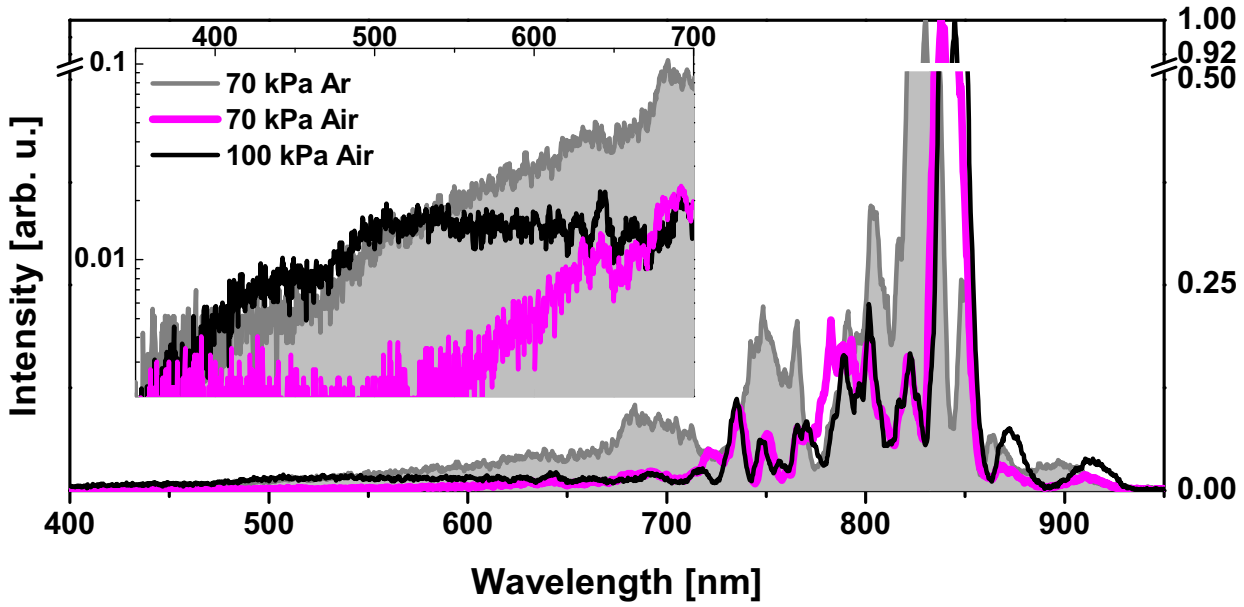

Figure 3.15: Comparison between Ar and air. Ar at 70 kPa is given as filled gray curve. 70 and 100 kPa pressure of air are plotted in pink and black, respectively.

3.1.3 Pulse splitting and self shortening

From the previous parameter dependence it is seen, that the general evolution of filamentation increases with increasing nonlinearity. The latter can be steered either by the input pulse energy, the gas pressure or the n_2 of the medium. The nonlinearity broadens the spectrum, in the beginning primarily via SPM and then due to self action during propagation. Broadening increases with rising nonlinearity, but only up to a certain point from which on the pulse first splits temporally and later on also spatially. Examples for pulse splitting occur for instance in the right row of Fig. 3.13. Another example is given in Fig. 3.16 for 30 kPa Kr at 0.9 mJ. The TG-FROG trace in Fig. 3.16a shows a temporally split NIR part with a sub pulse separation of 80 fs. The vertical green line indicates the time slice for which the spectrum is extracted in Fig. 3.16b. The modulation period has a peak distance ($\Delta\lambda$) of about 28 nm in the range from 750–900 nm. From this "amplitude modulation", the sub pulse separation (ΔT) can be calculated with

$$\Delta T = \frac{1}{\Delta\nu} = \frac{\lambda_0^2}{c\Delta\lambda} \tag{3.1}$$

to be 76 fs which is in very good agreement with the separation of 80 fs in the trace (red arrows). It is stressed, that this modulation frequency is much higher than expected from SPM. Thus it arises from self induced changes during the nonlinear propagation. Such a splitting was also observed in air, as shown in Fig. 3.20a. There the red arrows mark a temporal separation of 60 fs in combination with the spectral modulation period of 35 nm, marked in green. The calculated sub pulse separation of 61 fs perfectly matches the observation in the trace.

Besides pulse splitting [75, 81, 82], also self-steepening and self-shortening as a result of nonlinear propagation are claimed in literature [33, 35, 71, 74, 175]. These phenomena shall be investigated by analyzing the time projection of the former two examples. The corresponding time plot for WL generation in air according to Fig. 3.20a is given in Fig. 3.17a. As described above, splitting in air (Fig. 3.20a) creates sub pulses with a separation of 60 fs. These can be assigned to the three peaks (1,2 and 3) in Fig. 3.17a. The circles denote the measured data whereas the solid red curve displays a Gaussian fit. The fit duration of 28 fs is clearly shorter than the FWHM of the input pulse which is about 45 fs.

The time projection for the Kr trace in Fig. 3.16a is seen in Fig. 3.17b. In this next example, the time projection in Fig. 3.17b hardly allows identification of the split NIR part, due to contributions

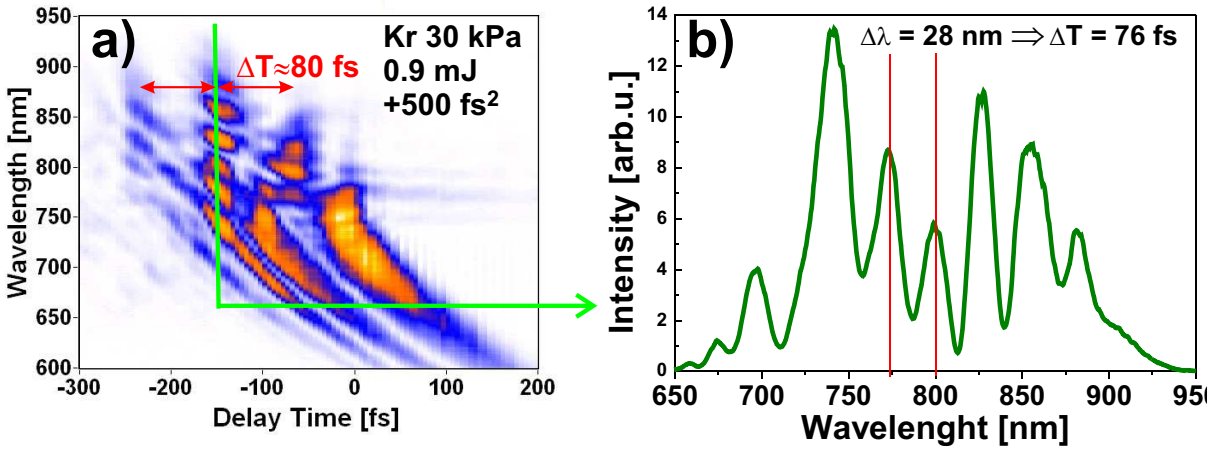

Figure 3.16: Pulse splitting in Kr. b) spectrum of the time slice according to the labeling in the TG-FROG trace in a).

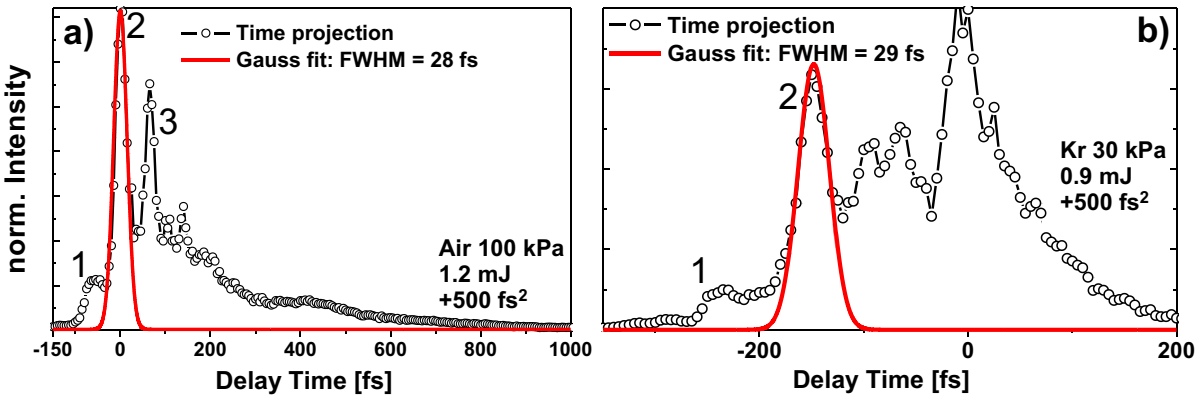

Figure 3.17: Self shortening of pulse structures in Air a) and Kr b). The plot in a) shows the time projection for the trace of Fig. 3.20a and Fig. 3.17b corresponds to the trace of Fig. 3.16a. The duration of the input pulse was 45 fs in both cases.

from multiple VIS tails. The maximum at time zero in Fig. 3.17b is mainly caused by the VIS part. Peak 1 and 2 can be assigned to the NIR splitting with 80 fs separation. A Gaussian fit for peak 2 gives a duration of 29 fs, again for an input pulse of about 45 fs. Although embedded in a huge underground, these measurements prove that self induced effects do not only lead to temporal broadening, as discussed in Fig. 3.3, but also force parts of the pulse to shorten in time.

Self-shortening was not only observed in situations where the main pulse splits in several sub-structures, but also in Fig. 3.18a where the trace shows a single NIR structure, followed by a VIS tail. In order to get rid of the positive chirped tail, only an extraction of the full trace indicated by the dashed square, was projected onto time axis. The result is plotted in Fig. 3.18b. The filled gray curve gives the TG-FROG measurement of the initial pulse, the circles are the values for the extracted projection and the solid line is a Gaussian fit. The duration after filamentation shrinks to roughly 33 fs. It is pointed out, that the self-shortening observed in the current work does not compete with other experimental measurements [84–86] in terms of real pulse compression. However, the measurements of Figs. 3.17 and 3.18 clearly show self induced changes, come to light not only as spectral broadening but also as shortened sub structures.

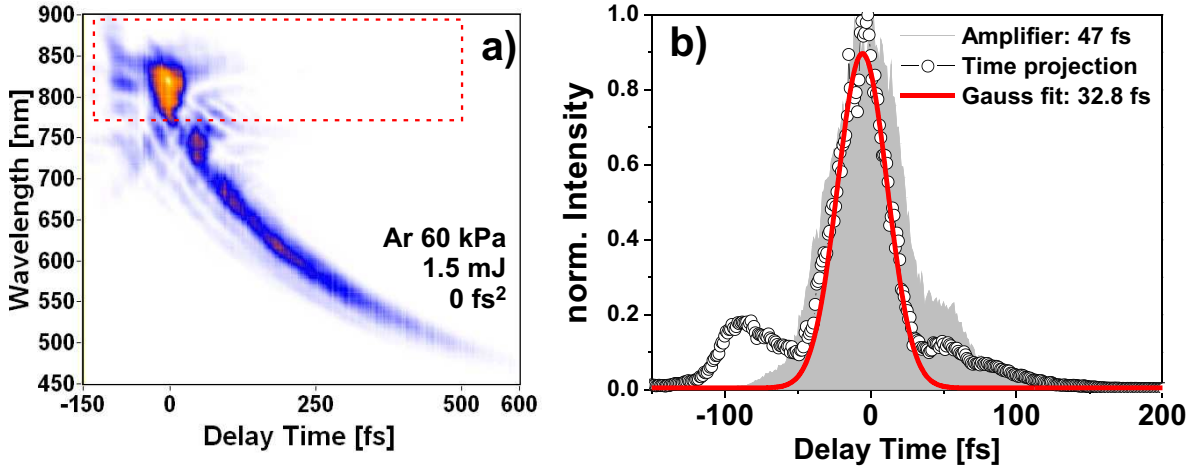

Figure 3.18: Self shortening in Ar. Only the marked part of the trace in a) was projected onto time axis in b). The input pulse (gray filling) is longer than the Gaussian fit (red) of the data (circles).

Another reason for investigating TG-FROG trace extractions in the described manner was to search for self-steepening of pulse fronts, in particular the trailing one, like simulated in Fig. 1.8. Sudden self-steepening (or even optical shock waves) at the trailing edge is supposed to be one origin for the generation of VIS wavelengths [71, 75]. The expected temporal asymmetry should occur on a sub 10 fs timescale at a center wavelength of 800 nm with a corresponding period of 2.7 fs. In all ways of performing filamentation during this thesis, no definite asymmetric pulse shape could be identified. Asymmetry in this sense does not mean pulse forms like in Fig. 3.4 where the flanks of front and tail are stretched to approximately 100 fs, but rather on a time scale of a few optical cycles. Since all parameter dependences where carried out with the beam splitter TG-FROG, which is limited to duration measurements of about 10 fs, it might have been a question of temporal resolution to measure pulse asymmetries.

3.2 Controlling filamentation

Controlling the filamentation in this sense denotes understanding how input parameters influence the outcome properties of the filament. Desired outcome properties in this regard are a clean beam profile without spatial chirp, homogeneous spectral broadening ($cf.$ Sec. 3.2.1), suitability for pulse compression evident as a flat spectral phase ($cf.$ Sec. 3.2.2) and a good repeatability from day to day. Insight in the filamentation process was achieved by monitoring its development as a function of different input parameters, carried out in the previous section. In addition to the experimental approach numerical simulations (Sec. 3.5.2) were performed in order to support a qualitative interpretation. Nonetheless, gaining comprehensive insight in those complex propagation mechanisms definitely lies outside the scope of the present work.

Of course it is not possible to fulfill all desired outcome properties at a time. A clean symmetric spatial beam profile was decided to be the main precondition to be fulfilled because subsequent shaping and frogging crucially depends on the beam profile. The benchmark for spatial beam characteristics is shown in Fig. 3.19. Filamentation was performed while reducing the input energy from 1.4 mJ to 1.0 mJ by adjusting the iris prior to the focusing mirror. Besides the "white"

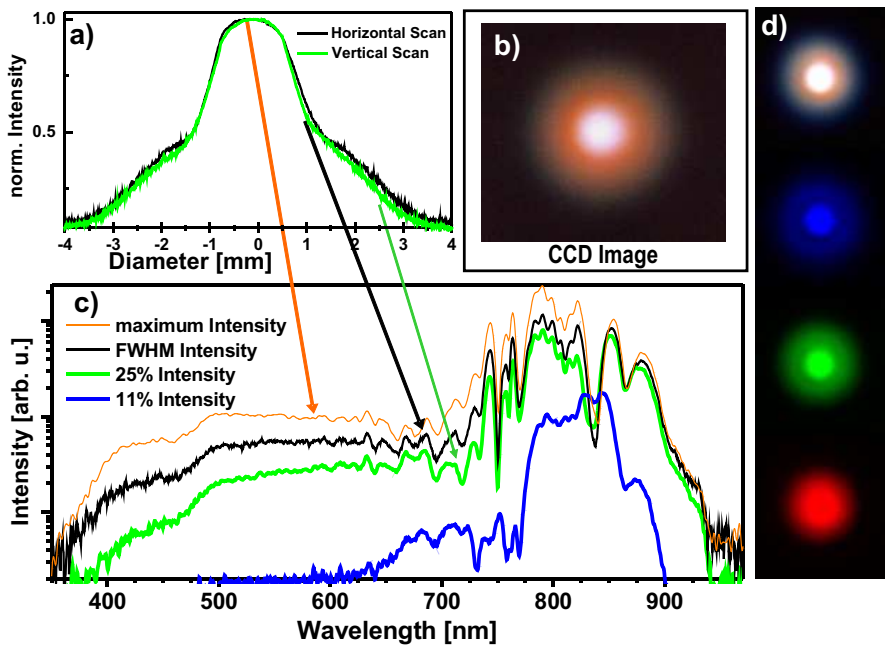

Figure 3.19: Spatial beam characteristics. a) Horizontal (light green) and vertical (black) line plots of the corresponding CCD image in b). Spectra taken at different transverse intensities in c): maximum (light orange), 50% (black), 25% (light green), 11% (blue). Below the 20% intensity region the spectrum becomes significantly narrower and the changed NIR structure is shifted towards the red side. d) shows color extraction images of the WL.

apparent color, the clean, radial symmetric intensity profile is a striking property of plasma filamentation in gaseous media. Figure 3.19b illustrates this quality as a CCD camera image as well as the horizontal and vertical cuts through the center of the beam profile, plotted in Fig. 3.19a. In order to characterize the spatial homogeneity, the beam was scanned transversely across a small diaphragm in Fig. 3.19c. Within a radius of 80% of peak intensity, all general spectral signatures remain virtually constant except for the high frequency cut-off. Particulary noteworthy in Fig. 3.19c is the conformity of the amplitude modulations in the spectral signature form approximately 500 to 950 nm within 25% of peak intensity of the transversal mode. An estimate of the conversion efficiency towards visible wavelengths region ranging from 450–720 nm was carried out by numerically integrating the corresponding area in plot of Fig. 3.19c. At given conditions, typically 15%–20% of overall intensity are transferred to the visible range. In contrast to the center of the mode, the peripheral region at 10% of maximum intensity clearly exhibits a narrower bandwidth with different spectral signatures and a slight red-shift. Fig. 3.19d shows color extraction images indicating the spatial symmetry for different colors of the WL.

A time-frequency characterization of the WL is presented in Fig. 3.20. The TG-FROG trace in Fig. 3.20a is exceptional in two ways. First it directly demonstrates the coherence of the octave exceeding WL which is the basis to be measurable in a optical gating device. Second, this trace for the first time demonstrates optical gating for more than one octave reaching from 375–950 nm in a single scan. It shows a split NIR structure with its subsequent VIS tail. The marked details of the splitting have already been discussed in Sec. 3.1.3. The gate pulse has a temporal extend of about 200 fs and the chirped VIS part lasts up to 1 ps. Again, the VIS tail seems to be attached to the trailing flank of the NIR pulse. Generating this trace was achieved by closing the iris to transmit 1.3 mJ and tuning the prechirp to about 500 fs^2. These settings denote limiting values for air at atmospheric pressure before intensity fluctuations and spatial distortions of the beam profile occur. The plot in Fig. 3.20b shows the retrieved spectral phase and intensity as well as the independently measured spectra. The retrieval of the current and all the following traces was carried out with an inversion algorithm utilizing the PCGP method for calculating new guesses for the iterative reconstruction of the real pulse, as described in Sec. 1.3.2. The strong modulations around the laser fundamental arise when the nonlinear propagation extends beyond initial SPM to complex phase distortions, manifesting themselves in the apparent temporal splitting with time structures shorter than the input pulse. The highly irregular contour of the spectral phase in the inset of Fig. 3.20b further displays phase distortions beyond SPM. A very different picture is seen in the visible part of the obtained TG-FROG trace and the spectral phase. In the corresponding retrieval the unmodulated part of the continuum primarily obeys a smooth quadratic behavior. Here, truncation of the spectral phase function at 560 nm is caused by numerical unwrapping when dealing with very steep slopes as well as by the termination of the retrieved spectral amplitude. However, a total hight stroking over 300 radian was obtained by the retrieval. This phase function corresponds to a GVD of approximately 900 fs^2 assuming a purely linear chirp.

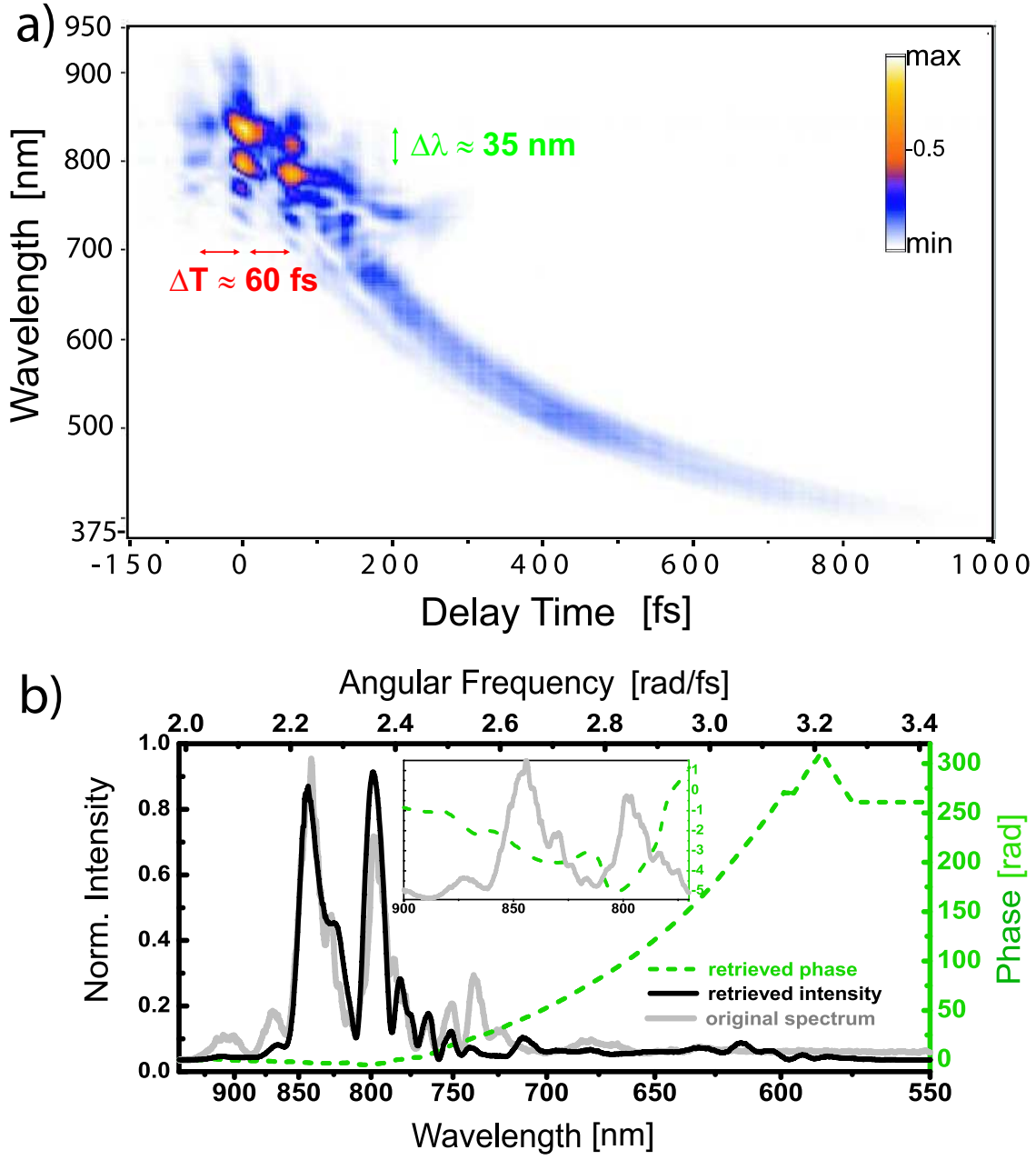

Figure 3.20: Octave exceeding gating of the WL. The gated spectrum in a) reaches from 375–950 nm and exhibits a split NIR pulse followed by a smooth, linearly chirped VIS tail. Retrieval of the spectral phase and intensity in b) connotes a strongly perturbed phase (olive dashed line) around the fundamental frequencies and a quadratic function in the VIS with a chirp value of 900 fs^2.

3.2.1 White light quenching

One experience from the parameter investigations in the previous section is, that broadening saturates from a certain intensity (or nonlinearity) level on, after which the beam breaks up spatially with increasing power. In He however, no clue for such effects was found, as shown in Fig. 3.21. The gray line illustrates broadening in the evacuated cell due to FS windows. 100 kPa He (black line) or 200 kPa He (bright green line), respectively, make almost no difference to the vacuum case. The question arises, how an admixture of He for instance to air would influence filamentation. The graphs of Fig. 3.22a–d show spectra for mixtures at different ratios of He and air, whereby the sum of both gases was constantly 100 kPa. The intensity signal is not normalized to allow comparison of absolute values. Spectra for the mixture (bright pink) and the spectrum for pure air at its corresponding pressure (black) are always plotted together in each graph. Spectra for pure He are omitted, because they equal the vacuum broadening. The procedure for mixing the gases was, first inserting the desired partial pressure He and then opening the valve to fill up the tube with air until the total pressure of 100 kPa was reached. The following observations were made for different mixtures:

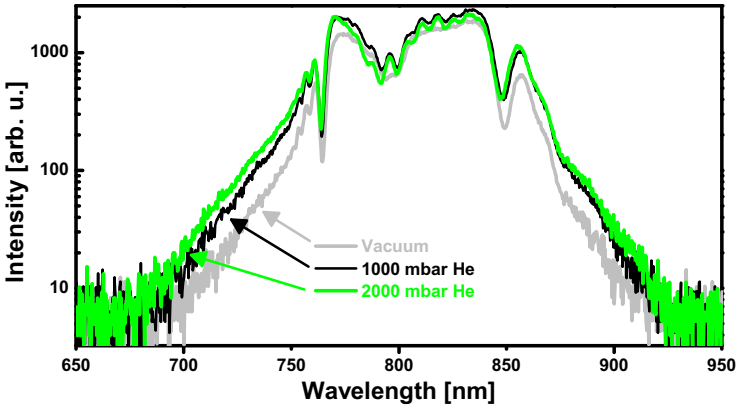

Figure 3.21: Spectral broadening in He. The broadening in the evacuated cell arises from the nonlinearity of the FS windows. He at high pressure of 200 kPa adds no significant contribution to the spectrum.

- A 1/9 ratio of He/air is identical to solely air in Fig. 3.22a. In both cases, the NIR spectrum is strongly modulated, whereas the VIS part remains smooth whereby the spectra are virtually identical. The spectra for 90 kPa air is almost identical to 100 kPa air (data not shown).
- A 2/8 ratio of He/air in Fig. 3.22b leads to spectral changes only around the laser fundamental (marked by a vertical line), but not in the VIS part. The suppression of the whole signal for filamentation in air is likely due to a different collimation of the outgoing light than to absorption. Three peaks of equal hight are generated in the mixture which agrees quite well with pure SPM in the range from 770–925 nm ($cf.$ the same plot on a linear scale in Fig. 3.40). Such a definite SPM modulation was never observed in other cases in this work. The weak peak above 950 disappears with this small amount of He.
- Further addition of He (3/8 ratio in c) keeps the clear SPM signature at 800 nm at a reduced strength. Now, broadening in the VIS part is inhibited and both spectra are obviously different. The spectrum of the mixture is homogeneous from 770–925 nm except of one dip at 850 nm. In the VIS part, broadening terminates at 650 nm but a small peak arises at 625 nm which is unusual for the VIS light when comparing to the parameter dependence measurements of the previous section.
- In Fig. 3.22d, the VIS part and light above 925 nm is completely quenched at a ratio of 4/6. Remarkably, the broadening at the fundamental is equal to the case of vacuum, although 600 kPa air remained in the cell. That means, the addition of He seems cause a collapse of the filament at given conditions which is further discussed in Sec. 3.5.1.

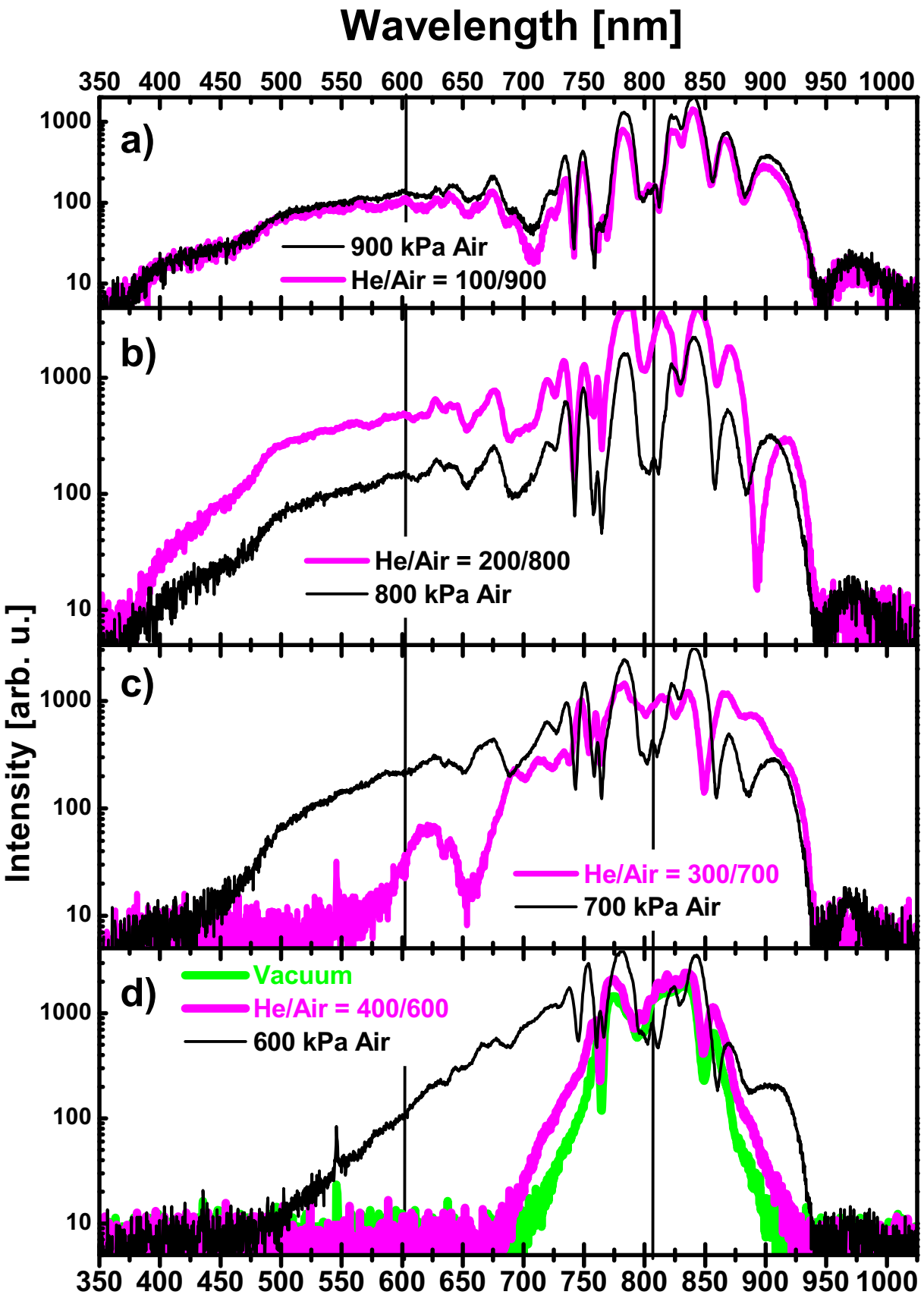

Figure 3.22: White light quenching with He. Successive ratio change between He and air enables the steering of NIR and VIS wavelengths. The sum of both gases was constantly 100 kPa and the broadening for pure air is given as a reference in each plot. For details see text.

3.2.2 Compression down to few optical cycles

The task of temporally compressing ultrashort pulses is at least as demanding as the generation of coherent bandwidth itself. In order to achieve this aim several methods were established during past 20 years. In this thesis three types of manual compressors, $e.g.$ no active shaping device, have been compared experimentally: a prism compressor, chirped mirrors and a telescope-grating compressor. They all base on the principle of providing different path lengths for different colors of the pulse when passing the compressor to compensate for dispersion. The different path lengths translate in a spectral phase whose sign is opposite to the incoming pulse. It is pointed out, that this conventional pulse compression is only possible at appropriate conditions for filamentation. Meaning that a complicated or split structure like in Fig. 3.20 was not compressible at all. In general, tuning the filamentation parameters to optimum was more important than tuning the compression device.

Prism compressor Prism compressors are the simplest optical setups which allow flexible dispersion control. A common arrangement consists of two Brewster prisms and one retro reflector. The total negative dispersion depends on different optical paths for different wavelengths in the second prism which can be steered by changing distance between the prisms or by changing the beam distance from the prism apex. Detailed description on the operation principle is given in Refs. [27, 176–178]. Due to ease of use, a FS prism compressor was first employed in this thesis for white light compression and brought quick success. Compression down to 11–15 fs was straightforward achieved in combination with the amplitude splitting TG-FROG of Sec. 2.2.1. Examples at different center wavelengths are given in Ref. [170]. Unfortunately, compression of the full bandwidth failed because of clipping at the second prism whose edge length of 35 mm was too small. The clipping also lead to an unattractive spatial profile. The compressed pulses often showed side pulses whose origin from either the filamentation process or from spectral cutting was difficult to assign. Beating the 10 fs barrier was not possible with this setup. Further, on account of the strongly chirped white light out of the prism shaper (Fig. 2.12), this compression method seemed unpromising, since it adds significant dispersion to the WL due to the prism material. Thus effort was concentrated on other shaper strategies, described in Sec. 2.3.1, and other compression methods.

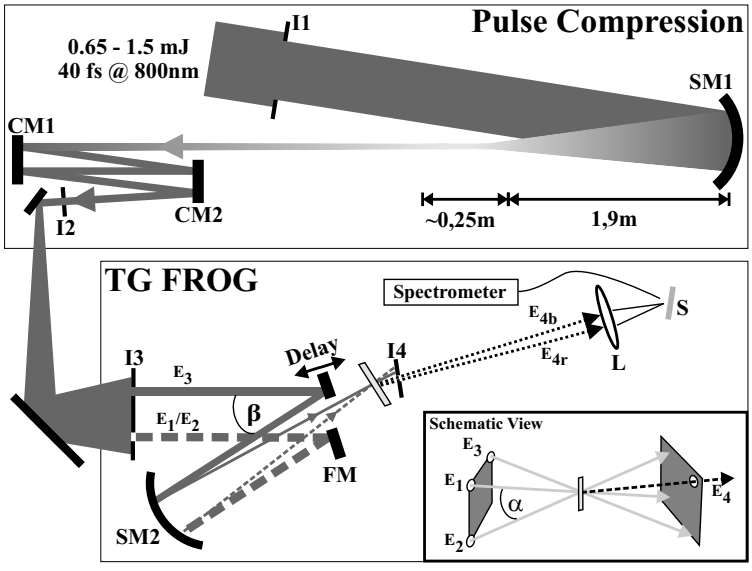

Figure 3.23: Complete few cycle setup. Filamentation stage and FROG have been explained in Secs. 2.1.2 and 2.2.2, respectively. Negative dispersion is accomplished by chirped mirrors (CM) from 700-900 nm with a reflectivity of 99%. Once the right number of bounces on CMs is found, the setup is robust and easy to use for daily operation in the few cycle regime. The whole arrangement consists of 10 optical components only.

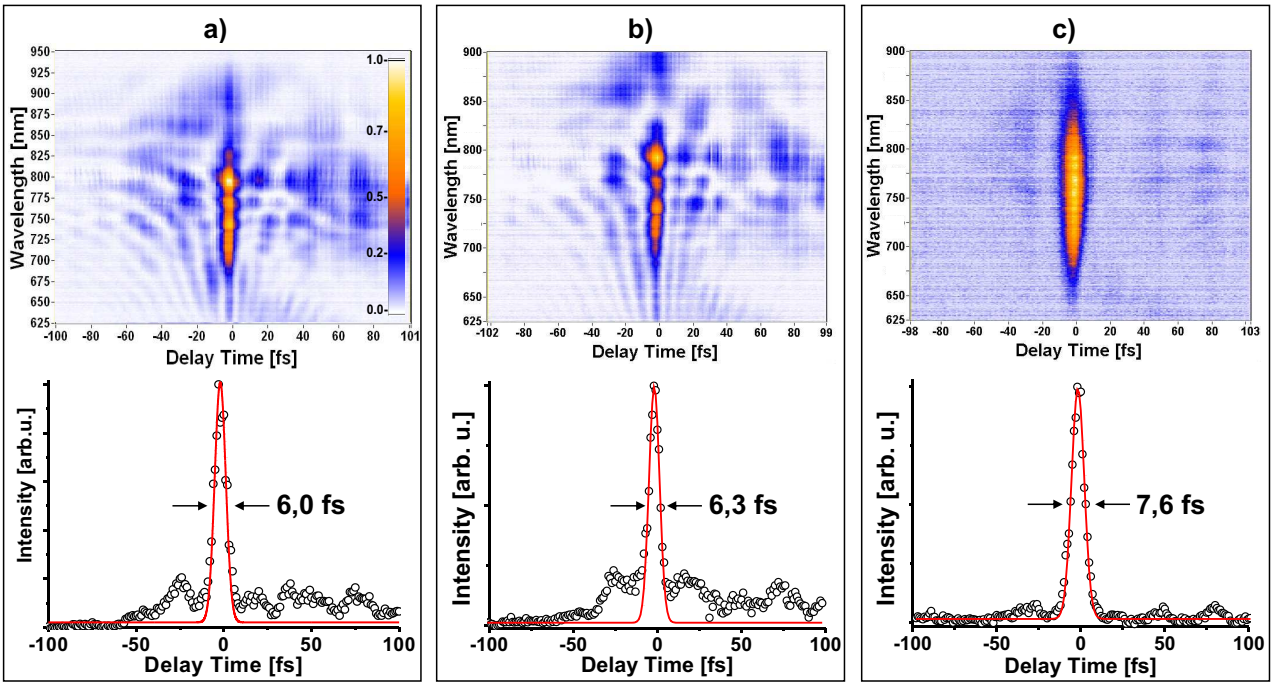

Figure 3.24: Few cycle pulses achieved by chirped mirror compression. TG-FROG traces in the upper row and projection onto time axis underneath. Shortest durations of 6.3±0.3 fs in a) and b) were achieved with high power of 1.0 mJ by closing iris I1 and positive prechirp. Typically, those shortest pulses have a back ground with the first satellite at -25 fs. In contrast, opening I1 and reducing the energy to 650 μJ generates a clean pulse with 7.6 fs.

Chirped mirrors More sophisticated pulse compression can be achieved with a pair of chirped mirrors, labeled CM in Fig. 3.23. It gives a complete overview of required components for generation and measurement of really short pulses on the order of 6 fs. Compression is carried out with four bounces on the CM, which are characterized in Sec. 2.4. This strategy employed for the generation as well as full characterization of few cycle pulses and octave exceeding SC is distinguished in both cases by the ease of realization and the high economy in optical components (10 standard optics only). The filamentation stage is content of Sec. 2.1.2 and the TG-FROG setup is explained in Sec. 2.2.2. For the pulse measurement, iris I2 (located roughly 3 m subsequent to the filament) is closed to about half a millimeter in order to reduce intensity for the FROG. A distance of approximately 4 m is spanned between iris I2 and I3, in order to provide a beam diameter of 6 mm on I3. 4WM typically was carried out with an energy of about 1–2 μJ for all three beams (E_1, E_2, E_3) together. The energy impinging on I3 typically ranged from 10–20 μJ. Attaining the few cycle pulses in Fig. 3.24 was highly sensitive to small changes of I1. Furthermore, fine adjustment of the grating separation in the amplifier compressor was necessary for finding the shortest pulses. In general, best compressibility was achieved with a slightly positive prechirp of 400 fs^2 of the input pulse for filamentation, which agrees with other observations by Hauri *et al.* [159]. Noteworthy, the total amount of positive dispersion accounts to 550 fs^2 when including 7 m optical path in air but the implemented negative GVD of four bounces on chirped mirrors is only -240 fs^2. It is again assumed that this is an indication of self-induced temporal changes taking place during nonlinear propagation in the filament. In this manner, pulse durations as short as 6.0 fs were generated with a single filament, shown in Fig. 3.24a. Therefore, I1 was closed down to 7 mm, reducing the input energy from 1.5 mJ to 1.0 mJ. Fig. 3.24b denotes a representative TG-FROG

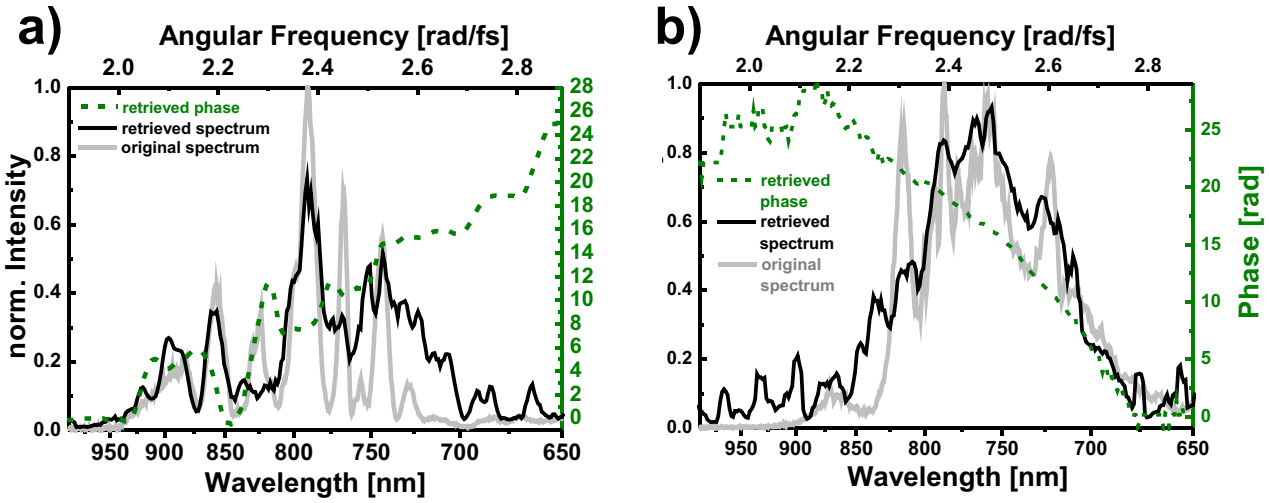

Figure 3.25: Phase retrieval of few cycles pulses containing retrieved intensity (black) and phase (green dashed) as well as the original spectrum (gray). Fig. a corresponds to the 6.3 fs pulse of Fig. 3.24b. Phase jumps of π (or multiples of π) in the region from 800–650 nm are equivalent to a flat phase function. The complicated phase above 825 nm correlates to the "cloudy" trace in the same wavelength region. The retrieval according to Fig. 3.24c in the left graph displays an almost flat phase. The linear slope has no effect on the pulse duration.

trace which displays a long term average measurement. Repeatability was verified by taking 41 traces during a period of 10 days. The mean FWHM value for 41 measurements during this time period is 6.3 ± 0.3 fs. Important to note for this case are the satellite structures clearly evident in the FROG trace in the upper part of this figure and the projection on the time axis in the lower row. The appearance of these structures can partially be understood from the reconstructed spectral phase for this pulse as shown in Fig. 3.25a. The spectral phase function is inhomogeneous with two distinct spectral regions. While the wavelength region from 650–820 nm shows phase jumps of π or 2π, respectively, the spectral domain above 820 nm exhibits an irregular spectral phase profile. From this, the satellite structures around the primary pulse can be attributed to the compromise made when trying to balance these two distinct spectral regions with CM compression having a nearly quadratic phase correction over the full bandwidth. In this context, it is worth mentioning that a reduced amplifier output of 1 mJ and opening of iris I1 increases the pulse width and the strength of satellite structures, $i.\ e.$ not only the absolute amount of input energy influences the filament output strongly, but also the spatial beam characteristics and diffraction effects.

However, a fully opened iris I1 and reduced input energy of 650 μJ for filamentation enables the generation of clean temporal profiles with reduced spectral modulations as depicted in Fig. 3.24c. This is noteworthy, since generation of sub 10 fs with a single filament has previously been presented with distinctly higher energies [84] than 1 mJ. The absence of satellites in the FROG trace of Fig. 3.24c is accompanied by a smoother NIR spectrum and a cut-off wavelength around 550 nm. Furthermore, the corresponding spectral phase is almost linear as shown by the phase retrieval in Fig. 3.25b for this low energy case.

Disadvantageously aspects of utilizing CM are their fixed, small amount of negative dispersion per bounce, typically 50 fs[21]. This was, however, not a big concern in this work since only four bounces were employed. Second, the wavelength range (700–950 nm) is restricted due to the

[1]Meanwhile fabrication of high dispersive mirrors with GVD on the order of 10^2 fs^2 is currently under research [179].

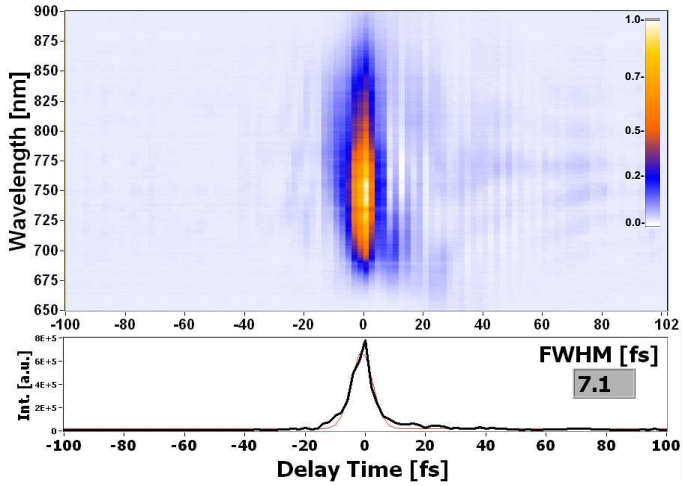

Figure 3.26: Pulse compression via telescope-grating setup. TG-FROG trace is plotted on top and the time projection underneath. The thin line is a Gaussian fit to the measured data (thick black). The TGC setup enables tunable compression in the operating range of the shaper from 450–1000 nm for moderate chirp rates.

coating. An extension of the operating range is usually accompanied by stronger GVD oscillations, as seen in Fig. 2.21. Although ultra broadband operation has been demonstrated recently [180], it is not jet commercial available. Unique to compression with CM is the high reflectivity of the optics, reducing the losses in grating based methods tremendously.

Telescope-grating compressor Like a prism compressor, a grating setup allows for flexible tuning of the GVD, however, without introducing additional material dispersion. The working principle of a telescope-grating compressor (TGC), which is nothing more than earlier described 4-f setup (Fig. 2.13), differs from a conventional grating compressor. Unlike the latter, a TGC enables positive and negative chirp rates as explained in Sec. 2.3.1. On the other hand, a TGC implies a spatial chirp if used away from the zero dispersion alignment. A spatial chirp simultaneously causes higher order temporal chirp. This can be circumvented by a back reflection of the outgoing beam in order to pass the setup twice. Fortunately, the required compression to compensate the chirp out of the filament in the NIR region, from the FS windows and the travel through air was that small, that the minimal spatial chirp could be completely removed by proper alignment. In this way, the TGC allowed the flexible chirp control over the entire transmission range of the shaper setup from 400–1000 nm, as seen in Fig. 3.37b. A 7.1 fs pulse is shown in Fig. 3.26, which proofs the absence of higher order chirp. Filamentation was carried out in a He/air mixture with a ratio of 3/7 at absolute pressure of about 70 kPa, which was tuned for maximal broadening in the VIS range. However, compression of the strongly chirped VIS tail of the WL was not possible. The required higher chirp rate could be achieved by passing the setup twice.

One remark on the radial dependency of the few cycle pulses is given here. As one would expect from the beam profile measurement of Fig. 3.19, a lengthening of the pulse duration was measured to be only about 15-20% for the outer beam part. Likewise, a correlation of the full mode by using a reflection from a glass surface instead of closing iris I2, lead to a 15% longer pulse duration.

3.3 Utilizing filamentation - arbitrary pulse shapes

Since the presented spectral broadening with simultaneously good beam profile and the "manual" pulse compression to few cycles already denotes a utilization, the outline of this subsection goes further and presents computer controllable, arbitrary pulse shapes and the compression of complicated pulses. The measurements in the current section were carried out by directly coupling the filament output in the 4-f setup (Fig. 2.13). The combination of WL shaper and octave exceeding

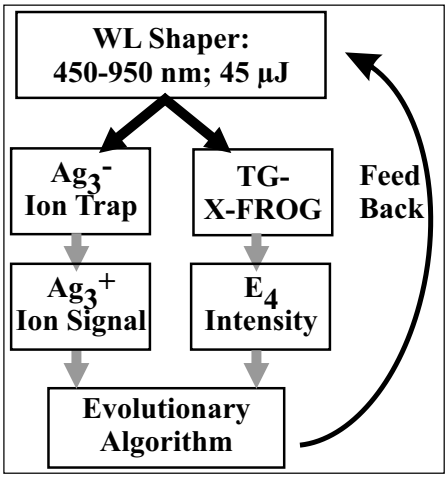

Figure 3.27: Applications of the closed loop scheme in Fig. 1.18. It basically merges the techniques of WL generation, pulse shaping, 4WM and cluster spectroscopy in an rf-ion trap. Either the 4WM process (right path) or the stored Ag_3^- clusters (left path) represent the quantum target whereas the strength of E_4 or the charge reversed Ag_3^+ display the observable for the evolutionary algorithm (EA). The right path is followed in this section, the left one in Sec. 4.2.

gating brought apart a novel utilization, namely the single beam TG-X-FROG, being explained in the next section. Following up the last section comprising few cycle pulses, the question of further compression with the help of a LCM arises. The first attempt, generating WL and writing quadratic phase functions with negative sign on the mask, shortened the pulse duration but hardly gained results comparable to conventional compression with chirped mirrors. The reason is that for pulse compression schemes with linear chirp compensation, the tuning has to be carried out already at the generation stage by setting the right filamentation conditions, rather than by tuning the subsequent compressor.

The right path of Fig. 3.27 shows a new way of pulse compression which does not require the knowledge on the properties of the incoming laser field. Furthermore, less attention has to be paid on finding appropriate filamentation conditions. Figure 3.27 shows both ways of applying the closed loop scheme, as introduced in Fig. 1.18. The aim in this section is to follow the second path on the right hand side of Fig. 3.27. This integrates the field of SC generation into a coherent control scenario. Therefore, the step motor which is responsible for time delaying beam E_3 of the TG-FROG was set to maximum signal of the uncompressed pulse which usually is the best choice to "center" the correcting phase function. 4WM in the TG-FROG generated the feedback signal (E_4 in Fig. 2.8) for the EA. The spectrally integrated area from 600–900 nm served as optimization parameter which was enhanced by phase only shaping.

The TG-FROG trace is in Fig. 3.28a shows an unshaped WL pulse. Notably, this trace is recorded after passing the shaper setup which was aligned for zero dispersion inclusive of the LCM. The optimization started from random phase noise and increased about a factor of 500 during 160 iterations of the algorithm, shown in Fig. 3.28b. Here, the curves for the best, mean and worst population are plotted for every iteration. The signal for the best population is about twice the signal for an unshaped pulse like in Fig. 3.28a. The clean trace for the resulting few cycle pulse with a FWHM duration of 7.4 fs is presented in Fig. 3.28c and its projection onto the time axis in Fig. 3.28d. The measured data given by the circles in Fig. 3.28d is fitted with a Gaussian function (red curve).

The few cycle pulse in Fig. 3.29 was achieved by firs using the EA as described above and second, by manual amplitude suppression of spikes under observation with the spectrometer. Therefore, the polarizer (P) was inserted subsequent to the pulse shaper in Fig. 2.13. The final 5.8 fs pulse in Fig. 3.29 is no big step further compared to the 6 fs achieved with the CM, but now compression was carried out by tuning the compression setup after the filamentation stage. A second advantage is the absence of underground and satellites, as in Fig. 3.24a and b. The noisy back-

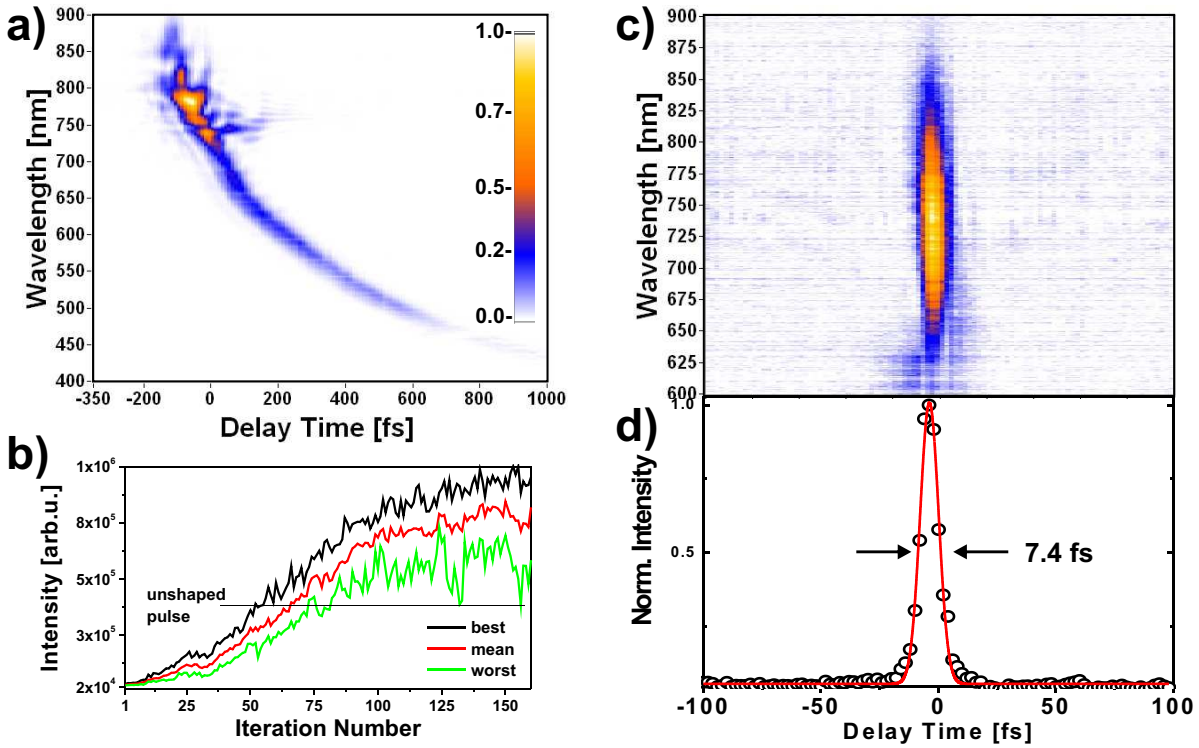

Figure 3.28: Adaptive pulse compression of the WL-SC. FROG trace of the unshaped pulse directly after filamentation in air in a), optimization curves for phase only shaping in b). This approach does not require knowledge of the phase function of the WL and leads to a clean few cycle pulse whose trace is shown in c). The projection on time axis for the 7.4 fs pulse is plotted in d).

ground in Fig. 3.29 indicates a lower signal due to strong amplitude filtering.

Once the pulse is transform limited, like in Fig. 3.28c, the resulting pixel settings of the LCM mask can be defined as a reference. To this reference a desired phase function can be written and the way towards parametric shaping of the SC is opened. This reference mask, found by the EA, displays the starting point for generating defined pulse structures like the pulse train in Fig. 3.30.

It was achieved by adding a sinusoidal phase function to the mask after optimizing the 4WM

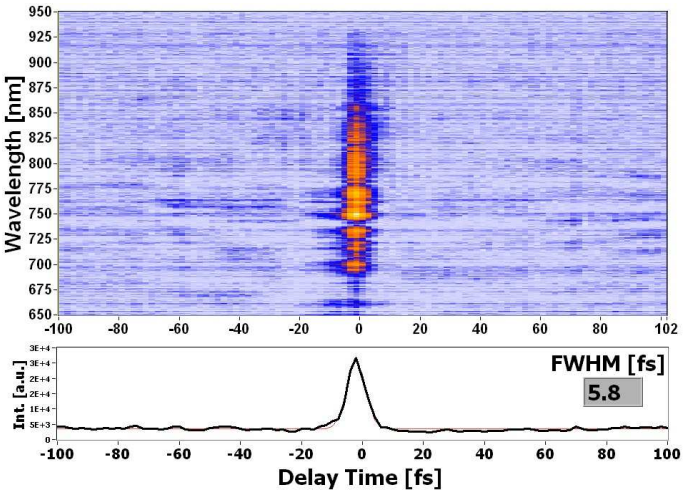

Figure 3.29: Adaptive pulse compression with the feed back loop for phase optimization and additional, manual amplitude reduction of the sharp spectral spikes results in a clean 5.8 fs pulse. The TG-FROG trace is shown and the corresponding time projection underneath. The thin line is a Gaussian fit to the measured data (thick black line).

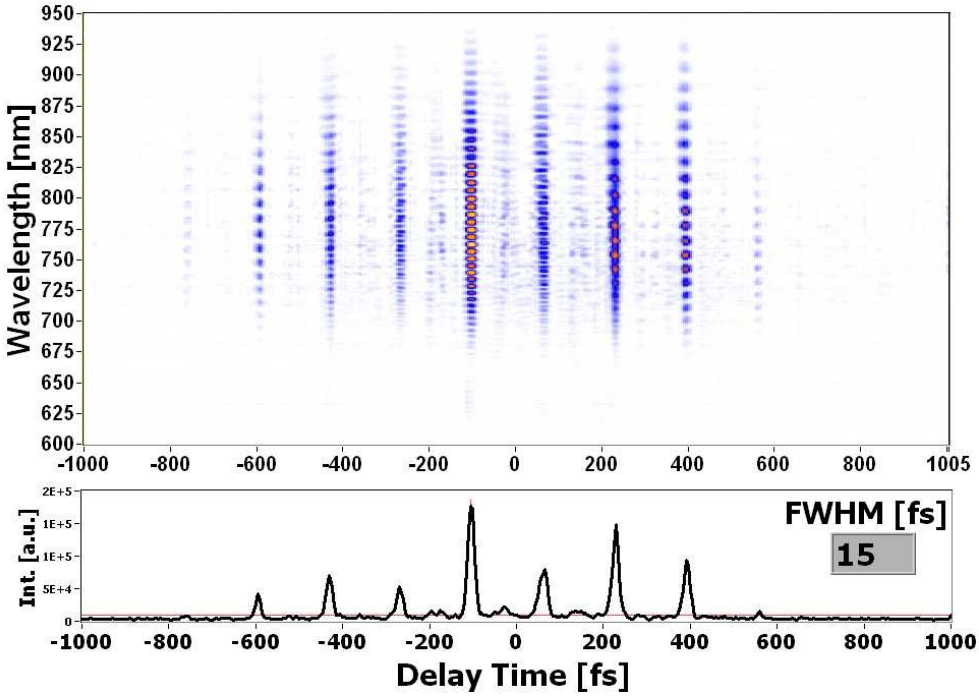

Figure 3.30: White light pulse train from 675–950 nm. A pulse separation of 180 fs was achieved by adding a sinusoidal phase to the transform limited mask, which was found by the EA.

signal in the region from 450–900 nm with the closed loop setup. A compression of wavelengths below 675 nm was not satisfying. Thus, an extremely weak signal can be recognized underneath the main peak at -100 fs. The pulse separation of 180 fs is a relevant value for the pulse train excitation of Ag_2 in Sec.4.1, since it is equal to the vibrational period of the neutral cluster.

In general, a TG-FROG trace where all frequencies form a vertical line at time zero was not detected. One of the closest examples can be seen in Fig. 3.31a. Beginning with a short NIR pulse, free optimization of the spectral window between 500-725 nm was carried out at time zero. The FWHM of the total pulse is about 12 fs and a clean few cycle pulse was not reached. A residual chirp for the NIR and a temporally modulated part from 550–700 nm are the reason for this "long" pulse. The unclean VIS part might be caused by steep phase function on the SLM, leading to the so called space time coupling.

Figure 3.31b shows a slightly smoother VIS pulse. Here the scan beam E_3 was delayed for

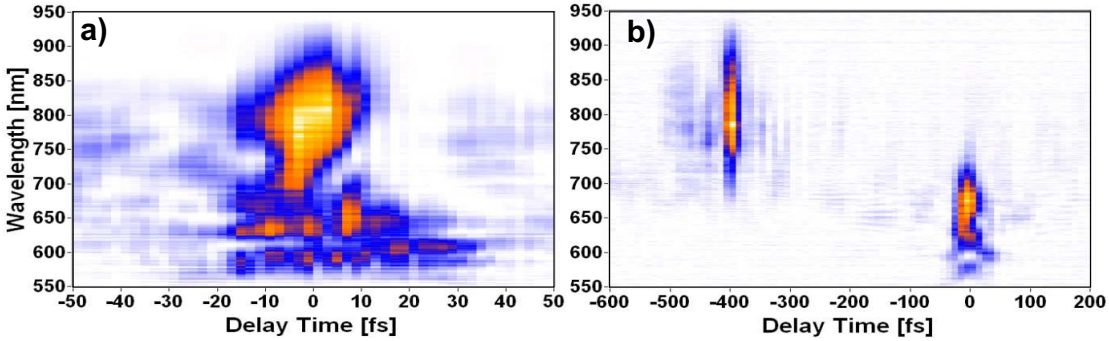

Figure 3.31: Adaptive compression of the VIS part. Precursory was a optimization of the NIR part(700–950 nm). For the trace in a) subsequent optimization from 500-750 nm was carried out at time zero and with a delayed (400 fs with respect to the gate pulse) scan beam E_4 in b).

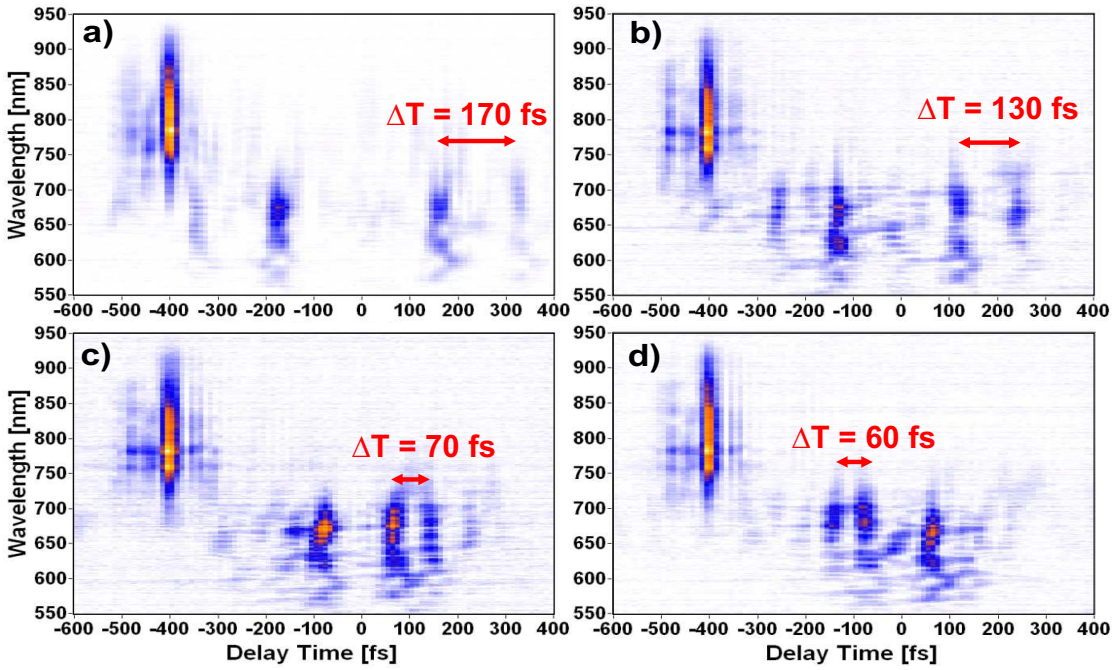

Figure 3.32: White light pulse train with variable period in the VIS region. Starting point for adding a sinusoidal phase was the trace of Fig. 3.31b. Sub pulse separations of 170/130/70/60 fs were set in a/b/c/d. The measurement conforms to a single beam TG-X-FROG, see Sec. 3.4.2

400 fs with respect to the NIR pulse and the free optimization between 500-750 nm was carried out at this step motor position. Thus the zero time is centered on the VIS pulse and the NIR pulse appears shifted to -400 fs. Since the VIS tail of the WL is inherently located at later times, compression at this delay point is accomplished with flatter phase functions, thus the VIS pulse is cleaner than in Fig. 3.31a. Pulse sequences with a variable period in the VIS range complete the demonstration of arbitrary pulse shapes in this section. With Fig. 3.31a as starting point, a sinusoidal phase was written on the SLM to generate the VIS pulse train of Fig. 3.32a–d). In this sequence, the phase of the NIR pixel was not changed. The desired separations from 170/130/70/60 fs in a)/b)/c)/d) are recognizable in the trace. The mathematical description of this sinusoidal phase modulation can be included in the spectral representation $\widetilde{E}(\omega)$ of the pulse in Eq.(1.11)

$$\widetilde{E}(\omega) = e^{-\left(\frac{\omega}{\Delta\omega}\right)^2} e^{i\,a\,\cos(\pi/2-\Delta T\omega)} \tag{3.2}$$

with a being the amplitude of the phase modulation and $\cos(\phi) = \sin(\pi/2 - \phi)$. The value ΔT corresponds to the temporal separation of the sub pulses. The cos phase modulation can be described by the help of Bessel functions of the first kind and m-th order [181]

$$e^{i\,a\,\cos(\phi)} = \sum_{m=-\infty}^{\infty} J_m(a) e^{im(\pi/2-\phi)} \,. \tag{3.3}$$

Since $J_0(a)$ is zero for $a = 2.4$, a hight of stroke for the phase modulation of 2.4 radian sets the carrier to zero, and thus the center of the pulse train vanishes. With this vanishing of the center of the VIS pulse at time delay zero in Fig. 3.32, the calibration of the pulse shaper can be tested. Already an amplitude of $a = 2.2$ in a) and c) blanked the center pulse completely, whereas in b) and d) a small portion remained. For short sub pulse separations denoting a low modulation period on the mask, the quality decreases and the distinction of sub pulses is reduced below $\Delta T = 50$ fs.

3.4 Ultra broadband gating of filamentation WL

In nonlinear processes the interaction of several photons lead $e.g.$ to the generation of new frequencies or to self-diffraction of light, respectively. Thereby conservation of energy ($E = \hbar\omega$) and momentum ($\mathbf{p} = \hbar\mathbf{k}$) has to be fulfilled at the same time. In order to fulfill these requirements in parametric processes, birefringent materials are used for SHG, and non-collinear interaction is applied in parametric amplifiers (like NOPA [147, 182]). The problem of phase matching (see Eq.(1.73) and Fig. 1.15) is also relevant for self diffraction of light ($cf.$ Fig. 1.14), above all if the induced scattering is desired for more than one octave. The geometry for 4WF accorded a forward box arrangement (see $cf.$ Fig. 2.3) as described in Secs. 1.3 and 2.2. Spatial and spectral properties of the diffracted light and a comparison between both, the rhomb and TG (Sec. 2.2.1) geometry will be discussed in this section.

3.4.1 Degeneracy grade of Four Wave Mixing (4WM)

At first glance, assuming degeneracy is evident because all three intersecting beams are identical. However, three unexpected observations are associated with the gating of octave exceeding WL spectra which consists of an intense NIR structure and a long ranging VIS tail.

(I) The first noticeable aspect is apparent in traces Fig. 3.31b and Fig. 3.32. According to the convolution theorem [49], an autocorrelation of a double pulse leads to a FROG trace with three peaks. However, the TG-FROG trace in Fig. 3.31b contains only two peaks and no signal at other times or other spectral regions, although the two grating pulses E_1 and E_2 are identical with the scan pulse E_3. The data array for this measurement reaches from -800 to 400 fs and from 350–1024 nm and is not shown completely for clarity reasons. Further on, in case of equal contribution to the grating generation, the VIS pulse trains in Fig. 3.32 should reproduce the single NIR pulse at other delay times, which is not observed This hints that the 4WM process for these asymmetric WL spectra is not degenerate over the entire octave, even though the three incoming beams are identical. This observation can be explained by the fact, that effectively only the intense NIR wavelengths generate the transient grating. This means the NIR part gates itself in autocorrelation like process and the much weaker VIS part is cross correlated with the NIR pulse.

(II) Second, the efficiency of the diffracted light E_4 does not follow a quadratic dependence versus frequency, as one would expect from Eq.(1.72) for a degenerate 4WM process [34]. Accordingly, the TG-FROG intensity should exhibit a quadratic increase towards higher frequencies [161, 183]. As is obvious in the trace of Fig. 2.5b, the original spectrum and the projection of the FROG trace onto wavelength are directly proportional. This behavior is further evaluated in Fig. 3.33 for different WL pulses. The filled gray area shows the intensity of the projected TG-FROG trace signal ($|E_4|^2$). The original spectrum is overlaid as black curve, and both plots are normalized to the maximum (being at the same wavelength in all cases). Since both the amplitude -and the geometrical splitting TG-FROG were employed, the original spectrum was measured directly in the scan beam path ($|E_3|^2$) in order to neglect filtering effects of any optics. A relative diffraction efficiency as the ratio of the diffracted beam over the scan beam I_4/I_3 is shown by red circles. Plotting the efficiency runs in numerical trouble when the curves are strongly modulated and in the presence of noise. Thus the plot is restricted to smooth spectral parts in a) and b) and omitted at the highly modulated NIR frequencies. A direct proportionality of scan beam I_3 and diffracted beam I_4 can be seen in Fig. 3.33a, giving rise to a constant efficiency from 700–470 nm and a good matching of spectral peaks in the region from 900–700 nm. The variance of the circles below 470 nm indicates an increase of noise in the integrated spectrum. The fact that sharp peaks at

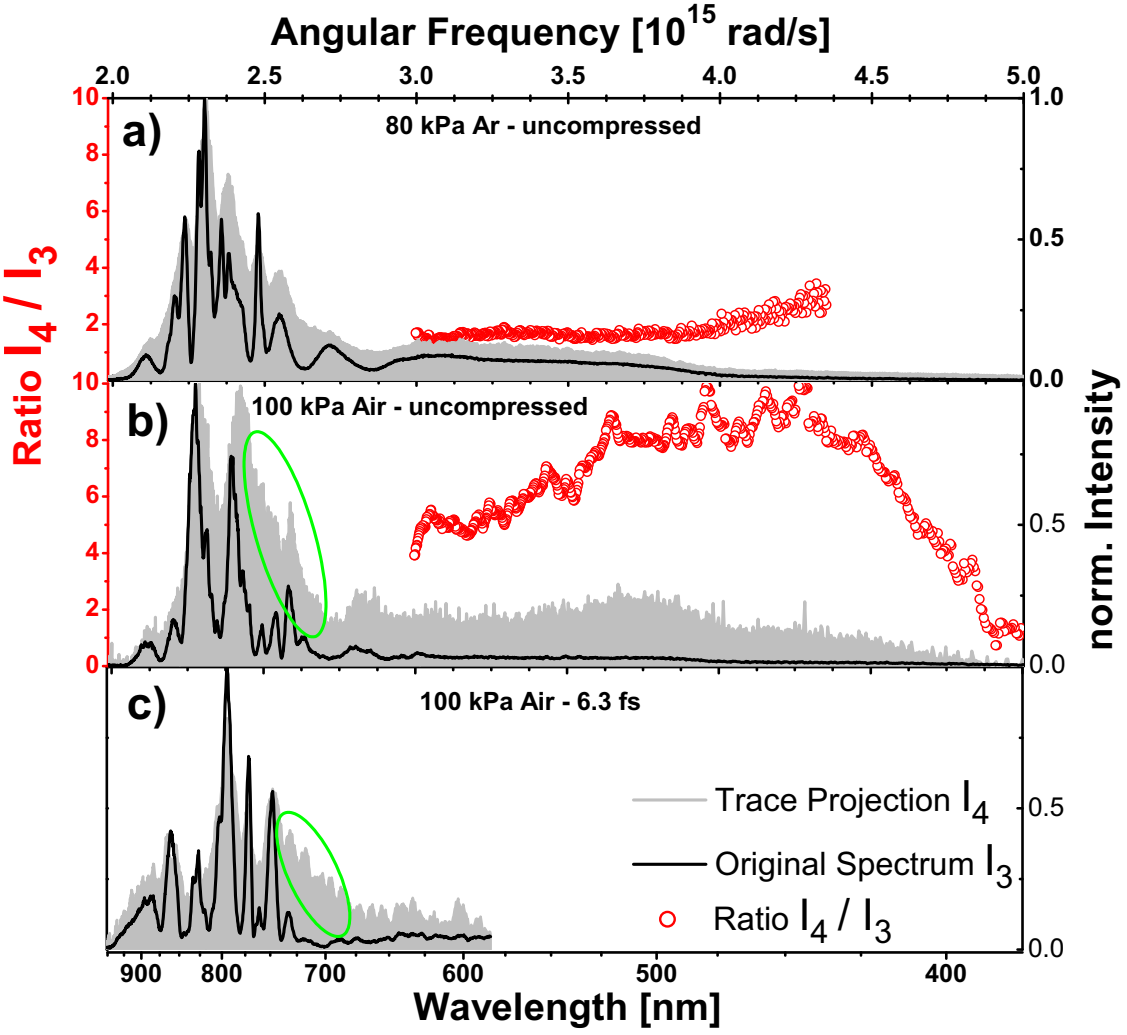

Figure 3.33: Directly measured (I_3, black curve) and integrated spectra from TG-FROG traces (I_4, gray filling) for different WL pulses in a)–c). A relative diffraction efficiency (I_4/I_3) is shown by the red circles. The spectrum axis is equidistant in angular frequency. Uncompressed WL of Fig. 2.5b attained in 80 kPa Ar in a), uncompressed WL of Fig. 3.20a at 100 kPa air in b) and the spectrum for the 6.3 fs pulse of Fig. 3.24b. A unitary diffraction efficiency was found for the various WL spectra.

the NIR are broadened, due the convolution process during nonlinear optical gating, is responsible for a ratio (I_4/I_3) greater than one. This smearing causes the gated peaks to appear broader than in the real spectrum is apparent in all cases a)–c). Thus, the VIS spectrum is weighted differently in the convoluted spectrum.

In case of the WL trace of Fig. 3.20a, the efficiency in Fig. 3.33b shows a linear increase for the VIS wavelengths down to 450 nm and drops afterward. The real spectrum extends from 370–950 nm. Again, the trend from 900–750 nm is a resembling of spectral peaks but with some deviation on the high frequency side of the peaks, marked by the green ellipse. These two examples represent the most constant and the strongest dependency, respectively, which were found in the evaluated measurements. Other cases are lying in-between. Both discussed traces of the uncompressed WL were recorded with the beam splitter TG-FROG (Fig. 2.4), while the 6.3 fs pulse of Fig. 3.24b whose spectral curves are plotted in Fig. 3.33c, was recorded with the geometrical splitting TG-FROG (Fig. 2.8). A efficiency for the VIS part is not evaluated since the operating range of the chirp mirrors extends from about 700–900 nm (high reflectivity is specified from 650–

1000 nm). The behavior at the NIR region is comparable to the uncompressed WL of Fig. 3.33a and b). The spectral peaks in the signal beam are broadened whereby the relative heights are comparable to the original spectrum. Again, the green ellipse marks a spectral region with a certain overhang of the diffracted light. Recapitulating the general spectral dependence of the diffracted beam, a quadratic increase with angular frequency ω was not observed in this work.

(III) The assumption of an intense IR structure acting as a gating mechanism for the entire, octave exceeding bandwidth is supported by the third observation, namely the spatially dispersed signal beam E_4, as already indicated in Fig. 2.8 as $\mathbf{k_{4blue}}$ and $\mathbf{k_{4IR}}$. The subscripts $4blue$ and $4IR$ denote the attribution to blue or infrared wavelengths, respectively, of the 4WM signal. In general, 4WM in a forward box configuration (see Fig. 2.3) constitutes focusing of three parallel incoming beams with the corresponding wave vectors $\mathbf{k_1}$, $\mathbf{k_2}$ and $\mathbf{k_3}$, located in three corners of a square. This situation is illustrated in Fig. 3.34. To satisfy the phase-matching condition (Eq.1.78), the 4WM signal $\mathbf{k_4}$ points to the vacant corner of the rectangle in outgoing direction. This vector addition is graphically illustrated in Fig. 3.34 for an NIR beam with center frequency ω_0. The grating vector $\mathbf{k_g} = \mathbf{k_2} - \mathbf{k_1}$ is added to the scan beam $\mathbf{k_3}$. The resulting point in space defines the direction of the signal beam $\mathbf{k_4}$. However, in the case of correlating a chirped, octave spanning WL with an asymmetric spectral profile, the signal beam exhibits angular dispersion. This shows up as a movement of the signal beam $\mathbf{k_4}$ along the x-axis in Fig. 3.34 when the frequency of the scan beam $\mathbf{k_3}$ changes at the corresponding delay time.

The measured spatial dispersion of the 4WM signal is given as a series of CCD camera images in Fig. 3.35. The upper part consists of three white spots, labeled E_1, E_2 and E_3. These are the three identical incoming beams for 4WM. A weak (infrared) spot is located to the left of the grating beams E_1 and E_2, which is the self diffraction (SD) of the two grating pulses. The signal beam E_4 appears in the forth corner of the square. It is not white because the pulse is temporally stretched like in Fig. 3.20a. The filamentation conditions for the measurement of Fig. 3.35 are similar. At time zero in Fig. 3.35 only the NIR wavelengths are present. This leads to a deeply red appearing spot on the CCD camera, carrying a center frequency ω_0. Underneath the SD spot appears another diffraction order of the 4WM signal, also at ω_0. A white, dashed line indicates the center of the half square and is plotted for orientation. The series of colorful images below was taken with a fixed CCD camera and successively time delaying the scan beam E_3. Each color slice corresponds to a delay step of 100 fs compared to its nearest neighbor, increasing from -200 to 1000 fs time delay. Although the FROG signal is maximal at time zero, a slightly better matching to corner position of E_4 might be seen towards -100 fs delay time. Clearly, the signal beam E_4 moves along the lower edge of the square. It travels towards the center for blue frequencies and outwards for IR frequencies.

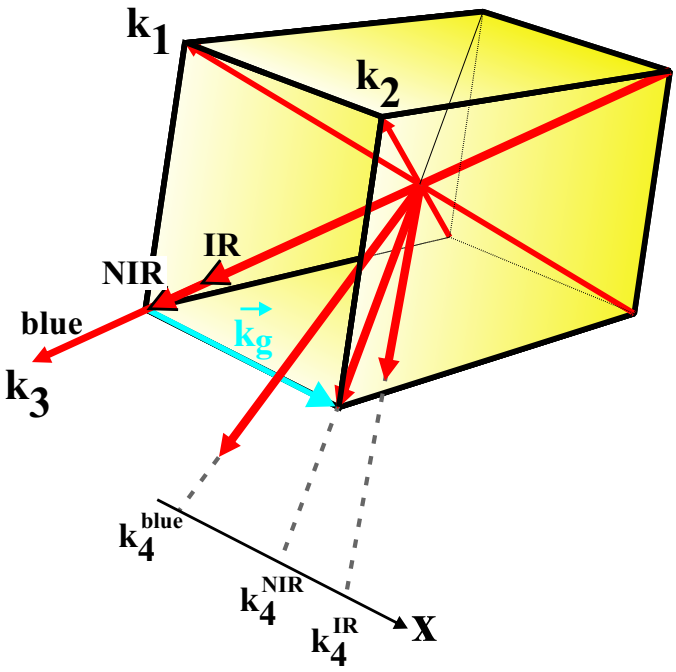

Figure 3.34: Vector addition in 4WM for a degenerate case at ω_0. The grating vector $\mathbf{k_g} = \mathbf{k_2} - \mathbf{k_1}$ is added to $\mathbf{k_3}$, leading to a point in space which is located exactly in the vacant corner of the square. The beam pointing of the signal $\mathbf{k}_4^{IR}$ and $\mathbf{k}_4^{blue}$ is drawn corresponding to the measurement of Fig. 3.35.

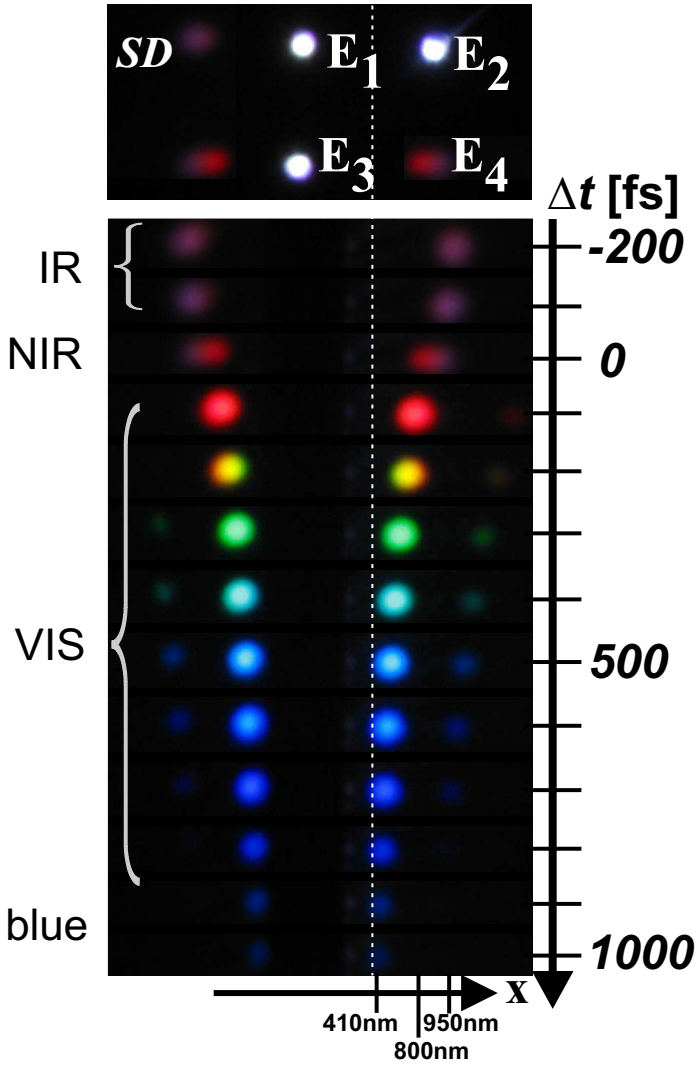

Figure 3.35: Induced diffraction of white light in TG arrangement (*cf.* Fig. 2.6). The upper part shows the three incoming beams and the 4WM signal E_4 in the residual corner of the square. E_1 and E_2 are the grating beams and E_3 is the scan beam. A self diffraction spot and another diffraction order can be seen to the left of the square. In the lower part, a series of images is sorted below each other, which shows the horizontal beam movement of the signal beam E_4 at different time delays (Δt) of the chirped WL. In case of degenerate 4WM, one would expect all wavelengths to be located exactly at the corner E_4 of the square.

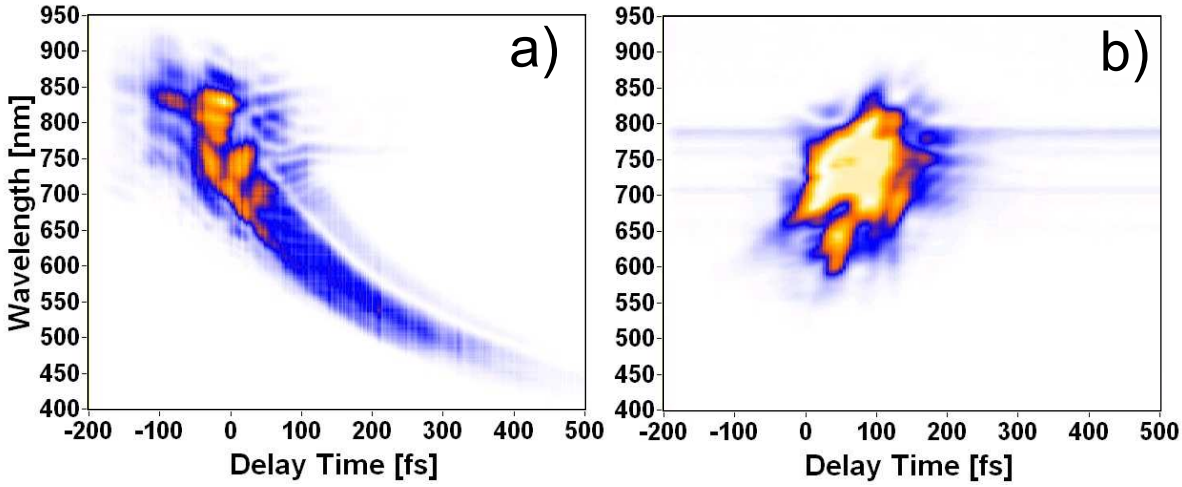

Figure 3.36: Comparison of FROG measurements in TG arrangement in a) and in rhomb geometry b). Both traces result from similar filamentation in Ar (70 kPa, 1.2 mJ). For measurements in the rhomb setup, wavelengths below 600 and above 900 nm never showed up in the FROG trace, thus it is not feasible for gating an octave of frequencies. Furthermore, both traces look substantially different.

Comparison of TG- and rhomb geometry Trace a) in Fig. 3.36 results from a TG measurement whereas the right one displays a measurement in rhomb geometry, as they were introduced in Sec. 2.2.1. The same filamentation output (70 kPa Ar, 1.2 mJ) was used in a) and b). The TG trace in a) consists of a modulated NIR part and a smooth VIS part as seen throughout all the parameter dependence measurements. Different to this, the VIS tail and the IR wavelengths above 870 nm are completely missing in the trace of Figure b). Besides the reduced wavelength range, the traces in Fig. 3.36a and b) look substantially different. The gated part from 600–850 nm in b) shows short wavelengths in the beginning of the pulse and red wavelengths at its end, corresponding to a negative chirp which is inverse compared to the order of frequencies in a).

3.4.2 Single beam TG-X-FROG

Sometimes, the consideration of principles leads to new developments. In this sense, the considerations about 4WM of WL as a non degenerate process, as is discussed in Sec. 3.5.3, is already turned into new applications.

The practical meaning of the angular compensating phase-matching of the TG geometry, in which exclusively the intense NIR part serves as gate function, is that it enables a cross-correlation frequency resolved optical gating (X-FROG) of wavelengths in the VIS range. So far, X-FROG is usually carried out with two pulses having different temporal shapes but same color [105,184]. The herein presented method cross-correlates pulses with different center wavelengths and different temporal shapes. A comparable experiment was carried out very recently in which Lee $et\,al.$ gated VIS wavelengths from a SC with NIR grating pulses directly from the laser in a TG setup [107]. They demonstrated the gating of a separate WL beam reaching from 425–675 nm with grating pulses of 5 nm bandwidth at 800 nm according to the laser fundamental. However, the claim of the present work is, that cross-correlation can be obtained within one single beam in the presence of a short NIR pulse in the WL pulse. Therefore this arrangement is referred to as single beam TG-X-FROG. In order to prove this statement, the possibility of gating one part of the spectrum with a different one within the same beam, the traces of Fig. 3.37 were measured. For these traces various parts of the spectrum were filtered out in the 4-f setup. Therefore, the spectrally dispersed beam in the shaper setup was partially blocked in the plane of the cylindric mirror CM1 in Fig. 2.13 to avoid

sharp cutting edges in the spectrum. All traces are recorded with the amplitude splitting TG-FROG of Fig. 2.4. The trace in Fig. 3.37a) shows the direct output after filamentation containing the full bandwidth from 420–930 nm. The total extension of the chirped WL pulse lasts for about 1100 fs. Filamentation in air aimed for generating a large bandwidth with a pronounced maximum at the NIR region which is seen to appear at 854 nm in gray plot of Fig. 3.38 (note the broken axis). All traces of Fig. 2.13 are normalized to their respective maximumand in all of the remaining measurements b)–i), the light passed the 4-f setup. In Fig. 2.13b, the grating separation of G2 in Fig. 2.13 was manually tuned to compensate for linear chirp of the SC which reduced the temporal spread to about 700 fs. For all the following traces the scan range is kept constant. Although the NIR wavelengths appear at the same time, the pulse is temporally split and everything else but a short pulse. It is also obvious that NIR and VIS part experience different spectral phase functions which cannot be corrected for by a conventional pulse compression scheme. Transmission of the full spectrum according to Fig. 3.37b delivers an input energy of 10 μJ. Starting from this reference trace in b), the outstanding traces in c)–i) were generated with a pulse spectrum which was partially blocked in the NIR region as will be explained in the following.

In the first series from c)–e) attenuation began at the long wavelength side and was shifted towards shorter wavelengths which leads to a decrease of the whole 4WM signal. The transmission function in c) reaches from 865–420 nm and from 830–420 nm in d) like indicated by the hatched square. Comparison between c) and d) shows, that blocking the intense peak at 850 nm causes a strong decrease of the VIS signal. In Fig. 3.37e, all wavelengths above 820 were blocked (green curve in Fig. 3.38) and the low 4WM signal is the reason for the noisy background in the trace. Cutting the spectrum further down to 780 nm ensued no measurable signal under the given conditions. The corresponding trace containing only noise is shown in the inset of Fig. 3.37e. Also any other spectral range below 780 nm gave no FROG measurement at unchanged input power.

For the next series of Figs. 3.37f–i, band pass filtering in the NIR was investigated with a constant VIS part transmitting from 650–420 nm and a variable NIR width in the interval from 750–950 nm. The transmission function for Fig. 3.37f allowed the illumination from 750–900 nm and in the VIS range. Cutting the wavelengths from 650–750 nm has no effect, neither on the remaining VIS nor the NIR part of the trace. The 4WM signal in both wavelength ranges is similar to Fig. 3.37b. In Fig. 3.37g the range from 650–800 nm was blocked and the corresponding spectrum given as black curve in Fig. 3.38 consisting mainly of a narrow peak at 845 nm ($\Delta\lambda =$ 6 nm). This spectrally narrow and thus temporally long gate pulse reflects its temporal structure in the VIS tail of Fig. 3.37g due to convolution in the X-FROG process. This convolution can be verified by comparing Fig. 3.37g and d) where the VIS tail is narrower in the first case. Noticeably, a FWHM of 6 nm in the NIR can gate a width of 250 nm in the VIS regime.

The red curve of Fig. 3.38 displays a further spectral suppression between 650–865 nm corresponding to the TG-X-FROG trace in Fig. 3.37h. In this case only a very reduced spectrum was sufficient to gate the VIS part. Spectral slicing from 865–950 nm for the gate pulse reduced the total input power to 18% compared to the trace of Fig. 3.37b. The remaining wavelengths above 865 nm can not be seen in the trace due to a limited dynamic range of the spectrometer. The integration time of the spectrometer was constant for all measurements to allow direct comparison between differnt pulse spectra. Important to mention is that the total input power for the TG-X-FROG measurement of Fig. 3.37h was more than two times lower compared to Fig. 3.37e. However, the over all 4WM signal is much higher as can be seen by the better S/N ratio in the VIS.

The result of Fig. 3.37i is particularly interesting, because the IR gate spectrum is too weak to gate itself. The arrow in Fig. 3.38 indicates the little hill at 930 nm which was, however, sufficient to gate the VIS spectrum. The integrated area at 930 nm is about four times lower than the area in the VIS. That means, it is not necessary that the gating structure is more intense than the signal to

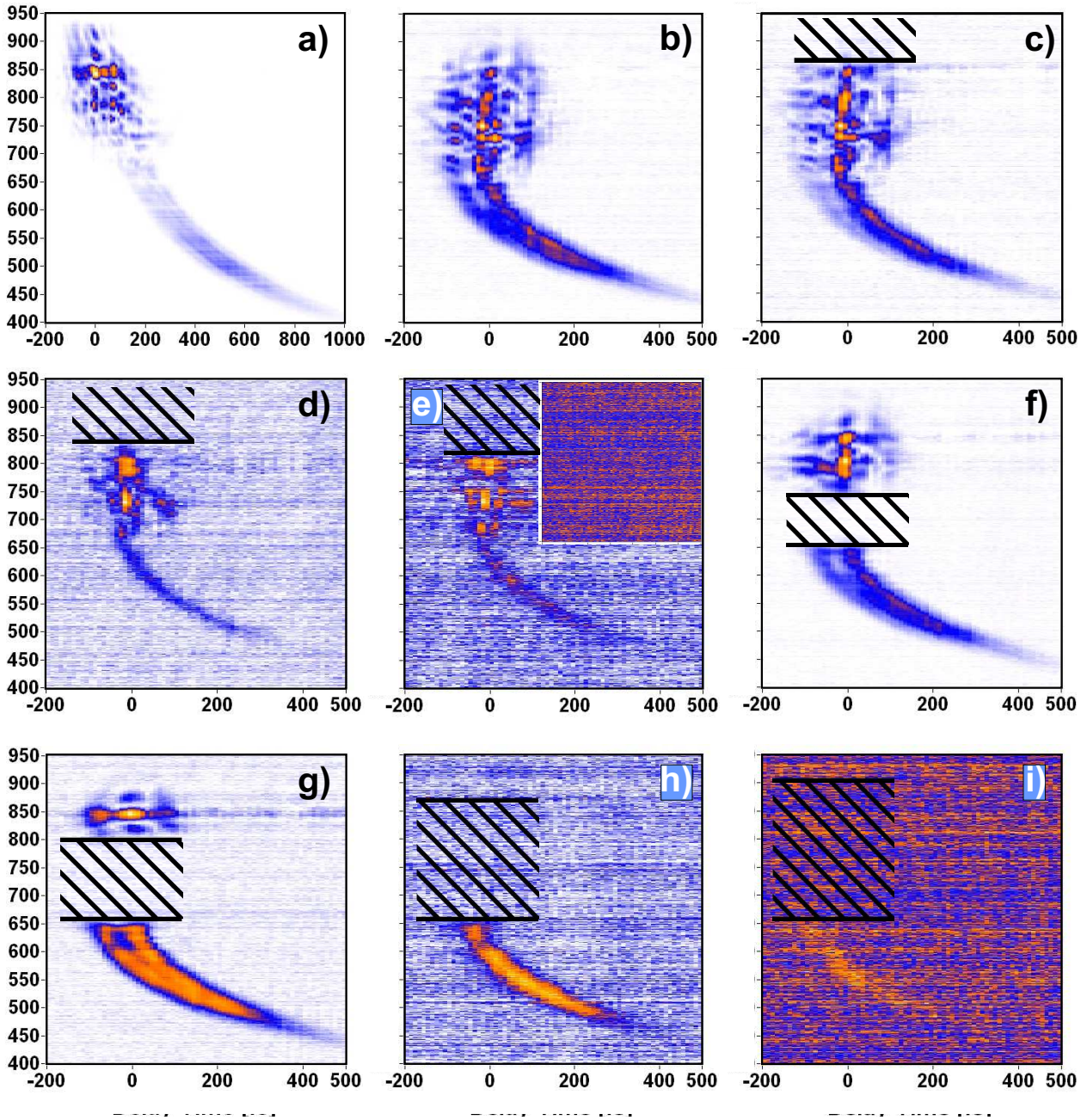

Figure 3.37: Non Degenerate Four Wave Mixing. The vertical axis corresponds to the wavelengths and the horizontal one to the delay time in all plots. The capability of cross-correlation measurements within a single beam is verified by gating different spectral distributions. Unfiltered filamentation output directly measured in a) and after passing the 4-f setup in b). The remaining traces in c)–i) are carried out with partially filtered spectra according to the plots in Fig. 3.38. A continuous spectral cutting beginning from the long wavelength side in c)–e) causes the whole 4WM signal to decrease. Cutting the complete NIR part above 780 nm (transmission from 420–780 nm) disables optical gating at current intensities as indicated in the inset of Fig. 3.37e. However, bandpass filtering in f)–i) enables gating of the VIS part at very low NIR intensity, even if the NIR is to weak to gate itself in h) and i).

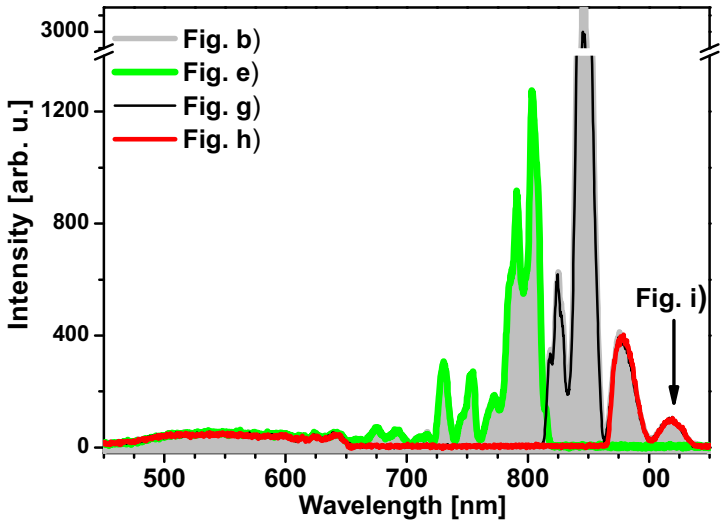

Figure 3.38: Directly measured spectra for measuring the TG-X-FROG traces according to Fig. 3.37. The gray back ground shows the full bandwidth after filamentation generating the trace of Fig. 3.37b), the green line belongs to Fig. 3.37e, the black line to Fig. 3.37g and the red curve to Fig. 3.37h. The trace of Fig. 3.37i is gated with the small hill at 920 nm indicated by an arrow.

be gated.

Furthermore, the spectral slicing experiment showed that a spectral shift of the NIR gating structure for 120 nm from about 800 nm (green plot in Fig. 3.38) to 920 nm (indicated by the arrow on the red curve in Fig. 3.38) does not cause a spectral change of the gated VIS tail from 450–650 nm.

The capability of performing multi color cross-correlation measurements, where a small spectrum around the laser fundamental gates any desired wavelength region towards the blue spectral side, can be applied also for UV excitations of biological systems which is a growing topic of research. The combination with a pulse shaper which enables flexible generation of desired wave forms was already demonstrated in Fig. 3.32 by the generation of VIS pulse trains. In a similar fashion, double color excitation within a single beam is demonstrated in Fig. 3.39. The sequence in Fig. 3.39a–d) is a realization of the pump probe or pump dump scheme [122], respectively. The starting point was a two colored double pulse with one compressed NIR pulse at time zero and a shortened VIS pulse (λ_0 = 609 nm, $\Delta\lambda$ = 25 nm) at a time delay of 300 fs (Fig. 3.39a). The spectral range covered in this single beam pump probe example spans from 550–900 nm. The successive time delays were carried out by applying a liner phase ramp to the VIS pulse. Thereby the steepness of the slope determines the temporal separation of the two sub pulses. In that way the VIS pulse was shifted up to a negative time delay of -100 fs with respect to the NIR pulse.

3.5 Discussion of white light applications

The two issues addressed throughout the following discussion concern the properties of WL generation as well as its underlying mechanism, and the subsequent application of the WL, like pulse shaping and 4WM.

3.5.1 Filamentation properties

In a nutshell, continuum generation in laser induced plasma filaments begins as symmetric broadening (SPM). With increasing nonlinearity it becomes asymmetric towards higher frequencies. This asymmetric broadening towards the blue side is attributed to a sudden change of the nonlinear refractive index due to plasma generation, possibly in combination with optical shock waves at the back side of the pulse. An increase in nonlinearity can be achieved by either rising the pulse energy or the gas pressure and by changing the type of gas. A continuing increase leads to tem-

poral -and spatial breaking up of the beam. The discussion of filamentation properties starts with effects observed for low energies.

Red shift In contrast to the plasma blue shift (Sec. 1.2.2) which sets in at high intensities, small nonlinearities can place emphasis on the red side of the spectrum. This happens when rotational or vibrational response of the nonlinear medium arises. In contrast to atomic noble gases, the molecular gases (N_2 and O_2) exhibit an additional contribution from nuclear dynamics. For molecules, the Kerr nonlinearity consists of different contributions: besides an electronic part which is instantaneous on a fs time scale, several types of nuclear response due to rotational and vibrational motions can contribute [89, 185]. Off-resonant excitation of linear molecules with intense fs laser pulses will induce electronic $n_2^{\text{electronic Kerr}}(t)$ and pure rotational $n_2^{\text{rotational Kerr}}(t)$ contributions whereby the latter shows a time delayed relaxation. Thus the nonlinear refractive index n_2 of Eq.(1.34) extends with [43] to

$$n_2^{\text{total}}(t) = n_2^{\text{electronic Kerr}}(t) + n_2^{\text{rotational Kerr}}(t)\,. \tag{3.4}$$

The non instantaneous rotational Kerr effect leads to a deviation of the $n_2^{total}(t)$ from the Gaussian pulse envelope in a way that it exhibits an extended flank on the trailing edge. This acts opposite to plasma generation explained in Sec. 1.2.2 which forces a drastic change of the refractive index at the rear side. Thus the spectrum becomes red shifted [43, 87]. This effect was seen in our lab for

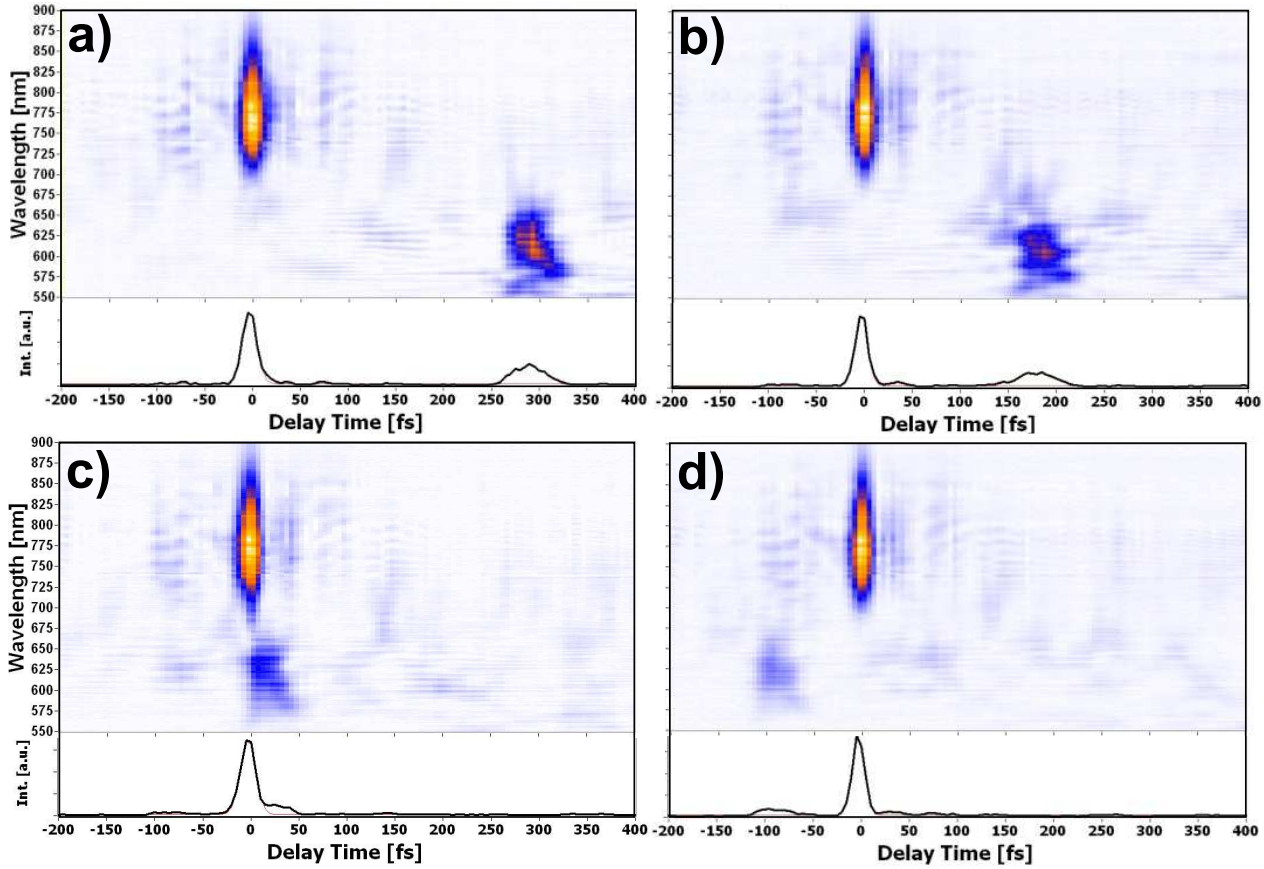

Figure 3.39: Generation of single beam pump probe excitation with sub pulses of different color. Time delaying of the VIS pulse is carried out by applying a linear phase ramp with the pulse shaper. The measurement conforms to a single beam TG-X-FROG.

broadening in air at about 240 μJ pulse energy [170] and is seen in the spectra of Fig. 3.5a where the pressure is increased. Noteworthy, in Fig. 3.1 a red shift also occurs with an evacuated cell due to the FS windows only. With increasing nonlinearity, a further red shift cannot be distinguished from the SPM broadening around the laser fundamental, for instance when the energy is increased.

The role of ionization - comparison Xe and O_2 In general, all investigated gases exhibit similar effects for filamentation at higher energies (0.7–1.5 mJ). The most conspicuous distinguishing between different gases lies in their threshold combination of input energy and absolute pressure which generally becomes lower with low ionization potential (IP). Nevertheless, taking the IP as the only attribute is not sufficient. For instance, Xe and O_2 have a similar IP (IP_{Xe} = 12.13 eV, IP_{O_2} = 12.06 eV), thus both gases require eight NIR photons for MPI. On the other hand, the nonlinear refractive index of Xe $n_2(Xe)$ is 1.6 times higher compared to O_2. This might explain why spectral broadening for Xe is considerably stronger than for O_2, as is shown in Fig. 3.14. The spectral broadening in O_2 at a pressure of 30 kPa (pink line) and in 23 kPa of Xe (gray filling) behaves substantially different. The different spectral shapes around the laser fundamental are not of major concern in this regard, because they might origin from different initial prechirps of the amplifier, which was tuned to gain the widest broadening in both gases. Both curves show a comparable extend of the broadening for the modulated NIR part which reaches from 720–920 nm. However, the striking difference is that broadening in O_2 drops at 720 nm while the Xe WL exhibits a continuous part reaching from 720 nm further down to 400 nm. From this observation, the question might be raised whether the Kerr effect in the form of self-steepening and optical shock waves, respectively, is more relevant for the generation of the asymmetric VIS spectra than the formation of plasma, since the IPs of Xe and O_2 are the same.

This view point on the origin of the difference in WL generation between Xe and O_2 changes completely, when higher order ionization processes are taken into account, as were described in Sec. 1.2.2. Talebpour $et.\ al$ calculated a tunnel ionization (TI) probability being two orders of magnitude higher for Xe than for O_2 at an intensity level of 10^{13} W/cm^2. This indicates, that the IP is a less meaningful quantity to fully characterize ionization in strong laser fields, where mechanisms other than MPI come into play. In order to get to the bottom of this competition between plasma generation and Kerr effect, the experiment of Sec. 3.2.1 is taken up, where WL generation in air is quenched by the addition of He into the gas cell.

WL quenching with He For the interpretation of this experiment it is assumed, that adding a partial pressure of He to an already present pressure of air (black curve) slightly increases the nonlinear refractive index of the mixture (pink curve) due to the He contribution. The total pressure in all cases was 100 kPa. However, although the density of air itself remains unchanged in every individual mixture, ionization was reduced due to He acting as a buffer gas. To further investigate this finding, a partial pressure of 10 kPa He was added to 90 kPa air in Fig. 3.22a, which means an addition of 11% He to the original air density. The additional He concentration had no influence on the spectral brodening, which is seen by the two identical curves in a). The modulated NIR part reaches from about 710–940 nm in the logarithmic plot and the VIS wavelengths extend beyond 400 nm on the blue side. When 25% of He was inserted in the gas cell additional to the 80 kPa air (Fig. 3.22b), the VIS part remained the same. Certainly, the undefined modulations in the NIR part switch to a symmetric SPM pattern, shown also on a linear scale in Fig. 3.40. The lower signal for filamentation with pure air (black line in Fig. 3.22b) might result from a larger beam divergence. In Fig. 3.22c, a significant change on both the VIS and the NIR side occurs if a partial pressure of 43% He is added to the 70 kPa air. The changes in the NIR are attributed to a change of the effective n_2. In the case of this He/air mixture (pink line), the VIS shoulder was quenched, apart from a small reoccuring hill at 625 nm. This quenching might arise

from a disturbed balance between Kerr effect and its conterplaying plasma generation. Such an unbalancing might origin from He acting as a buffer gas which halts the plasma generation and therefore self-stabilizing is inhibited. Thus, nonlinear propagation in the n_2 medium is reduced as well, which suppresses spectral broadening around the laser fundamental. The quenching gets even stronger when 66% He was added to 60 kPa air in Fig. 3.22d. Then the VIS shoulder present in air (black line) collapsed completely (pink line) and the spectrum is equal to the case of vacuum (green line), even though 60 kPa air were still present. The observed effects of quenching the VIS shoulder in plots c) and d) might result from a diminished plasma generation in the presence of He. However, the complete termination of broadening in d) is surprising and demonstrates the strong dependancy of the filamentation process on the surrounding conditions. Allthough, a clear identification of the underlying mechanisms is not yet at hand, empirically determined mixtures of gases with high and low nonlinearity could be applied to scale the filamentation process towards higher pulse energies and simultaneous avoidence of a spatial beam break up. This mixing technique could be advantageous over reducing only the density of one gas type in order to prevent from multi filamentation. Decreasing the pressure reduces the achievable bandwidth which cannot be fully compensated for by an increased pulse energy. In this way, the He buffer gas method enlarges the parameter space within which a good beam profile, high power and wide broadening are simultaneously reached.

Input beam profile dependence The following paragraph discusses effects observed in Fig. 3.2. The explanation why a beam profile exhibiting a diffraction pattern changes the filamentation output in Fig. 3.2 has two aspects. Firstly, the iris takes on the role of cleaning up spatial inhomogeneities which are seldom absent in real beam profiles. Even on days with some experimental luck in regard to spatial mode quality, closing of iris I1 in Fig. 2.1 prior to the focusing mirror always improved the performance in terms of wider broadening towards the blue spectral side and the generation of the shortest pulse durations ($cf.$ Fig. 3.24). The second aspect besides this mode cleaning is, that the diffraction pattern reinforces the local field distribution. Thus fine adjustments with the iris corresponds to fine adjustments of the local intensity in the focal spot. This fine tuning has a huge impact on subsequent self-lensing and other intensity dependent nonlinearities, especially when a ten photon process like MPI in air is associated with. The influence of spatial amplitude or phase patterns, respectively, on the filamentation process is a topic of current research and the following references are suggested for further reading [186–188].

Pressure and energy dependence An increase in nonlinearity by either increasing the pressure or the pulse intensity causes stronger broadening with a wide dropping off spectral tail into the VIS wavelength region, as is seen in Figs. 3.20 or 3.14. Since the spectral phase predominantly exhibits quadratic behavior (Figs. 3.20b), the VIS tail is also temporally elongated for several hundreds of fs. The extension towards short wavelengths saturates around 370–470 nm, depending on the combination of input conditions like prechirp and iris closing. Further increasing the nonlinearity is accompanied by temporal splitting like can be followed up in the series of Fig. 3.6. Followed to this temporal splitting, higher nonlinearity causes a spatial beam break up which makes the filament output unusable for subsequent pulse shaping and 4WM based on geometrical beam splitting. For applications where the beam quality plays a miner role ($e.\ g.$ transient absorption spectroscopy), uniform spectra with a high power spectral density in the VIS can be achieved, as was shown in Fig. 3.12b).

Chirp dependence Another possibility to steer the filamentation process, without changing the input energy lies in varying the prechirp in the amplifier, as carried out for the measurements of Fig. 3.8. Generally, small changes of the prehirp strongly influences the evolution of the NIR temporal and spectral structure. On the other hand, no direct influence on the shape of the VIS tail

is observed for modest chirp deviations, besides the long wavelength cut-off being shifted towards the fundamental. Although the sign of the prechirp is different in Fig. 3.8b and e), the TG-FROG trace of the tail, especially its curvature, is almost identical. The chirp variation measurement clearly proves, that the appearance of the strong positive chirped VIS tail is not restricted to a TL or positive chirped input pulse. In other words, the spectral phase of the VIS tail does not depend on the input chirp. This observation clarifies, that the generation of the VIS spectrum results from a threshold like behavior at the rear side of the pulse when propagating through a nonlinear medium. Of course, larger chirp factors in Fig. 3.8a and g) suppress the WL generation because the temporally elongated pulse experiences only a weak nonlinearity. However, a small positive prechirp on the order of 400 fs^2 caused the widest spectral extension towards the blue side in most experiments. This setting was also necessary to achieve the few cycle pulses of Fig. 3.24.

When comparing the traces for positive and negative prechirp in Fig. 3.8 it is mentioned, that the positive chirped 115 fs pulse in b) with a duration of about three times the TL (40 fs), generates WL down to 470 nm. In contrast, although the duration of the negatively chirped 80 fs input pulse in g) is only twice the TL, no VIS spectrum is generated at all. That means, a pulse with lower peak intensity in the positive chirp regime results in wider broadening compared to a pulse with negative prechirp and even higher peak intensity. The average pulse energy is not changed by pulse chirping. Both, energy and chirp variation, lead to the insight that a positive quadratic spectral phase of the input pulse provides better conditions for the generation of short wavelengths. Further on, beneficial effects of positive prechirps on the compression of few cycle pulses has been reported by other groups as well [159, 160].

A possible explanation for the enhanced extension to the blue side is an enhanced ionization for positive prechirps. MPI enhancement in Ca atoms with positive chirped pulses instead of TL pulses is described by Brixner and Gerber [133]. The explanation is as follows: The ponderomotive energy shift ($U_p = (e^2 \langle E_0^2 \rangle)/(4m_e\omega_0^2)$, see Eq.(1.50)) of the atomic IP increases linearly with the laser intensity ($\propto E^2$). Since the continuum density of states is highest close to the ionization level, MPI is enhanced when exactly those states are populated by the exciting light field. In a positive chirped pulse, low energy components arrive at the beginning where the ponderomotive shift is small. According to Eq.(1.51) a weak intensity of 5×10^{13}W/cm^2 @800 nm results in a huge ponderomotive shift of about 3 eV which is roughly twice the energy of the center frequency photon. An "optimal pulse form" where higher energy photons appearing at later times, which corresponds to a higher ionization threshold, thus might enhance the ionization rate.

Comparison of gases Generally filamentation in noble gases and air is quite similar. It consists of an intense gating structure at NIR wavelengths followed by a VIS tail with positive chirp. The dependence on parameter changes, like intensity variation, was found to be equal for all investigated gases. Increased nonlinearity provides wider broadening towards the blue spectral side until saturation is reached. As pointed out above, positive prechirps favour wider broadening and better compressibility of the WL. Around to the zero chirp position, a defined temporal splitting occurs for the noble gases, like seen in the right column of Fig. 3.13. An analysis of split pulses was carried out in Sec. 3.1.3.

The temporal splitting in air at zero prechirp differed from that in noble gases, such that it gained more complex structures, as shown in Figs. 3.4 and 3.20. However, the VIS spectrum is smooth and reaches as far as in the case of Xe (Fig. 3.14). If the cut-off region on the blue side is extended beyond 400 nm, the spectra typically exhibit a step-like pattern at 500 and about 400 nm. This observation was made in air (Figs. 3.5, 3.15, 3.19) and in Xe (Fig. 3.14). On the other hand, reduced spectral broadening down to only 500 nm shows a monotonic decay at the blue side for all gases.

It was further observed, that control over multi filamentation is more difficult with increasing n_2 of the material, because parameter tolerances became much smaller. For instance in Fig. 3.11, pulse splitting already occurs at 0.6 mJ, before maximal broadening is achieved. Simultaneously, the spatial mode was corrupted and completely broke up above 0.9 mJ. This is one reason why air was the chosen medium for the coherent control experiments in Sec. 4.2. Filamentation in air allows for WL generation at the 1.0 mJ level with perfect beam quality. Its excellent spatial quality enabled geometrical splitting in the TG-FROG setup after passing the pulse shaper setup. Since the tolerance on input conditions is larger, the day to day reproducibility of octave spanning spectra reaching from 380–950 nm (see Fig. 3.19) was easiest with air. Remarkably, the stability of this highly nonlinear process allowed the closed loop experiments extending over many hours.

Indeed, Kr and Xe showed the best efficiency for converting energy to the VIS region. However, the impressive spectra in Figs. 3.12 and 3.14 were certainly achieved on cost of spatial beam quality. Besides geometrical aspects, very high nonlinearity with maximal broadening disabled pulse compression with a conventional scheme like CM or grating based methods, as can be seen in comparison of Fig. 3.37a and b).

Manual compression As already pointed out in the corresponding Sec.3.2.2, pulse compression schemes which introduce additional dispersive material itself like the prism compressor, are not recommendable for a few cycle pulse. Grating based compressors overcome this problem. In particular, the telescope grating compressor in a 4-f configuration (see Fig. 2.13) was aligned such, that higher order dispersion like TOD was eliminated, as is seen by the 7 fs pulse in Fig. 3.26. Simultaneously an excellent beam profile could be obtained. The capability of chirping an octave exceeding WL spectrum is illustrated in Fig. 3.37a and b), where the direct output of the filament in a) was launched into the 4-f setup in b).

The CM turned out to be nearly alignment free once the right number of bounces and the optimal conditions for filamentation were found. The robustness and straightforward operation for few cycle pulse generation in air at atmospheric pressure is demonstrated by the repeatability of the 6.3 fs pulses over a period of 10 days and its retake several months later.

Arbitrary Pulses Compared with conventional methods of pulse compression discussed in the previous paragraph, the adaptive shaping technique with a SLM in the 4-f setup is most flexible. Up to a certain degree, it enables correction of unclean temporal structures exhibiting a higher order phase function. And even more, the utilization of a feedback loop scenario for pulse compression eludes the problem of precise phase measurements, as demonstrated in Fig. 3.28. Thus, compression of pulses with large time-bandwidth products can be carried out without knowledge of the initial phase function. Indeed, other methods as spectral phase interferometry for direct electric field reconstruction (SPIDER) or multiphoton intrapulse interference phase scanning (MIIPS) [189] directly measure the spectral phase, but have not been demonstrated for complex pulse shapes [99]. Furthermore, since 4WM can be carried out in any isotropic medium, this pulse compression method is wavelength independent and can be applied throughout the whole transparency range of glassy material. The limited transmission range of the SLM can be overcome by reflective shaping devices or by acousto optic programmable dispersive filter (AODPF). Another advantage in utilizing a $\chi^{(3)}$ nonlinearity, is the cubic power dependence of the 4WM signal which makes the method robust in terms of getting stuck in a local minimum during optimization. The examples for phase only optimization in Fig. 3.28 and for additional smoothing of the spectral amplitude in Fig. 3.29 reveal the reliability of this approach. The practical benefit is, that one is not in need to find filamentation conditions for short pulses to get ≈ 10 fs pulses. The spectrum can be broadened as much as possible and the complex phase function in the NIR ($cf.$ Fig. 3.20) is transferred to its TL by the evolutionary algorithm. In this manner, ultra short NIR pulses with the whole VIS part

remaining for arbitrary shaping can be generated. These novel possibilities of ultra fast techniques were utilized for the first time when performing the octave spanning shaping of Ag_3 in Sec. 4.2.

3.5.2 Filamentation mechanism

To prevent misunderstandings, the herein after presented simulations don't lay claim to rigorous propagation calculations but rather to draw an intuitive picture about the fundamental interplay between the main actors, Kerr effect and plasma generation. Full propagation simulations include solving the nonlinear envelope equation Eq.(1.67) or simplifications of it in three dimensions plus time. This comprehensive task with widespread theoretical complexity requires high numerical effort and thus lies outside the scope of this thesis. Literature on numerical modeling of nonlinear propagation is given for instance by Refs. [33, 35–37, 53, 53, 71, 75, 82, 175].

On the other hand, the observations in the lab do not uphold the existence of long extended and self guided light-plasma channels. Plasma fluorescence in our experiments is observed only in an interval around the geometrical focus with an extension of about 20–25 cm which is less than twice the Rayleigh length of 16 cm, see Eq.(A.31). In some cases the plasma was hardly visible at all, even though bright WL was emitted. The interpretation is: Initially, the beam is focused by the spheric mirror, then it undergoes spatial and temporal self induced changes but never refocuses like the long distance WL filaments in LIDAR experiments [14]. After a restricted nonlinear interaction with the medium, it emerges as a nearly collimated and spectrally broadened beam.

Spectral broadening due to Kerr effect and plasma generation was introduced in Secs. 1.2.1 and 1.2.2. Clearly, neither the SPM in Fig. 1.5 nor the plasma blue shift of Fig. 1.7 approximate the measured spectra in a satisfactory manner. The question was, how the interplay between Kerr- and plasma effect influences the broadening. The basis for the simulation is achieved by inserting Eq.(1.65) in Eq.(1.64) and omitting the tunnel ionization. It is neglected, because geometrical focusing leads to intensities about 6×10^{13}W/cm^2 which is just below the strong field regime of nonlinear optics in which the probability for tunneling is low. The defined starting point for the calculations is:

$$\omega(t) = -\frac{d\phi(t)}{dt} \propto \omega_0 + \frac{\omega_0 z}{c}\left(\underbrace{-n_2\frac{\partial I(t)}{\partial t}}_{\text{Kerr effect}} + \frac{1}{2n_0\rho_{crit}}\left[\underbrace{\sigma^{(K)}I(t-t_0)^K\rho_{atm}}_{\text{MPI}} + \underbrace{\frac{\sigma_e}{E_I}I\rho_e(t-t_0)}_{\text{AI}}\right]\right). \tag{3.5}$$

The three marked terms in Eq.(3.5) generate spectral broadening by changing the instantaneous frequency $\omega(t)$. First, there is the intensity dependent SPM term (Kerr effect), followed by two plasma contributions in the square braces. The plasma related terms do much more depend on intensity than the Kerr part. Multi photon ionization (MPI) scales with the Kth power, where K is the number of photons necessary for ionization ($cf.$ Table 3.1). Avalanche ionization (AI) increases exponentially with intensity. The carrier frequency ω_0 was chosen to be 2.3218×10^{15}[rad/s] and the order of magnitude for the nonlinear refractive index change given by the product $n_2 I$ was 10^{-5}. For the calculations[2], the temporal phase $\phi(t)$ displayed by Eq.(3.5) is added to the complex field $E(t)$ and subsequently Fourier transformed in order to get the power spectrum of the pulse. Accordant to the experimental situation, the input pulse duration was set to 50 fs (FWHM). The multi photon cross section $\sigma^{(K)}$ and the electron impact ionization cross section σ_e were adapted to achieve reasonable results within the used intensity ranges. Both plasma related terms contain

[2]For instance the product $n_2 I$ for focusing 1 mJ, 40 fs pulses according to Fig. 2.1 in air ($n_2 \approx 3 \times 10^{-19}$cm^2/W) is about 2×10^{-5}

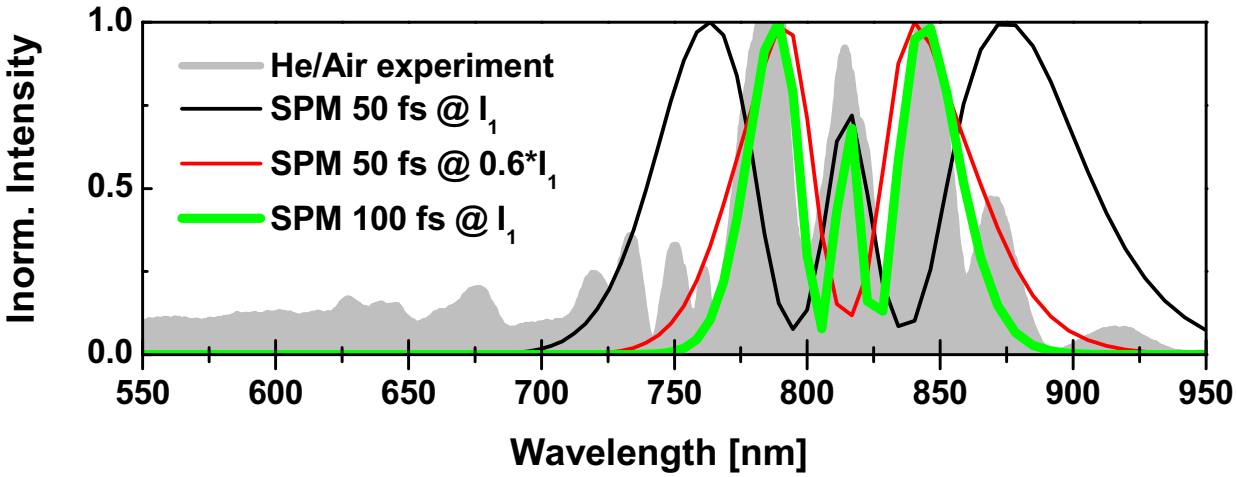

Figure 3.40: SPM in He/Air mixture, experiment vs. theory. The measure data (gray filling) shows an unambiguous SPM signature. When simulating 50 fs input pulses corresponding to the experimental conditions, the calculations of SPM match either in the right FWHM (red line) or in the number of central (peaks black line). The intensity of the weaker SPM (red) is 60% of the stronger SPM case (black). A correct spectral shape and FWHM can only be obtained at double the experimental pulse duration of 100 fs (green line). Obviously, the VIS tail which extends down to 400 nm is of different origin than SPM.

an additional degree of freedom, that is a translation along the time axis $t - t_0$. This term is novelly introduced and its relevancy will be discussed in the following.

As first example, the spectrum of Fig. 3.22b is taken up, because it exhibits the most significant SPM structure around the laser fundamental ever found during the parameter dependence experiments. The measurement data is given as gray back ground in Fig. 3.40 and two different calculation are overlaid as solid black or dashed red line, respectively. The calculations include only the SPM term in Eq.(3.5) without plasma contributions. The simulations fulfill different constrains concerning the real spectrum. The black curve simulates the experimental conditions of a 50 fs input pulse @810 nm (at intensity level I_1) and exhibits a fitting spectral shape, but an overestimated FWHM. The red curve was calculated with the same duration but lower intensity $0.6 * I_1$ and shows the same FWHM as the data whereas the central peak is missing, because of the reduced nonlinearity. This mismatch already demonstrates the gap between straightforward text book knowledge and real facts. Interestingly, a perfect simulation can be achieved when the pulse duration is doubled to 100 fs, denoting a bisection of the spectral width in the experiment. Green and black curve have the same shape, because of the same nonlinearity $n_2 I_1$. A increase of the initial spectra FWHM causes a wider broadening while keeping the SPM shape constant. Clearly, the VIS wavelengths underneath 700 nm have no relation to any means of SPM.

From there, additional plasma contribution is taken into account in Figs. 3.41 and 3.42, first only in the form of MPI. Figure 3.41a shows the temporal evolution of the refractive index $n(t) = n_0 + n_{Kerr}(t) + n_p(t)$ which consists of the constant, linear refractive index n_0, of a time dependent Kerr part $n_{Kerr}(t) = n_2 I(t)$ and the plasma influence $n_p(t) = -\rho_e(t)/2\rho_{crit}$ according to Eq.(1.48). Straight lines in Fig. 3.41a denote the total refractive index $n(t)$ whereas the dashed lines solely display the lowering of the refractive index as if only plasma generation would be present. For convenience, the linear refractive index is set to 1.

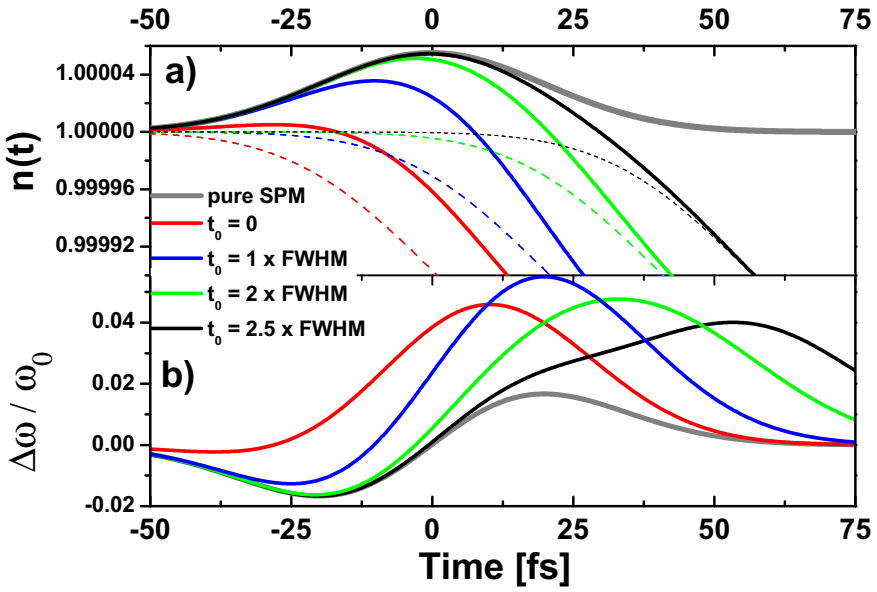

Figure 3.41: Simulation of SPM and plasma evolution with increasing time delay $(t - t_0)$ between SPM and plasma onset. The nonlinearity $n_2 I$ and $\sigma^{(K)}$ is constant. For comparison pure SPM is given in gray. The straight colored lines show the evolution of the total time dependent refractive index $n(t)$ in a) and the corresponding instantaneous frequency $\omega(t)$ in b). The evolution of the plasma can be deduced from the dashed lines which plot only the plasma refractive index $n_p(t)$. The timing of the plasma onset defines the slope of $n(t)$ and thereby the spectral extension towards the blue side as well as the modulations on the spectrum.

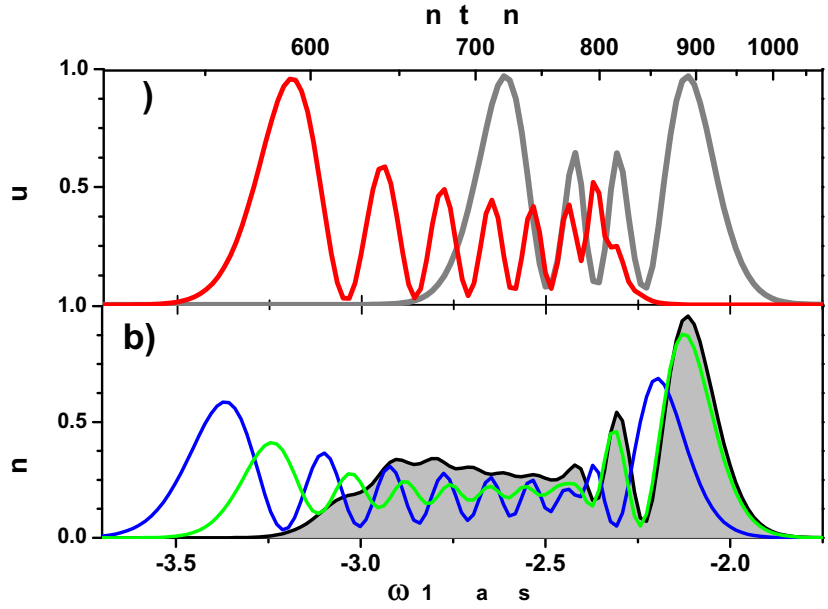

Figure 3.42: Simulation of SPM and delayed plasma spectral broadening according to Fig. 3.41. The color coding conforms to the legend in Fig. 3.41 (the black curve is filled with gray to improve visibility). It shows, that appropriate modeling of the plasma flank in the $n(t)$ diagram changes the appearance of blue spectral side and determines how much of the IR spectrum is depleted.

The time varying refractive index causes a change of the instantaneous frequency $\omega(t)$, as shown in Fig. 3.41b. The corresponding power spectra for the time varying refractive index $n(t)$ are plotted in Fig. 3.42a and b) with the same color coding. To see the difference which arises when plasma generation is included, pure SPM is shown in gray as a reference.

Now the respective curves and their meaning are discussed step by step. The four SPM peaks in Fig. 3.42a conform to Fig. 1.5, where the intensity was increased for about one order of magnitude during simulation. Such an increase matches well with experimental conditions, where $e.g.$ broadening in air was investigated from 0.2–1.5 mJ. In case of pure SPM, the $n(t)$ and $\omega(t)$, respectively, are symmetric with respect to the pulse maximum at time zero and $n(t)$ is always positive. The extrema of $\omega(t)$ in Fig. 3.41b correspond to the peripheral area in the spectrum in Fig. 3.42a and the deflection points of $\omega(t)$ leads to the global maxima of the simulated spectrum.

All the following straight curves simulate the action of both, plasma- and Kerr effect. The straight, red curve in Fig. 3.41a comprise a positive contribution to the refractive index due to the Kerr effect and a negative one owing to the free electrons generated by MPI. The parameter $\sigma^{(K)}$ for plasma generation was chosen such, that the broadening on the blue side reached up to 600 nm, a value which was easily observed for all investigated gas types in the experiment. The simulated $n(t)$ shown in red in Fig. 3.41a is no longer symmetric and drops after the pulse reaches about the half intensity at -25 fs. Since than, the plasma influence dominates, and the monotonic decrease of $n(t)$ is giving rise to an instantaneous frequency $\omega(t)$ which creates new frequencies only on the blue side. Thus the red $\omega(t)$ curve in Fig. 3.41b stays upon the ω_0 level. The result is a completely blue shifted spectrum in Fig. 3.42a with strong modulations and a depletion of NIR frequencies. The moment in which the $\omega(t)$ curve reaches its maximum coincides with the maximum pulse intensity. This transfers a big amount of energy towards the blue spectral side and is in disagreement with any experimental data. Further on, varying the values for $n_2,\ K,\ \sigma^{(K)}$ and intensity lead to no further convergence to measured spectra.

At this point, the novelly introduced time shift $t-t_0$ in Eq.(3.5) opens a new possibility to modify the simulations of the VIS continuum. The simulation changes significantly when a time delayed plasma generation is introduced. Shifting the onset of plasma generation by $t_0 = 1\times$ FWHM towards the trailing side of the pulse is shown as blue curve. The deviation of $n(t)$ from the SPM curve in Fig. 3.41a sets in later when compared to the red curve and thus does not deplete the NIR frequencies to the same extent, as can be seen in the spectrum of Fig. 3.42b as blue plot. Thus, the blue curve is shifted further towards high frequencies but has a lower intensity than the red curve in Fig. 3.42a. Accordingly in Fig. 3.41b, $\omega(t)$ increases to a higher value because the gradient, which is the driving force for nonlinear pulse broadening, of the blue curve is steeper compared to the red one. But still, an unrealistic modulation remains in the VIS part.

The green curves are calculated for a time delayed plasma onset of $t_0 = 2\times$ FWHM. The $n(t)$ in Fig. 3.41a almost reaches the same maximum value as in case of pure SPM (gray curve), meaning that the part in the spectrum which is red shifted with respect to the center frequency, is similar to SPM. Since the $n(t)$ plots of the green and gray curve differ from the pulse maximum on, the blue side of the spectrum in Fig. 3.42b also differs in its shape. Because the increase for $\omega(t)$ in Fig. 3.41b of the green curve is comparable to the red $\omega(t)$ curve, the spectral extend towards the blue side is identical. Now, the spectral intensity for the delayed case is weaker compared to the unshifted case in red. This is because plasma generation sets in at the back side of the pulse where the pulse intensity already decreases, which is seen by the green, dashed line in Fig. 3.41a. Thus less energy is left to create blue frequencies.

Delaying the plasma even further to $t_0 = 2.5\times$ FWHM is plotted as black curve in Fig. 3.41 and as filled black curve in Fig. 3.42b. The onset of ionization becomes visible around the pulse maximum which leads to a deviation of $n(t)$ compared to the SPM case (gray) in the last part

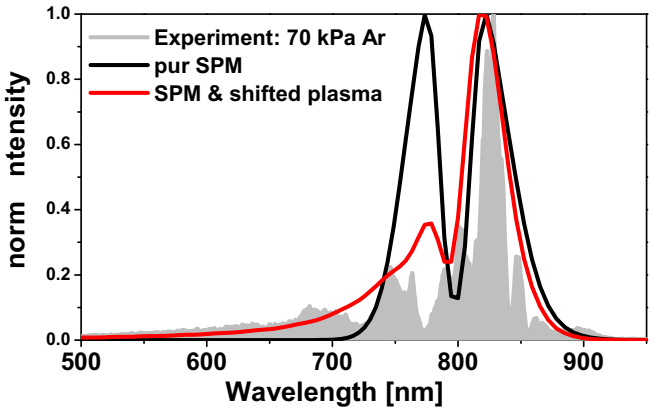

Figure 3.43: Simulation of filamentation in Ar with pure SPM (black) and time delayed plasma onset (red). Experimental data (gray) according to Fig. 3.6b. While the IR part of the SPM spectrum remains, modeling of the plasma flank reduces the Antistokes peak of pure SPM and spreads out the energy into the VIS tail.

of the pulse. Thus $\omega(t)$ in Fig. 3.41b does not increase for the same amount as for other plasma timings. The strong retardance keeps the IR spectrum unchanged compared to SPM and causes less broadening on the blue side. Interestingly, the VIS part lost its oscillatory structure and appears as a plateau. In principle this tendency agrees with the shapes found for WL filamentation in the experiments. In particular the VIS tail can be compared to the broadening in 100 kPa air in Fig. 3.5b. Both show a strong maximum on the IR end of the spectrum, a smaller peak at the fundamental and a long, smooth tail in the VIS part. Also the plateau like behavior at the blue side is comparable for example to Fig. 3.14. Certainly, the relative heights of the individual parts and spectral extensions are different.

The main insight gained with these simulations is: (i) A straightforward calculation due to refractive index change via SPM and free electrons fails in explaining the measured spectra. (ii) Introducing a time delayed plasma onset keeps the IR spectrum on the same level as pure SPM and enables modeling of the VIS tail. The later the plasma formation sets in, the more the original SPM structure remains. (iii) For a certain balancing of simulation parameters, a smooth VIS tail is calculated (filled black curve in Fig. 3.42b) which is in principal agreement with experimental data. With this back ground a very asymmetric filamentation spectrum in 70 kPa Ar at 1.5 mJ pulse energy was calculated in Fig. 3.43. The measured spectrum (gray curve) is compared with two simulations. From calculating the geometrical focus, the estimated experimental nonlinear Kerr coefficient $n_2 I$ is 0.7×10^{-5}. Modeling the red curve with delayed plasma onset was carried out with $n_2 I = 2 \times 10^{-5}$ which is in rough agreement. The difference could be interpreted as an underestimation of the experimental value which is likely, since the intensity increases if self focusing takes place. Pure SPM is plotted in black and the red line shows how the energy from the Antistokes peak can be transferred to a VIS tail with a shifted plasma onset. The stronger the spectral asymmetry, the more delay of plasma onset is required to fit the spectra. In this case the plasma sets in $4.5\times$FWHM later with respect to the pulse front. Therefore, only the red shifted peak of the SPM structure (black) at 825 nm remains. The bluer SPM peak shrinks and its energy content is outspread as long tail reaching up to 500 nm. In the real spectrum, the second peak and the minimum are shifted more to the blue side than in the simulation. Nevertheless, the general shape agrees in a range from 500–900 nm.

Summarizing the main ingredients of the filamentation mechanism reads as follows. SPM is proportional to the pulse intensity and $n(t)$ thus follows the symmetric pulse envelope. It generates symmetric spectral broadening. On the other hand, since the generated plasma does not collapse on a fs time scale, it causes an asymmetric decrease of $n(t)$, giving rise to asymmetric spectra which are strongly blue shifted with respect to its origin. The spectral shape for combined action

of Kerr- and plasma effect in Fig. 3.42a, however, is very different to measurement data. Besides plasma creation as a source of generating blue components, self steepening also causes a spectral blue shift ($cf.$ Fig. 1.9). Certainly, its oscillatory behavior in the VIS part differs compared to the plasma case ($cf.$ Fig. 1.7) and to experimental data. Experimental spectra can be simulated by introducing a delayed plasma onset, shifted to later times. Although not included in the calculation, self steepening might be the origin for an energy shift from the center of the pulse to its rear side. This can be seen in Fig. 1.8, where the center of mass is shifted towards the back side leading to a steep trailing -and a flattened front side. An experimental example where the energy redistribution towards the back of the pulse can be tracked as a function of either increasing pressure or pulse energy, is given in the TG-FROG traces of Figs. A.2, A.1 and 3.11.

Clearly this simplified simulations cannot model self-induced temporal changes and modifications of the spatial beam profile which definitely occur during the nonlinear propagation. Another important parameter missing in these simulations (as well as in the literature) is the prechirp of the driving laser pulse, which also causes asymmetries in the SPM spectrum.

3.5.3 4WM with white light

TG-FROG of highly structured pulses Before discussing the particularities of ultra broadband gating, some general comments on measuring complex pulses with TG-FROG are made. In order to sample time and frequency domain equally directly at the measurement, it would be convenient to implement automatic adaption of the scan properties like the full scan range Δt and delay increment dt according to [163]

$$\frac{d\omega}{\Delta\omega} = \frac{dt}{\Delta t} \tag{3.6}$$

with $d\omega$ being the frequency increment and $\Delta\omega$ the frequency range. With $d\omega dt = 1/N$, either the number of data points N or the delay increment can be determined:

$$N = \frac{\Delta\omega}{d\omega^2 \Delta t}, \qquad dt = \sqrt{\frac{\Delta t}{N\Delta\omega}} \tag{3.7}$$

Paying attention to these conditions during measurement might be beneficial for the following resampling of the time and frequency axis which have to consist of the same number of data points. Furthermore, performing a long extended scan in case of complex pulses will improve the quality of the Fourier transformation. The most intense structure in the trace should be located in the center of the matrix. The avoidance of noise will lead to cleaner retrieval of low intensity parts of the pulse and the overall spectral phase. Further improvements for the retrieval could be achieved through:
- Low pass filtering of the raw data
- Suppression of the signal in the corners of the trace
- Implementation of time and frequency marginals [190] to the PCGP algorithm

Ultra broadband gating

Interestingly, the spectral efficiency of the signal beam E_4 like investigated in Fig. 3.33 did not show a quadratic dependence as expected from relation (1.72). An analytical efficiency function was not found neither for the strongly chirped WL (Fig. 3.20) nor for the few cycle pulses (Fig. 3.24). The different efficiency curves in Fig. 3.33 result from WL pulses which differ in their spectral and temporal shape, and thus lead to unpredictable spectral dependencies. This might become a serious concern if the 4WM is used for spectroscopic applications and if the pulse durations break the 5 fs barrier [183]. A correction by simple division of the normalized, projected

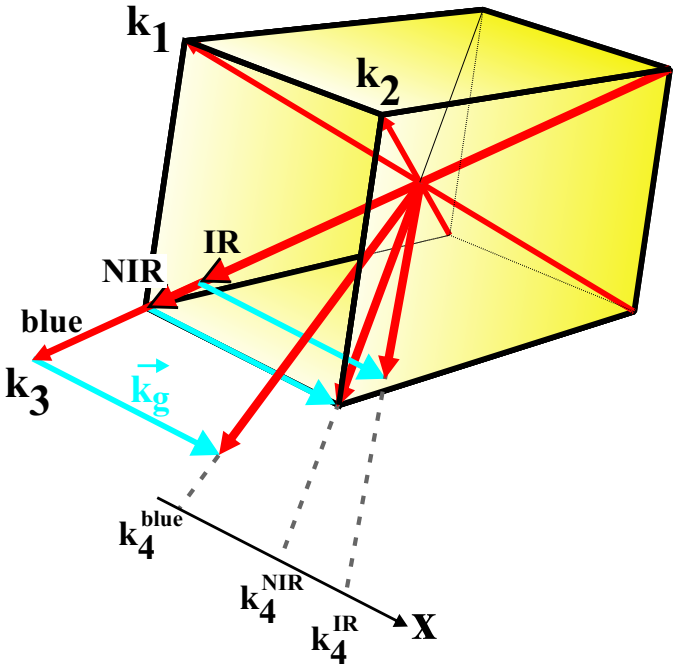

Figure 3.44: Vector addition assuming non degenerate 4WM for frequencies which do not equal the grating frequencies. The grating vector $\mathbf{k_g} = \mathbf{k_2} - \mathbf{k_1}$ is supposed to be constant regardless of the current absolute wave vector value of the scan beam $\mathbf{k_3}$. To fulfill conservation of momentum ($\mathbf{k_2} - \mathbf{k_1} + \mathbf{k_3} - \mathbf{k_4} = 0$) and energy ($\omega_4 = \omega_1 + \omega_2 + \omega_3$) simultaneously, the wave vector $\mathbf{k_4}$ has to changes its direction for wavelengths other than those which form the grating vector. Thus the 4WM signal is shifted along one axis and does not remain in the corner of the square, like in case of degenerate 4WM.

TG-FROG spectrum with the real spectrum fails because the recorded TG-FROG spectrum is convolved with the Fourier transform of the temporal gate function. One way of correcting the raw data could be as follows: First, convolute the real spectrum with the Fourier transform of the temporal projection of the TG-FROG trace. Then divide this convoluted spectrum with the spectral projection of the TG-FROG and use the resulting efficiency curve for correcting the raw data of the FROG trace by multiplying each time slice with this efficiency curve.

Concerning the measurements in Fig. 3.37 one could perform further power dependence measurements for both spectral areas and investigate the corresponding 4WM signal. For instance the signal strength of NIR and VIS part could be measured as a function of NIR power and as a function of VIS power. Further more, the 4WM signal could be investigated depending on different spectral and temporal shapes of the NIR gating pulses. In particular the signal dependence on defined temporal structures from the chirped to the few cycle case seems interesting in regard of better understanding the process of octave exceeding gating.

Non degenerate 4WM & Single beam TG-X-FROG In the degenerate case ($\omega_1 = \omega_2 = \omega_3 = \omega_0$) phase matching is automatically achieved for every frequency and one would expect the signal beam to point always to the fourth corner of the square in Fig. 3.44. However, in the case of correlating an octave spanning WL with an asymmetric spectral profile, the signal beam exhibits angular dispersion ($\mathbf{k}^4_{blue}$ and $\mathbf{k}^4_{IR}$). Whereby $\mathbf{k}^4_{NIR}$ points exactly in the corner of the rectangle. This is the degenerate case. While the signal beam $\mathbf{k_3}$ delivers blue wavelengths, $\mathbf{k}^4_{blue}$ travels along the outer edge towards the opposite corner (towards $\mathbf{k_3}$ in Fig. 3.44). This can be understood when supposing a contribution to the grating generation only from the NIR wavelengths. This means the grating vector ($\mathbf{k_g}$) is constant regardless of current frequency of the scan beam E_3 with $\omega_1 = \omega_2 \neq \omega_3$, as depicted in Fig. 3.44. Then the laws of conservation of momentum ($\mathbf{k_2} - \mathbf{k_1} + \mathbf{k_3} - \mathbf{k_4} = 0$) and energy ($\omega_4 = -\omega_1 + \omega_2 + \omega_3$) can only be satisfied when $\mathbf{k_4}$ changes its direction for wavelengths other than those which form the grating vector. If $\mathbf{k_3}$ contains wavelengths, red shifted to the gating pulse, the signal beam $\mathbf{k}^4_{IR}$ points outside the box, but still on one line (denoted as x - axis) with the residual spectrum. The situations when a blue or IR beam is diffracted at the constant NIR grating is drawn in Fig. 3.44.

This description exactly matches the observation of Fig. 3.35. Clearly, for a negative delay of -200 fs, meaning diffraction of red shifted wavelengths compared to the grating pulses, the spot moves outwards. On the other hand, the bluer the wavelengths get, the more the signal points towards the dashed middle line. The lowest spot at 400 nm almost has reached the center. A degenerate 4WM for the entire WL would have caused all spots to appear in the corner position instead of being dispersed along the x - axis.

The above described situation, where two NIR pulses carry out the gating for the entire spectrum is simulated in Fig. 3.45a. It represents another view of Fig. 3.44. In Fig. 3.45a, the light propagates along the z axis, that means it travels towards the reader. For simplicity, the induced grating is assumed to consist of one center frequency (ω^{NIR}) only. In reality, likely a certain wavelength distribution contributes to the grating formation. A WL scan of an octave exceeding SC reaching from 400–1000 nm is simulated by vector addition of the three incoming beams ($\mathbf{k_1}, \mathbf{k_2}, \mathbf{k_3}$) assuming a constant grating vector $\mathbf{k_g}$. The vector addition leads to a certain point in space. The connection of this point and the origin, located in the focus of the three beams, defines the direction of the signal vector $\mathbf{k_4}$. The distance to the origin gives the length of $\mathbf{k_4}$. In general the vector length is related to the frequency by

$$|\mathbf{k}| = \frac{2\pi}{\lambda} = \frac{\omega}{c}. \tag{3.8}$$

The center wavelength is set to 800 nm for the calculations. The 4WM configurations equal the case in Fig. 2.6. According to the experimental conditions of Fig. 3.35 a simulation of the spatial behavior of the signal beam E_4 is carried out in Fig. 3.45a. The beams E_1 and E_2 form the transient grating on which the time delayed scan beam E_3 is diffracted. The grating vector is kept constant in the calculation, while E_3 is varied. The left most signal ray (E_4^{blue}) denotes a wavelength of 400 nm and points almost in the middle of the square, like in Fig. 3.35. The frequency increment from one ray to the next one is constant in energy. It can be seen that for shorter wavelengths, the spatial movement along the x axis becomes smaller. One increment towards longer wavelengths causes a larger x-movement of the beam than for shorter wavelengths, like in Fig. 3.35. The two dimensional sketch below in Fig. 3.45a shows the movement as red arrow. As stated in Sec. 1.3.2, TG-FROG exhibits no frequency conversion. This is because the absolute value of the two grating vectors adds to zero $|\mathbf{k_2}| - |\mathbf{k_1}| = 0$, as can be described by the phase matching relation of Fig. 3.45a. Thus the length of $\mathbf{k_4}$ corresponds to the one of $\mathbf{k_3}$ for all wavelengths of the scan beam E_3.

Unlike in TG, a frequency conversion occurs in the rhombic arrangement of Fig. 3.45b where $\mathbf{k_2}$ and $\mathbf{k_3}$ generate the grating. As can be seen by the phase matching relation of Fig. 3.45b, the absolute value of $|\mathbf{k_2}| - |\mathbf{k_1}|$ does not add to zero if the wavelength is different. This is indicated by the different colors in the equation. Since the energy is conserved, the signal $\mathbf{k_4}$ is red shifted with respect to the grating vectors ($\mathbf{k_2}$ and $\mathbf{k_3}$) if the scan beam $\mathbf{k_1}$ is bluer than the grating vectors and vice versa. The latter case is named Coherent Anti Stokes Raman Scattering (CARS) in literature. As described in Sec. 2.2.1, the first employed setup for 4WM accorded the rhomb geometry, of Fig. 2.6. Although the difference between TG and rhomb arrangement seems to be small, the effect on ultra broadband gating is enormous. The rhomb setup allowed the creation of beautiful higher order diffraction patterns when used with WL. For taking the picture of Fig. 2.7 the input energy laid around 35 μJ which by far exceeds the typical input energy of 5 μJ for recording FROG traces. However, gating of whole WL spectra was not successful with the rhomb arrangement which can be verified by comparing the two FROG traces of Fig. 3.36.

The simulation for the pointing of the 4WM in the rhomb geometry is shown in Fig. 3.45b. Now, E_2 and E_3 generate the transient grating on which E_1 is diffracted. For $\omega_1 = \omega_2 = \omega_3 =$

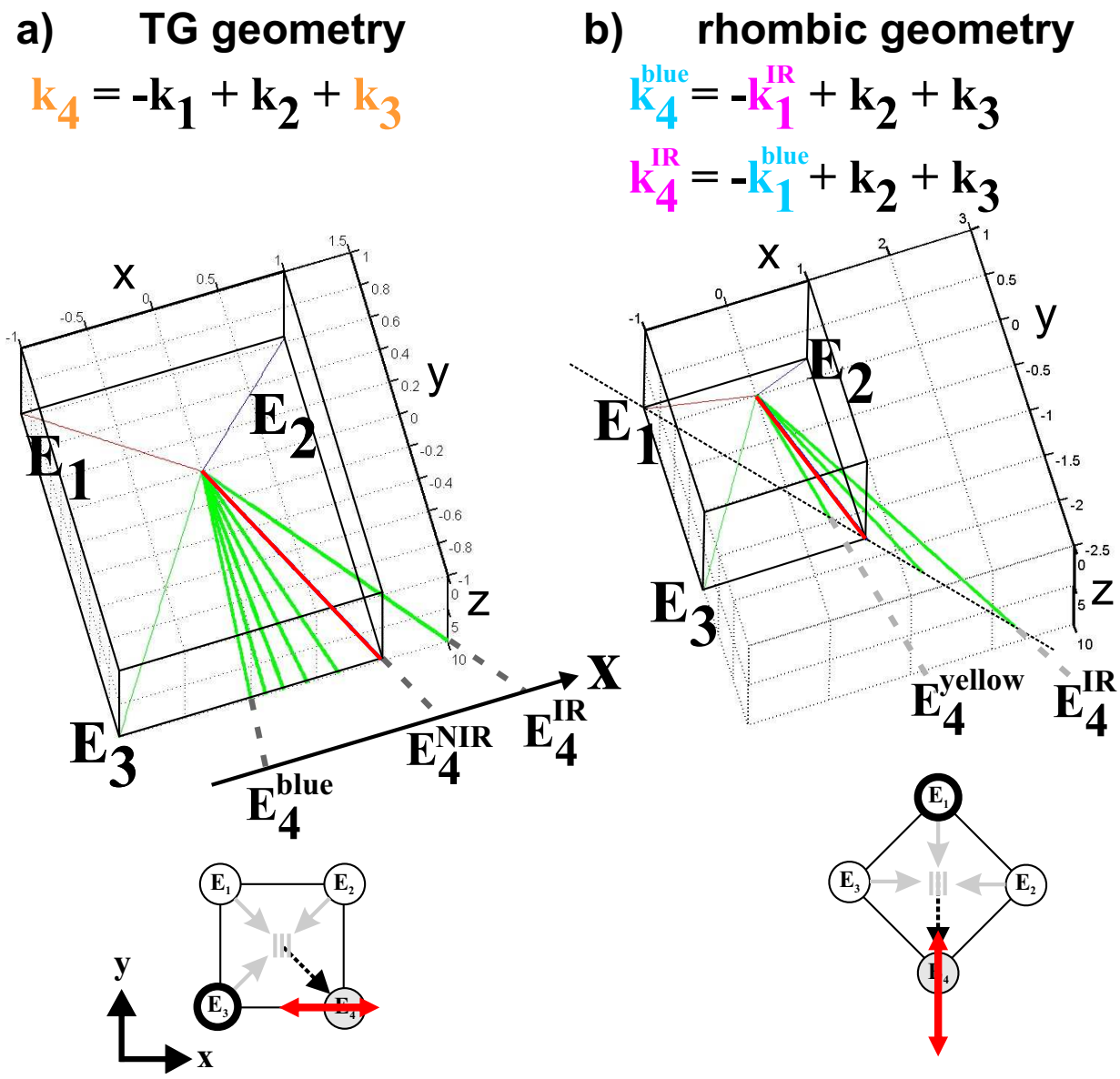

Figure 3.45: Photon billiards in TG and rhomb geometry by calculating the vector addition for a scan of chirped WL which is diffracted onto a induced grating, generated at 800 nm (E^{NIR}). The light propagates along positive z direction towards the reader. Left side a) corresponds to TG and right side b) to rhomb geometry according to Fig. 2.6. The red ray E_4^{NIR} denotes the degenerate case, which always points exactly in the corner of the forward box. The green rays represent different wavelengths of the diffracted WL. E_4^{blue} corresponds to 400 nm, E_4^{IR} to 1000 nm and E_4^{yellow} to about 600 nm. In both situations, vector addition was performed with a constant grating vector ($\mathbf{k_g}$) and a varied scan beam. In TG case a), the scan beam is E_3 while the transient grating is generated through E_1 and E_2 by $\mathbf{k_g} = \mathbf{k_2} - \mathbf{k_1}$. In rhomb geometry b), the scan beam is E_1, and E_2 and E_3 add to the grating vector ($\mathbf{k_g} = \mathbf{k_2} + \mathbf{k_3}$). Movement of the signal beam E_4 in a) is orientated along the square edge (x-axis) and is much fewer in TG than in rhomb case. In the latter, movement occurs along the square diagonal (dashed line in b)). The two dimensional sketches below indicate the movement of E_4 as red arrows. The length of the green rays does not correspond to the absolute value of the $\mathbf{k}$ vector, but resembles the puncture on a screen far away, like in the recording of Fig. 3.35. In TG, the length of $\mathbf{k_4}$ automatically equals the length of $\mathbf{k_3}$ because the grating vectors add to zero. In the rhomb case however, a frequency conversion occurs. If the scan beam $\mathbf{k_1}$ is red shifted with respect to the grating, the signal beam $\mathbf{k_4}$ is blue shifted and vice versa.

ω_4^{NIR} the signal is located in the corner of the square. However, the signal beam E_4 moves in a different direction when E_1 is swept upon the stationary grating. It moves along the diagonal of the square (dashed line in Fig. 3.45b) for shorter wavelengths E_4^{yellow} than the grating pulses and points far out of the box for longer wavelengths E_4^{IR}. This behavior is also indicated in the two dimensional sketch below as red arrow. The beam movement parallel to the diagonal of the square qualitatively confirms the observations in the laboratory. The frequency increment for each ray in Fig. 3.45b is equal to Fig. 3.45a. The longer axis of the mesh grid means that beam movement is much stronger in b) than in a). In b) the drawing of the simulation ends with beam E_4^{yellow} which is generated by the scan beam $E_3^{(IR)}$ with a wavelength of about 1000 nm. The E_4^{IR} beam is caused by 600 nm wavelengths in the scan beam $E_3^{(yellow)}$. For comparison, drawing the signal beam for 400 nm in the scan beam $E_3^{(400)}$ would not fit on a DIN A page. Such a wide movement was not observed in experiment. After leaving the box marginals, the signal beam broke up in three spots and disappeared. Wavelengths below 600 and above 900 nm were not obtained in this geometry.

As an additional remark it is mentioned the TG approach can be extended to wavelengths other then the VIS range. A setup similar to the TG arrangement was also used for atto second (as) streaking spectroscopy [191]. In this approach one measures the streaked electron kinetic energy spectra by photoionizing atoms with an as XUV pulse in the presence of an infrared laser field. Varying the delay between the XUV and the NIR pulse leads to a sequence of streaked spectra, known as a streaking spectrogram. This spectrogram contains complete phase and amplitude information about the XUV and IR field that can be extracted using FROG retrieval.

Comparison between TG and rhomb arrangement The claim in the previous discussion is, that gating of an octave exceeding WL is obtained from diffraction off a transient grating which is generated by NIR frequencies only. In other words, although the three incoming beams are identical, the 4WM process is non degenerate in case of symmetric WL spectra. From the investigation according to Fig. 3.37 it is seen, that a necessary condition for gating the WL is the presence of an intense NIR gating structure, which is fulfilled in case of asymmetric filamentation broadening.

With this hypotheses, vector addition of the incoming beams $\mathbf{k_1}, \mathbf{k_2}, \mathbf{k_3}$ was performed in Fig. 3.45 in order to simulate the movement of the generated signal beam E_4. The MATLAB program calculates vector addition according to the equations written on top in Fig. 3.45 which means considering the law of conservation of momentum. Simulating a temporal scan of the chirped WL is achieved by changing the length of E_3, but not its orientation. Adding all three vectors leads to a new point in space like shown in Fig. 3.44. The connection line from this point to the origin defines the vector $\mathbf{k_4}$. Thus conservation of momentum is fulfilled ($\Delta\mathbf{k} = 0$). In order to check the conservation of energy, the length difference of the scan -and signal beam ($|\mathbf{k_{Scan}}| - |\mathbf{k_{Signal}}|$) was calculated according to

$$\Delta E_{TG} = \frac{|\mathbf{k_3}| - |\mathbf{k_4}|}{|\mathbf{k_3}|} \tag{3.9}$$

$$\Delta E_{rhomb} = \frac{|\mathbf{k_1}| - |\mathbf{k_4}|}{|\mathbf{k_1}|} \tag{3.10}$$

whereby the difference is divided by the current length of the scan beam for normalization. In TG (rhomb) arrangement $\mathbf{k_3}$ ($\mathbf{k_1}$) is the scan beam. The signal beam is $\mathbf{k_4}$ in both cases. The length difference ΔE_{TG} gives a measure for the energy mismatch in the TG and ΔE_{rhomb} the mismatch in the rhombic configuration. Both energy differences are plotted in Fig. 3.46 versus length of the scan vector, black for ΔE_{TG} and gray for ΔE_{rhomb}. In the degenerate case $|\mathbf{k_{Scan}}| = |\mathbf{k_{Grating}}| = |\mathbf{k_{Signal}}|$ where all four beams are located in the four corners of the rectangle in Fig. 3.45 the energy mismatch is zero $\Delta E_{TG} = \Delta E_{rhomb} = 0$ in both configurations. If the wavelength of the scan

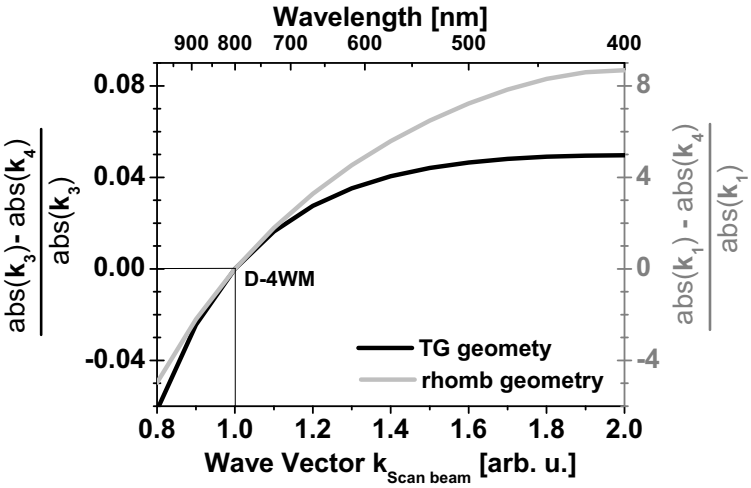

Figure 3.46: Energy mismatch of 4WM for TG (black) and rhomb (gray) geometry in the range from 400–1000 nm. The arbitrary vector length of one corresponds to a wavelength of 800 nm (a length of two to 400 nm). The curves characterize conservation of energy, whose violation is more than two orders of magnitude stronger for the rhombic configuration (right y-axis) than for the TG case (left y-axis). The calculation bases on the assumption of grating generation by a single NIR frequency, which diffracts the whole WL. Moreover, it supposes a given beam geometry ($cf.$ Fig. 3.45), meaning that the signal beam points to a certain point in space.

beam (the length of $\mathbf{k_{Scan}}$) differs compared to the grating beams, an energy mismatch arises for wavelengths shorter and longer than the grating wavelengths as can be seen in the plots of Fig. 3.46. Note that the mismatch in the rhomb case is more than two orders of magnitude higher than for TG, especially at the blue spectral side. Now, with these findings, the difference between both traces in Fig. 3.36a and b) is interpreted. (i) Since the violation of energy conservation is much stronger for broadband gating at narrow gating pulses in the rhomb geometry, this might explain why it was not suitable for octave exceeding gating and why the wavelength range in Fig. 3.36b is less than in a). (ii) The significant difference in the shape of traces can be understood by considering a frequency conversion process in the rhomb case which leads to inelastic scattering other than for TG. Let's assume a wavelength of the grating vectors between 750 and 800 nm. Then, the IR pulse front at 900 nm converts to blue wavelengths at the beginning of the pulse in Fig. 3.36b. At later times, frequencies bluer than the grating pulse convert to red shifted wavelengths at the trailing part. (iii) Of course energy can not be created or annihilated. Thus the energy mismatch might turn to either a change in frequency of the diffracted light or a change of its pointing direction and cause the FROG trace to look different while scanning the WL. Now the question arises, why both traces appear different at time zero. Concerning this matter, one has to keep in mind, that the spectrum exhibits a total width of about 300 nm at this delay position. Thus, the force to compensate the energy mismatch by changing the diffracted frequency in combination with the fact, that the rhomb geometry inherently posses a frequency conversion of the signal beam, suggests why both traces are not equal at time zero or at the signal maximum, respectively. A missalignment of the temporal and spatial overlap of the two grating beams might be a reason too, but is less probable because alignment was always carried out for maximum signal.

In both cases the mismatch towards red shifted frequencies increases more rapidly than to the blue side, as shown in Fig. 3.46. This could denote a limitation of the gatable bandwidth also for the TG case. However, a frequency shift of the diffracted light was not found in the measured TG data in the range from 400–950 nm.

Single beam TG-X-FROG Analysis of the TG-X-FROG traces of Fig. 3.37 and Fig. 3.47 revealed following insights.
(i) The TG-X-FROG mechanism allows a cross-correlation of pulses with different spectral re-

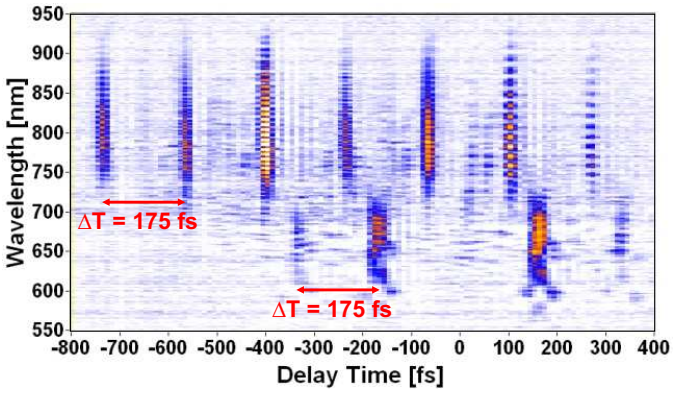

Figure 3.47: Convolution of gating pulses and scan beam in TG-X-FROG after pulse shaping. Starting with the TG-X-FROG trace of Fig. 3.31b, a sinusoidal phase was added to the NIR only. The VIS mask remained unchanged, that is a short pulse. However, due to convolution the sub pulse spacing of the NIR is recovered in the VIS spectrum.

gions within one beam.
(ii) Spectrally narrow gating pulses ($\Delta\lambda = 6$ nm at 845 nm) are able to gate a lucidly broader VIS continuum from 425–675 nm (other experiments showed a gating from 420–750 nm).
(iii) The temporal structure of the gate function convolutes with the function to be gated. This is demonstrated in Fig. 3.47 where a NIR pulse train with a sub pulse spacing of 175 fs and a single, short VIS pulse at time zero were generated with the pulse shaper. A sinusoidal phase modulation with a hight of stroke of 2.4 radian was applied to the NIR spectrum while the VIS part was set for a short pulse. Due to the cross-correlation, the temporal spacing of the NIR pulses is recovered in the VIS part. Noteworthy, the center pulse in the VIS at time zero is missing, although the NIR pulse train exhibits a pulse in its center at about -240 fs. This is because the convolution in the NIR auto-correlation mechanism "fills" the center of the train but recovers the actually blanked pulse in the cross-correlation with VIS part. The blanking of the NIR center pulse results from Eq.(3.3). The spectrum of the gated pulse is not changed thereby.
(iv) The more red shifted the gating wavelengths became, the less energy of the gate pulse is necessary to perform the cross-correlation with the VIS part ($cf.$ Fig. 3.37i). This lead to the observation that the NIR gate can be much weaker than the VIS pulse.
These investigations could be continued by measuring the power dependence of the 4WM signal in the VIS and NIR region. With help of the pulse shaper, the dependence of diffracted VIS light can be measured as function of ingoing VIS and NIR intensity, respectively. Also the irregular diffraction efficiency for the VIS according to Fig. 3.33 could be studied as function of the NIR pulse form and spectral shape.

Chapter 4

NeNePo Spectroscopy of Ag_2 and Ag_3

As introduced in Sec.1.4.3, in the framework of charge reversal spectroscopy one begins with a thermal ensemble of a negative species which is subject to photodetachment, leading to a neutral state from which the final ionization step generates a positive ion (NeNePo). Main aspects are the possibility to investigate ultrafast dynamics in the ground state of the neutral candidate and to resolve the dynamics of catalytic reactions [141, 143]. One advantage in utilizing small clusters in the context as model systems to study catalysis [144], lies in their finite density of states. It allows a diversification of different ultrafast dynamics like geometrical relaxation, internal vibrational relaxation (IVR), various ionization pathways and fragmentation channels. To enhance the selectivity between reactions which are partly competitive, or rather to trace small coherences after the intramolecular collision after the Ag_3 relaxation process, the NeNePo technique was extended by means of excitation with tailored fs pulses in this work. In the case of the silver dimer experiment in Sec. 4.1, an analytical approach, meaning excitation with pulse trains, was carried out. For the more complex case of the silver trimer in Sec. 4.2, a closed loop scheme applying octave spanning WL pulses was utilized.

Experimental conditions Generally, NeNePo spectroscopy is carried out as a gas phase experiment. Since the charged clusters are stored in an ion trap up to the space charge limit at a density of about 10^6 /cm^3 [192], they are assumed to undergo no interactions. This enables fundamental investigations of the current species which are not affected by any environment. As many in-detail descriptions of the used apparatus are available [192–194], only a brief summary will be given here. The provision of Ag_x clusters was carried out with a tandem mass spectrometer ion trap system (which is described in more detail in [193]). Briefly, Ag_x anions were generated in a recently built sputter source [195] and afterwards mass-selected and accumulated in a linear radio-frequency hexadecapole ion trap in which they were irradiated by the shaped laser pulses. The detection of the generated Ag_x cations was achieved through a channeltron behind a second mass filter. The guiding decapoles allow phase space compression of the ions due to focusing through electrostatic lenses and thermalization by collisions with He gas at small pressures ($10^{-2} - 10^{-4}$ Pa). All experiments in this work were carried out at room temperature (300 K).

4.1 NeNePo spectroscopy of Ag_2 with pulse trains

First, a summary on previous Ag_2 single color pump probe experiments carried out in the Wöste group are given in Sec. 4.1.1. The reproduction of former results by a double color excitation are presented first in Sec. 4.1.2. Finally, those experiments are expanded by applying a pulse train with variable sub pulse separation as a pump step in the NeNePo process in Sec. 4.1.3.

4.1.1 Previous work on Ag_2

A dimer is the simplest molecule since it has only one internal degree of freedom, thus IVR does not occur. Ag_2 is a well characterized system, experimentally, $i.\,e.$ through absorption spectra in

Ref. [196], ground state spectroscopy in [197], fluorescence spectra in [198] and resonant two photon ionization [199]). Also several theoretical studies can be found in Refs. [200–202]. According to previous experimental NeNePo work by Socaciu-Siebert *et al.*, Fig. 4.1a shows the NeNePo signal for Ag_2 which was obtained in a one color experiment with pump -and probe wavelength

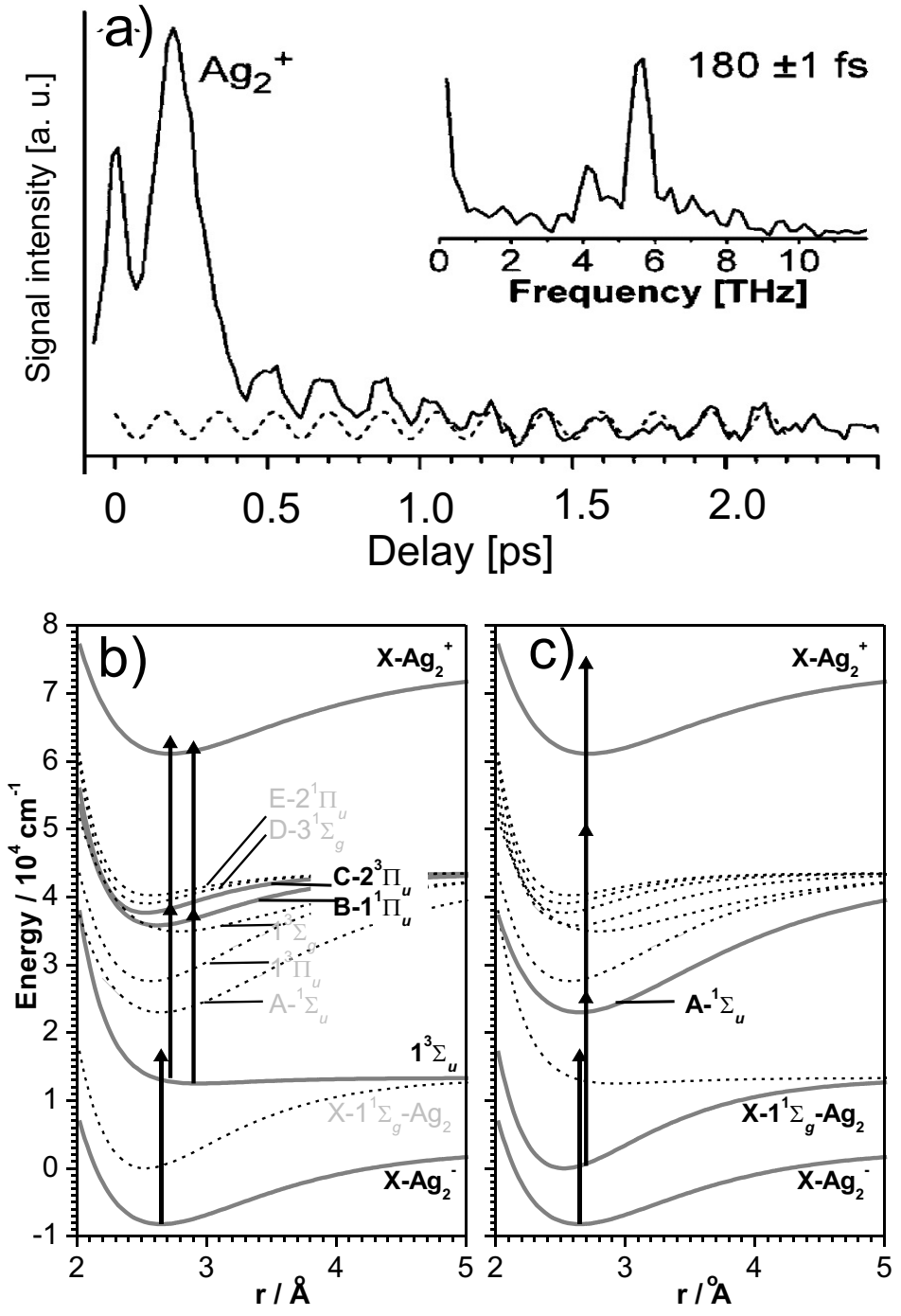

Figure 4.1: NeNePo trace of Ag_2^+ in a), recorded in a one color experiment at a wavelength of 406 nm and 100 K ion temperature (solid line) corresponding to Ref. [141]. The dashed line corresponds to a sine fit to the Ag_2^+ data with a period of 180 fs. This leads to the maximum of the Fourier transformed power spectrum in the inset. b) and c) Potential schemes with two channels indicated for the charge reversal process. The participating PES are highlighted by bold solid lines. For details see text.

of 406 nm (3.05 eV) [141]. At a temperature of 100 K, the population probability in the vibrational ground state ($v' = 0$) of the anion is 96% according to the Boltzmann's distribution. The remarkable features in the solid line of Fig. 4.1a are the high peak at pump probe of 190 fs delay and a weaker oscillatory structure at time scales larger than 400 fs. The evaluation of the oscillation period by Fourier transformation in the inset of a) yielded a maximal value around 6 THz (182 cm^{-1}). This confirms the vibrational period of 180 fs at longer times, which was also found by a sinusoidal fit of the spectrum, shown as dashed line in the main plot of Fig. 4.1a. The peak at time zero corresponds to a multi photon cross-correlation of both pulses.

The explanation of the transient signal is given with the help of the potential energy curves in Fig. 4.1b and c). Single photon photo detachment from the anion creates a vibrational wave packet (WP) on the electronic ground state $Ag_2(X - 1^1\Sigma_g)$ and on the first excited triplet state $Ag_2(1^3\Sigma_u)$ of the neutral dimer. The second transition is also spin allowed since the detached electron can carry the spin of $\pm 1/2\hbar$. While propagating along the triplet potential curve, a population transfer to the cation might take place at two locations via resonance enhanced multi photon ionization (REMPI). This is indicated by the two double arrows in Fig. 4.1b. The $Ag_2(C-2^3\Pi_u)$ and $Ag_2(B-1^1\Pi_u)$ states are the two most probable participants for these two ionization steps, laying close together. This leads to the pronounced maximum at 190 fs delay time in the transient signal. The missing reoccurrence of this high peak indicates, that the WP propagates freely on the dissociative level on the $Ag_2(1^3\Sigma_u)$ state and is thus not bound by the potential. The width of the peak is lucidly broader then the autocorrelation at time zero. This could be an indication for a dispersing WP on the repulsive potential [140].

The second ionization path way is depicted in Fig. 4.1c. Due to the high Franck-Condon factors, vibrational levels from $v = 0 - 6$ are populated on the electronic ground state $Ag_2(X - 1^1\Sigma_g)$ of the neutral [140, 141]. The initial WP is located at the outer turning point of the potential, because the equilibrium internuclear distance is shorter for the neutral than for the anionic ground state. The WP propagates back and forth between the outer and the inner turning point with an oscillation period of 180 fs. Population transfer to the cation requires three photons of 406 nm and occurs when the WP is localized at the outer turning point. Ionization could be resonantly enhanced via the $Ag_2(A - 1\Sigma_u)$ state. The sinus extrapolation of the oscillating structure by the dashed line in Fig. 4.1a shows a maximum at time zero. This confirms, that ionization takes place at the outer turning point and not at the inner one. Ionization at the inner turning point would cause a minimum of the sine fit for time zero, because then the WP would require half a vibrational period to propagate to its inner ionization position. The oscillation and the high peak show up symmetrically also for negative time delays (not displayed in Fig. 4.1a) [140].

4.1.2 Double color pump probe spectroscopy of Ag_2

The current work on NeNePo began as a continuation of the previously shown pump probe excitation on the silver dimer with an optical setup according to Fig. 2.20. It is discussed in detail in the diploma thesis of Juri Demuth [195]. The cluster temperature and the excitation conditions were different compared to the previous work. The pump pulse had a center wavelength of 800 nm (1.54 eV) containing a pulse energy of 10 μJ and the probe pulse remained at 400 nm with 25 μJ. At room temperature (300 K), 50% population remains in the vibrational ground state $v' = 0$ of the anion. About 24% and 11%, respectively, are already transferred to $v' = 1$ and $v' = 2$ [195]. Adjustment of time zero was carried out by THG in a BBO outside the vacuum chamber. Due to the different refractive index, a group delay between the 800 nm pump and 400 nm probe pulse is introduced when passing the entrance window of 2 mm Sapphire. The group delay is given by $\Delta n d/c = 173$ fs with d being the optical path and Δn the difference of the refractive indicees according to Ref. [203].

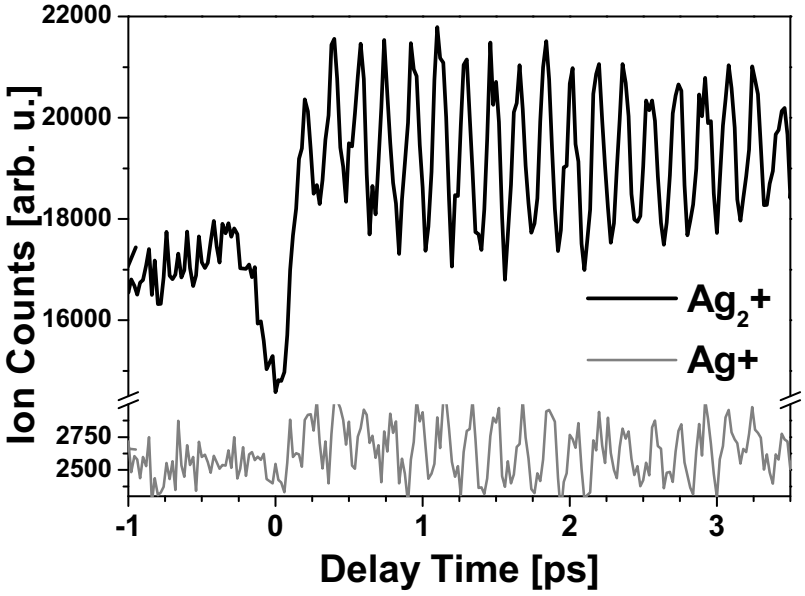

Figure 4.2: Double color pump probe experiment on Ag_2 with 800 nm pump and 400 nm probe wavelength at 300 K. The Ag_2^+ ion signal is given in black and the Ag^+ fragment signal used for control as gray line. Both, parent ion and fragment signal oscillate in-phase with a period of 178 fs which agrees well with previous experiments in Fig. 4.1a. The pronounced Ag_2^+ signal drop at time zero has a total extension of about 360 fs.

The new experimental NeNePo spectrum is given in Fig. 4.2. The black curve shows the Ag_2^+ ion signal and the gray curve the atomic fragment ion Ag^+. The scan step width of the delay stage was 20 fs. When the blue pulse leads, no transient signature for the Ag_2^+ ion signal is observed for negative time delays. Passing through time zero, that means both pulses are present at the same time, causes a strong drop of the Ag_2^+ signal which extends about 360 fs around the zero point. At positive time delays a clear modulation with a period of $182 \pm 8\text{cm}^{-1}$ (178 fs) was evaluated in [195] which very well agrees with the previous results of $185 \pm 1\text{cm}^{-1}$ [141]. The modulation contrast $K = (Max - Min)/(Max + Min)$ in this two color pump probe experiment accounts to 10.5% which is much higher than in the previous experiments in Ref [141]. The Ag^+ fragment signal (gray line) stays constantly at about 5% of the maximum Ag_2^+ signal (black line) and exhibits the same periodicity for positive time delays. It shows a noisy but constant level for negative delay times.

4.1.3 Pulse train excitation of Ag_2

As mentioned in Secs. 1.4.2 and 1.4.1, selective excitation of vibrational modes can be enhanced by tailored laser fields. Especially fs-pulse trains have been utilized to amplify vibrational resonances in favor of a dissipative background [137, 204].

The setup for the pulse train excitation is shown in Fig. 2.20. In this scheme, excitation is carried out with a pulse train at a center wavelength of 800 nm and an envelope width of about 35 nm. The temporal multi pulse structure was achieved by amplitude modulation with the SLM (CRI, 2×128 pixel). Figure 4.3 shows the spectral transmission of the pulse shaper setup. The two gray lines denote minimal and maximal extinction, respectively, for amplitude shaping of an unmodulated single pulse. The black curve shows the transmission function with a peak separation of 8 nm ($\omega = 2.356 \times 10^{13}$ rad/s) corresponding to a temporal sub pulse separation of $\Delta T = 260$ fs. Other than in the case of sinusoidal phase shaping of Fig. 3.30, a sinusoidal amplitude transmission produces only a single temporal double pulse. Since the aim was to generate many sub pulses with a flat spectral phase, a $sin(\omega t/2)^8$ modulation was written as the transmission function in the Fourier plane with the SLM. Inserting the sine function into the argument of an exponential function reduces the spectral width of the individual peaks. This is the reason why the black curve does not reach the gray curve for maximal transmission in Fig. 4.3.

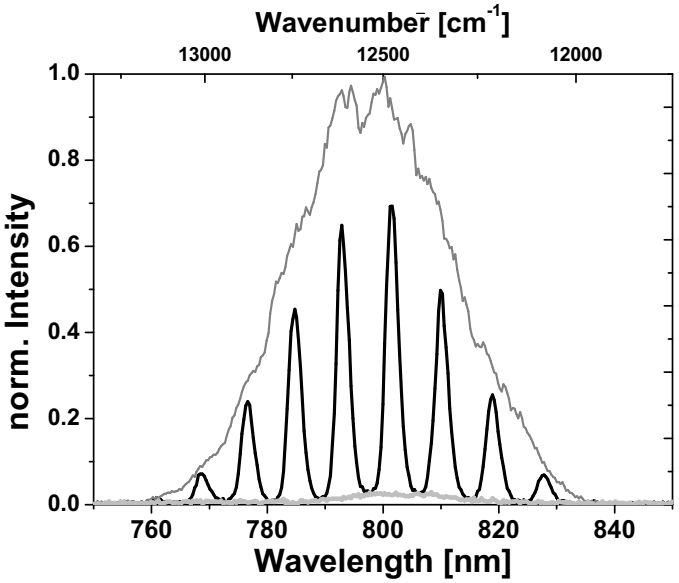

Figure 4.3: Amplitude modulation for Ag_2 with a $sin(\omega t/2)^8$ function to provide a long extended temporal pulse train (black line). According to the Fourier relations of Sec. 1.1.2, the total FWHM of the spectrum defines the pulse duration of every sub pulse, whereas the number of sub pulses increases with narrower spectral peaks. The spectral peak separation is inversely proportional to the temporal separation. The gray curves denote minimal and maximal shaper transmission for a single pulse.

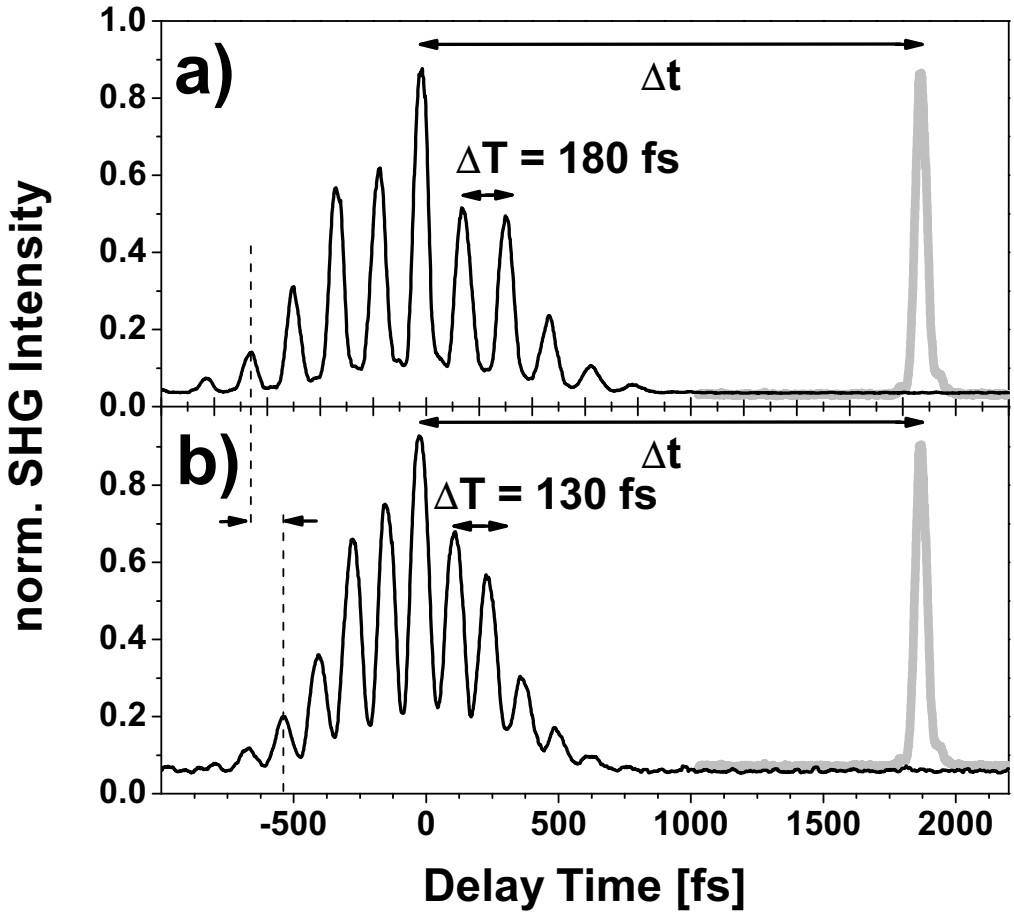

Figure 4.4: Auto-correlation measurements of pulse trains for the Ag_2 pump step (black curve). They are applied for resonant excitation at a center wavelength of 800 nm with sub pulse separation $\Delta T = 180$ fs in a) and off resonant excitation with $\Delta T = 130$ fs in b). The gray curve symbolizes the 400 nm probe pulse where Δt is the time delay between the pulse train maximum and the probe pulse.

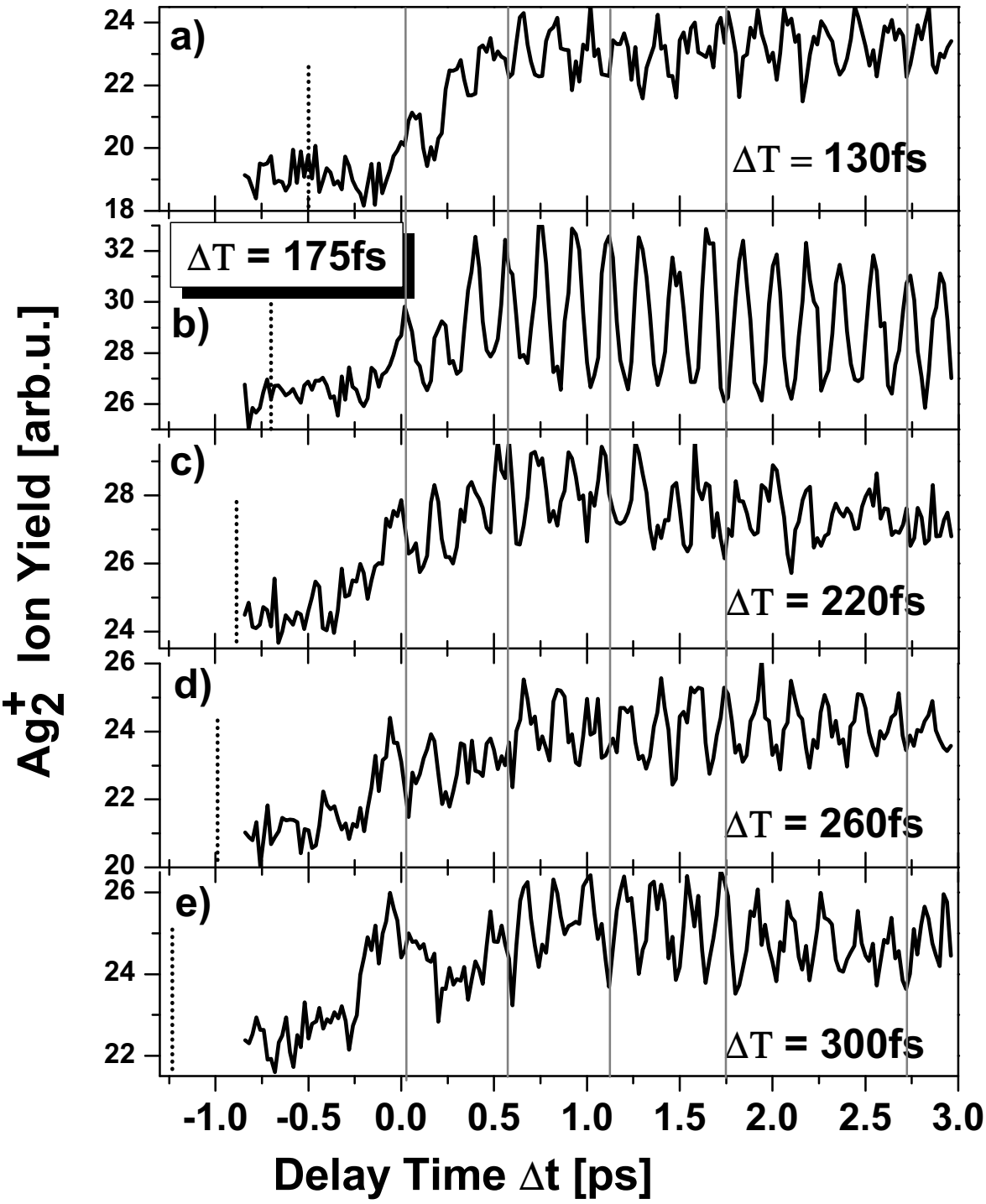

Figure 4.5: NeNePo spectra of Ag_2 with photo detachment by pulse train pump excitation and probing with a single Gaussian pulse ($\lambda_{probe} = 400$ nm). The center wavelength of the pulse train is located at 800 nm and the sub pulse separation ΔT is changed as labeled in the corresponding legends in a)–e). When ΔT matches the vibration period of the electronic ground state ($Ag_2(X - 1^1\Sigma_g)$) of the neutral in b), a clear maximum of the total ion counts and the best modulation contrast arises for the charge reversal process. The dotted vertical lines indicate the center of the corresponding pulse trains.

This peak narrowing causes an increased number of sub pulses as can be seen in Fig. 4.4. The plots show the measured SHG autocorrelation of the pulse train with two different sub pulse separations ΔT. The pulse train in a) with $\Delta T = 180$ fs corresponds to a resonant excitation of the $Ag_2(X - 1^1\Sigma_g)$ ground state dynamics of the neutral dimer. For off-resonant excitation in b) ΔT is shifted to 130 fs. To get the real number of sub pulses the plots of Fig. 4.4 have to be deconvolved, that means the correct number is equal to the measured number of peaks minus two (minus one in case of a double pulse). Thus, typically 10 sub pulses were generated by amplitude shaping in the described manner. The $sin(\omega t/2)^8$ transmission modulation was chosen because it displays a compromise between large number of sub pulses and reasonable laser intensity behind the shaper setup. The frequency argument ω in the sin function can be changed variably with the SLM so that the sub pulse separation is increased in step widths of 10 fs.

Having this capability at hand, the pump probe excitation is modified compared to the former case. It is illustrated as pulse train pump (black line) and time delayed (Δt) probe pulse in Fig. 4.4. The NeNePo transient signals for photo detachment of Ag_2^- with the pulse train and probing by a Gaussian pulse at center wavelength of 400 nm is shown in Fig. 4.5 for various sub pulse separations ΔT in a)–e).

At negative delay times Δt when the blue pulse arrives prior to the pulse train, no modulation is identifiable in all spectra. Time zero corresponds to the situation, when the maximum of the pulse train coincides with the blue probe pulse. In the spectra of a) and c)–e) the anion was excited with a sub pulse separation ΔT of the pump sequence being far away from the vibration period of the neutral electronic ground state ($Ag_2(X - 1^1\Sigma_g)$). The transient signals for positive time delays in plots a) and c)–e) all exhibit a period of about 180 fs which is partially noisy. The periodicity remains constant until the end of the scan at 3 ps regardless of the exciting sub pulse separation ΔT. Only the spectra in Fig. 4.5c loses its modulation contrast almost completely for delays larger than 2 ps. However, the modulation contrast of all spectra is significantly reduced compared to the resonant excitation in b), where a sub pulse separation of 175 fs was used for the photo detachment step. In this case, the ion counts reach their maximal level and the modulation contrast exceeds the other cases by far. The contrast in b) is 10.4% and therefore equal to the pump probe excitation in Fig. 4.2. When comparing the relative positions of the modulation maxima in all spectra of Fig. 4.5, a phase shift for the cases a) and d)–e) with respect to b) is visible. This spectra with ΔT = 130, 260 and 300 fs obey a phase shift of 180°. The NeNePo spectrum in c) with ΔT = 220 and the lowest modulation contrast stays in phase up to 1.26 ps, but becomes chaotic afterwards. In order to follow the maximal ion signal as a function of sub pulse separation ΔT, a resonance curve was measured in Fig. 4.6. Therefore, a fixed time delay $\Delta t = 1860$ fs was set between the blue probe

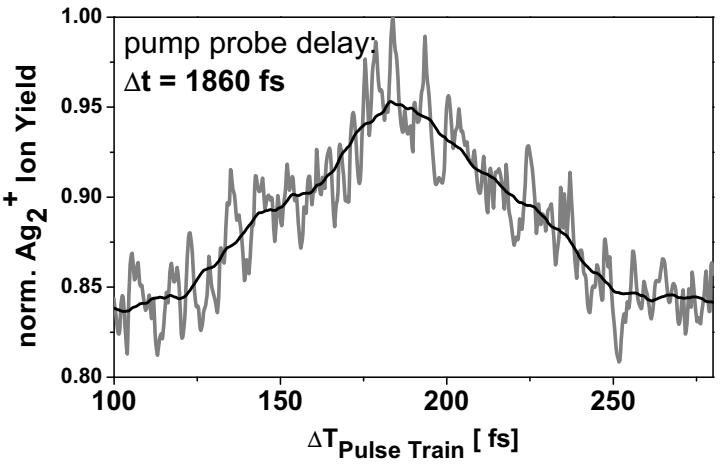

Figure 4.6: Resonance curve for charge reversal on Ag_2. The time delay between the maximum of the pulse train and the probe pulse was fixed at $\Delta t = 1860$ fs, where the NeNePo spectrum has a modulation maximum. The Ag_2^+ ion yield is plotted $vs.$ sub pulse separation ΔT which is varied from 120–260 fs. It exhibits a maximum at about 184 fs. Measure data are given in gray and smoothed (average over 10 data points) curve in black.

pulse and the center of the pulse train, as schematically drawn in Fig. 4.4. At this Δt, the Ag_2^+ signal reaches a modulation maximum. Such a long time delay was chosen to guarantee, that most of the sub pulses have been acting before the probe pulse sets in. In the case of resonant excitation, meaning that the sub pulse separation is equal to the vibration period of the neutral ground state, all nine sub pulses having past before the probe pulse acts on the cluster in case of excitation with $\Delta T = 180\ fs$. Recording the resonance curve of Fig. 4.6 was carried out by increasing the sub pulse separation ΔT from 120–260 fs in steps of 10 fs. The signal has a bias level of 80% for off resonant excitation and increases up to 95% in the resonant case at about 184 fs.

4.2 White light shaping of Ag_3 - NeNePo

The previously described progress of the NeNePo technique (Sec. 1.4.3) consisted in introducing parametrically shaped pump pulses for the photo detachment step in the form of pulse trains. By matching the sub pulse separation to the vibrational period of the ground state in the neutral species, a control of the charge reversal process of Ag_2^- was achieved (Sec. 4.1.3). Increasing the cluster size of the linear diatomic Ag_2^- by one atom creates the linear trimer Ag_3^- [10]. Photo detachment from the anion induces ultrafast nuclear dynamics including a geometrical relaxation to a triangular structure followed by strong IVR [11, 12]. To get a deeper insight on the evolution of the neutral species, an improvement of the coherent control method (Sec. 1.4.2) by means of arbitrary shaped WL pulses reaching from 450–950 nm was developed (Sec. 2.3). This SC is attained throughout filamentation in air at atmospheric pressure (Sec. 2.1.2) and subsequently tailored in an octave exceeding pulse shaper (Sec. 2.3). The WL pulses are characterized in a transient grating setup (Sec. 2.2.2) which enables cross correlation measurements (TG-X-FROG) within one single beam, only when an appropriate phase function is applied on the shaper (Sec. 3.4.2). In a feedback loop experiment, charge reversal of Ag_3^- was carried out on time scales, significantly shorter than the evolution of the IVR process. The optimized pulse structures exhibit ultrafast time sequences much shorter than observed in previous pump-probe experiments [10, 18, 19, 205, 206]. The free optimization of the entire spectrum was supplemented by also shaping selected spectral regions and by applying parametric WL pulse forms. Further on, different starting conditions for the evolutionary algorithm (EA), $i.\ e.$ different initial guesses, were tested. Out of this, a new successive optimization procedure is presented with the measurements of Exp. VIII. The new results of Sec. 4.2.2 will be discussed in Sec. 4.3.2 in the context of previous work on Ag_3 which is summarized in the following section.

4.2.1 Previous work on Ag_3

Other than in the foregoing NeNePo investigations of diatomic Ag_2 (Sec. 4.1), the three atomic Ag_3 cluster undergoes geometrical changes after photo detachment with the first fs laser pulse. NeNePo spectroscopy on Ag_3 has been firstly carried out by Wolf $et\ al.$ in the Wöste group [10]. Supplementary experiments followed, in which the dependence on probe wavelength and cluster temperature was investigated [18, 19, 205, 206]. While the anion Ag_3^- has its lowest energy in a linear configuration, the neutral Ag_3 takes a triangular configuration for minimum energy and never returns back to the linear chain. That means, a strong geometrical change is expected to occur. In addition to experimental investigations, this view on the cluster dynamics has been supported by semi classical calculations of Hartmann $et\ al.$, who yielded a theoretical analysis of the NeNePo transient signals of Ag_3 [11, 142]. A comprehensive background on the geometrical and electronic structure of Ag_n clusters as well as simulations of NeNePo experiments on Ag_3 was carried out, among others, in the group of Bonačić-Koutecký [145, 200–202]. Full three-dimensional quantum mechanical calculations were carried out by Andrianov $et\ al.$ [12].

The symmetric structure of the neutral Ag_3 allows a decomposition of nuclear dynamics into

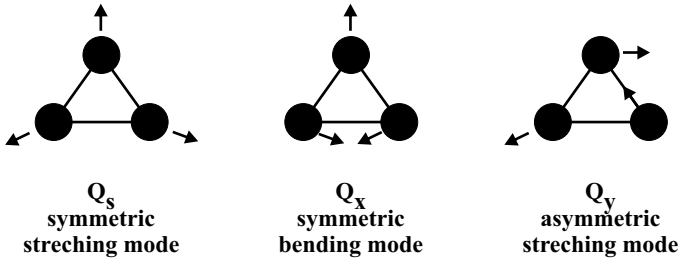

Figure 4.7: Schematic representation of the normal modes of the triangular Ag_3. The arrows indicate the deflections of the atoms in the corresponding mode.

three normal modes, as shown in Fig. 4.7. These modes of the obtuse triangular structure are the symmetric stretching mode (Q_s), the symmetric bending mode (Q_x) and the asymmetric stretching mode (Q_y). Since the WP propagation mainly takes place along the steepest gradient of the PES, the multi dimensional PES can be reduced to a one dimensional cut along a certain reaction coordinate. Figure 4.8 represents such a one dimensional cut along the $Q_r = (Q_x^2 + Q_y^2)^{1/2}$ coordinate according to [11]. It displays the initial anionic ground state $X - Ag_3^-$ and the cationic target state $X - Ag_3^+$ both as bold gray curves. The bold black line displays the ground state of the neutral Ag_3 and the thin black curves in between correspond to electronically excited states of the neutral cluster. The fact that this reduced, one dimensional representation causes a loss of information can be seen by the barrier in the neutral ground state $^2B_2$ (bold black line), marked by the small arrow. By taking into account the Q_s coordinate, a monotonic decreasing path opens up which is indicated as dashed line, followed Ref. [19, 205].

With the help of the energy scheme of Fig. 4.8, the observed multi state dynamics will be explained in the following. All existing pump probe excitations follow the scheme in Fig. 4.8, where optical transitions are represented by the two time delayed (Δt), gray vertical arrows pump and probe. Starting from the Ag_3^- ground state equilibrium position in linear chain configuration, a pump pulse (bottom arrow) transfers population to the ground state $^2B_2$ of the neutral cluster. According to the Franck-Condon principle, the fs laser excitation is indicated vertically, meaning that on the time scale of the electronic excitation, the nuclei are considered to remain in their linear configuration. This, however, corresponds to a highly excited vibrational state of the $^2B_2$, since its minimum energetic configuration is at $Q_r = -0.22$ Å in the triangular configuration. Geometrical relaxation from this non equilibrium position $Q_r = -2.73$ Å of the nuclei predominantly takes place along the Q_x coordinate [205]. Inclusion of the Q_s coordinate gives rise to the black dashed line added to the ground state potential of $^2B_2$ in Fig. 4.8. The potential hill along the Q_r coordinate can be overcome in this way [205]. During the geometrical relaxation, the asymmetric stretch mode Q_y does not play a significant role [12]. A subsequent probe pulse (top arrow) ionizes the system to the cationic ground state $X - Ag_3^+$, which is experimentally detected via second mass filtering.

In order to draw conclusions from the measured cation signal on the nuclear dynamics in the neutral ground state, it is important to consider the different possibilities for the ionization or probe step, respectively. The energy difference between one point on the PES of the neutral $^2B_2$ in Fig. 4.8 and the vertical point above on the PES of the cation $X - Ag_3^+$ is equal to the ionization potential (IP) for this specific configuration along the Q_r coordinate. Since this energy difference is dependent on the reaction coordinate Q_r, the time delayed probe pulse can sensitively probe the instantaneous cluster configuration. At $\Delta t = 0$, where the neutral cluster is still in a linear configuration, the IP is highest ($\mathrm{IP}_{lin} = 6.67$ eV [11, 142, 145]). Starting in the non equilibrium position, the linear cluster starts to bend. Thus the IP decreases with increasing pump probe delay Δt and reaches its minimum ($\mathrm{IP}_{tri} \approx 5.73$ eV) at $\Delta t \approx 700$ fs. In between this time, the cluster has undertaken a geometrical relaxation from the linear to the obtuse triangular structure as indicated by the two geometries in Fig. 4.8. Subsequent to the collision of the terminal atoms (at $Q_r =$

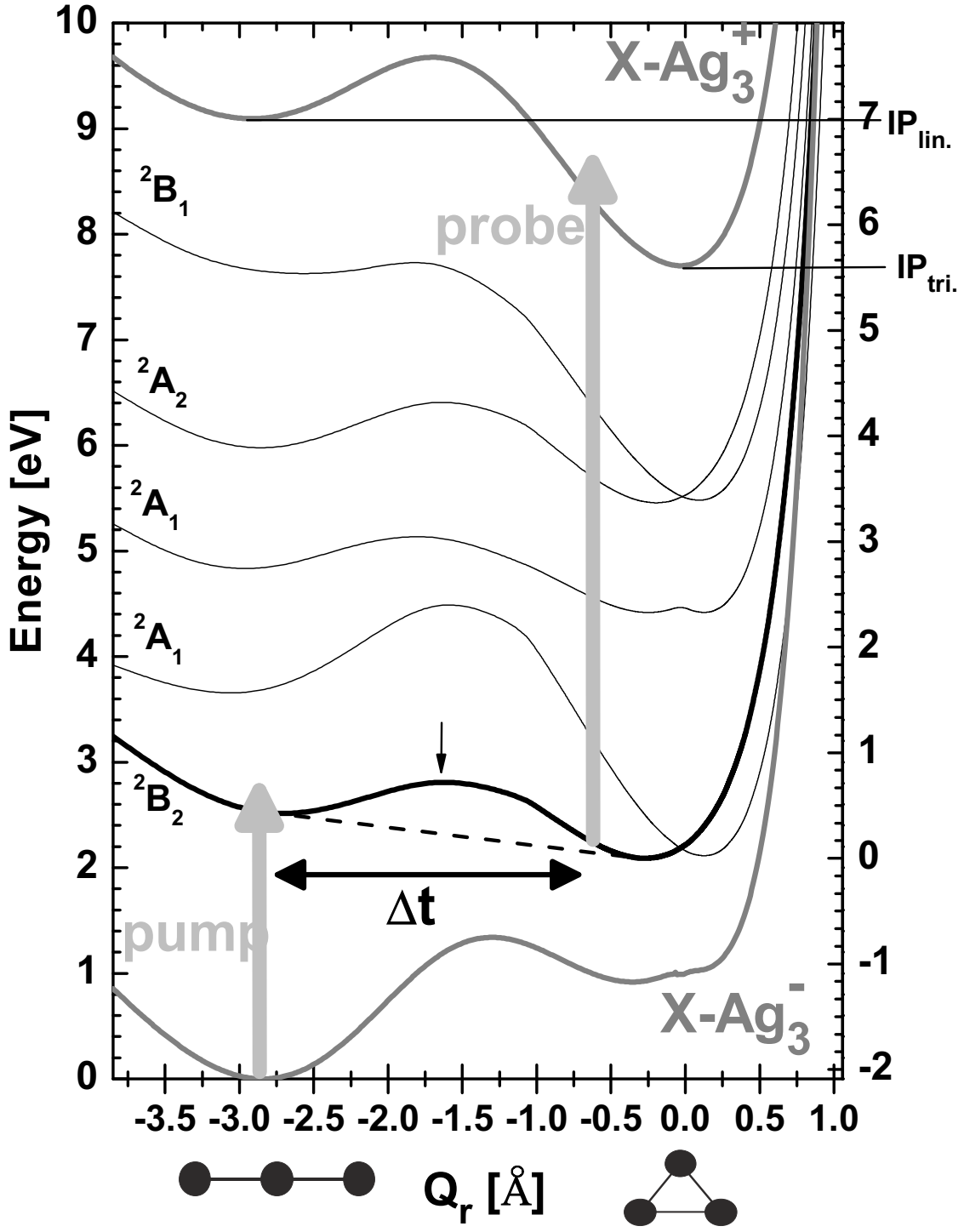

Figure 4.8: The geometrical relaxation of the neutral Ag_3 (black line) can be best rationalized along the reaction coordinate $Q_r = (Q_x^2 + Q_y^2)^{1/2}$ [11]. It involves the bending of the linear chain to an obtuse triangular structure on a time scale of ≈700 fs, depending on the cluster temperature. Calculations of the PES according to Ref. [11] for the electronic ground states $X - Ag_3^-/X - Ag_3^+$ are plotted as bold lines, where the ground state of the neutral $^2B_2$ is plotted in black. Higher lying excited states of the neutral cluster are given as thin black lines. A schematic pump probe excitation is indicated as thick gray arrows. The global minima of the cationic ground state assumes equilateral triangular structure.

-0.22 Å and $\Delta t \approx 700$ fs), the vibrational energy of the Q_r mode can be redistributed along the other two modes, leading to internal vibrational redistribution of energy.

If the photon energy of the probe pulse exceeds IP_{lin}, the cluster is ionized at every point on the PES, thus no information on the cluster dynamics can be gained. But if one keeps the photon energy below IP_{lin} and in the case of resonant ionization, a variation of the probe wavelength allows the assignment of the probe position on the PES. Then, the ionization enhancement as a function of wavelength can be interpreted in two ways. First, since the ionization step is usually achieved via two photon excitation, the first photon might access one of the excited states of the neutral resonantly (thin black lines in Fig. 4.8) and thus enhances the cation signal. Second, a perfect matching of the photon energy to the IP of the cationic cluster ($2 \times \hbar\omega_{photon} = \mathrm{IP}$), could lead to an enhancement due to a high Franck-Condon overlap of the neutral and the cationic ground state wave functions. The latter case, where the released electron carries no kinetic energy is referred to as zero kinetic energy electron (ZEKE)-NeNePo [11, 142, 207]. In general the electron will carry away kinetic energy, whereby the incorporation of the continuum states leads to a temporal signal broadening, thus to a loss of information.

To give an example for the mentioned resonant ionization step, the most recent NeNePo pump probe experiments on Ag_3 are presented in Fig. 4.9 according to Ref. [19]. The time dependent Ag_3^+ yield is given for various ionization wavelengths. The center wavelength of the pump pulse leading to photo detachment was fixed at 400 nm with a duration of 100 fs, denoting that one photon of 3.1 eV considerably exceeds the vertical detachment energy (VDE) of 2.45 eV. Due to negligible Franck-Condon factors for excitation around 3 eV, it is inferred that the excess photon energy above VDE is transferred to kinetic energy of the ejected electron, while the initial vibrational distribution of Ag_3 is essentially determined by the vibrational overlap between Ag_3^- and Ag_3 [19, 142]. The probe pulse with a duration of 120 fs was varied from 384–347 nm in the corresponding plots which also means a two photon probe step. This set of measurements was chosen to use the $^2A_2$ state in Fig. 4.9 as intermediate resonance. In all cases the signal exhibits a minimum at time zero and rises steeply to a maximum at $\Delta t =$ 600–700 fs. Then it converges to a constant value at about 8 ps. Similar to previous, non resonant ionization experiments [10], in no case oscillatory behavior of NeNePo spectrum was found. The authors explain the small modulations at $\Delta t \geq 700$ fs as a change of the potential energy difference between the ground state and the $^2A_2$ excited state of the neutral Ag_3 along the relaxation path way. A difference occurs in the separation of the rising slope with respect to time zero with increasing pump energy. It gradually moves towards $\Delta t = 0$ for shorter probe wavelengths. These measurements together with calculations in the group of Bonačić-Koutecký confirm the picture of a geometrical relaxation process after photo detachment [12, 145]. Both terminal atoms of the linear neutral cluster start to bend to reach a triangular geometry after their collision.

The intramolecular collision time for a cluster ensemble at 300 K is determined to be 710 fs [19, 142]. At the same time, this collision induces IVR and transfers kinetic energy to the symmetric stretching mode Q_s, see Fig. 4.7. About 250 fs later, the antisymmetric stretching mode Q_y is also excited and the IVR process is completed on the time scale of $\approx$ 1.6–1.8 ps. Generally, for a lower cluster temperature of 50 K, the same dynamics takes place but are shifted for about 250 fs towards later times. However, the details in dynamics differ for the mentioned temperatures after the onset of IVR. The question of remaining coherence after the collision strongly depends on the cluster temperature [11, 142]. At low temperature of 50 K, the simulated trajectories stay bundled in phase space immediately after the collision leading to oscillations predominantly along the stretching coordinate Q_s, exhibiting more pronounced resonant IVR than for a cluster ensemble at 300 K. Beyond the 2 ps time scale dissipative IVR distributed the kinetic energy along all three modes which from then on remain in a vibrational equilibrium.

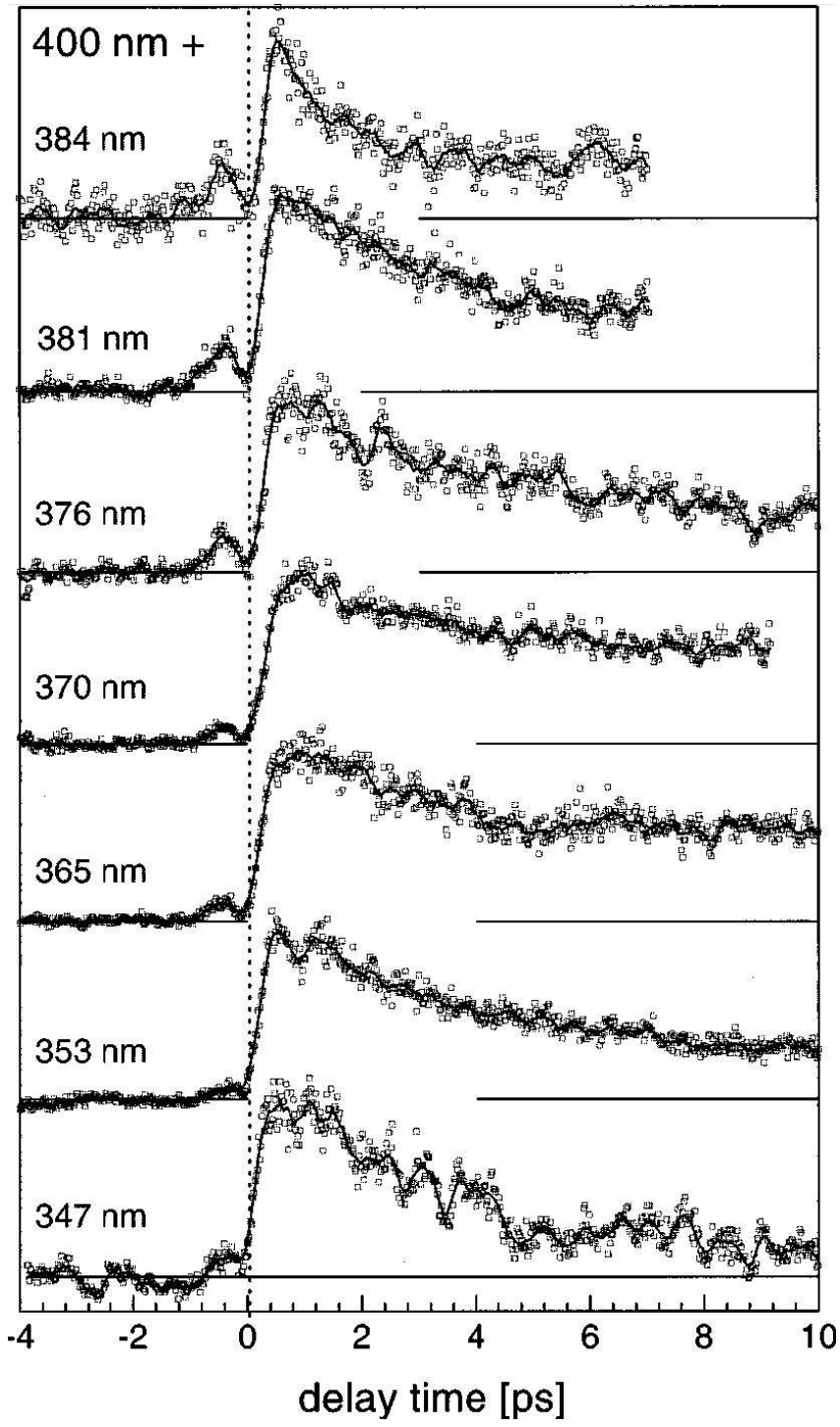

Figure 4.9: Set of double color pump probe measurements on Ag_3 NeNePo with varying probe wavelengths according to [19]. Taking advantage of the resonance with the $^2A_2$ state of the neutral cluster. The pump step at 400 nm requires one photon and various the probe wavelengths are indicated in the plots. Generally, the rising slope within the first 700 fs is assigned to the geometrical relaxation. A oscillatory structure after the atomic collision could not be identified for probing in the range of 347–384 nm. The authors assign the small modulations to potential energy differences between neutral ground- and intermediate excited state $^2A_2$.

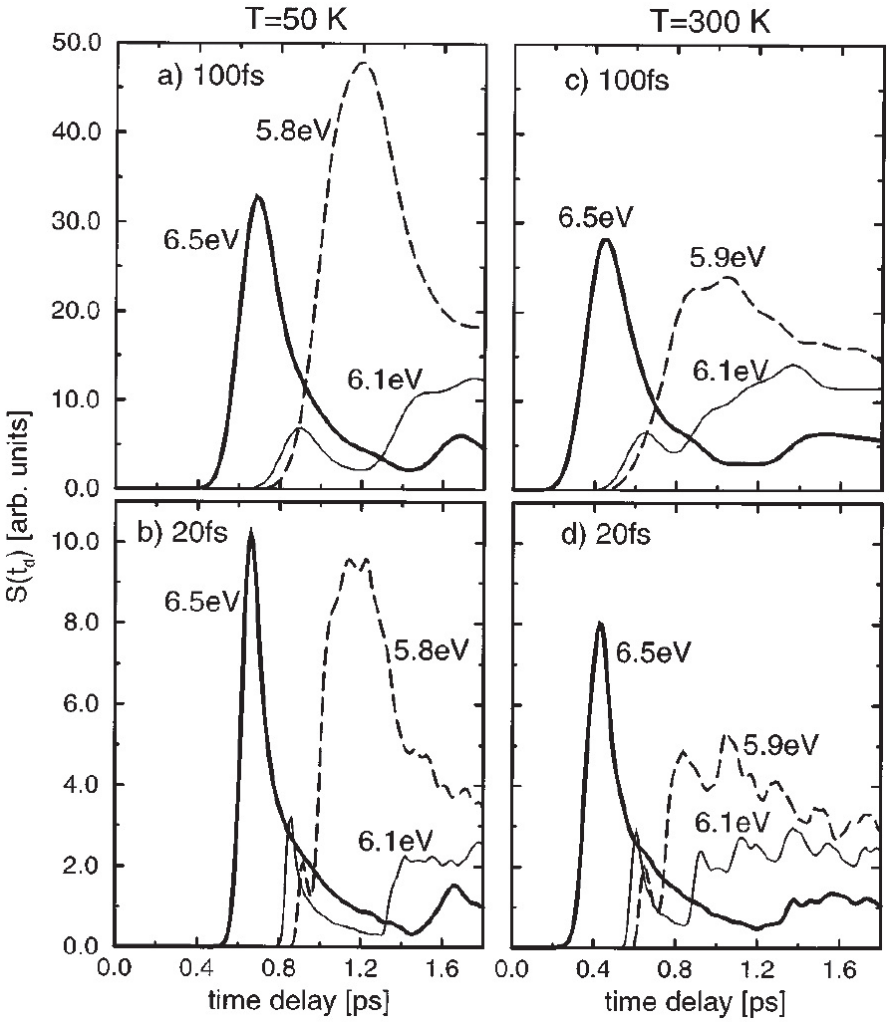

Figure 4.10: Ag_3 NeNePo-ZEKE spectra for an ensemble temperature of 50 K (left side) and 300 K (right side) according to [11, 142]. The pump pulse is assumed to be infinitely short whereas the probe pulse is 100 fs in the upper row and 20 fs in the lower one. The corresponding probe energies are labeled in the plots a)–d). The counterintuitive result in d) is, that after the intramolecular collision coherence can be traced by the distinct oscillations for the hotter clusters rather than for the initially cooled system in b), when the detection step is as short as 20 fs. This is seen by the oscillations of simulated Ag_3^+ signal as dashed and as thin solid line in d). Probing at 6.5 eV corresponds to a three photon step at a wavelength of 574 nm and 5.9 eV can be bridged by three photons of 630 nm.

Up to now, no oscillatory transients as an indication for coherent effects after the onset of IVR were observed in existing experiments [10, 18, 19, 205, 206]. However, the simulations of Fig. 4.10 show pump probe signals with a rich structure in d), which will be explained in the following. These spectra provide the motivation for the investigations with the WL shaper of this work. The prerequisites in these calculations are NeNePo-ZEKE conditions and the assumption of an infinitely short pump pulse. The latter denotes, that the classical phase space density of the Ag_3^- anion at a given temperature is transferred to the PES of the neutral cluster and then propagated classically on the multi dimensional PES. Calculations of the transient cation signal Ag_3^+ for an initial temperature of 50 K are presented in Fig. 4.10 in the left a) and b) and for 300 K in the right column c) and d), respectively. The probe pulse duration in the upper row a) and c)

is 100 fs and 20 fs in the lower row b) and d). Different line styles thereby represents probing at 6.5 eV (bold solid line), at 5.8 and 5.9 eV (dashed line) and at 6.1 eV (thin solid line). The high energy of 6.5 eV probes the geometrical relaxation whereas the lower energies probe the evolution during and after the IVR process, induced by intra-cluster collision. For detailed description of the corresponding spectra the reader is referred to the discussion in Refs. [11, 11]. Surprisingly, a pronounced vibrational coherence occurs as a modulation of the transient signal for an initial cluster temperature of 300 K in Fig. 4.10d but not, as one would expect, at 50 K in b), when probed at 5.9 or 6.1 eV, respectively. Certainly, this behavior is only observed in the presence of a very short pump pulse of 20 fs. The coherence effects are washed out in case of pump pulse durations of about 100 fs in c).

In the light of these simulations in combination with previous double color pump probe results [18, 19], the utilization of the newly developed WL shaping setup is motivated. It provides few cycle pulses, as the most reasonable experimental realization of an infinitely short pump pulse. On the other hand, the possibility of freely choosing the right probe wavelength at any desired time might satisfy the NeNePo-ZEKE condition, denoting a maximum overlap between the wave function of the neutral and cationic cluster. Since the WL setup does not operate in the deep UV spectral region, the probe step requires three photons $\omega_{probe} = 3 \times \omega_{laser}$. However, the energy range from 5.9–6.5 eV corresponds to a three photon excitation in the wavelength range from 630–574 nm which is easily accessible with the WL setup. To cover the same vertical transition with 800 nm radiation, about 4 photon are needed.

4.2.2 White light pulse forms for Ag_3 NeNePo

From this previous experiments where the dynamics of Ag_3 were intensively studied by well established pump probe methods, the stimulus to apply the closed loop scheme was to get a grip on the coherences remaining after the intramolecular collision, as depicted in Fig. 4.10d. Therefore, the search space for the EA was extended to an octave of frequencies by filamentation in laboratory air. The conceptional layout of the experiment is depicted schematically in Fig. 4.11. It basically merges the techniques of WL generation, pulse shaping and cluster spectroscopy in an rf-ion trap. Performing the "closed loop" experiment according to Fig. 1.18 is realized with trapped Ag_3^- ions which represent the quantum target. Its change of property means a change of the charge state from minus to plus. Thus, the observable is the amount of Ag_3^+ signal measured in the channeltron detector. It serves as feedback signal for the EA, provided with the following attributes. The number of parents was set to 30, the initial mutation rate typically was 0.008, the mutation parameter was set to 0.25. The influence of those parameters on the evolution of the optimization is described in great detail in Ref. [16]. All optimizations were carried out with one survivor, $i.e.$ the best of the former parents remained unchanged in the next iteration. Furthermore, the option to start with an initial guess is implemented. All closed loop experiments on Ag_3 are obtained by

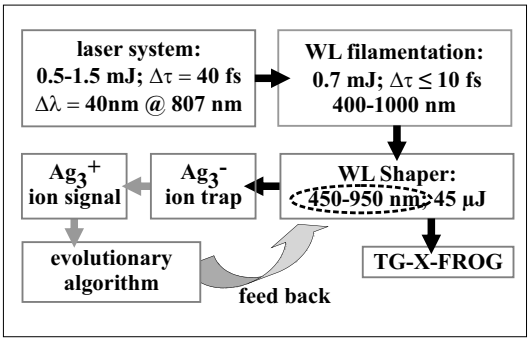

Figure 4.11: Schematic layout of the Ag_3 "closed loop" experiment according to Fig. 1.18. The quantum target were Ag_3^- ions whose charge reversed species Ag_3^+ denoted the observable for the free optimization of the spectral phase in a range from 450–950 nm. The variation of experimental conditions (dashed line) laid in the provision of different spectral ranges for optimization. $\Delta\tau$ and $\Delta\lambda$ denote the FWHM of the pulse duration and spectral width.

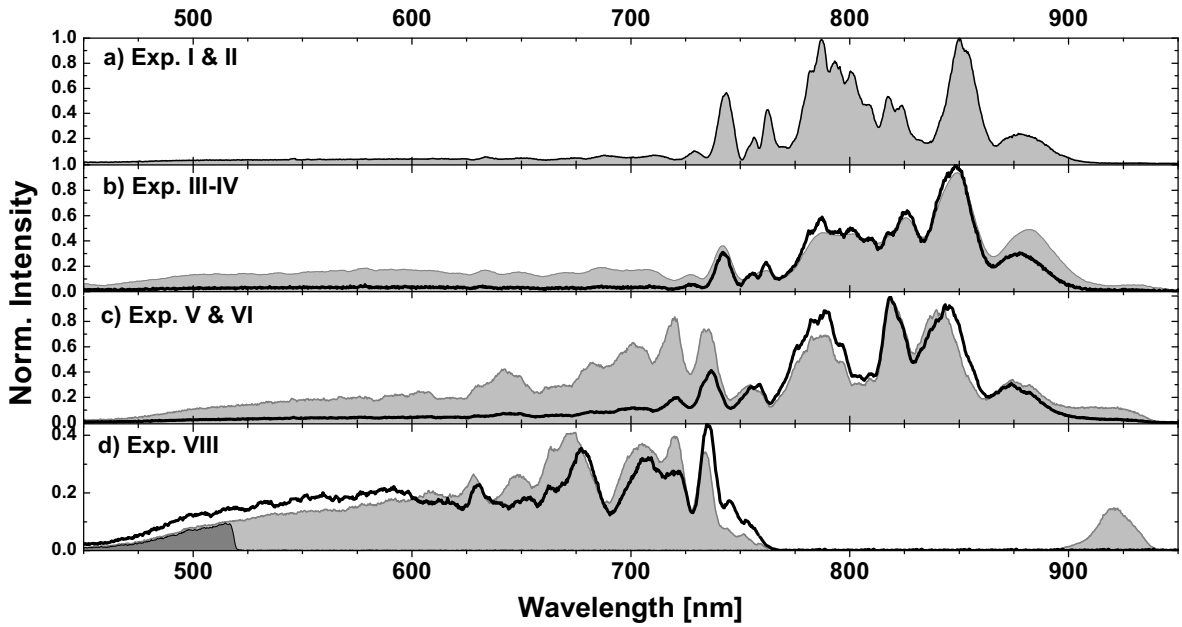

Figure 4.12: Different excitation spectra provided for free optimization of spectral phase in NeNePo spectroscopy of Ag_3-. All spectra are taken after the shaper setup but without phase modulation. a) plots a typical WL spectrum of filamentation air at atmospheric pressure, as used in Exp. I & II. b) shows a spectrum before filtering (black line) and with subsequent filtering (gray filling), according to Fig. 2.14. c) gives a WL spectrum with additional enhancement of the VIS part as black line. Additional filtering provided the most uniform octave spanning spectrum, shown as gray filling in c). Referring to c), spectral slicing enabled shaping of selected frequency regions like shown in c). The slicing was achieved by manual blocking. All spectra are normalized to their corresponding maximum in the NIR. For details see text.

free optimization with the measured amount of the Ag_3+ ion signal as feedback for the EA. The amount of ion signal was increased by optimizing the spectral phase of the WL spectrum. Three different starting conditions for the EA were tested in the following experiments which were either random noise, a certain initial guess or the unshaped mask. However, the starting conditions differed in their optimized spectral ranges and power spectral densities of certain wavelength areas, as shown in Fig. 4.12. In order to trace different excitation pathways, the spectral content applied for NeNePo on Ag_3 was modified according to the plots in Fig. 4.12a–c). The relevancy of each respective spectrum is explained in the paragraphs for the corresponding experiments. To facilitate the assignment of the different experiments, they are labeled **Exp. I–VII** and are presented in a purposive order. It begins with the unshaped filament output (Exp. I), followed by solely shaping the NIR region (Exp. II) to test the whole closed loop scheme and later on applying the full spectrum (Exp. III-VI). Finally, only parts of the entire spectrum were utilized for free optimization (Exp. VII & VIII).

Typical values for the pulse energy after passing the complete optical setup are $\approx$ 40-50 μJ, depending on the selected spectrum. The maximum transmission of the WL shaper is 31% for the integral spectrum spanning 450–950 nm. Focusing the slightly diverging WL beam with a silver mirror (f = 1 m) into the vacuum chamber resulted in an effective focal length of 1.15 m. Thus a beam diameter of 12 mm at the focus mirror generates a focal radius of r_{NIR} = 49 μm at 800 nm and a VIS focus being 20 % smaller with a radius of r_{VIS} = 40 μm at 650 nm.

As carried out in Secs. 3.4.2 and 3.5.3, the unique properties of 4WM with asymmetric WL

allow to perform a TG-X-FROG measurement within one single beam. This new invention was utilized to characterize the results of WL optimization unambiguously. Several significant TG-FROG traces were selected to retrieve phase and intensity of the shaped WL pulse. Although the mechanism is equal to a cross-correlation measurement, an X-FROG retrieval algorithm for TG-FROG traces was not yet at hand. However, the PCGP algorithm (Sec. 1.3.2) for inverting FROG traces facilitates a phase retrieval in a way where the gate pulse is a function of the probe pulse. The good quality of this "blind" retrieval can be seen by comparing retrieved (black lines) and projected intensity (red lines) in Figs. 4.13 and 4.19

Exp. I First the unshaped WL output is characterized by the results in Fig. 4.13a and b), before discussing the various conditions at which optimization of the Ag_3^- NeNePo signal was carried out. This plot shows the joint time-frequency representation as a TG-FROG trace of the uncompressed WL after passing the shaper setup (including the SLM set to full transmission). The corresponding temporal representation of the pulse is given above. In the trace, one recognizes the intense NIR part with perceivable temporal as well as spectral modulations. The latter are also apparent in the direct measured spectrum of Fig. 4.12a. Such a distorted NIR pulse structure typically emerges from the WL filaments when emphasis is made on achieving a preferable large bandwidth. The unmodulated VIS part (450–700 nm) obeys a primarily linear chirp, $i.e.$ a quadratic spectral phase in this region ($cf.$ Fig. 3.20b). The positive chirp is found as retrieved quadratic temporal phase, depicted as green plot in Fig. 4.13a. The black line is the retrieved temporal intensity and the bold red line denotes the projection of the raw data of the trace onto the time axis. This excitation pulse of Fig. 4.13a/b will be referred to as the unshaped case in the following. In every respective optimization experiment, this unshaped case denotes a reference to which the ion signal is normalized. Thus, different efficiencies for charge reversal by different optimized pulse shapes are expressed with respect to the unshaped mask to enable comparability.

Transmitting the full spectrum according to Fig. 4.12a lead to a pulse energy of 60 μJ at the sample containing 14% in the VIS region from 450–730 nm (7.8 μJ). The FWHM duration for the NIR part is about 100 fs and about 200 fs for the VIS part. Giving consideration to the different focal lengths and pulse durations in the NIR and VIS, the corresponding intensities and electric field strenghts, respectively, can be estimated to:
$I_{NIR} = 70 \times 10^{11}$ W/cm^2, $I_{VIS} = 7.9 \times 10^{11}$ W/cm^2, and
$E_{NIR} = 7.2 \times 10^9$ V/m, $E_{VIS} = 2.4 \times 10^9$ V/m.

Exp. II Figure 4.13c/d displays the first optimization which was carried out applying the power spectrum of Fig. 4.12a. From this octave, shaping was carried out in the wavelength region from 700–950 nm only. That means, wavelengths from 450–700 nm passed the shaper without modification. Thus the VIS trace is equal to the VIS part of the trace in Fig. 4.13b. The NIR components in c) are clearly compressed at -70 fs. Since the plots are normalized to the maximum, the VIS tail in c) only seems weaker than in b). In c), optimization began with random phase noise. During optimization the ion signal increased by one order of magnitude, as is seen in the optimization curve of Fig. 4.14a. It shows the evolution of the best (black line), mean (red line) and worst (green line) individuals during the 83 iteration steps. The optimization was stopped after the signal ceased rising. Sharp spikes appearing in the curves can be attributed to electronical noise rather than to a change in ion signal.

The unshaped trace in Fig. 4.13b exhibits a positive chirp. Now, the compressed, clean NIR pulse in c) even exhibits a small negative prechirp. This is better visualized in the magnified trace of Fig. 4.14b, where a fine scan was carried out. The retrieved temporal phase (green line in the time plot of Fig. 4.13d exhibits an almost linear ramp (due to the coarse resolution) for the short NIR pulse and also at negative time delays from -500 to 0 fs. The phase in the VIS tail from 0–600 fs keeps its quadratic behavior corresponding to linear chirp. Remarkably, the compressed NIR pulse is not only negatively chirped but also advances the VIS tail for about 200 fs. This is higher compared to b) where the temporal distance of the maximum at 800 to 650 nm is about 100 fs. Further on, tiny differences compared to the unshaped case in b) are highlighted by gray dashed ellipses in trace of Fig. 4.13c. Their assignment is discussed in the corresponding part of Sec. 4.3.2. Charge reversal with the mask in c) enhanced the Ag_3^+ signal for 10% compared to the unshaped pulse in b). In anticipation of the following experiments, no temporal structures were

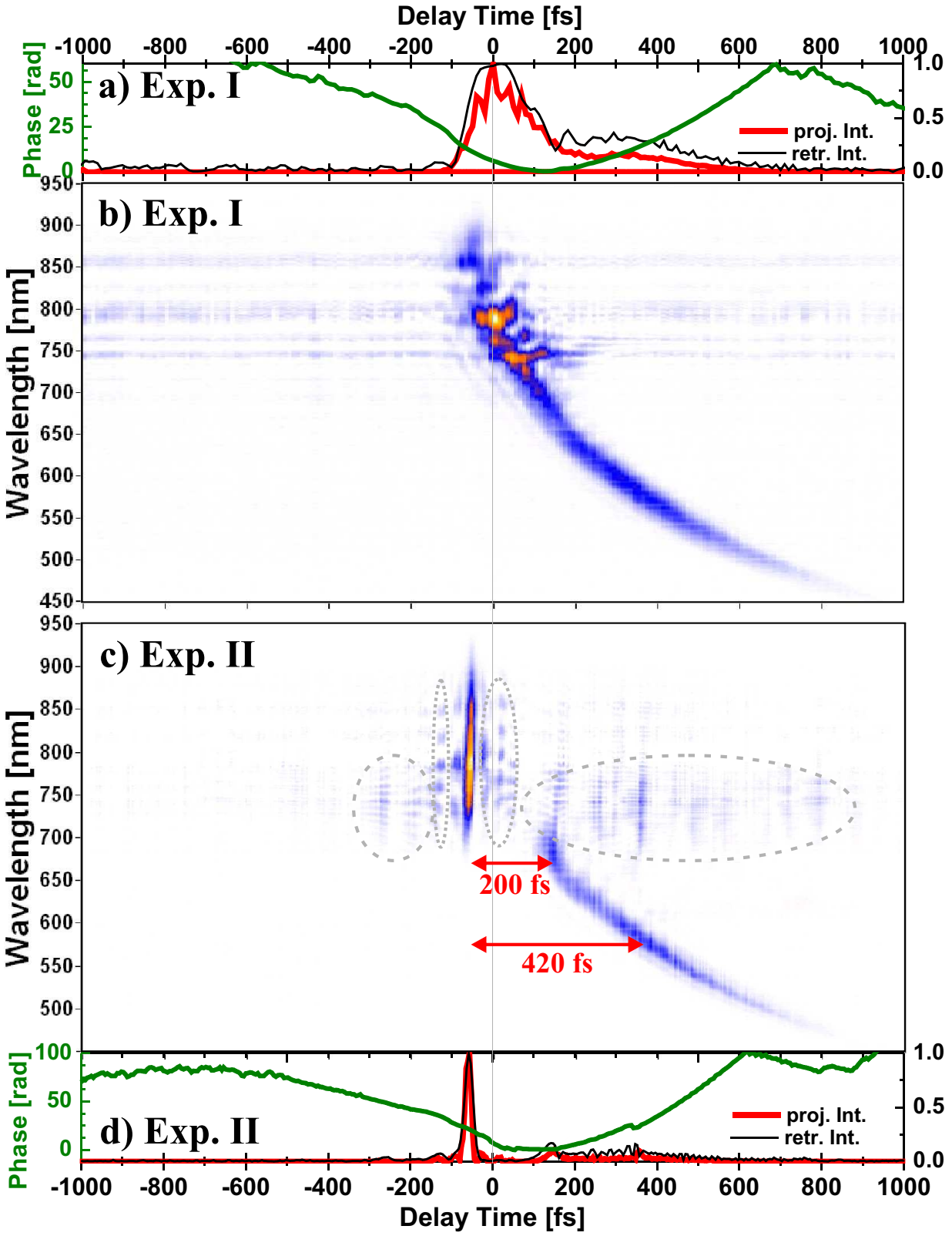

Figure 4.13: TG-FROG traces and temporal representation of WL pulses applied for NeNePo on Ag_3 in Exp. I in a)/b) and in Exp. II in c)/d). The scan interval is equal in both cases, whereby a)/b) shows an unshaped WL pulse and the lower part c)/d) gives an example for free optimization of the spectral phase in the region from 700-950 nm (the VIS tail passed the Shaper unmudulated). The corresponding time plots on top and bottom of this figure consist of the projected raw data onto time axis (red line) and of the retrieved intensity (black line) which are both normalized to unity. The retrieved temporal phase (green line) belongs to the left axis.

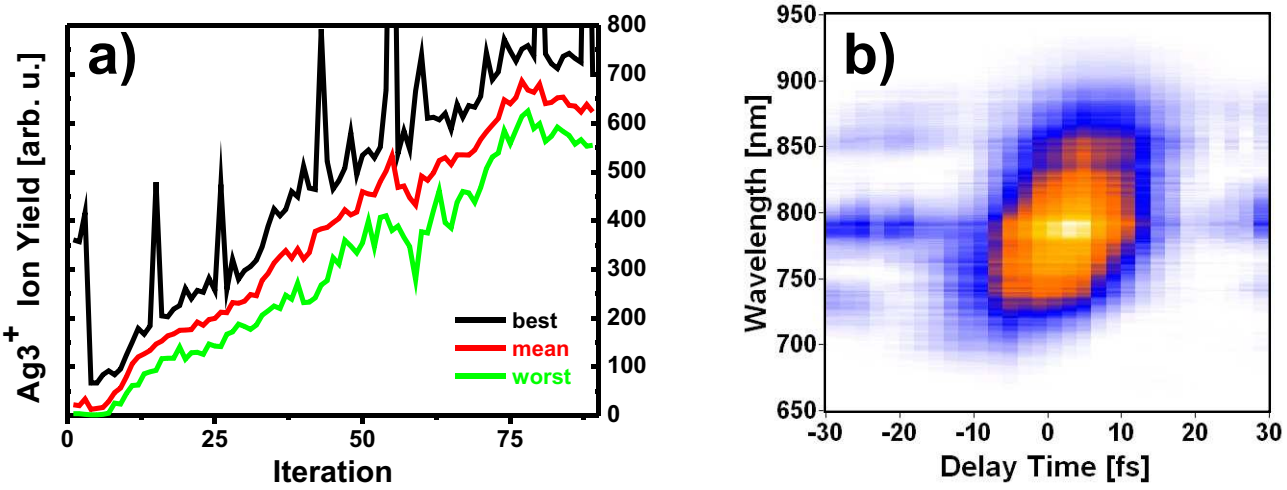

Figure 4.14: Exp. II: Optimization of Ag_3 NeNePo signal beginning with phase noise lead to a compressed NIR pulse. Ion signal for free phase optimization in the wavelength range from 700–950 nm in a), where the best (black), mean (red) and worst (green) population is plotted $vs.$ the iteration number. The trace in b) is a fine scan of the NIR part in Fig. 4.13c. The tilt indicates a slight negative prechirp found by the EA to enhance the ion signal.

found by the EA in the NIR wavelength region from 760–950 nm, which could be assigned to nuclear dynamics. Repetitions of this experiment confirmed this observation.
Transmitting the spectrum according to Fig. 4.12a (prechirping the NIR does not change the spectral contend) provided 48 μJ in the NIR (15 fs FWHM) and 7.8 μJ in the VIS (200 fs FWHM) and lead to:
$I_{NIR} = 430 \times 10^{11}$ W/cm^2, $I_{VIS} = 7.9 \times 10^{11}$ W/cm^2, and
$E_{NIR} = 18 \times 10^9$ V/m, $E_{VIS} = 2.4 \times 10^9$ V/m.

With the aim of investigating the nonlinearity order of the multi photon charge reversal, an independent experiment concerning the power dependence of the cation signal exclusively on this NIR spectrum was carried out. To achieve a large energy range up to 200 μJ, few cycle pulses as short as 7.3 fs with a slightly negative prechirp were generated with the CM compressor instead of

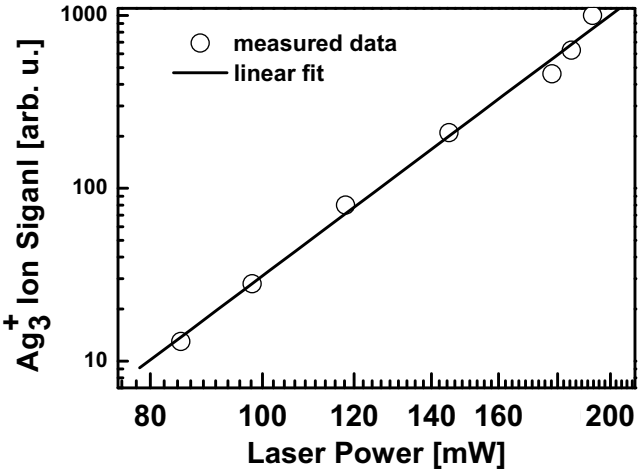

Figure 4.15: Ag_3^+ power dependence corresponding to Exp. II. Compression by CM was utilized instead of the pulse shaper to achieve a larger intensity range for the power dependence measurement. The excitation condition of slightly negative chirped 7.3 fs pulses at 800 nm was adapted from the optimized pulse form of Fig. 4.13c. A linear fit to measured date (circles) ensued a slope of 5.0 ± 0.2.

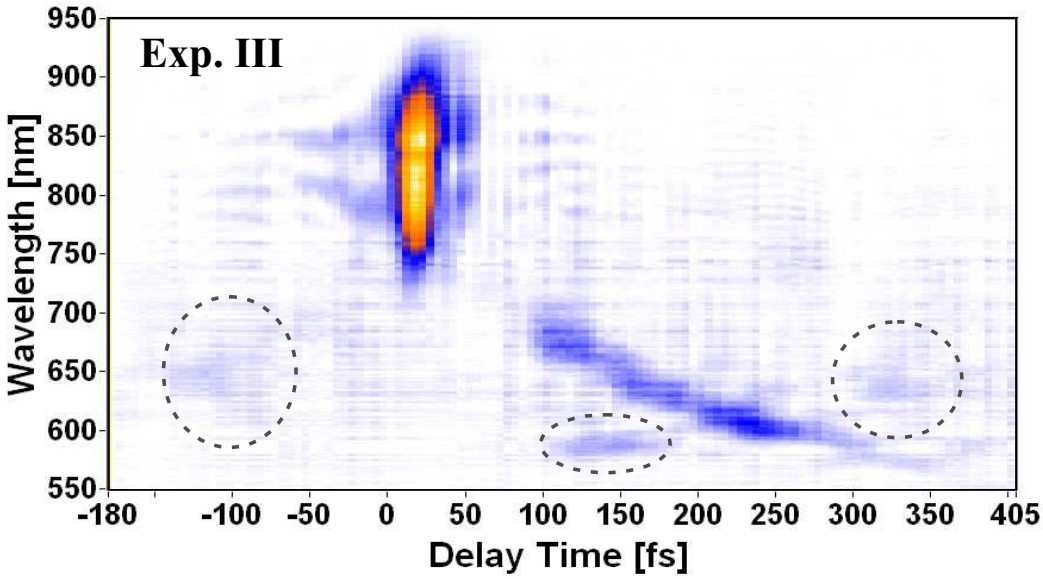

Figure 4.16: Optimization utilizing the entire spectrum from 450–950 nm and beginning with an unshaped mask like in Fig. 4.13b as starting point for the EA. The NIR structure is cleaned up and slight modifications in the VIS tail become visible (hinted by dashed lines).

the pulse shaper. The double logarithmic plot in Fig. 4.15 contains the measured ion yield (circles) versus laser power. A straight line with a slope of 5.0 ± 0.2 is fitted to the measured data, denoting that at least five photons are necessary for the charge reversal with 7.3 fs pulses centered at 800 nm. Thus, the bridged energy gap with 5 simultaneously acting photons is 5×1.55 eV $= 7.75$ eV. The intercept value in the fit is at -8.5 ± 0.4 .

Exp. III Subsequent to the successful demonstration of the closed loop experiment by shaping a reduced bandwidth in Exp. II, now the whole octave was enabled for free optimization. With the special designed WL beam splitter (WL-BS, characterized in Fig. 2.14), a reduction of roughly 80% in the NIR was carried out. The equalized hight of the VIS spectrum can be verified in Fig. 4.12b which displays the direct filament output as black line and the filtered spectrum as gray filling (both plots are normalized to the same NIR wavelength). Starting point for the EA was the unshaped mask with a pulse like in Fig. 4.13c. The resulting TG-FROG trace in Fig. 4.16 shows a clean, short pulse around 800 nm and a VIS tail with some weak changes compared to Fig. 4.13c which are marked by dashed ellipses. Two sub pulses at 580 and 640 nm were shifted to earlier times with respect to their original position in the VIS tail, one even up to -100 fs. A third pulse around 625 nm starts emerging at later times. Wavelengths below 550 nm did not contribute in this optimization and were thus dropped by the EA. The corresponding optimization curves are shown in Fig. 4.17. Strikingly, the black curve for the best individuals does not start at the noise level like in Fig. 4.14a or at a comparable hight as the mean and worst population of Fig. 4.17, respectively. This is explained, considering the initial unshaped mask, as the start from a local optimum in the search space. Because of the implemented survivor, the black curve sticks to the high start level until the crossover caused the rest of the population to catch up, as is seen by the quick rise of both grayish curves. They start at the noise level because the mask settings for the remaining 29 individuals consist of random noise. The overall evolution of the optimization is moderate and the experiment stops at a level which is only about three times the noise level.

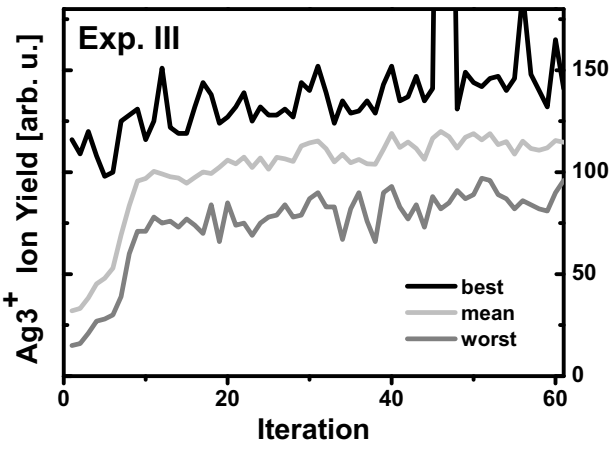

Figure 4.17: Exp. III: Starting with an unshaped mask as initial guess, keeps the best individual on a high level due to the implemented survivor for the previous iteration, until crossover improves the genes of the remaining population. The progress in evolving from this local maximum is less compared to a start from noise in Fig. 4.14a.

Exp. IV After proving that optimization with the full spectrum works and can be started from an unshaped mask in the previous Exp. III, now it is initiated from phase noise over the entire octave from 450–950 nm. Two optimization results achieved in this manner are presented in Fig. 4.19a/b and c/d). Again, successful optimization leads to a signal increase by more than one order of magnitude, comparable to Exp. II ($cf.$ Fig. 4.13c). Both measurements in Fig. 4.19a/b and c/d) were carried out in turn, assuring identical conditions. Each optimization with about 125 iterations lasted nearly two hours and a good matching of the general pulse shapes was achieved. As described previously, the NIR spectrum exclusively was compressed to a short pulse. Complementary, the VIS part was not compressed to a single time event but spread over more than one ps. Free optimization of the spectral phase lead to a rich structure in the wavelength range from 520–760 nm. As in the Exp. II, the retrieved temporal intensity profile (black line in a) and d)) is in very good agreement with the projected intensity (red line in a) and d)). further on, the retrieved phase (green line) shows a similar trend in both time plots. To facilitate comparability of the traces, the chirped VIS tail according to Fig. 4.13c of the unshaped VIS pulse is insinuated as transparent yellow line in both images. Concerning the VIS part, five basic features show up in the current and also in the following optimization experiments:

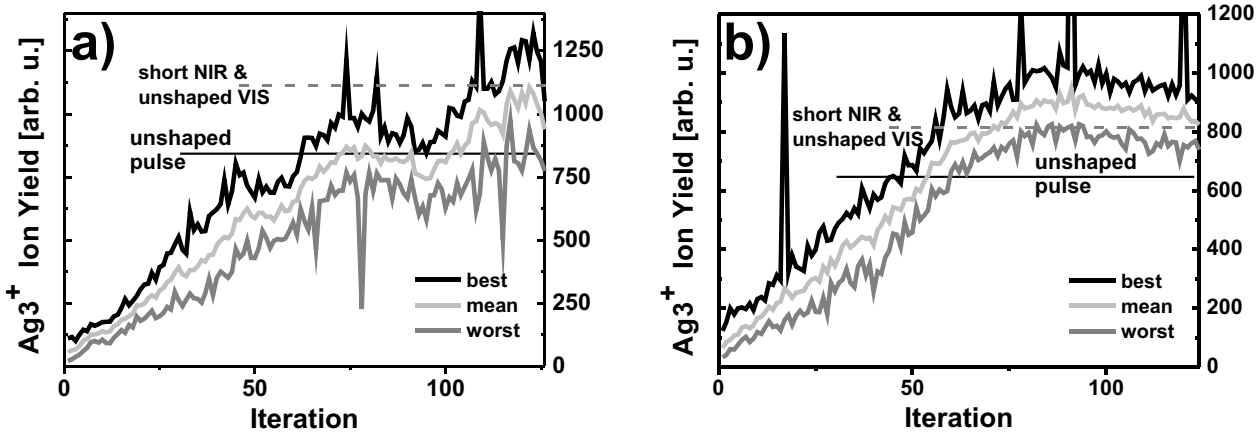

Figure 4.18: Exp. IV: Optimization curves in a) and b) correspond to the upper and lower part of Fig. 4.19, respectively. Both curves show an signal increase by more than one order of magnitude when starting from noise in the range of 450–950 nm.

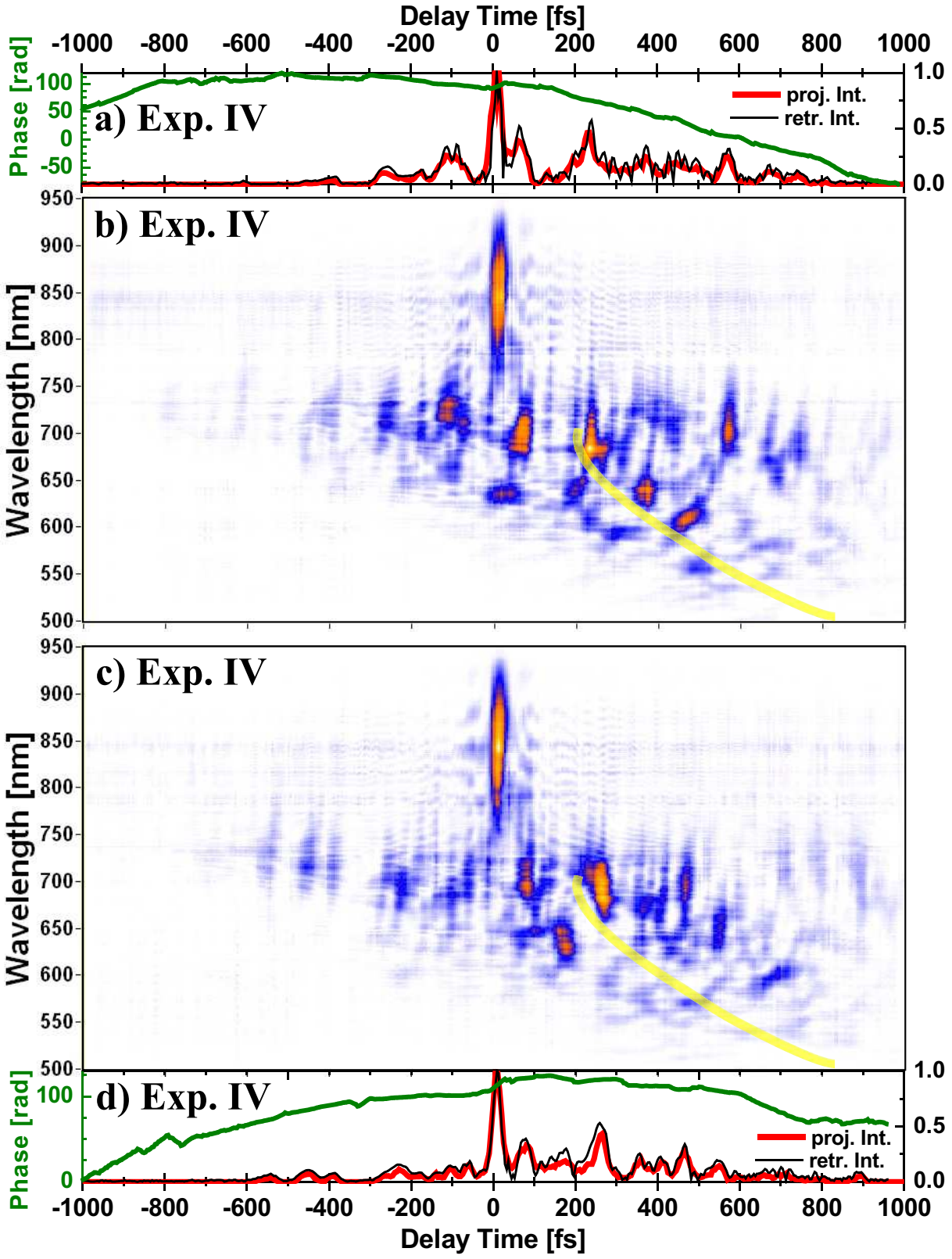

Figure 4.19: Exp. IV: TG-FROG traces and temporal representation in a/b) and c/d) as resulted from free phase optimization in the wavelength range from 450–950 nm. Starting condition of Exp. IV was random noise. Comparing both measurements, carried out at identical conditions, demonstrates the reproducibility and the uncertainty of the free optimization of Ag_3 NeNePo with WL filaments. The position of the yellow line corresponds to the VIS tail in Fig. 4.13c.

(i) The temporal extend of this complex, multi colored pulse sequence lasts for more than one ps and can be identified from -800 up to 1000 fs in a/b) and from -700 up to 100 fs in c/d). The more intense core structure reaches from about -300 to 750 fs in both cases.
(ii) The short NIR pulse appears at time zero after one third of the intense VIS part has passed. Therefore, the relative timing of the two distinct spectral regions (NIR and VIS) is equal in a/b) and c/d).
(iii) During the temporal evolution, the utilized VIS pulse, setting off at -300 fs, starts with longer wavelengths of about 760 nm and expands towards shorter wavelengths. The maximal spectral width occurs at 500 fs in both cases and ranges from 530–760 nm. This appearance turned out to be an universal property in all performed feedback loop experiments on NeNePo of Ag_3^-/Ag_3/Ag_3^+ in the following.
(iv) Generally, the VIS part doesn't show up as a cohesive flow of energy, for instance with a continuously chirp of the pulse, but as several short pulses without a clear periodicity.
(v) The actual appearance of most of the peaks is not congruent for both traces.
The corresponding optimization curves for the traces of Fig. 4.19b and c) are given in Fig. 4.18a and b), respectively. In spite of the spikes originating from electronic noise, the EA leads to continuous signal increase (until saturation in Fig. 4.18b). The signal drops after the 80th iteration in a) due to small experimental drifts. The reference values indicated by horizontal lines are measured at the end of each optimization. The solid line corresponds to the value of the unshaped mask (trace of Fig. 4.13b) and dashed line represents the ion counts for a short NIR pulse with the chirped VIS tail of Exp. II (trace of Fig. 4.13c). Both curves in Fig. 4.18a and b) exhibit an elucidate enhancement over the level of an unshaped WL pulse. However, the signal improvement compared to a pulse with short NIR and chirped VIS tail is less.

Besides the relevance for nuclear dynamics of the Ag_3 cluster, the measurements of Fig. 4.19 disclose the versatility of the complete optical setup. The ability of performing TG-X-FROG measurements of the complex VIS structure within a single beam is the basis for analyzing these optimization results, achieved by octave exceeding shaping of filamentation WL.

Transmitting the spectrum according to the filled gray curve of Fig. 4.12b provides 41 μJ (shaped pulse) for focusing into the ion trap. 53% (23.8 μJ) are contained in the VIS fron 450-750 nm and 21 μJ remain for the NIR region. The following intensity and field strength approximations in the interaction region are:
$I_{NIR} = 178 \times 10^{11}$ W/cm^2, $I_{VIS} = 14 \times 10^{11}$ W/cm^2, and
$E_{NIR} = 11 \times 10^9$ V/m, $E_{VIS} = 3.2 \times 10^9$ V/m.

Exp. V It was shown with the former experiment, that the signal difference between WL pulses, consisting of a short NIR and an either shaped or unshaped VIS part, is quite small. This is evident when comparing the dashed horizontal line, representing the unshaped VIS light, in Fig. 4.18 with the corresponding optimization yield which is only slightly higher. This small difference is caused by the high intensity of the compressed NIR pulse, although the integrated spectral power is slightly higher for the VIS than for the NIR part. To further enhance the VIS spectrum, spectral broadening with emphasis on the VIS part was pushed to the limit before spatial inhomogeneities arose. This was accomplished by inserting one fused silica glass (1 mm thickness) prior and one subsequent to the filament in order to increase nonlinearity during propagation. Additional fine tuning of the amplifier compressor and the iris prior to the filament enabled further homogenizing the octave exceeding spectrum, as plotted in Fig. 4.12c. It turned out, that this way of filamentation in air in combination with two FS glasses is advantageous over any other gas type in terms of high power in the VIS and very good spatial beam quality. The spectral change can be verified when

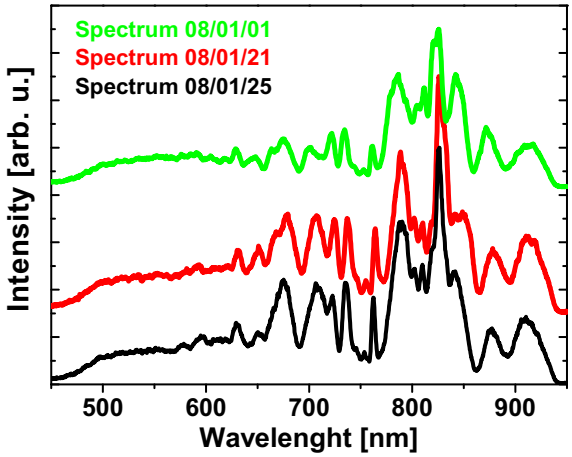

Figure 4.20: The three spectra measured over a period of 24 days demonstrate the reproducibility when WL is generated in air with additional FS glasses prior and subsequent to the filament. The additional glass material enabled homogenization of the octave exceeding spectrum. An offset is added to the red and green curve for better visibility.

comparing this especially broadened WL shown in Fig. 4.12c to the previous spectrum in b). The black line in c) denotes the unfiltered filament output and the gray filling displays the filtered spectrum provided for WL shaping.

Since the following optimization experiments were continued for about three weeks, another concern is the reproducibility of the spectral amplitude and phase. This issue is relevant when comparability of pulse forms achieved on different days is required. The excellent reproducibility can be followed up by the three curves of Fig. 4.20 which show filamentation spectra taken over a period of 24 days.

With these spectra launched into the 4-f setup, the optimization began with noise over the entire

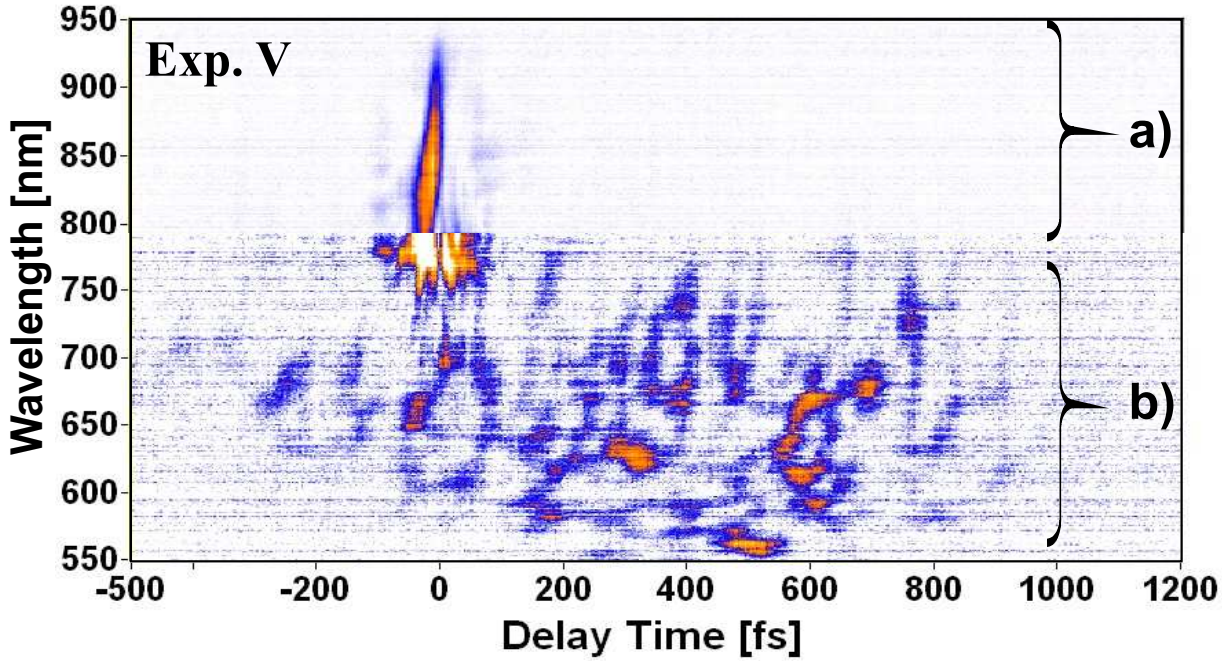

Figure 4.21: Exp. V: Free phase optimization from noise @450-950 nm with a homogenized WL input spectrum confirmed the result of Fig. 4.18. A negative chirped NIR is accompanied by a rich structure in the VIS. The color coding in the two parts in a) and b) is normalized to different values to enhance the visibility in the VIS part whose maximum is about 15% of the intense NIR pulse.

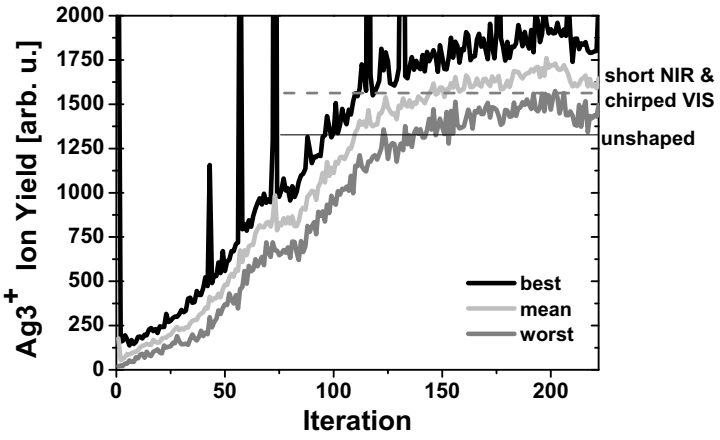

Figure 4.22: Exp. V: Optimization from 450–950 nm with the homogenized WL spectrum (gray filling in Fig. 4.12c) basically confirmed the result of Fig. 4.18. Values for the unshaped and partially shaped WL pulses are indicated by horizontal lines. The pronounced spikes are caused by electronically noise.

spectrum (450–950 nm). The new result of Fig. 4.21 is in good agreement with the previous result of Fig. 4.18b and c). The image of Fig. 4.21 consists of two representations a) and b) with different normalization of the color coding for better visibility. Following observations are associated with this trace:
(i) The upper part a) is normalized to the maximum at 840 nm and reproduces the known result of a negative chirped NIR pulse. The maxima of the VIS part of the trace in b) has a FROG signal intensity of about 15% compared to the peak at 800 nm.
(ii) The pulse sequence in the VIS range is fairly consistent with the previous results of Fig. 4.18a and b). Its intense part begins at -300 fs and lasts to 800 fs. Weaker structures are visible from -450 up to 900 fs.
(iii) Conspicuously visible, in the onset of the VIS structure only a reduced wavelength region (680 $\pm$30 nm) is utilized at -300 fs, whereas the temporal evolution increases towards higher frequencies.
(iv) Finally, in the trailing part from 400–900 fs the EA made use of the spectral range from 530–760 nm. Repetitions of this experiment ensued qualitatively similar results.

The corresponding optimization curves in Fig. 4.22 show an increasing ionization yield during the first 200 out of the 222 iterations. Again, the increase by more than one order of magnitude leads to a higher value than for the short NIR pulse with a chirped VIS tail (dashed horizontal line as a reference). This enhancement compared to a short NIR and chirped VIS pulse is similar to the result in Fig. 4.18. Associated with these small differences, one has to address the issue how relevant the VIS structure influences the charge reversal process.

Exp. VIa - parametric pulse forms Although the very specific VIS structure was reproduced several times, the meaning of each sub structure on the NeNePo process is not obvious. Therefore, parametric pulse forms in the VIS range with a remaining short NIR pulse were generated. The first pulse forms to be applied were pulse trains, which have been beneficial to NeNePo on Ag_2. Now, the spectral range from 550–750 nm is different to the NIR excitation of Ag_2. This VIS sequence was carried by first constructing a spectral double pulse with a short NIR and a short VIS pulse according to Fig. 3.31b. Then, a sinusoidal phase was added solely to the VIS mask. The result is an excitation consisting of a short NIR and a delayed VIS pulse train with tunable sub pulse distance ΔT, as demonstrated in Fig. 3.32a–d). A scan of the sub pulse separation, as presented successfully in the case of Ag_2 ($cf.$ Fig. 4.6), was carried out. However for Ag_3, no evidence of matching a vibrational period occurred for an excitation with equidistant pulses.

The second employed pulse form consisted of a short NIR pulse and a VIS pulse which was steered by two parameters. Firstly, the time delay between VIS and NIR components was ad-

justable by applying a linear phase ramp to the spectrum, as demonstrated in Fig. 3.39a–d). Secondly, the sign of the VIS prechirp was continuously varied from positive to negative values. This parametric shaping, by means of manually scanning these two parameters, resulted in a maximum

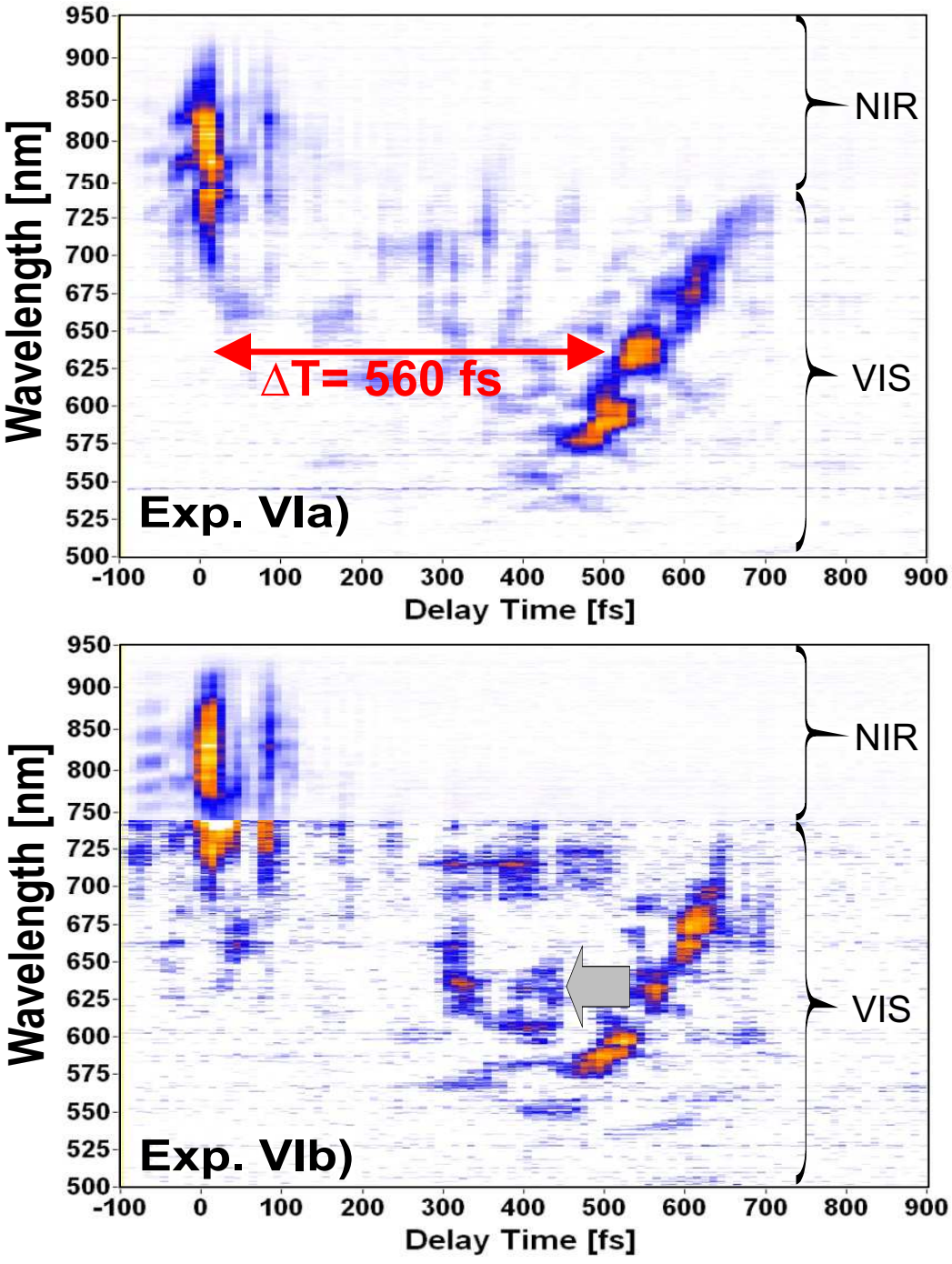

Figure 4.23: Exp. VIa shows a parametric pulse form consisting of a short NIR pulse and a time delayed, negatively chirped VIS pulse. This trace in a) yielded the maximum ion signal compared to other time delays ΔT between the two excitation pulses and prechirp values for the VIS part. Free optimization starting from the trace in a) lead to the result of Exp. VIb underneath. Now, a cleaned NIR pulse with a side peak at 100 fs and slight modifications in the VIS lead to a signal enhancement of a factor of two compared to the trace in a).

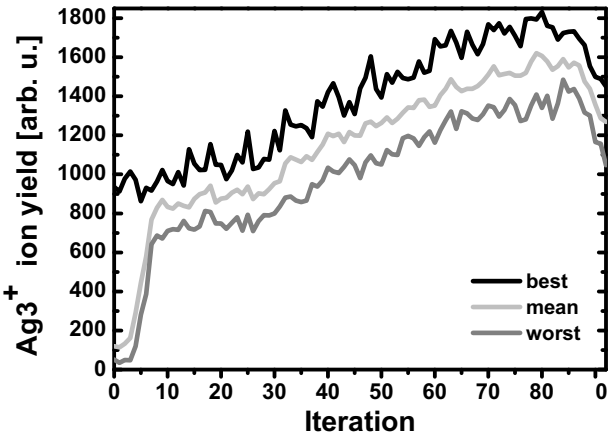

Figure 4.24: Exp. VI: Successful optimization starting with the trace of Fig. 4.23a as initial guess. During the first iterations, the fittest genes were spread out over the whole population by crossover. The resulting trace is given in Fig. 4.23b. Termination of the optimization was caused by technical problems as is seen by the simultaneous decrease of all three curves.

of the Ag_3^+ ion signal for the pulse form shown in Fig. 4.23a. As before, the NIR and VIS wavelengths are shown in different color coding parts to improve the visibility in the corresponding areas. This TG-X-FROG illustrates a short NIR pulse and a time delayed VIS pulse with a clear negative slope in the trace. The time delay ΔT for the pulse centered at about 630 nm is 560 fs. For this pulse, the Ag_3^+ ion signal was 10% higher compared to the unshaped VIS tail like in Fig. 4.13c.

Exp. VIb Taking the parameterized result from Fig. 4.23a as an initial guess, free phase optimization in the wavelength region from 450–950 nm was performed. Looking at the trace in Fig. 4.23b, shows a shortened and cleaned up NIR structure with an increased side peak at 100 fs. This side peak is apparent in the initial trace of a), too, but somewhat weaker. Also changes in the VIS range become noticeable, where a part of the pulse at 625 nm was shifted to earlier times, as indicated by the broad gray arrow.

The corresponding optimization curves for the best, mean and worst individuals in Fig. 4.24 exhibit the known behavior when starting from a maximum in the search space. After nine iterations, the average and the lowest ion signal (plotted as light gray and dark gray) approach the best individuals (black line) and evolve proportional to each other for the rest of the experiment. Unlike the optimization of Fig. 4.17, the start from a local optimum in the search space now lead to an improvement by a factor of two after 80 iterations. The collective decrease of all three curves after the 80th iteration is due to experimental misalignment.

From this and the previous observations the question arises, how the two distinct spectral regions (NIR and VIS) depend on each other, or if they act individually on the charge reversal.

Exp. VII In order to address this question the two distinct spectral regions were treated as follows: The shaped VIS part from 450–760 nm always completely irradiated the ion trap. The NIR part was blocked either fully or partially in the 4-f setup. The attenuation was carried out by manual filtering the corresponding spectral parts at the position of the cylindric mirror in the shaper setup of Fig. 2.13. Spectral cutting out of the Fourier plane prevents sharp edges in the spectrum and therefore avoids unwanted temporal satellite pulses. The associated excitation spectra are shown in Fig. 4.12d as black curve for complete NIR blanking and as filled gray plot for partial blanking, see Exp. VIII. For the current Exp. VII, the NIR wavelengths were completely blocked, as shown by the black line in spectrum of Fig. 4.12d. Optimization in the range from 450–750 nm started with random noise. Starting from the noise level of 60 ion counts, the signal went up to 170 counts. For comparison, an unshaped mask in the NIR (Fig. 4.13c) produced 90 counts. For relation, the optimal parameterized mask of Fig. 4.23a only showed about 20% more than the noise level in this restricted wavelength range. A TG-FROG measurement of the pulse with the optimized mask setting in the VIS is shown in Fig. 4.25. It contains only noise, although the optimization was

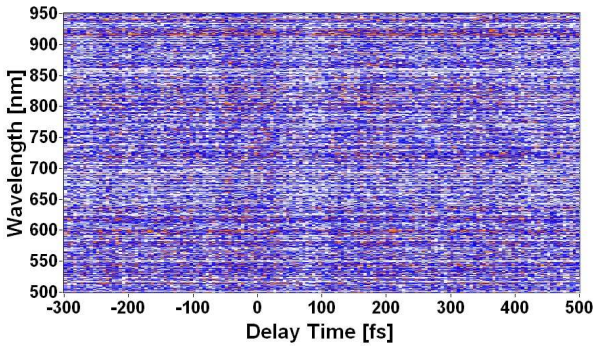

Figure 4.25: If the NIR gating pulse is not written on the SLM like in Fig. 4.26, measurement of the VIS part is impossible at given intensities.

successful. This noise recording is explained by the missing NIR gating pulse. In the absence of the NIR gating pulse, a 4WM signal is not measurable due to the low intensity of the VIS structure. This is is of great fortune for the characterization, since an auto-correlation of this complex VIS structure would lead to a very non-intuitive measurement. The proof, that only the TG-X-FROG method enables the characterization of such an optimization output is given by Fig. 4.26.

It is mentioned that for recording this TG-X-FROG trace, the shaper mask consisted of two parts. One part from 450–750 nm contained the phase information which was gained by the algorithm during optimization of the Ag_3^+ signal. The phase mask of the second part, $i.e.$ the NIR area which was blocked during optimization, was programmed to obtain a short NIR pulse, only for the recording of the TG-X-FROG trace. Thus, the definition of time zero is arbitrary. It simply

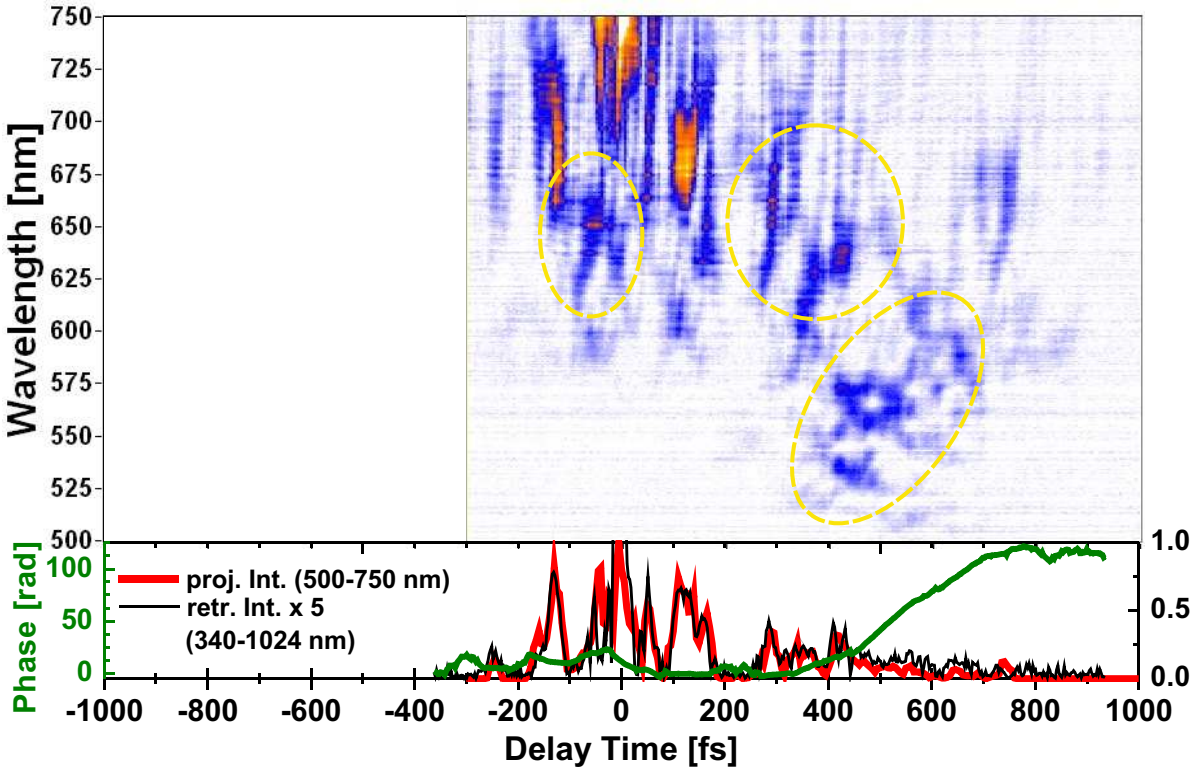

Figure 4.26: Exp. VII: VIS-only optimization @450-750 nm, NIR was completely blocked during the optimization. However, to enable the optical gating process, a short NIR pulse was added to perform the cross-correlation type measurement. This is a further proof of the TG-X-FROG mechanism. The overall shape of the VIS pulse is equal to the previous optimizations.

coincides with the maximum of the short NIR gating pulse. As described previously in Secs. 3.4.2 and 3.5.3, this NIR part serves as ultra short gating in the transient grating process for the entire WL spectrum. On this NIR induced grating the highly structured VIS part is diffracted in a cross-correlation manner as a single beam experiment.

The optimization result as TG-X-FROG trace is shown in Fig. 4.26. The time scan was only performed over 1.3 ps, however, the axis is scaled identically to the other plots to preserve comparability. The presentation of the spectral axis of the TG-X-FROG trace is reduced to the region from 500–750 nm to allow a more detailed presentation of the shaped VIS part. This pulse sequence achieves an ion signal which is twice that of the unshaped case. The general structure of the trace has many similarities to the ones in Exp. IV and V where the NIR light participated to the NeNePo process:
(i) The temporal extent of the shaped VIS pulse lasts at least for one ps and contains short pulse sequences with non uniform spacing. First sub pulses occur before -200 fs at wavelengths of 675–725 nm, followed by a more intense double structure at $\pm$125 fs around the gating structure which defines the zero point in the current scan.
(ii) Close to the zero point the excitation spectrum congregates components at 650 nm and expands this tendency up to +500 fs.
(iii) During the pulse evolution more and more shorter wavelengths were added.
(iv) Wavelengths below 520 nm did not contribute to the charge reversal process.
(v) Wavelengths above 725 nm play a minor role in the current pulse structure.
The dashed ellipses are drawn for better orientation and will be picked up later for comparison with Fig. 4.27a/b and c/d).

Exp. VIII The last experiment in this row utilizes an excitation spectrum shown as light gray filling in Fig. 4.12d. It contains the VIS part from 450–750 nm and a left over in the NIR above 900 nm. Phase optimization was carried out in those two regions simultaneously. Starting point was random noise for the whole area. The NIR spectrum from 750–900 nm was filtered out in the 4-f setup for the optimization. The resulting TG-X-FROG traces and their corresponding time plots are given in Fig. 4.27. Like in the former Exp. VII, a cross-correlation type of measurement was performed, thus NIR components are required. However, the TG-X-FROG method needed further extension. The new add-on is given by the fact, that the cross-correlating NIR spectrum is now embedded in between the spectrum under investigation (gray plot in Fig. 4.12d). therefore, a short NIR pulse for the optical gating was set only in the spectral range from 750–900 nm with the SLM. For the mask settings of higher and lower wavelengths the optimization result was taken over. This combined mask created the pulses, shown in Fig. 4.27a/b and c/d).

Both optimizations in a/b) and c/d) were performed at identical conditions. Compared to the previous experiments (Exp. IV, V and VII), an overall agreement can be stated:
(i) The NIR wavelengths from 900–960 nm were not utilized. This was verified in three different optimization runs from which one is shown in Fig. 4.28. Because there is no pulse information besides the NIR gating pulse, traces are plotted only from 500–750 nm. The gate pulse is located at -250 fs. (i) The temporal extent of the shaped VIS pulse lasts at least for one ps and contains pulse sequences which are non uniformly spaced. Clearly the sub pulses have a very short duration of less than 40 fs in some cases.
(iii) Wavelengths below 520 nm were not utilized for the charge reversal by the algorithm.
(iv) The leading pulse edge consist of red shifted frequencies than the trailing one. However, wavelengths at 725 nm are missing at early times in Fig. 4.27b and c) other than in the traces of Exp. IV of Fig. 4.19.
(v) At about 260 fs and 590 nm, an intense pulse is accompanied by a particularly striking feature

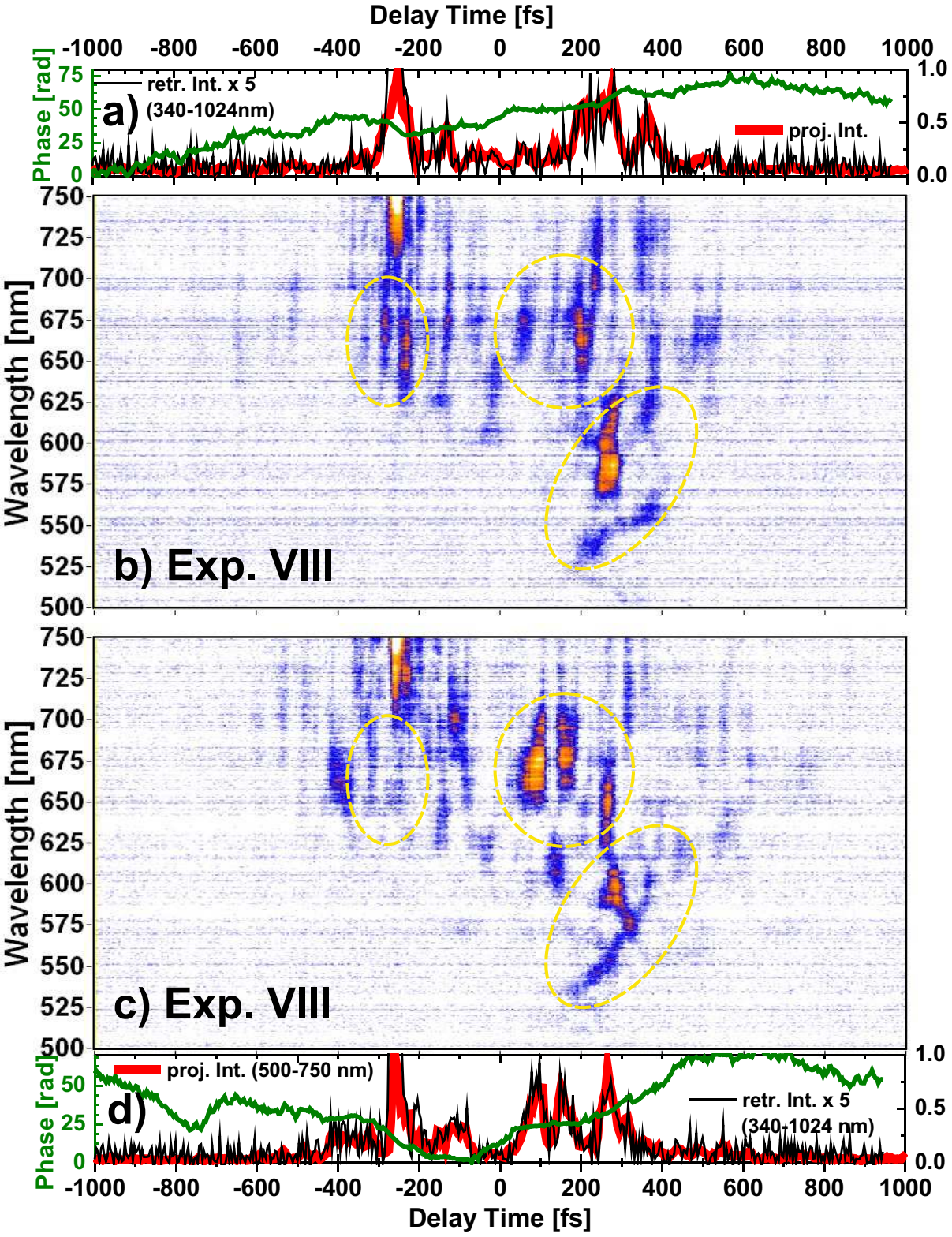

Figure 4.27: Exp. VIII: Simultaneous double color optimization from 920–960 nm and 450-750 nm. The NIR part from 750–900 nm was exclusively used for gating IR and VIS frequencies. However, the IR part (920–960 nm) was not utilized at all by the EA and thus not shown in the traces. Exp. a/b) and c/d) are carried out at identical conditions and are in good agreement among each other and with Fig. 4.26.

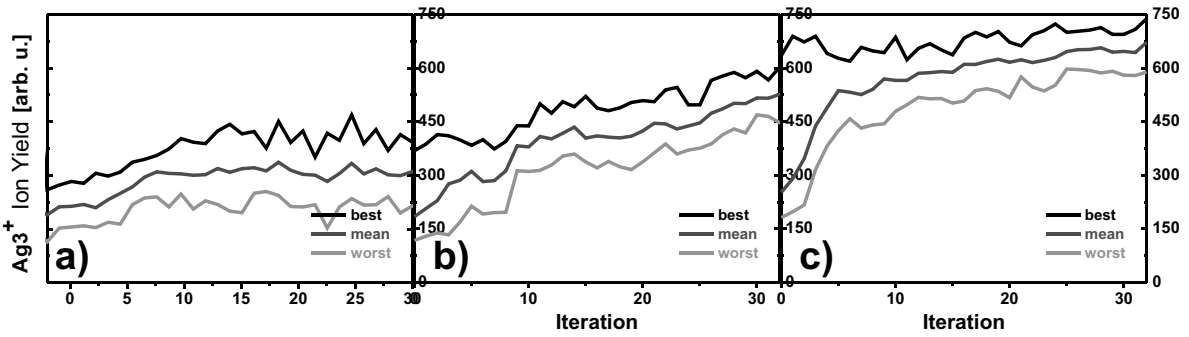

Figure 4.28: Exp. VIII: Curves for successive optimizations according to the trace of Fig. 4.27a. a): start from random noise, b): start with the best mask of a) and c): start with best mask of b). All three curves together show that the successive optimization approach is suitable to find the way towards the global maximum for huge search spaces.

which is a negatively chirped sequence from 525–600 nm in both images. It can be recognized, in the trace of Exp. VII in Fig. 4.26, too, for the same wavelength region. The yellow, dashed ellipses have the same temporal and spectral proportions in all three cases (Fig. 4.27 and Fig. 4.26).

In the current experiments, the optimized VIS pulse lead to a noisy TG-X-FROG trace. Within this trace showing a similar pulse envelope compared to Exp. IVa and b) in Fig. 4.19, individual sub pulse are very short in time. These very sharp temporal features reflect in an ion signal about 3.9 times above the noise level in Fig. 4.28.

Successive optimization For the last experiment, the optimization curves consist of three parts a), b) and c) in Fig. 4.28, because three successive optimizations were carried out. Random noise was the starting point in a) which was stopped after optimization stagnated. The best mask of a) was used as the initial guess for the next run in b) and lead to a clear improvement of 50%. Again, the best mask of b) was used as the initial guess in c). After another 20% improvement, the experiment had to be stopped unfortunately due to experimental imponderableness. However, the start with an initial guess and the addition of new genes in b) and c) lead to a continuous march towards the global maximum. The final mask of this three step successive optimization was used to measure the trace of Fig. 4.27a and a two step procedure was carried out for the optimization of Fig. 4.27b.

4.3 Discussion

4.3.1 Discussion on Ag_2

Double color pump probe The double color pump probe experiment of Fig. 4.2 confirms the previous findings of Refs. [140,141] in Fig. 4.1a at longer delay times. The periodic modulation of 182 fs (182$\pm$8 cm^{-1}) at delay times > 0.5 ps in Fig. 4.2 is assigned to nuclear dynamics at $v' \approx 6$ in the neutral electronic ground state $Ag_2(X-1^1\Sigma_g)$ [195]. This matches the 180 fs in the previous measurements excellently. Differences are visible close to time zero and for negative delay times. In the previous single color pump probe excitation at 406 nm the transient signal was symmetric for the reversed action of pump and probe pulse [140] (not plotted in Fig. 4.1a). The new experiments with 800 nm pump and 400 nm probe wavelengths however exhibit a constant level for negative time delays. About 90% of this level is solely caused by the action of the 400 nm pulse and thus time independent. The fact that no oscillation occurs at negative time delays with advanced 400 nm excitation indicates, that the NIR pulse reaches the neutral state via a one photon transition.

A conspicuous difference to the previous results of Fig. 4.1a is given by the strong signal drop at time zero in Fig. 4.2. A possible loss channel in the simultaneous presence of both pulses is multi photon double ionization to Ag_2^{2+}. In principle, the measured quantity of a quadrupole mass filter is the ratio of charge over mass [192], thus Ag_1^+ and Ag_2^{2+} are indistinguishable by their trajectory. However, the absence of a pronounced peak in the fragment signal (gray line), where even a noisy minimum is recognizable, contradicts a double ionization mechanism. Thus, this assumption is not supported and fragmentation in the neutral state of the cluster seems more likely since neutral particles cannot be detected with the mass filter. Such a fragmentation channel might be opened by the first excited state $Ag_2(1^3\Sigma_u)$ of the neutral Ag_2. Then, like in the experiment of Fig. 4.1a, a WP is generated on this excited state when both pulses temporally overlap. However, in Fig. 4.2, no second UV probe pulse exists and thus (resonant) ionization is avoided. In Ref. [141], the question was raised whether the WP propagating to longer core distances is bound by the triplet potential or dissociative. The lack of a recurrence of the strong peak at 190 fs in Fig. 4.1a, was attributed to non bounding state $Ag_2(1^3\Sigma_u)$ on which the WP further propagates freely to dissociation. In the same manner, the unique signal drop in the current experiment might confirm the former assumption.

An alternative loss channel could be a pump dump excitation whereby the blue pulse detaches the electron to generate an excited neutral species and the NIR pulse dumps the population down to the $Ag_2(X-1^1\Sigma_g)$ ground state, from where ionization is reduced. The long extending signal drop (about 360 fs), which is broader than the cross-correlation of both pulses, might be an evidence for the second explanation.

Pulse train excitation of Ag_2 In Fig. 4.2 the signal drop at time zero was discussed for the double color excitation with a single 800 nm pump and a 400 nm probe pulse. It vanishes in Fig. 4.5a-e) when pumping with a pulse train. Due to the energy reduction in each sub pulse of the pulse train compared to a single pulse, only the $Ag_2(X-1^1\Sigma_g)$ state is populated. As expected, a resonant sub pulse separation of $\Delta T = 175\ fs$ matching the round trip time of the WP on the ground state coherently adds up population when the WP is located at the turning point of the potential. This sharpened WP can be probed most efficiently. It leads to highest Ag_2^+ signal in b) and the best modulation in the NeNePo spectrum, compared to the off resonant excitations in a) and c)–e). The first unambiguous peak at time zero in b) is not the highest one. This will be explained with the help of Fig. 4.4a. The dashed line indicates the location of the fourth sub pulse with respect to the maximum at time zero. At time zero the center of the pulse train and the probe pulse coincide. One half of the train already induced photo detachment, while the second half arrives after the probe pulse. The dashed line indicates the location of the fourth sub pulse with respect to the maximum at time zero. Maximum amplitude of the NeNePo spectrum in Fig. 4.5b therefore occurs at later times at about 380 fs. No clear signal increase from peak to peak in b) with increasing numbers of exciting sub pulses is observed in the NeNePo trace. Further on, an improvement of the modulation contrast with respect to excitation with single Gaussian pulse in Fig. 4.2 was not achieved.

Complementally, to describe the resonant excitation in time domain, an analogous picture is provided in frequency domain. Due to the Fourier relation between time and frequency domain, the sub pulse separation of the vibrational period of the neutral Ag_2 corresponds to a certain frequency comb in the spectral domain, as plotted as black line in Fig. 4.3. A larger ΔT corresponds to a narrower comb distance in the spectrum. If the separation of the comb teeth exactly matches the vibrational ladder of eigenfrequencies of the ground state potential, preferentially these states add up coherently in Fig. 4.5b. The pump step thereby sets a defined phase relation for all excite vibrational energies which then propagate in phase unless the system is disturbed.

Although the signal is lower for the off-resonant excitations in a) and c)–e), the visible modulation exhibits the same periodicity of about 180 fs. Within the scan range of -1 to 3 ps and a scan

resolution of 20 fs, a change of the oscillation period is not obvious for the off-resonant cases. Unlike a driven classical harmonic oscillator, the periodicity of the driven quantum system remains at the vibrational period of about 180 fs, regardless of the periodicity of the excitation. This is because the WP can be probed most efficiently only at the outer turning point of the potential. The amplitude of the Ag_2^+ ion signal for off-resonant excitation is determined by the amount of WP spreading. However, the average value of the modulated ion signal is increased for positive time delays compared to negative ones.

Taking the trace in b) as a reference, an unambiguous assignment of a phase shift in c) is difficult, however, most peaks seem to overlap temporally. In Fig. 4.5a), d) and e) a phase shift of the maxima with respect to b) is clearly visible.

The phase shift might originate from different starting times for the action of the pulse trains. Referring to Fig. 4.4, only the maximum of all various pulse trains coincides with the maximum of the probe pulse at time zero. The overlap between the first sub pulses and the probe pulse, however, is found at different delay times, as indicated by the dotted lines in Fig. 4.5. These lines mark the position of the fourth sub pulse (with respect to the center) which represents the beginning of the pulse train, as drawn in Fig. 4.4. Since this distance to the maximum of the train is not an integer value of the vibrational period, it might be responsible for the phase shift in the ion signal.

4.3.2 Discussion on Ag_3

The pulse train excitation described in the previous section is a first step in expanding the pump-probe NeNePo scheme by introducing a shaped pump excitation to the Ag dimer. Therefore, appropriate pulse trains within the spectrum of the laser fundamental were generated which served as resonant electron detachment step. Since diatomic molecules have only one vibrational degree of freedom a parametric approach for the excitation is straightforward. The addition of one atom creates the simplest system with different vibrational modes in which IVR occurs. In the particular case of the neutral Ag_3, the details of the nuclear dynamics show a sequential process beginning with configurational changes predominantly along the bending coordinate Q_x, intra-molecular collision of both terminal atoms, the onset and evolution of IVR, and finally vibrational equilibration [11, 142]. As pointed out before, the nuclear dynamics of the vibrationally excited Ag_3 does not exhibit IVR during geometrical relaxation before the collision of the terminal atoms [142]. Surprisingly, for an ensemble temperature of 300 K, weak vibrational coherence effects have been predicted in the IVR time domain opening at about 800 fs, as shown by the dashed and thin solid line in Fig. 4.10d. This simulation assumes an infinitely short pump pulse which is probed with a 20 fs probe pulse at an excitation of 5.9 eV. Therefore, one would expect an optimized pulse shape consisting of a very short pump pulse followed by a time delayed short pulse sequences in the VIS spectrum which act as three photon probe step. Precursory to the general discussion, the respective experiments of WL shaping on Ag_3 are commented.

Discussion Exp. II From the optimization in Exp. II in Fig. 4.13c where only the NIR of the spectrum was optimized and the chirped VIS tail passed the shaper unaffected, following findings are deduced:
(i) The sharp spikes, in the optimization curve of Fig. 4.14a for the best individuals (also appearing at the beginning), arose from electronic noise. Although unwanted, the appearance of these spikes demonstrate the robustness of the EA because the signal still increases continuously.
(ii) The ion signal is enhanced for more than one order of magnitude during 83 iterations by generating a clean pulse structure which is even negatively chirped. This negative pre-chirp can be verified in the detail of the trace in Fig. 4.14b where the blue frequencies arrive prior to the red shifted ones. However, the prechirp does not fully compensate for the entrance window of the vacuum chamber to provide a TL pulse in the ion trap. Although this result of direct multi photon

ionization at NIR wavelengths seems trivial from the viewpoint of nuclear dynamics, the compression to a short pulse when starting from phase noise is a good proof for the capability of the closed loop comprising of WL filamentation and charge reversal of Ag clusters.
(iii) Two dotted vertical oriented ellipses in the trace of Fig. 4.13c mark satellite structures in the $\pm$ 100 fs region. They are assigned to an inhomogeneous NIR spectrum rather than to wave packet (WP) dynamics on the Ag_3 cluster. That this is true can be seen from Sec. 3.3, where similar satellite structures were found in case of adaptive pulse compression experiments when optimizing the 4WM signal in the TG-FROG. These satellite arise due to the modulated spectral shape.
(iv) Weak multiple pulses in the wavelength range from 700–760 nm are visible in Fig. 4.13c, marked by dashed horizontal ellipses. In contrast to the satellites around 800 nm, these multi pulses are not subject to improper mask settings or optimization artefacts, since they were not observed in pure pulse compression experiments. Their temporal extension can be identified from -280 fs up to 900 fs and their role has to be clarified in future.
(v) From the unshaped trace in Fig. 4.13b, the distance of the maximum at 800 nm and the beginning VIS tail at 700 nm can be estimated to be about 100 fs. Compared to that, the compressed NIR part in Fig. 4.13c is shifted towards earlier times for about 200 fs with respect to the onset of the VIS part. Such a shifting was never observed in the adaptive pulse compression experiments of Sec. 3.3 and thus indicates that the relative timing of both pulse parts has an influence on the ion signal. The second arrow in Fig. 4.13c indicates 420 fs delay of the VIS part at 575 nm with respect to the short NIR pulse. By comparison, in the calculation of the NeNePo-ZEKE signal of Fig. 4.10c, the first and strongest maximum in the probe window occurs at about 450 fs delay time when probing at 6.5 eV. This energy corresponds exactly to three photons at a wavelength of 575 nm and thus could possibly be the origin of the shift of the NIR pulse towards earlier times. In this picture the NIR pulse fulfills the condition of an extremely short pump pulse, populating also the neutral ground state which is subsequently probed by an uncompressed ionization pulse at 575 nm.
(vi) Starting from Exp. II and its repetitions which are not shown, it is safe to say that the NIR wavelengths were never utilized to create a second time delayed ionization step after the photo detachment. Besides a weak indication for temporal dynamics in the region from 700–760 nm, the ion signal merely increased due to pulse compression in the NIR as the driving force for direct multi photon ionization with NIR light centered at 800 nm.

Discussion Exp. II - Power dependence The power dependence of Fig. 4.15 resulted in a slope of 5 for direct charge reversal at time zero with a short NIR pulse centered at 800 nm, indicating a 5 photon process. According to the PES scheme of Fig. 4.8, it is likely that Ag_3 remains in its initial linear configuration and the total energy consists of the VDE of 2.45 eV and the ionization energy $\mathrm{IP}_{lin} = 6.67$ eV adding up to 9.12 eV. From the power dependence, a lower total energy gap for charge reversal of $5 \times 1.55 = 7.75$ eV is calculated. In this context, it is mentioned that a very good matching of experimental NeNePo traces and simulations is described in Ref. [205] on page 72, under the assumption of an IP roughly lower by 9%. This assumption of a lowered IP ≈ 8.28 eV would lead to a reasonable agreement between measured and simulated values also in this measurement. On the other hand, power dependencies of highly multi photon processes might underestimate the real order of the process.

Discussion Exp. III When starting from an unshaped mask (Fig. 4.13b), optimization of the complete spectrum (450–950 nm) again lead to a clean NIR pulse but hardly gains more insight into the role of the VIS wavelengths. This can be explained by the fast convergence for NIR wavelengths due to the highly nonlinear power dependence (at least five photons) of the ion signal on the NIR pulse and the weak contribution of the VIS spectral components. The contribution to

the ion signal of the unshaped VIS part was only about 6% of the total ion signal in the presence of a short NIR pulse.

Furthermore, the unshaped mask as an initial guess denotes a local maximum in the search space from which the EA cannot escape to find for instance the slightly negative prechirp of the NIR pulse. Due to the same reason, the temporal separation between the NIR peak and the VIS tail remained at its intrinsic gap of 100 fs. Linking the small changes on the VIS tail, indicated by dashed ellipses in Fig. 4.16, to an improvement of the Ag_3^+ signal is difficult since the VIS contribution is still very low compared to the NIR part (≈ 6 %).

Discussion Exp. IV Preventing the starting from a local maximum in the search space (ranging from 450–950 nm) by optimizing the phase mask from an initial noise level, lead to a novel result compared to Exp. III. Besides pulse compression at NIR frequencies, the VIS part shows a sequence of short pulses containing different colors at different delay times, as mentioned in the beginning of the discussion. However, the sequential appearance of VIS frequencies in Fig. 4.19b and c) is unexpected compared to the progress of the PES of Fig. 4.8. This shows the necessity to begin a pulse sequence with high energy components ($\mathrm{IP}_{lin} \approx 6.67 = 3 \times 2.24$ eV) when the cluster is in the linear configuration and it predicts lower energies ($\mathrm{IP}_{tri} \approx 5.73 = 3 \times 1.91$ eV) for ionization in the vicinity of the triangular structure. According to this energy scheme, first, wavelengths around 560 nm ($\triangleq$ 2.24 eV) would be required and later, longer wavelengths of about 650 nm ($\triangleq$ 1.9 eV). The VIS traces in Fig. 4.19 shows an inverted pulse sequence, beginning with long wavelengths about 730 nm ($\triangleq$ 1.7 eV) ranging from -600 to -400 fs and short wavelengths down to 530 nm ($\triangleq$ 2.34 eV) at later times around 500 fs.

Discussion Exp. V The current optimization started with the same preconditions as the previous experiment (phase noise from 450–950 nm) but with an enhanced VIS spectrum to favor sequences in the VIS part. Optimization of the provided homogeneous spectrum (see Fig. 4.12c) confirmed the results of Exp. IV, as is seen in the trace of Fig. 4.21. A difference occurs in the leading edge of the VIS pulse, where only wavelengths at about 680 nm are utilized in contrast to the 730 nm in Exp. IV. Also a lucid concentration of the VIS spectra around 600 fs was found.

Discussion Exp. VI - Parametric pulse shapes Since the assignment of optimized pulse forms to nuclear dynamics is not trivial, an analytical approach was undertaken consisting of parametric pulse shapes in the VIS part. The short NIR pulse served as "pump" pulse and the VIS light excited the ensemble with a pulse train of variable sub pulse separation in the first attempt. However, a clear Ag_3^+ signal dependence on the pulse spacing like in the shaping experiment with Ag_2 in Fig. 4.6 was not obvious (data not shown). The minor changes of the ion signal were mainly caused by the fidelity of generating different pulse trains rather than by induced dynamics.

The second approach with a time delayed and chirped VIS pulse showed a maximum of the ion yield for a negative prechirp, shifted to about +560 fs like in Fig. 4.23a. Noteworthy, due to the negative chirp wavelengths of 575 nm ($\triangleq$ 2.16 eV) appearing at a delay time of about 480 fs which very well agrees with the simulation of the 6.5 eV ($\approx 3 \times 2.16$ eV) peak of the probe pulse in Fig. 4.10c that reaches its maximum at 450 fs. Appositely, the lower energies (5.9 eV correspond to three photons at 630 nm) arrive later in the trace of Fig. 4.23a, but much earlier than expected from the calculation, shown as dashed curve in Fig. 4.10c. The more interesting, when this parameterized mask of Fig. 4.23a is utilized as an initial guess for the EA, exactly these wavelengths at 630 nm are shifted even further towards earlier instead of later times, as is hinted by the gray arrow in Fig. 4.23b. A similar shift of 640 nm wavelengths towards the NIR pulse is also seen in the optimization of Fig. 4.16 in Exp. III.

Discussion Exp. VII In order to investigate the interplay between NIR and VIS frequencies, the relative strength of the NIR part was reduced with respect to the VIS in Exp. V in Fig. 4.21. For the current experiment, the NIR was completely blocked during optimization leading to the mask in the lower part of Fig. 4.26. As before, lower frequencies arrive in the beginning and higher ones later in the pulse. In the main, the trace compares to the previous ones, but slight changes become visible. The long extending sequence around 730 nm like in Fig. 4.13b and Fig. 4.19b/c is missing. Further on, most of the VIS sub pulses are very short, since several isolated sub pulses exhibit durations on the order of 30 fs. The yellow ellipses have the same temporal and spectral proportions as the two traces of the last presented experiment.

Discussion Exp. VIII The partial low pass filtering of the NIR part from 900-1000 nm in the shaper setup generally confirmed the result of Exp. VII, as can be compared by the ellipses with Figs. 4.26 and 4.27. The wavelengths around 925 nm were not utilized in Fig. 4.27 to generate a short pump pulse, meaning that the VIS part solely completed the charge reversal process. A striking feature of Fig. 4.27 is the negative chirp at around 550 nm ($\triangleq$ 2.25 eV) which is visible in two independent optimizations. This wavelength is too low for two photon ionization (4.5 eV) at any point of the PES of Fig. 4.8. Assuming a three photon process (6.67 eV) this energy would match the potential energy gap for ionization of the linear Ag_3 ($\mathrm{IP}_{lin} = 6.67$ eV [11, 142]).

Discussion - successive optimization Finally, one issue is addressed concerning EA: The problem of finding the global maximum in the search space rather than getting stuck in a local minimum. As can be seen in hitherto presented optimization curves, convergence of best, mean and worst population curves was not guarantied, even when the global optimum was found. This proof of reaching a global optimum can be clearly stated in the case of adaptive pulse compression in Fig. 3.28. This task has a uniquely defined (physical) optimum, namely a flat spectral phase for the exiting light field. However, although the shortest pulse was found, convergence of the optimization curves in Fig. 3.28a is not identifiably. If such curves occur during optimization, the question arises whether the global optimum is found or not.

In order to tackle this inherent problem of EA, the method of successive optimization was introduced for generating the pulses of Fig. 4.27a and b). This means that the final pulse structure was achieved by consecutive optimization runs, as is shown by the three linked optimization curves in Fig. 4.28. The first optimization in a) starts with noise in the VIS and remaining NIR region and shows no further increase after 15 iterations. At this point the question raises whether the global maximum is already reached or not. In such a situation, the genes of all individuals are related to each other. Simultaneously, the mutation rate is automatically reduced, meaning that the EA is caught on this hill in search space and cannot escape to find the global maximum.

One way to force the algorithm to create new populations is to increase either the mutation rate (σ) or the cross over. However, both ways expand the search space only around the local position. This restriction can be overcome by starting a new optimization with the best population from the previous run as the initial guess. This has the advantage of including completely new genes to the populations which were not assessable by changing the mutation rate or the cross over. Figure 4.28b shows the evolution when beginning with this kind of staring conditions. The wave form of the initial guess lead to a considerably higher ion yield (black line) than the noise level which contributes to the values for mean and worst population. Therefore, in the beginning the difference between best and mean/worst population is larger than in the first run. The successful second optimization shows a signal increase from 375 to 600 counts. Thus, stagnation of optimization, as it occurred after 15 iterations in a) is now bettered. In the following third optimization, this procedure was repeated. Again, during the first five optimizations it can be seen how the crossover leads to a new gen pool which still enables a slight increase of the ion signal.

Concluding remarks Reproducible feedback loop experiments with shaped white light pulses, generated by means of plasma filamentation in air have been demonstrated. The idea of utilizing shaped fs white light pulses has been successfully applied for the optimization of charge reversal on $Ag_3^-/Ag_3/Ag_3^+$ in a gas phase experiment. More than one optical octave was provided for the spectral search space for the evolutionary algorithm. The experiments clearly showed different excitation mechanisms for different wavelength regions, emerging on much shorter time scales than in previous pump probe measurements.

In comparison to the previous NeNePo results of Fig. 4.9, where configurational relaxation dynamics of bending from a linear to the triangular structure were investigated via pump probe measurements, the new experiments with shaped WL pulses for the first time exhibit temporal structures far below the time scale of the IVR process, occurring after 700 fs. Free optimization of the spectral phase from 450–950 nm gained an extremely short pulse at NIR wavelengths from 760–950 nm and a highly structured VIS sequence from 530–760nm. The very pronounced temporal as well as spectral VIS signatures, which were never observed before, indicate that a matching of the ionization energy is found at the corresponding times. This defined excitation could be interpreted as a consequence of fulfilling the ZEKE-NeNePo conditions. Although the optimized WL pulses, especially the traces of Fig. 4.19b and c) exhibit ultra short pulse sequences and a rich structure in the VIS spectral range around 600 nm, which correspond to the aimed energy region between 5.9 and 6.5 eV in a three photon order, the main goal from the coherent control aspect, namely a differentiation of the predicted coherence effects [11, 142] after the intramolecular collision was not just jet assigned in the current optimization results. Theoretical calculations on this issue are currently under investigation in the group of Bonačić-Koutecký.

This key experiment of my thesis not only displays thus the consolidation of generating the octave spanning WL continuum with the ability to freely manipulate this spectrum in a pulse shaper. Even more - stimulated by theory work [11, 142], a new and promising ultrashort pulse sequence was found, at present in the status of being "unfettered by the limits of human mind" [130]. Now the ball is in the court of theory again.

Conclusion and Outlook

This thesis describes two research goals. First to extend the charge reversal (NeNePo) spectroscopy of small Ag clusters by adaptive coherent control strategies to enhance the excitation selectivity of a desired quantum state. Second, to improve the control tool by providing one octave of coherent frequencies, spanning from the VIS to the NIR region.

For this purpose both high stability and reproducibility of the broadened spectrum are indispensable. This was realized by filamentation in atmospheric air through slightly focusing amplified fs laser pulses of about 1 mJ. In the development of this light source as a tool for investigations of ultrafast dynamics, the filamentation process itself was studied to learn more about the interplay between the Kerr effect and weakly ionized plasma. The characterization of different gases (noble gases, air and 0_2) confirmed an analogous mechanism based on the initial action of self-phase modulation, causing spectral broadening around the laser fundamental and the retarded generation of an asymmetric spectral shoulder approaching the UV range. One explanation found in the literature for this pronounced broadening on the short wavelength side is a plasma blue shift which was also retraced in simulations for this work. Generally, gases with higher nonlinear refractive index n_2 require lower pulse energy and gas pressure, respectively, to achieve WL generation. The shape of spectral broadening around the fundamental strongly depends on the prechirp. In contrast, the VIS tail keeps its spectral shape and positive chirp, unless a strong prechirp completely terminates filamentation. Zero prechirping at high input energy or pressure, respectively, causes the highest nonlinearity and the pulse tends to first split temporally. Later, with still increased nonlinearity it also splits spatially. An alternative for tuning the filamentation conditions lies in adding He to the air which tends to halt the filamentation process. This quenching effect due to the low nonlinearity of He might be utilized to scale filamentation towards even higher energy throughput. However, with the right preconditions a reliable pulse compression down to 6.3 fs for filamentation in air was enabled with four bounces on chirped mirrors in the range from 600–900 nm. Currently, these are the shortest pulses generated via filamentation in air. Variable compression from 450–1000 nm can be achieved with the bare 4-f setup which actually corresponds to a telescope-grating compressor.

Since the characterization of few optical cycles and octave exceeding bandwidths, respectively, is as demanding as its generation, a commercial solution is not available. By implementing a TG-FROG, bandwidths ranging from 380–950 nm were optically gated for the first time. This provided the basis for extensively studying the temporal and spectral properties of the WL. This FROG variant utilizes 4WM of the three incoming beams according to a forward box scenario and requires only BK 7 glass as the nonlinear medium. Several special features of this gate mechanism are very promising for a wide range of applications in ultrafast pulse characterization: First, it does not convert the frequency of the gated pulse (unlike SHG, THG or SFG), and therefore leads to intuitive traces avoiding ambiguities of other FROG methods. Second, it handles the entire transmission range of the nonlinear medium and is realized with standard optical components. The problem of choosing appropriate beam splitters to provide the three beams can be overcome by geometrical beam separation, as was successfully demonstrated for the measurement of the few cycle pulses. Furthermore, the combination of WL shaping and 4WM not only allows the

characterization of very complex pulse forms but also the unique possibility of cross-correlation measurements in a single beam arrangement, which was named single beam TG-X-FROG.

Its prerequisite is a controllable pulse shaping device. To assure this controllability from 450–950 nm, the WL shaper built in this work needed to be calibrated for every pixel due to the wavelength dependent operation of the liquid crystals in the spatial light modulator (SLM). In this manner, the realization of a double color pump probe excitation scheme was demonstrated likewise as a single beam setup. In this example, a short VIS pulse centered at 625 nm was time delayed with respect to a short NIR pulse centered at 800 nm by applying a linear phase ramp to the VIS part by the SLM. Since the third order optical nonlinearity of the 4WM process connotes a high sensitivity of the 4WM signal on the input pulse duration, it was utilized for adaptive pulse compression with the shaper. By this, optimizing the 4WM signal in a feedback loop experiment with an evolutionary algorithm turned out to be a straight forward approach for pulse compression of the filament output. This technique differs from others, in that knowledge of the phase of the incoming light field is not required and the optimized spectral phase function on the SLM defines a correcting reference from which analytical functions can be generated.

As the other goal of the thesis was the extension of the NeNePo scheme by shaped pulses, an analytic approach was established first on the diatomic Ag_2 before the free optimization of the WL was applied for Ag_3 NeNePo spectroscopy. The analytic approach covers the generation of pulse trains with variable sub pulse separation by amplitude shaping the laser fundamental spectrum. This delivered a cyclic driving of the photo detachment step, being subsequently probed by a single time delayed ionization pulse. Due to the Fourier relation between the time and frequency domains, a synchronization of the sub pulse separation to the vibrational period of the neutral Ag_2 preferentially excites the vibrational eigenstates of the neutral species, leading to an enhanced localization of the wave packet which can be probed most efficiently. This experiment opens the door towards mode selective pumping and probing of the NeNePo process of more complex systems.

When adding one atom to create the trimer Ag_3, the nuclear dynamics gains complexity. In particular, the neutral Ag_3 undergoes configurational changes from linear to an obtuse triangular structure by bending the outer atoms. The bending ends with an intra-molecular collision, followed by IVR which populates other vibrational modes. Since coherence effects after that collision were never identified in previous pump probe experiments, free optimization of WL pulses denotes a new and promising approach. The optimized supercontinuum exhibits two distinct spectral regions, each containing very short pulses or pulse sequences, respectively. The NIR spectral region from 750–950 nm was exclusively optimized to a compressed pulse when starting from phase noise. In contrast, the VIS part from 530–760 nm contains a rich structure apparent in all optimization experiments. The time scales of the spectrally and temporally modulated VIS sequences exhibit for the first time temporal structures far below the time scale of the IVR process. Thus they refrain from an intuitive interpretation in the aimed direction of finding indications for preserved coherences after the collision. In a similar sense Talbot annotated his Photogenic Drawings [3]:

" *They are impressed by Nature's hand; and what they want us jet of delicacy and finish of execution arises chiefly from our want of sufficient knowledge of her laws.*"

To further verify the excitation path to the cationic species, a collaboration with the theory group of Bonačić-Koutecký is in progress. However, the closed loop results for free phase optimization of the NeNePo process witness the first-time application of shaped WL, generated via filamentation, for coherent quantum control.

Utilizing the output of the filamentation process as a light source emphasizes the generation of new wavelengths, blue shifted with respect to the inducing laser fundamental. The investigated TG-X-FROG mechanism was proven to gate frequencies which lie one octave below the grating pulses. Why not transfer this scheme to a fundamental wavelength of 400 nm? Although the frequency doubling from 800 to 400 nm reduces pulse energy, filamentation will benefit from the increased nonlinear index n_2 at shorter wavelengths and increasing cross sections for multi photon ionization at higher photon energy [37]. The spectral operation for TG FROG is limited by the transmission range of the nonlinear medium which closes at about 190 nm in case of Fused Silica. Since reflective pulse shapers with mirrors are already available, the single beam pump probe excitation and the single beam TG-X-FROG can be applied for investigation on biological systems which typically absorb in the UV range. By this, the artists palette will be further extended for drawing new images of nature.

Bibliography

[1] H. Temporini and J. Vogt. *Aufstieg und Niedergang der römischen Welt*. Walter de Gruyter, 1972.

[2] P. Pollack. *Die Welt der Photographie von ihren Anfängen bis zur Gegenwart*. Econ-Verlag, Wien, Düsseldorf, 1962.

[3] W. H. F. Talbot. *The Pencil of Nature*. Hogyf Edito, Budapest, Reprint 1998.

[4] M. Drescher, M. Hentschel, R. Kienberger, M. Uiberacker, V. Yakovlev, A. Scrinzi, T. Westerwalbesloh, U. Kleineberg, U. Heinzmann, and F. Krausz. Time-resolved atomic inner-shell spectroscopy. *Nature*, 419:803, 2002.

[5] F. Krausz. Tracking light oscillations: attosecond spectroscopy comes of age. *Photonics News*, 13:62, 2002.

[6] J. Itatani, J. Levesque, D. Zeidler, H. Niikura, H. Pepin, J. C. Kieffer, P. B. Corkum, and D. M. Villeneuve. Tomographic imaging of molecular orbitals. *Nature*, 432:867–872, 2004.

[7] M. Dantus, M. J. Rosker, and A. H. Zewail. Real-time femtosecond probing of "transition states" in chemical reactions. *J. Chem. Phys.*, 87:2395, 1987.

[8] O. Kühn and Wöste (*Ed.*) L. *Analysis and Control of Ultrafast Photoinduced Reactions*. Springer Series in Chemical Physics, 2007.

[9] P. Fayet, F. Granzer, G. Hegenbart, E. Moisar, B. Pischel, and L. Wöste. Latent-image generation by deposition of monodisperse silver clusters. *Phys. Rev. Lett.*, 55(27):3002–3004, Dec 1985.

[10] S. Wolf, G. Sommerer, S. Rutz, E. Schreiber, T. Leisner, L. Wöste, and R. Stephen Berry. Spectroscopy of size-selected neutral clusters: Femtosecond evolution of neutral silver trimers. *Phys. Rev. Lett.*, 74(21):4177–4180, May 1995.

[11] M. Hartmann, J. Pittner, V. Bonačić-Koutecký, A. Heidenreich, and J. Jortner. Theoretical exploration of femtosecond multi-state nuclear dynamics of small clusters. *The Journal of Chemical Physics*, 108(8):3096–3113, 1998.

[12] I. Andrianov, V. Bonačić-Koutecký, M. Hartmann, J. Manz, J. Pittner, and Sundermann K. Ab initio three-dimensional quantum dynamics of Ag_3 clusters in the nenepo process. *Chem. Phys. Lett.*, 318:256–262, 2000.

[13] A. Braun, G. Korn, X. Liu, D. Du, J. Squier, and G. Mourou. Self-channeling of high-peak-power femtosecond laser pulses in air. *Opt. Lett.*, 20(1):73, 1995.

[14] J. Kasparian, M. Rodriguez, G. Mejean, J. Yu, E. Salmon, H. Wille, R. Bourayou, S. Frey, Y.-B. Andre, A. Mysyrowicz, R. Sauerbrey, J.-P. Wolf, and L. Woeste. White-light filaments for atmospheric analysis. *Science*, 301:61–64, 2003.

[15] A. Cho. Connecting the dots to custom catalysts. *Science*, 299:1684–1685, 2003.

[16] S. M. Weber. *New concepts for optimal control experiments using femtosecond pulse shaping*. Phd thesis, Freie Universität Berlin, 2007.

[17] P. Nuernberger, G. Vogt, T. Brixner, and G. Gerber. Femtosecond quantum control of molecular dynamics in the condensed phase. *Phys. Chem. Chem. Phys*, 9:2470–2497, 2007.

[18] D.W. Boo, Y. Ozaki, L.H. Andersen, and W.C. Lineberger. Femtosecond dynamics of linear Ag_3. *Journal of Physical Chemistry A*, 101(36):6688–6696, 1997.

[19] T. Leisner, S. Vajda, S. Wolf, L. Wöste, and R. S. Berry. The relaxation from linear to triangular Ag_3 probed by femtosecond resonant two-photon ionization. *The Journal of Chemical Physics*, 111(3):1017–1021, 1999.

[20] Ed. H. Niedrig. *Bergmann Schaefer Lehrbuch der Experimentalphysik Band 3*. Walter de Gruyter, Berlin, 1993.

[21] U. Zinth W. Zinth. *Optik*. Oldenburg, München, Wien, 2005.

[22] K. Kosma W. E. Schmid S. A. Trushin, S. Panja and W. Fuß. Supercontinuum extending from >1000 to 250 nm, generated by focusing ten-fs laser pulses at 805 nm into ar. *Appl. Phys. B*, 80:399–403, 2005.

[23] E. Goulielmakis, S. Koehler, B. Reiter, M. Schultze, A. J. Verhoef, E. E. Serebryannikov, A. M. Zheltikov, and F. Krausz. Ultrabroadband, coherent light source based on self-channeling of few-cycle pulses in helium. *Opt. Lett.*, 33(13):1407–1409, 2008.

[24] J.-W. Kim E. P. Ippen J. G. Fujimoto Franz X. Kaertner V. Scheuer T. R. Schibli, O. Kuzucu and G. Angelow. Toward single-cycle laser systems. *IEEE Journ. Selected Topics in Quant. Electron.*, 9:990–1001, 2003.

[25] Ed. C. Rulliere. *Femtosecond laser pulses: principles and experiments*. Springer Verlag, Berlin, Heidelberg, 2005.

[26] W. Rudolph J.-C. Diels. *Ultra short pulse phenomena*. Academic press, San Diego, 1996.

[27] M. M. Murnane S. Backus, C. G. Durfee and H. C. Kapteyn. High power ultrafast lasers. *Rev. Si. Instr.*, 69:1207–1223, 1998.

[28] T. Brabec and F. Krausz. Intense few-cycle laser fields: Frontiers of nonlinear optics. *Rev. Mod. Phys.*, 72(2):545–591, Apr 2000.

[29] G. Mourou D. Strickland. Compression of amplified chirped optical pulses. *Opt. Commun.*, 56(3):219, 1985.

[30] T. H. Maiman. Stimulated optical radiation in ruby. *Nature*, 187:493–494, 1960.

[31] P. A. Franken, A. E. Hill, C. W. Peters, and G. Weinreich. Generation of optical harmonics. *Phys. Rev. Lett.*, 7(4):118–119, Aug 1961.

[32] Robert W. Boyd. *Nonlinear Optics*. Academic Press, London, 2003.

[33] G. P. Agrawal. *Nonlinear fiber optics*. Academic Press, San Diego, 2001.

[34] Y. R. Shen. *Principles of nonlinear optics*. Wiley, New York, 1984.

[35] T. Brabec and F. Krausz. Nonlinear optical pulse propagation in the single-cycle regime. *Phys. Rev. Lett.*, 78(17):3282–3285, Apr 1997.

[36] L. Bergé, S. Skupin, R. Nuter, J. Kasparian, and J.-P. Wolf. Ultrashort filaments of light in weakly-ionized, optically-transparent media. *Rep. Prog. Phys.*, 70:1633—-1713, 2007.

[37] A. Mysyrowicz A. Couairon. Femtosecond filamentation in transparent media. *Physics Reports*, 441:47–189, 2007.

[38] R. Y. Chiao, E. Garmire, and C. H. Townes. Self-trapping of optical beams. *Phys. Rev. Lett.*, 13(15):479–482, Oct 1964.

[39] Fujio Shimizu. Frequency broadening in liquids by a short light pulse. *Phys. Rev. Lett.*, 19(19):1097–1100, Nov 1967.

[40] J.H. Marburger. Self-focusing: Theory. *Prog. Quant. Electr.*, 4:35—-110, 1975.

[41] D. E. Spence, P. N. Kean, and W. Sibbett. 60-fsec pulse generation from a self-mode-locked ti:sapphire laser. *Opt. Lett.*, 16(1):42, 1991.

[42] B. S. Prade C. Grillon C. Le Blanc E. T. J. Nibbering, M. A. France and A. Mysyrowicz. Measurement of the nonlinear refractive index of transparent materials by spectral analysis after nonlinear propagation. *Opt. Com.*, 119:479–484, 1995.

[43] E. T. J. Nibbering, G. Grillon, M. A. Franco, B. S. Prade, and A. Mysyrowicz. Determination of the inertial contribution to the nonlinear refractive index of air, N_2, and O_2 by use of unfocused high-intensity femtosecond laser pulses. *J. Opt. Soc. Am. B*, 14(3):650–660, 1997.

[44] R. R. Alfano and S. L. Shapiro. Observation of self-phase modulation and small-scale filaments in crystals and glasses. *Phys. Rev. Lett.*, 24(11):592–594, Mar 1970.

[45] H. D. Ladouceur, A. P. Baronavski, D. Lohrmann, P. W. Grounds, and P.G. Girardi. Electrical conductivity of a femtosecond laser generated plasma channel in air. *Opt. Commun.*, 189(4):107, 2001.

[46] Kegel. *Plasmaphysik, eine Einführung*. Springer, Berlin, 1998.

[47] D. Attwood. *Soft x-rays and extreme ultraviolet radiation*. Cambridge University Press, Cambridge, 2000.

[48] S. Tzortzakis, M. A. Franco, André, Y.-B., A. Chiron, B. Lamouroux, B. S. Prade, and A. Mysyrowicz. Formation of a conducting channel in air by self-guided femtosecond laser pulses. *Phys. Rev. E*, 60(4):R3505–R3507, Oct 1999.

[49] J. D. Gaskill. *Linear Systems, Fourier Transforms, and Optics*. John Wiley Sons Inc, New York, Chichester, Brisbane, Toronto, 1978.

[50] E. Yablonovitch. Self-phase modulation of light in a laser-breakdown plasma. *Phys. Rev. Lett.*, 32(20):1101–1104, May 1974.

[51] E. Yablonovitch. Self-phase modulation and short-pulse generation from laser-breakdown plasmas. *Phys. Rev. A*, 10(5):1888–1895, Nov 1974.

[52] I.G. Koprinkov. Ionization variation of the group velocity dispersion by high-intensity optical pulses. *Appl. Phys. B*, 79:359, 2004.

[53] I. G. Koprinkov, Akira Suda, Pengqian Wang, and Katsumi Midorikawa. Self-compression of high-intensity femtosecond optical pulses and spatiotemporal soliton generation. *Phys. Rev. Lett.*, 84(17):3847–3850, Apr 2000.

[54] P. B. Corkum. Plasma perspective on strong field multiphoton ionization. *Phys. Rev. Lett.*, 71(13):1994–1997, Sep 1993.

[55] S. Tzortzakis, G. Méchain, G. Patalano, Y.-B. André, B. Prade, M. Franco, A. Mysyrowicz, J.-M. Munier, M. Gheudin, G. Beaudin, and P. Encrenaz. Coherent subterahertz radiation from femtosecond infrared filaments in air. *Opt. Lett.*, 27(21):1944–1946, 2002.

[56] N. B. Delone and V. P. Krainov. *Multiphoton Processes in Atoms*. Springer-Verlag, Berlin, 1994.

[57] S. L. Chin and P. Lambropoulos. *Multiphoton Ionization of Atoms*. Academic Press, New York, 1984.

[58] A. Staudt. *Atomare Zweielektronensysteme in intensiven Laserpulsen*. PhD thesis, Albert-Ludwigs-Universität Freiburg, 2005.

[59] A. Talebpour, J. Yang, , and S.L. Chin. Semi-empirical model for the rate of tunnel ionization of N_2 and O_2 molecule in an intense Ti:Sapphire laser pulse. *Opt. Commun.*, 163(1):29–32, 1999.

[60] K. Mishima, M. Hayashi, J. Yi, S. H. Lin, H. L. Selzle, and E. W. Schlag. Generalization of Keldysh's theory. *Phys. Rev. E*, 66:0334011, 2002.

[61] P. Agostini, F. Fabre, G. Mainfray, G. Petite, and N. K. Rahman. Free-free transitions following six-photon ionization of Xenon atoms. *Phys. Rev. Lett.*, 42(17):1127–1130, Apr 1979.

[62] P. Kruit, J. Kimman, H. G. Muller, and M. J. van der Wiel. Electron spectra from multiphoton ionization of Xenon at 1064, 532, and 355 nm. *Phys. Rev. A*, 28(1):248–255, Jul 1983.

[63] G. Paulus, F. Grabson, H. Walther, R. Kopold, and W. Becker. Atome im intensiven laserfeld - auf feynmans quantenpfaden. *Physik in unserer Zeit*, 33:74–81, 2002.

[64] B. Walker, B. Sheehy, L.F. DiMauro, P. Agostini, K.J. Shafer, and K.C. Kulander. Precision measurement of strong field double ionization of Helium. *Phys. Rev. Lett*, 73:1227, 1994.

[65] S. Larochelle, A. Talebpour, and S.L. Chin. Non-sequential multiple ionization of rare gas atoms in a Ti:Sapphire laser field. *J. Phys. B*, 31:1201—-1214, 1998.

[66] E. Eremina, X. Liu, H. Rottke, W. Sandner, M. G. Schätzel, A. Dreischuh, G. G. Paulus, H. Walther, R. Moshammer, and J. Ullrich. Influence of molecular structure on double ionization of N_2 and O_2 by high intensity ultrashort laser pulses. *Phys. Rev. Lett.*, 92(17):173001, Apr 2004.

[67] Weber, Th., Weckenbrock, M., Staudte, A., Spielberger, L., Jagutzki, O., Mergel, V., Afaneh, F., Urbasch, G., Vollmer, M., Giessen, H., Dörner, and R. Recoil-ion momentum distributions for single and double ionization of helium in strong laser fields. *Phys. Rev. Lett.*, 84(3):443–446, Jan 2000.

[68] H. Vogel. *Gerthsen Physik*. Springer Verlag, 20. Auflage, Berlin, Heidelberg, 1995.

[69] H. Tawara and T. Kato. Total and partial ionization cross sections of atoms and ions by electron impact. *At. Data Nucl. Data Tables*, 36:167—-353, 1987.

[70] J.E. Rothenberg. Space–time focusing: breakdown of the slowly varying envelope approximation in the self-focusing of femtosecond pulses. *Opt. Lett.*, 17(19):1340—1342, 1992.

[71] N. Aközbek, M. Scalora, C. M. Bowden, and S. L. Chin. White-light continuum generation and filamentation during the propagation of ultra-short laser pulses in air. *Opt. Commun.*, 191(4):353, 2001.

[72] L. Bergé F. Lederer T. Sokollik M. Schnürer N. Zhavoronkov S. Skupin, G. Stibenz and G. Steinmeyer. Self-compression by femtosecond pulse filamentation: Experiments versus numerical simulations. *Phys. Rev. E*, 74(5):056604, 2006.

[73] A. A. Zozulya, S. A. Diddams, and T. S. Clement. Investigations of nonlinear femtosecond pulse propagation with inclusion of Raman, shock, and third oder phase effects. *Phys. Rev. A*, 58(4):3303–3310, 1998.

[74] G. Yang and Y. R. Shen. Spectral broadening of ultrashort pulses in a nonlinear medium. *Opt. Lett.*, 9:510—-512, 1984.

[75] A. L. Gaeta. Catastrophic collapse of ultrashort pulses. *Phys. Rev. Let.*, 84(16):3582–3585, 2000.

[76] J. K. Ranka and A. L. Gaeta. Breakdown of the slowly varying envelope approximation in the self-focusing of ultrashort pulses. *Opt. Lett.*, 23(7):534–536, 1988.

[77] R. W. Schirmer J. K. Ranka and A. L. Gaeta. Observation of pulse splitting in nonlinear dispersive media. *Physical Review Letters*, 77(18):3783–3786, 1996.

[78] A. Suda M. Nurhuda and K. Midorikawa. Ionization-induced high-order nonlinear susceptibility. *Phys. Rev. A*, 66(4):041802, 2002.

[79] J.E. Rothenberg. Pulse splitting during self-focusing in normally dispersive media. *Opt. Lett.*, 17(8):583—-585, 1992.

[80] Y. R. Shen. Recent advances in nonlinear optics. *Rev. Mod. Phys.*, 48:1–32, 1976.

[81] S. A. Diddams, H. K. Eaton, A. A. Zozulya, and T. S. Clement. Amplitude and phase measurements of femtosecond pulse splitting in nonlinear dispersive media. *Opt. Lett.*, 23(5):379–381, 1998.

[82] Y. B. Band M. Trippenbach. Dynamics of short-pulse splitting in dispersive nonlinear media. *Physical Review A*, 56(5):4242–4253, 1997.

[83] A. A. Zozulya, S. A. Diddams, H. K. Eaton, and T. S. Clement. Propagation dynamics of intense femtosecond laser pulses: multiple splittings, coalescence and continuum generation. *Phys. Rev. Lett.*, 82(7):1430–1433, 1999.

[84] M. Zhavoronkov G. Stibenz and G. Steinmeyer. Self-compression of millijoule pulses to 7.8 fs duration in a white-light filament. *Opt. Lett.*, 31(2):274–277, 2006.

[85] T. Popmintchev I. P. Christov M. M. Murnane N. L. Wagner, E. A. Gibson and H. C. Kapteyn. Self-compression of ultrashort pulses through ionization-induced spatiotemporal reshaping. *Phys. Rev. Lett.*, 93(17):173902, 2004.

[86] J. Liu Y. Zhu R. Li X. Chen, Y. Leng and Z. Xu. Pulse self-compression in normally dispersive bulk media. *Opt. Commun.*, 259(1):331, 2006.

[87] N. Auby T. Lehner. Stabilization of the kerr effect by self induced ionization: Formation of optical light spatially localized structures. *Physical Review E*, 61(2):1996–2005, 2000.

[88] L. Cohen. Time-frequency distributions-a review. *Proceedings of the IEEE*, 77:941–981, 1989.

[89] Emily J. Brown, Qingguo Zhang, and Marcos Dantus. Femtosecond transient-grating techniques: Population and coherence dynamics involving ground and excited states. *The Journal of Chemical Physics*, 110(12):5772–5788, 1999.

[90] Y. Mairesse, D. Zeidler, N. Dudovich, M. Spanner, J. Levesque, D. M. Villeneuve, and P. B. Corkum. High-order harmonic transient grating spectroscopy in a molecular jet. *Physical Review Letters*, 100(14):143903, 2008.

[91] K. Isobe, S. Kataoka, R. Murase, W. Watanabe, T. Higashi, S. Kawakami, S. Matsunaga, K. Fukui, and K. Itoh. Stimulated parametric emission microscopy. *Opt. Exp.*, 14(2):786–793, 2006.

[92] E. Wolf M. Born. *Principles of Optics*. Pergamon Press, London, 1959.

[93] Goodman. *Introduction to Fourier optics*. McGraw-Hill, New York, 1996.

[94] P. Hariharan. *Optical holography: principles, techniques, and applications*. Cambridge University Press, Cambridge, 1996.

[95] D. W. Phol H. J. Eichler, P. Günter. *Laser-induced dynamic gratings*. Springer Verlag, Berlin, Heidelberg, 1986.

[96] D. Keusters, H-S Tan, P. O'Shea, Zeek E., R. Trebino, and W. S. Warren. Relative phase ambiguities in measurements of ultrashort pulses with well-separated multiple frequency components. *J. Opt. Soc. Am. B*, 20(10):2226–2237, 2003.

[97] P. Bowlan, P. Gabolde, A. Shreenath, K. McGresham, and R. Trebino. Crossed-beam spectral interferometry: a simple, high-spectral-resolution method for completely characterizing complex ultrashort pulses in real time. *Opt. Exp.*, 14(24):11892–11900, 2006.

[98] M. Wollenhaupt, A. Assion, and T. Baumert. *Handbook of Lasers and Optics, F. Träger, Ed., Chapter 12: Femtosecond Laser Pulses: Linear Properties, Manipulation, Generation and Measurement*. Springer Science and Business Media, New York, 2007.

[99] Lina Xu, Erik Zeek, and Rick Trebino. Simulations of frequency-resolved optical gating for measuring very complex pulses. *J. Opt. Soc. Am. B*, 25(6):A70–A80, 2008.

[100] I. A. Walmsley and V. Wong. Characterization of the electric field of ultrashort optical pulses. *JOSA B*, 13:2453–2463, 1996.

[101] L. Gallmann, D. H. Sutter, N. Matuschek, G. Steinmeyer, and U. Keller. Techniques for the characterization of sub-10-fs optical pulses: a comparison. *Appl. Phys. B*, 70:67–75, 2000.

[102] R. Morita, M. Hirasawa, N. Karasawa, S. Kusaka, N. Nakagawa, K. Yamane, L. Li, A. Suguro, and M. Yamashita. Sub-5 fs optical pulse characterization. *Meas. Sci. Technol.*, 13:1710—-1720, 2002.

[103] Rick Trebino and Daniel J. Kane. Using phase retrieval to measure the intensity and phase of ultrashort pulses: frequency-resolved optical gating. *J. Opt. Soc. Am. A*, 10(5):1101, 1993.

[104] D. N. Fittinghoff J. N. Sweetser M. A. Krumbügel B. A. Richman R. Trebino, K. W. DeLong and D. J. Kane. Measuring ultrashort laser pulses in the time-frequency domain using frequency-resolved optical gating. *Rev. Si. Instr.*, 68:3277–3295, 1997.

[105] S. Linden, J. Kuhl, and H. Giessen. Amplitude and phase characterization of weak blue ultrashort pulses by downconversion. *Opt. Lett.*, 24(8):569–571, 1999.

[106] Selcuk Akturk, Ciro D'Amico, and Andre Mysyrowicz. Measuring ultrashort pulses in the single-cycle regime using frequency-resolved optical gating. *J. Opt. Soc. Am. B*, 25(6):A63–A69, 2008.

[107] D. Lee, P. Gabolde, and R. Trebino. Toward single-shot measurement of a broadband ultrafast continuum. *J. Opt. Soc. Am. B*, 25(6):A34–A40, 2008.

[108] A. C. Eckbreth. Boxcars: Crossed-beam phase matched CARS generation in gases. *Appl. Phys. Lett.*, 32(7):421–423, 1978.

[109] A. Compaan and S. Chandra. Coherent anti-stokes raman scattering with counterpropagating laser beams. *Opt. Lett.*, 4(8):170–172, 1979.

[110] J. A. Shirley, R. J. Hall, and A. C. Eckbreth. Folded BOXCARS for rotational Raman studies. *Opt. Lett.*, 5(9):380–382, 1980.

[111] Kenneth W. DeLong, David N. Fittinghoff, Rick Trebino, Bern Kohler, and Kent Wilson. Pulse retrieval in frequency-resolved optical gating based on the method of generalized projections. *Opt. Lett.*, 19(24):2152, 1994.

[112] Daniel J. Kane. Principal components generalized projections: a review. *J. Opt. Soc. Am. B*, 25(6):A120–A132, 2008.

[113] D. J. Kane. Real time measurement of ultrashort laser pulses using principal component generalized projections. *IEEE J. Sel. Top. Quantum Electron.*, 4:278—-284, 1998.

[114] D. J. Kane, J. Weston, , and K.-C. J. Chu. Real-time inversion of polarization gate frequency resolved optical gating spectrograms. *Appl. Opt.*, 42(6):1140—1144, 2003.

[115] B Seifert, H. Stolz, and M. Tasche. Nontrivial ambiguities for blind frequency-resolved optical gating and the problem of uniqueness. *J. Opt. Soc. Am. B*, 21(5):1089–1097, 2004.

[116] H. Haken and H.C. Wolf. *Molekülphysik und Quantenchemie*. Springer, Berlin.

[117] D. J. Tannor. *Introduction to Quantum Mechanics, A Time-Dependent Perspective*. University Science Books, Sausalito, 2007.

[118] C. L. Cohen-Tannoudji, B. Diu, and F. Laloë. *Quantenmechanik*, volume I. Walter de Gruyter, Berlin, 1999.

[119] W. S. Warren, H. Rabitz, and M. Dahleh. Coherent control of quantum dynamics: The dream is alive. *Science*, 259:1581–1589, 1993.

[120] P. Brumer and M. Shapiro. Control of unimolecular reactions using coherent light. *Chem. Phys. Lett.*, 126:541–546, 1986.

[121] Ce Chen, Yi-Yian Yin, and D. S. Elliott. Interference between optical transitions. *Phys. Rev. Lett.*, 64(5):507–510, Jan 1990.

[122] David J. Tannor and Stuart A. Rice. Control of selectivity of chemical reaction via control of wave packet evolution. *J. Chem. Phys.*, 83(10):5013–5018, 1985.

[123] R. Kosloff, S.A. Rice, P. Gaspard, S. Tersigni, and D. J. Tannor. Wavepacket dancing: Achieving chemical selectivity by shaping light pulses. *Chem. Phys.*, 139:201–220, 189.

[124] R. J. Gordon and S. A. Rice. Active controll of the dynamics of atoms and molecules. *Annu. Rev. Phys. Chem.*, 48:601–641, 1997.

[125] A. Lindinger, C. Lupulescu, M. Plewicki, F. Vetter, A. Merli, S. M. Weber, , and L. Wöste. Isotope selective ionization by optimal control using shaped fs-laser pulses. *Phys. Rev. Lett.*, 93:033001, 2004.

[126] P. Nürnberger. *Adaptive Control of quantum Systems with Femtosecond Laser Pulses*. Phd thesis, Julius-Maximilians-Universität Würzburg, 2007.

[127] W. Salzmann, T. Mullins, J. Eng, M. Albert, R. Wester, M. Weidemüller, A. Merli, S. M. Weber, F. Sauer, M. Plewicki, F. Weise, L. Wöste, and A. Lindinger. Coherent transients in the femtosecond photoassociation of ultracold molecules. *Physical Review Letters*, 100(23):233003, 2008.

[128] U. Gaubatz, P. Rudecki, M. Becker, M. Külz, and K. Bergmann. Population switching between vibrational levels in molecular beams. *Chem. Phys. Lett.*, 148:463–468, 1988.

[129] A. P. Peirce, M. A. Dahleh, and H. Rabitz. Optimal control of quantum-mechanical systems: Existence, numerical approximation, and applications. *Phys. Rev. A*, 37(12):4950–4964, Jun 1988.

[130] Richard S. Judson and Herschel Rabitz. Teaching lasers to control molecules. *Phys. Rev. Lett.*, 68(10):1500–1503, Mar 1992.

[131] J. P. Heritage, A. M. Weiner, and R. N. Thurston. Picosecond pulse shaping by spectral phase and amplitude manipulation. *Opt. Expr.*, 10:609, 1985.

[132] A. M. Weiner. Femtosecond pulse shaping using spatial light modulators. *Rev. Sci. Instr.*, 71:1929, 2000.

[133] P. Niklaus G. Gerber T. Brixner, N. H. Damrauer. Photoselective adaptive femtosecond quantum control in the liquid phase. *Nature*, 57:57–60, 2001.

[134] Matthew Comstock, Vadim Lozovoy, Igor Pastirk, and Marcos Dantus. Multiphoton intrapulse interference 6; binary phase shaping. *Opt. Express*, 12(6):1061–1066, 2004.

[135] T. Hornung, R. Meier, D. Zeidler, K.-L. Kompa, D. Proch, and M. Motzkus. Optimal control of one- and two-photon transitions with shaped femtosecond pulses and feedback. *Appl. Phys. B*, 71:277, 2000.

[136] R. J. Cogdell D. Zeidler J. L. Herek, W. Wohlleben and M. Motzkus. Quantum control of energy flow in light harvesting complex. *Nature*, 417:533–535, 2002.

[137] N. Dudovich, D. Oron, and Y. Silberberg. Single-pulse coherently controlled nonlinear Raman spectroscopy and microscopy. *Nature*, 418:512–514, 2002.

[138] editor I. Rechenberg. *Evolutionsstrategie: Optimierung technischer Systeme nach Prinzipien der biologischen Evolution*. Frommann-Holzboog-Verlag, Stuttgart, 1973.

[139] L. D. Socaciu-Siebert. *Reaction Kinetics and Femtosecond Dynamics of Small Gold Clusters*. Phd thesis, Freie Universität Berlin, 2004.

[140] J. Hagen. *Reaktivität und Femtosekundendynamik kleiner Silbercluster und gemischter Silber-Gold-Cluster*. Phd thesis, Freie Universität Berlin, 2004.

[141] L. D. Socaciu-Siebert, J. Hagen, J. Le Roux, D. Popolan, M. Vaida, S. Vajda, T. M. Bernhardt, and L. Wöste. Ultrafast nuclear dynamics induced by photodetachment of Ag_2 and Ag_2O_2: oxygen desorption from a molecular silver surface. *Phys. Chem. Chem. Phys.*, 7:2706–2709, 2005.

[142] M. Hartmann, A. Heidenreich, J. Pittner, V. Bonačić-Koutecký, and J. Jortner. Ultrafast dynamics of small clusters on the time scale of nuclear motion. *Journal of Physical Chemistry A*, 102(23):4069–4074, 1998.

[143] V. Bonačić-Koutecký, R. Mitrić, U. Werner, L. Wöste, and R. S. Berry. Ultrafast dynamics in atomic clusters: Analysis and control. *Proceedings of the National Academy of Sciences*, 103:10594–10599, 2006.

[144] T. M. Bernhardt, J. Hagen, L. D. Socaciu, R. Mitrić, A. Heidenreich, J. Le Roux, A. Popolan, M. Vaida, L. Wöste, V. Bonačić-Koutecký, and J. Jortner. Femtosecond time-resolved geometry relaxation and ultrafast intramolecular energy redistribution in Ag_2Au. *Chem. Phys. Chem*, 6(2):243–253, 2005.

[145] V. Bonačić-Koutecký and R. Mitrić. Theoretical exploration of ultrafast dynamics in atomic clusters: Analysis and control. *Chemical Reviews*, 105(1):11–66, 2005.

[146] R. C. Baetzold. Properties of silver clusters adsorbed to agbr. *J. Phys. Chem. B*, 105(17):3577–3585, 2001.

[147] T. Wilhelm, J. Piel, and E. Riedle. Sub-20-fs pulses tunable across the visible from a blue-pumped single-pass noncollinear parametric converter. *Opt. Lett.*, 22(19):1494–1496, 1997.

[148] M. Takasaka A. Shirakawa, I. Sakane and T. Kobayashi. Sub-5-fs visible pulse generation by pulse-front-matched noncollinear optical parametric amplification. *Appl. Phys. Lett.*, 74(16):2268–2270, 1999.

[149] E. Riedle P. Baum, S. Lochbrunner. Tunable sub-10-fs ultraviolet pulses generated by achromatic frequency doubling. *Opt. Lett.*, 29(14):1686–1688, 2004.

[150] T. Srinivasan-Rao P. B. Corkum, C. Rolland. Supercontinuum generation in gases. *Physical Review Letters*, 57(18):2268–2272, 1986.

[151] P. St.J. Russell. Photonic-crystal fibers. *J. of Lightwave Technology*, 24:4729–4749, 2006.

[152] A. M. Zheltikov. Let there be white light: supercontinuum generation by ultrashort laser pulses. *Physics-Uspekhi*, 49:605–628, 2006.

[153] o. Svelto M. Nisoli, S. De Silvestri. Generation of high energy 10fs pulses by a new pulse compression technique. *Appl. Phys. Lett.*, 68:2793–2795, 1996.

[154] M. Nisoli, S. De Silvestri, O. Svelto, R. Szipöcs, K. Ferencz, Ch. Spielmann, S. Sartania, and F. Krausz. Compression of high-energy laser pulses below 5 fs. *Opt. Lett.*, 22(8):522–524, 1997.

[155] G. Korn N. Zhavoronkov. Generation of single intense short optical pulses by ultrafast molecular phase modulation. *Phys. Rev. Lett.*, 88(20):2039011–2039014, 2002.

[156] T. Sekikawa E. Matsubara, K. Yamane and M. Yamashita. Generation of 2.6 fs optical pulses using induced-phase modulation in a gas-filled hollow fiber. *J. Opt. Soc.*, 24:985–989, 2007.

[157] L. Gallmann, T. Pfeifer, P.M. Nagel, M.J. Abel, D.M. Neumark, and S.R. Leone. Comparison of the filamentation and the hollow-core fiber characteristics for pulse compression into the few-cycle regime. *Appl. Phys. B*, 86(4):561–748, 2007.

[158] C.P. Hauri, W. Kornelis, F.W. Helbing, A. Heinrich, A. Couairon, A. Mysyrowicz, J. Biegert, and U. Keller. Generation of intense, carrier-envelope phase-locked few-cycle laser pulses through filamentation. *Appl. Phys. B*, 79:673–677, 2004.

[159] C. P. Hauri, A. Guandalini, P. Eckle, W. Kornelis, J. Biegert, and U. Keller. Generation of intense few-cycle laser pulses through filamentation – parameter dependence. *Opt. Exp.*, 13:7541–7547, 2005.

[160] J.-H. Lee J. Park and C. H. Nam. Laser chirp effect on femtosecond laser filamentation generated for pulse compression. *Opt. Exp.*, 17(7):4465–4470, 2008.

[161] R. Trebino. *Frequency-Resolved Optical Gating: The Measurement of Ultrashort Laser Pulses*. Kluwer Academic Publishers, Boston, Dordrecht, London, 2000.

[162] U. Schmidhammer-S. Lochbrunner I. Z. Kozma, P. Baum and E. Riedle. Compact autocorrelator for the online measurement of tunable 10 femtosecond pulses. *Rev. Sci. Instrum.*, 75:2323–2327, 2005.

[163] C. Guo M. Li, J. P. Nibarger and G. N. Gibson. Dispersion-free transient-grating frequency-resolved optical gating. *Appl. Opt.*, 38:5250–5253, 1999.

[164] R. Ell K. X. Kärtner T. Binhammer, E. Rittweger and U. Morgner. Prism-based pulse shaper for octave spanning spectra. *IEEE Journ. of Quantum Electron.*, 41:1552–1557, 2005.

[165] D. W. Phol H. J. Eichler, H. Eichler. *Laser*. Springer Verlag, Berlin, Heidelberg, 1998.

[166] K. Nelson M. Wefers. Analysis of programmable ultrashort waveform generation using liquid-crystal spatial light modulators. *J. Opt. Soc. Am. B*, 12:1343, 1995.

[167] A. Bartelt. *Steuerung der Wellenpaketdynamik in kleinen Alkaliclustern mit optimierten Femtosekundenpulsen*. PhD Thesis, Freie Universität Berlin, 2002.

[168] Cambridge Research and Inc. Instrumentation. *Spatial Light Modulator (SLM) System*. CRI, U.S.A., 2004.

[169] LAYERTEC. *Femtosecond Laser Optics*. LAYERTEC, Mellingen, 2007.

[170] W. Unrau. *Erzeugung, Charakterisierung und Anwendung von ultrakurzen Weißlichtpulsen im Edelgasfilament*. Diploma thesis, Freie Universität Berlin, 2008.

[171] Femtosoft Technologies. *FROG Version 3.02*. 1999.

[172] E. R. Peck and J. D. Fischer. . *J. Opt. Soc. Am.*, (54):1362, 1964.

[173] M. Mlejnek, E. M. Wright, and J. V. Moloney. Femtosecond pulse propagation in argon: A pressure dependence study. *Phys. Rev. E*, 58(4):4903–4910, Oct 1998.

[174] H. J. Lehmeier, W. Leupacher, and A. Penzkofer. Nonresonant third order hyperpolarizability of rare gases an N_2 determined by third harmonic generation. *Opt. Commun.*, 56(1):67–72, 1985.

[175] A. Couairon, J. Biegert, C. P. Hauri, W. Kornelis, F. W. Helbing, U. Keller, and A. Mysyrowicz. Self-compression of ultra-short laser pulses down to one optical cycle by filamentation. *Journal of Modern Optics*, 53:75—-85, 2006.

[176] O. E. Martinez. Grating and prism compressors in the case of finite beam size. *J. Opt. Soc. Am. B*, 3(7):929, 1986.

[177] R.E. Sherriff. Analytic expressions for group-delay dispersion and cubic dispersion in arbitrary prism sequences. *J. OPt. Soc. Am. B*, 15(3):1224–1230, 1998.

[178] B. Proctor and F. Wise. Quartz prism sequence for reduction of cubic phase in a mode-locked $TiAl_2O_3$ laser. *Opt. Let.*, 17(18):1295–1297, 1992.

[179] V. Pervak, C. Teisset, A. Sugita, S. Naumov, F. Krausz, and A. Apolonski. High-dispersive mirrors for femtosecond lasers. *Opt. Express*, 16(14):10220–10233, 2008.

[180] Günter Steinmeyer. Femtosecond dispersion compensation with multilayer coatings: toward the optical octave. *Appl. Opt.*, 45(7):1484–1490, 2006.

[181] I. N. Bronstein, K. A. Semendjajew, and G. Musiol. *Taschenbuch der Mathematik*. Deutsch (Harri), 6. Auflage, 2005.

[182] C. Homann, C. Schriever, P. Baum, and E. Riedle. Octave wide tunable uv-pumped nopa: pulses down to 20 fs at 0.5 mhz repetition rate. *Opt. Exp.*, 16:5746–5756, 2008.

[183] A. Baltuska. *Hydrated electron dynamics explored with 5-fs optical pulses*. PhD Thesis, Rijksuniversiteit Groningen, 2000.

[184] H. Giessen S. Linden and J. Kuhl. Xfrog - a new method for amplitude and phase characterization of weak ultrashort pulses. *Phys. Stat. Sol. (b)*, 206:119–124, 1998.

[185] R. W. Hellwarth. Third-order optical susceptibilities of liquids and solids. *Prog. Quantum Electron.*, 5:1, 1977.

[186] G. Méchain, A. Couairon, M. Franco, B. Prade, and A. Mysyrowicz. Organizing multiple femtosecond filaments in air. *Phys. Rev. Lett.*, 93(3):035003, Jul 2004.

[187] H. Schroeder, J. Liu, and S. Chin. From random to controlled small-scale filamentation in water. *Opt. Express*, 12(20):4768–4774, 2004.

[188] P. Rohwetter, M. Queißer, K. Stelmaszczyk, M. Fechner, and L. Wöste. Laser multiple filamentation control in air using a smooth phase mask. *Physical Review A (Atomic, Molecular, and Optical Physics)*, 77(1):013812, 2008.

[189] Vadim V. Lozovoy, Igor Pastirk, and Marcos Dantus. Multiphoton intrapulse interference iv. ultrashort laserpulse spectral phase characterization and compensation. *Opt. Lett.*, 29(7):775–777, 2004.

[190] K. W. DeLong, D. N. Fittinghoff, and R. Trebino. Practical issues in ultrashort-laser-pulse measurement usingfrequency-resolved optical gating. *IEEE Journal of Quantum Electronics*, 32(7):1253–1264, 1996.

[191] J. Gagnon, E. Goulielmakis, and V. S. Yakovlev. The accurate frog characterization of attosecond pulses from streaking measurements. *Appl. Phys. B*, 92(1):25–32, 2008.

[192] G. Santambrogio. *Infrared Spectroscopy of Gas Phase Cluster Ions*. Phd thesis, Freie Universität Berlin, 2007.

[193] K. R. Asmis, M. Brummer, C. Kaposta, G. Santambrogio, G. von Helden, G. Meijer, K. Rademann, and L. Woste. Mass-selected infrared photodissociation spectroscopy of $V_4O_{10}^+$. *Phys. Chem. Chem. Phys.*, 4:1101–1104, 2002.

[194] Mathias Brümmer. *Spektroskopische Untersuchungen zur Struktur und Reaktivität von Vanadiumoxid–Clustern*. Phd thesis, Freie Universität Berlin, 2007.

[195] J. Demuth. *Pulszuganregung im Rahmen der Ladungsumkehrspektroskopie*. Diploma thesis, Freie Universität Berlin, 2007.

[196] C. M. Brown and M. L. Ginter. The absorption spectrum of the Ag_2 molecule. *Journal of Molecular Spectroscopy*, 69(1):25–36, 78.

[197] Joe Ho, Kent M. Ervin, and W. C. Lineberger. Photoelectron spectroscopy of metal cluster anions: Cu_n^-, Ag_n^- and Au_n^-. *The Journal of Chemical Physics*, 93(10):6987–7002, 1990.

[198] H. G. Krämer, V. Beutel, K. Weyers, and W. Demtröder. Sub-Doppler laser spectroscopy of silver dimers Ag_2 in a supersonic beam. *J. Chem. Phys.*, 193:331–334, 1992.

[199] V. Beutel, G. L. Bhale, M. Kuhn, and W. Demtröder. The ionization potential of Ag_2. *J. Chem. Phys.*, 185:313–318, 1991.

[200] V. Bonačić-Koutecký, L. Češpiva, P. Fantucci, and J. Koutecký. Effective core potential-configuration interaction study of electronic structure and geometry of small neutral and cationic ag[sub n] clusters: Predictions and interpretation of measured properties. *The Journal of Chemical Physics*, 98(10):7981–7994, 1993.

[201] V. Bonačić-Koutecký, L. Češpiva, P. Fantucci, J. Pittner, and J. Koutecký. Effective core potential-configuration interaction study of electronic structure and geometry of small anionic ag[sub n] clusters: Predictions and interpretation of photodetachment spectra. *The Journal of Chemical Physics*, 100(1):490–506, 1994.

[202] V. Bonačić-Koutecký, J. Pittner, M. Boiron, and P.J. Fantucci. An accurate relativistic effective core potential for excited states of Ag atom: An application for studying the absorption spectra of Ag_n and Ag_n^+ clusters. *J. Chem. Phys.*, 110:3876—-3886, 1999.

[203] Korth Kristalle. http://www.korth.de/calc/al2o3.htm.

[204] H. N. Ibrahim. *Tracking coherences in a dissipative ocean: Analysing and controlling Br_2/Ar matrix*. Phd thesis, Freie Universität Berlin, 2007.

[205] H. Heß. *Femtosekunden-Spektroskopie an kalten Metallclustern*. Phd thesis, Freie Universität Berlin, 1999.

[206] H. Hess, S. Kwiet, L. Socaciu, S. Wolf, T. Leisner, and L. Wöste. The influence of the anion vibrational temperature on the fs dynamics in a nenepo experiment. *Appl. Phys. B*, 71(3):337–341, 2000.

[207] E. W. Schlag and W. B. Peatman und K. Müller-Dethlefs. Threshold photoionization and ZEKE spectroscopy: a historical perspective. *Journal of Electron Spectroscopy and Related Phenomena*, 66:139–149, 1993.

[208] L. D. Dickson. Characteristics of a propagating gaussian beam. *Appl. Opt.*, 9(8):1854–1861, 1970.

Appendix A

Appendix

A.1 Nonlinear envelope equation

The aim is to come from Maxwell's equations to a nonlinear propagation equation which is the starting point to explain additional propagation effects of fs filamentation. Like all electromagnetic phenomena, generation and propagation of light is governed by Maxwell's equations

$$\nabla \cdot \mathbf{D} = \rho \tag{A.1}$$

$$\mu_0 \nabla \cdot \mathbf{H} = 0 \tag{A.2}$$

$$\frac{1}{\epsilon_0} \nabla \times \mathbf{D} = -\mu_0 \frac{\partial \mathbf{H}}{\partial t} \tag{A.3}$$

$$\nabla \times \mathbf{H} = \mathbf{J} + \frac{\partial \mathbf{D}}{\partial t} \tag{A.4}$$

where the electric $\mathbf{E}$ and magnetic $\mathbf{H}$ field vectors have been expressed by the corresponding electric and magnetic flux densities $\mathbf{D}$ and $\mathbf{H}$.

$$\mathbf{D} = \epsilon_0 \mathbf{E} \qquad\qquad \mathbf{B} = \mu_0 \mathbf{H} \tag{A.5}$$

With ϵ_0 and μ_0 being the vacuum permittivity and vacuum permeability, respectively. In absence of free charges the charge density $\rho = 0$ and current density vector $\mathbf{J} = 0$ vanish. By taking the curl of Eq.(A.3)

$$\nabla \times (\nabla \times \mathbf{D}) = -\epsilon_0 \mu_0 \frac{\partial}{\partial t} (\nabla \times \mathbf{H})$$

and usage of vector rule ($\nabla \times (\nabla \times \mathbf{a}) = \nabla(\nabla \cdot \mathbf{a}) - \nabla^2 \mathbf{a}$) in combination with Eq.(A.4) one obtains

$$\nabla(\nabla \cdot \mathbf{D}) - \nabla^2 \mathbf{D} = -\epsilon_0 \mu_0 \frac{\partial}{\partial t} \left(\frac{\partial \mathbf{D}}{\partial t} \right)$$

allowing for $\nabla \cdot \mathbf{D} = 0$ leads to the wave equation for propagation in vacuum

$$\nabla^2 \mathbf{D} = \epsilon_0 \mu_0 \frac{\partial^2 \mathbf{D}}{\partial t^2} \tag{A.6}$$

which can be written in favor of the field quantity $\mathbf{E}$ in one dimension

$$\frac{\partial^2 \mathbf{E}}{\partial x^2} - \frac{1}{c_0^2} \frac{\partial^2 \mathbf{E}}{\partial t^2} = 0 \tag{A.7}$$

where c_0 is the vacuum speed of light which equals the phase velocity for a monochromatic wave in vacuum.

$$c_0 = \sqrt{\frac{1}{\mu_0 \epsilon_0}} \tag{A.8}$$

However, in a dielectric medium (i.e. absence of free charges) the electric flux density $\mathbf{D}$ in Eq.(A.5) extends to

$$\mathbf{D} = \epsilon_0 \epsilon \mathbf{E} \tag{A.9}$$

where ϵ is the dielectric constant which is defined as

$$\epsilon = 1 + \chi \tag{A.10}$$

with χ being a material constant named susceptibility. This means that the electric flux density $\mathbf{D}$ arises in response to the electric field $\mathbf{E}$ propagating in the medium and is related to it by

$$\mathbf{D} = \epsilon_0 \mathbf{E} + \mathbf{P} \tag{A.11}$$

where $\mathbf{P}$ is the induced polarization

$$\mathbf{P} = \epsilon_0 \chi \mathbf{E} \tag{A.12}$$

The manner on which the material response can lead to nonlinear dependence of $\mathbf{P}$ on $\mathbf{E}$ is subject to the field of nonlinear optics. At this point two ingredients are introduced in order to find a propagation equation for ultra short and intense pulses in nonlinear media.

Firstly, attention is payed to high field strengths under which the matter response on the exciting light is no longer linear. In case of nonlinear optics (but still at moderate field strengths), the polarization $\mathbf{P}$ can be decomposed in linear $\mathbf{P^{(1)}}$ and a nonlinear part $\mathbf{P^{(NL)}}$

$$\mathbf{P} = \mathbf{P^{(1)}} + \mathbf{P^{(NL)}} \tag{A.13}$$

According to a perturbative ansatz a power series in the field strength $\mathbf{E}$ can be developed

$$\mathbf{P} \;=\; \epsilon_0 \chi^{(1)} \mathbf{E} + \epsilon_0 \mathbf{E} \left[\chi^{(2)} \mathbf{E} + \chi^{(3)} \mathbf{E}^2 + ... \right] \tag{A.14}$$

This treatment bases on the assumption of $\mathbf{P^{(NL)}}$ being a small perturbation compared to the total induced polarization. The quantity $\chi^{(1)}$ is known as linear electric susceptibility whereas $\chi^{(2)}$ and $\chi^{(3)}$ are referred to as second- and third order nonlinear optical susceptibilities. One linear property of dielectric media is dispersion which implies the wavelength dependence of a physical quantity. This holds for linear $\tilde{\chi^{(1)}}(\omega)$ as well as for nonlinear susceptibilities $\tilde{\chi}^{(n)}(\omega)$. A Fourier transformation results in a time dependent susceptibility

$$\chi^{(1)}(t) = (2\pi)^{-1} \int_{-\infty}^{\infty} d\omega \tilde{\chi}^{(1)}(\omega) e^{-i\omega t} \tag{A.15}$$

This time dependent susceptibility can be used in order to specify relation (A.13)

$$\mathbf{P^{(1)}}(\mathbf{r}, t) = \epsilon_0 \int_{-\infty}^{\infty} dt' \chi^{(1)}(t - t') \mathbf{E}(\mathbf{r}, t') \tag{A.16}$$

$$\mathbf{P^{(nl)}}(\mathbf{r}, t) = \epsilon_0 \int \int \int_{-\infty}^{\infty} dt_1 dt_2 dt_3 \chi^{(3)}(t - t_1, t - t_2, t - t_3) \mathbf{E_1}(\mathbf{r}, t_1) \mathbf{E_2}(\mathbf{r}, t_2) \mathbf{E_3}(\mathbf{r}, t_3) \tag{A.17}$$

where all higher order terms of the series in Eq.(A.14) were dropped except for the third order term. Eqs.(A.17 and A.16) are valid in the electric-dipole approximation and assume local medium

response [33, 34]. Now the wave vacuum equation can be extended including the induced linear polarization $\mathbf{P^{(1)}}(\mathbf{r},t)$

$$(\frac{\partial^2}{\partial z^2}+\nabla_\perp^2)\mathbf{E}(\mathbf{r},t)-\left[\frac{1}{c^2}\frac{\partial^2\mathbf{E}(\mathbf{r},t)}{\partial t^2}+\mu_0\frac{\partial^2\mathbf{P^{(1)}}(\mathbf{r},t)}{\partial t^2}\right]=0 \tag{A.18}$$

In order to be prepared for later assumptions the spatial coordinates x, y, z are separated in a propagation coordinate z and the transversal mode with index $_\perp$ where $\nabla_\perp^2=\frac{\partial^2}{\partial x^2}+\frac{\partial^2}{\partial y^2}$ is the transversal Laplace operator. When using Eq.(A.10-A.12) the wave equation (A.18) can be given by

$$(\frac{\partial^2}{\partial z^2}+\nabla_\perp^2)\mathbf{E}(\mathbf{r},t)-\frac{\partial^2}{c^2\partial t^2}\int_{-\infty}^{t}dt'\epsilon^{(1)}(t-t')\mathbf{E}(\mathbf{r},t')=0 \tag{A.19}$$

where the term in brackets of Eq.(A.18) is expressed by help of Eq.(A.10). The time integration displays a convolution which takes into account that the electric field has already interacted with the medium until the current time t. Now the nonlinear response of the medium can be included simply by adding the $\mathbf{P^{(nl)}}$ term on the right hand side of Eq. (A.19)

$$(\frac{\partial^2}{\partial z^2}+\nabla_\perp^2)\mathbf{E}(\mathbf{r},t)-\frac{\partial^2}{c^2\partial t^2}\int_{-\infty}^{t}dt'\epsilon^{(1)}(t-t')\mathbf{E}(\mathbf{r},t')=\frac{4\pi\partial^2}{c^2\partial t^2}\mathbf{P^{(nl)}}(\mathbf{r},t) \tag{A.20}$$

Electric field $\mathbf{E}$ and nonlinear polarization $\mathbf{P^{(nl)}}$ are supposed to be linearly polarized along x direction. If all incident light fields are same and interact on an instantaneous responding Kerr medium the time integrations in Eq.(A.17) shrinks to delta functions.

The second ingredient for deriving the propagation equation is the mathematical framework for extremely short pulse durations of the electric field. Therefore the complex field $\mathbf{E}$ is decomposed in a complex envelope $A(\mathbf{r}_\perp,z,t)$ and a rapidly oscillating part with a carrier frequency ω_0

$$\mathbf{E}(\mathbf{r},t)=A(\mathbf{r}_\perp,z,t)e^{i(k(\omega)z-\omega_0t+\phi_0)}+c.c. \tag{A.21}$$

where ϕ_0 is defined such that the imaginary part of the complex envelope $A(\mathbf{r}_\perp,z,t)$ is zero at $t=0$. The nonlinear polarization is treated in the same fashion

$$\mathbf{P^{(nl)}}(\mathbf{r},t)=B(\mathbf{r}_\perp,z,t,A)e^{i(k(\omega)z-\omega_0t+\phi_0)} \tag{A.22}$$

with which the nonlinear dependence of the polarization on the inducing laser field is expressed. For example, an instantaneous responding Kerr medium is represented by a function B [32, 33]

$$B(\mathbf{r}_\perp,z,t,A)=\frac{3}{8n_0}\Re(\tilde{\chi}^{(3)}(\omega))\left|A(\mathbf{r}_\perp,z,t)\right|^2A(\mathbf{r}_\perp,z,t) \tag{A.23}$$

This concept is applicable for pulse durations down to a single optical cycle if, among others, following condition is fulfilled. A phase shift $\Delta\phi$ of the electric field $E'(t)=E(t)e^{i\Delta\phi}$ does not change the center frequency ω_0 [35].
Finally, $k(\omega)$ is expanded in a Taylor series around ω_0 in order to account for dispersion and subsequently Fourier transformed. Within this framework the *nonlinear envelope equation* **(NEE)** of first order in propagation coordinate can be received from which a simplified derivation is given here [32, 35]:

$$\left[\frac{\alpha_0}{2}+\frac{\partial}{\partial\xi}-\frac{ic}{2\omega_0n_0}\left(1+\frac{i}{\omega_0}\frac{\partial}{\partial t'}\right)^{-1}\nabla_\perp^2-i\widehat{D}\right]A(\mathbf{r}_\perp,\xi,t')=i\frac{2\pi\omega_0}{n_0}\left(1+\frac{i}{\omega_0}\frac{\partial}{\partial t'}\right)B \tag{A.24}$$

Different compared to the *slowly varying envelope approximation* (**SVEA**)

$$|\partial/\partial z E| = |\partial/\partial \xi E - \beta_1 \partial/\partial t' E| \ll 2\pi |E| / \lambda_0 \tag{A.25}$$

the main idea in the derivation of (A.24) consists in assuming that the pulse envelope is slowly varying in the propagation direction $|\partial/\partial \xi E| \ll 2\pi |E| / \lambda_0$, but not in time. This requirement is referred to as *slowly evolving wave approximation* (**SEWA**). The expression "first order in propagation coordinate" means that the second ξ derivative is dropped because the envelope is assumed not to change significantly over a distance equal to the wavelength. Equation (A.24) is already converted in a retarded time moving with the pulse at group velocity v_g frame by coordinates $\xi = z$ and $t' = t - z\beta_1 = t - z/v_g$. The dispersion operator $\widehat{D}$ is defined as

$$\widehat{D} = -\frac{\alpha_1}{2}\frac{\partial}{\partial t'} + \sum_{m=2}^{\infty} \frac{\beta_m + i\alpha_m/2}{m!} \left(i\frac{\partial}{\partial t'}\right)^m \tag{A.26}$$

and

$$\beta_m = \Re\left[\left(\frac{\partial^m k(\omega)}{\partial \omega^m}\right)_{\omega_0}\right] \qquad \alpha_m = \Im\left[\left(\frac{\partial^m k(\omega)}{\partial \omega^m}\right)_{\omega_0}\right] \tag{A.27}$$

with (β_0^{-1}) being the phase velocity, (β_1^{-1}) the group velocity and (β_2) the GVD parameter introduced in Sec. 1.1.2 The imaginary term $(i\alpha_m)$ describes losses during propagation.

The expression $\nabla_\perp^2 A$ is the (spatial) diffraction term and $\widehat{D}$ describes effects of higher order dispersion. In literature $\left(1 + \frac{i}{\omega_0}\frac{\partial}{\partial t'}\right)$ is called self-steepening operator T [36]. And space time coupling which describes self focusing phenomena through connection of diffraction term with the time derivative.

The refractive index is related to the real part of the susceptibility

$$n_0(\omega) = 1 + \frac{1}{2}\Re\left[\tilde{\chi}^{(1)}(\omega)\right] \tag{A.28}$$

$$\alpha(\omega) = \frac{\omega}{nc}\Im\left[\tilde{\chi}^{(1)}(\omega)\right] \tag{A.29}$$

and the absorption coefficient $\alpha(\omega)$ is determined by the imaginary part.

A.2 Properties of Gaussian beams

The focus radius r_{foc} is given as the $1/e^2$ width of intensity [208]:

$$r_{foc} = \frac{\lambda f}{\pi r_0} \tag{A.30}$$

where r_0 is the $1/e^2$ radius of intensity at the entrance pupil and f is the focal length. The Rayleigh length z_R is defined as the distance towards both sides at which the focal beam diameter $w_{foc} = 2r_{foc}$ increases for a factor of $\sqrt{2}$:

$$z_R = \frac{\pi w_{foc}^2}{\lambda}\,. \tag{A.31}$$

A 800 nm beam with $r_0 = 5$ mm and $f = 2$m leads to a Rayleigh length of 16 cm.

A.3 Additional parameter dependences of filamentation

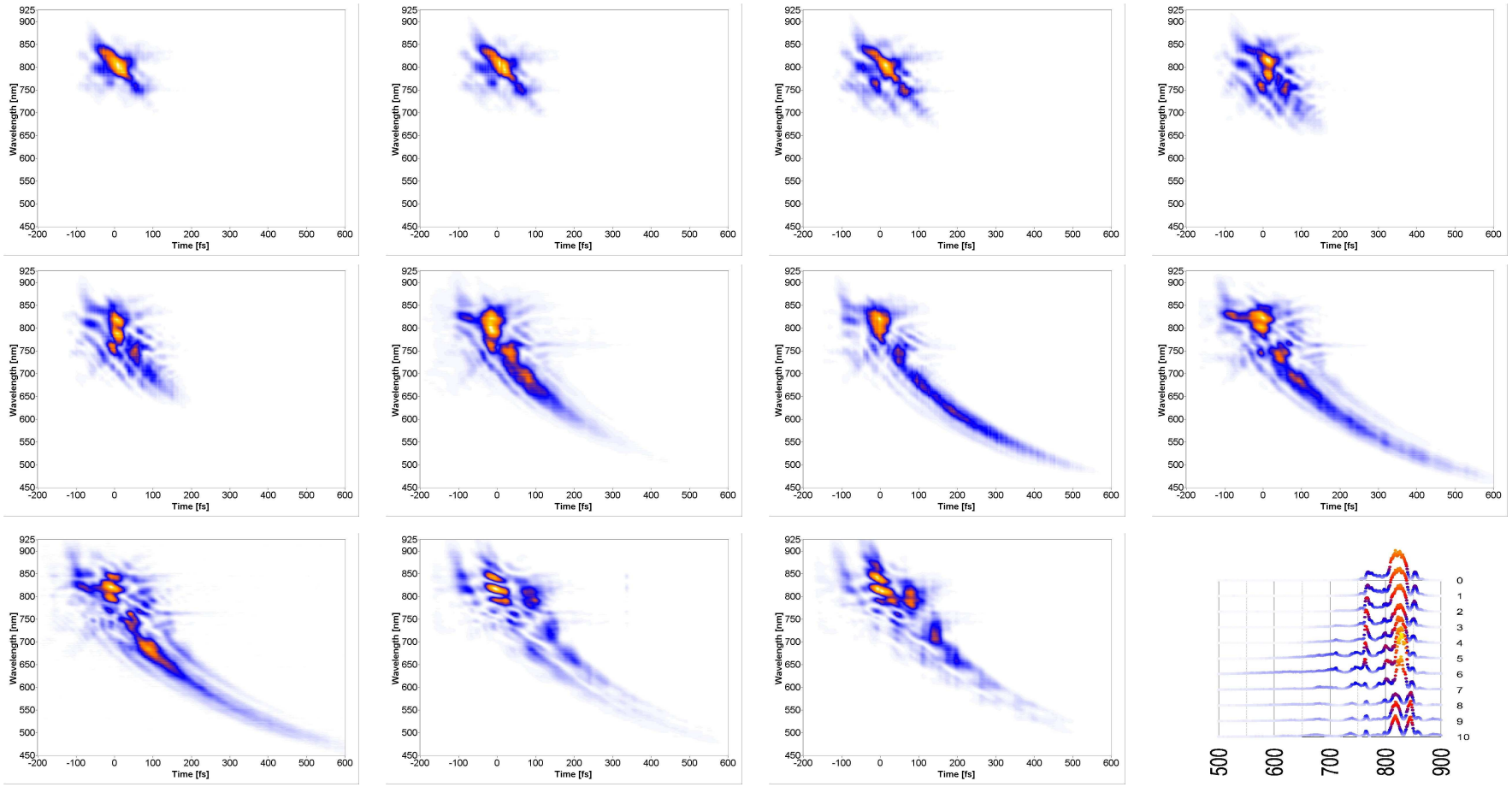

Figure A.1: *Ar* pressure dependence according to [170]. Pulse energy: $1,5$ mJ, zero chirp, pressure variation from 0 to 10 kPa in steps of 1 kPa. The relocation of energy can be seen in the last row in the weightings of the split peaks at NIR and in the VIS tail.

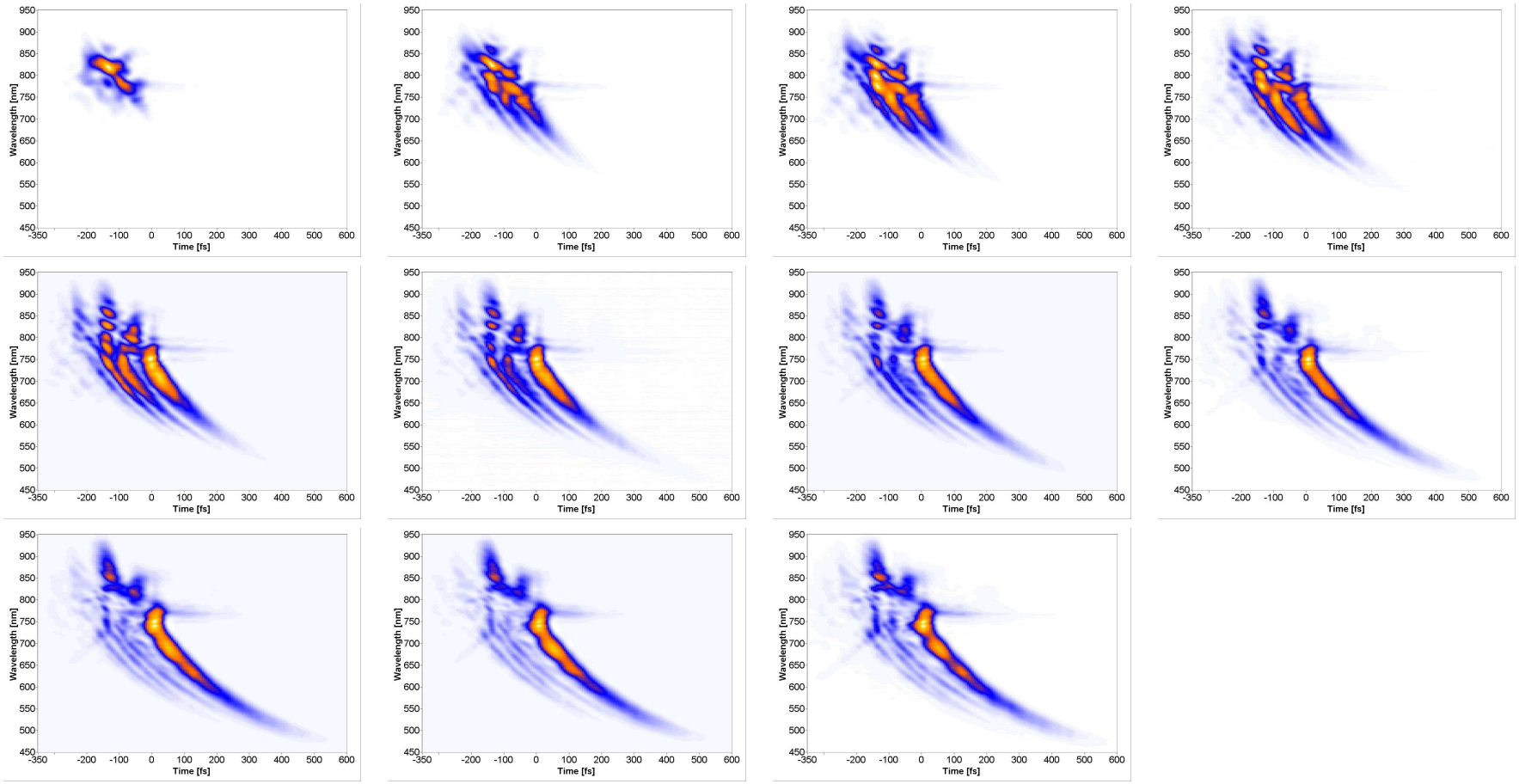

Figure A.2: Energy dependence in Kr at 30 kPa and positive prechirp of about 400 fs^2 (according to [170]). The energy increases from 0.5 to 1.5 mJ in steps of 0.1 mJ. A clear back shifting of energy can be verified for the multiple VIS structure in the last two rows.

Publications

Articles:

- M. Eichelbaum, B. E. Schmidt, H. Ibrahim and K Rademann, "Three-photon-induced luminescence of gold nanoparticles embedded in and located on the surface of glassy nanolayers", *Nanotechnology*, 18:1-8(355702), 2007
- Bruno E. Schmidt, Waldemar Unrau, Aldo Mirabal, Shaohui Li, Marcel Krenz, Ludger Wöste and Torsten Siebert, "Poor man's source for sub 7 fs: a simple route to ultrashort laser pulses and their full characterization", (accepted) *Opt. Exp.*, 2008
- Maik Eichelbaum, Janina Kneipp, Bruno E. Schmidt, Ulrich Panne, and Klaus Rademann, "Fabrication of Luminescent and SERS-Active Gold Micro- and Nanostructures by NIR Laser Irradiation for Bioanalytical Applications", (accepted) *Chem. Phys. Chem.*, 2008
- "Charge reversal of Ag_2 with parametric pulse trains", (in preparation)
- "Single beam transient grating X-FROG with shaped octave spanning white light pulses", (in preparation)
- "Discovering fastest processes in Ag_3 charge reversal with shaped white light pulses", (in preparation)
- "Femtosecond laser pulse optimization for in vivo two photon laser scanning microscope imaging of the honey bee brain", (in preparation)

Conference contributions (talks):

- "Filamentation in air - poor man's sub 7 fs setup", Spring Meeting of the German Physical Society, 2008
- "Imaging Neuronal Activity with Femtosecond Lasers", Spring Meeting of the German Physical Society, 2006
- "Continuum Generation for Ultrafast Spectroscopy", Lausanne Winter School, 2006
- "Imaging Neuronal Activity with Femtosecond Lasers", Seminar SFB 450, Berlin, 2005

Other:

- "Mit Femtosekunden ins Gehirn. Berliner Forscher beobachten die neuronale Aktivität von Bienen beim Riechen ", radio broadcast, Deutschlandfunk, 2006

Kurzfassung

Diese Arbeit verfolgte zwei Ziele. Erstens die Erweiterung der Pump Probe - Ladungsumkehrspektroskopie (NeNePo) an kleinen Silber Clustern mit geformten fs Pulsen. Zunächst wurde das Photodetachment des zweiatomigen Ag_2^- Anions mittels variabler Pulszüge zum neutralen Ag_2 etabliert, welches als einfachstes Modellsystem vibratorischer Kerndynamik zu sehen ist. Ein zeitverzögerter Probepuls löst ein weiteres Elektron ab und generiert das gemessene Ag_2^+ Signal. Mit dem Durchscannen des Subpulsabstandes um die Vibrationsperiode des Neutralteilchens herum konnte die Fokussierung des Ag_2 Wellenpaketes gesteuert werden, abzulesen an der Modulationstiefe des transienten Ag_2^+ Signals. Um neue Untersuchungsmöglichkeiten zur Analyse der Kerndynamik des Ag_3 Trimers zu eröffnen, bestand der zweite Teil der Arbeit in der Weiterentwicklung der kohärenten Kontrollmethode hin zu geformten fs-Weißlichtpulsen. Als Lichtquelle diente die Filamentierung verstärkter fs Pulse (0.6-1.2 mJ) überwiegend in atmoshärischer Luft. Die Steuerung der Filamentierungsbedingungen, die u.a. zu oktavüberschreitenden Spektren von 380-950 nm führten, wurde ebenso für die Edelgase $He,\ Ar,\ Kr$ und Xe, wie für O_2 untersucht. Generell zeichnete sich dabei ein einheitlicher Entstehungsmechanismus der stark unsymmetrischen Spektren ab. Die maßgebenden Effekte sind die spektrale Verbreiterung um die Fundamentale des Lasers aufgrund von Selbstphasenmodulation (SPM) bereits bei niedrigen Intensitäten, gefolgt von einer Plasmaflanke auf der Rückseite des Pulses, die eine kontinuierliche Verbreiterung bis hin zu UV Wellenlängen hervorruft.
Im Rahmen der Filamentcharakterisierung zeigte sich eine starke Abhängigkeit des NIR Spektrums vom Chirp des erzeugenden Pulses, bei konstanter Charakteristik des VIS Anteils - sofern vorhanden. Letzteres ist ein weiterer Hinweis auf zeitliche Selbständerung der Propagationsbedingungen im Filament. Wenngleich die Auswirkungen solcher zeitlicher Selbständerungen wie z.B. self-steepening aus den Messdaten nicht direkt ablesbar waren, so konnte doch das zeitliche Aufspalten in multiple Subpulse bei hohen Gasdrücken bzw. Intensitäten beobachtet werden. Außerdem konnten die bis dato kürzesten, an Luft generierten Pulse demonstriert werden. Die Kürze von 6.3 fs gelang durch Filamentierung in der Laboratmosphäre und anschließender Kompression mittels zweier standard Chirp-Spiegel. Mit einem in dieser Arbeit entworfenen TG-FROG wurden die Pulse vermessen. Die Besonderheiten dieses TG-FROG bestehen in der minimalen Anzahl optischer Komponenten, der geometrischen Strahlteilung zur Vermeidung von Materialdispersion und in der Verwendung von BK 7 Glass als nichtlinearem Medium. Dieses ermöglicht die Charakterisierung von Pulslängen mit nur wenigen optischen Zyklen einerseits, sowie oktavübergreifender Spektren (380-950 nm) andererseits, durch einen einfachen und robusten Aufbau. Die volle Leistungsfähigkeit des Aufbaus entfaltet sich in Kombination mit dem Pulsformer, dessen Konzeption und Kalibrierung unabhängige Phasen- und Amplituden-Änderungen im Bereich von 450-1000 nm erlauben. Diese Kombination ermöglicht: (i) adaptive Pulskompression zu wenigen optischen Zyklen mittels genetischer Optimierung, (ii) die Realisierung eines Zwei-Farben-Pump-Probe Experiments mit einem einzigen Strahl und (iii) die Möglichkeit einer optischen Kreuzkorrelation des NIR und VIS Anteils ebenfalls innerhalb eines Strahls (TG-X-FROG). Letztgenannte Funktionalität ergibt sich aus der Entstehung des transienten Gitters durch den intensiven NIR Anteil, an

welchem das im Allgemeinen schwächere VIS Spektrum gestreut wird. Das Zusammenspiel aller Bestandteile, die hohe Stabilität und das hervorragende Strahlprofil ermöglichten die erfolgreiche Implementierung in eine adaptive Rückkopplungsschleife, bei der ein evolutionärer Algorithmus die Ionenausbeute des Ladungsumkehrsignals von Ag_3 in der Gasphase optimierte. Die erstmalige Anwendung geformter Weißlichpulse aus einem Plasmafilament in der Ultrakurzzeitspektroskopie im Rahmen eines "closed loop" Experiments lieferte neuartige Anregungssignaturen für die Ladungsumkehr des Ag_3 Clusters. Dabei zeichnen sich sehr unterschiedliche Verhalten für den NIR und VIS Bereich aus den Spuren der optimierten Pulse ab. Wird der NIR Bereich als ein komprimierter Puls für multiphotonische Ionisation genutzt, ergeben sich im VIS Anteil sehr kurze, reichhaltige Strukturen, auf Zeitskalen die wesentlich kürzer sind als in bisherigen Experimenten beobachtet.

Curriculum vitae

Der Lebenslauf ist in der Online-Version
aus Gründen des Datenschutzes nicht enthalten

Danksagung

Meine Dankesliste beginnt bei Herrn Prof. Dr. Ludger Wöste für die Aufnahme in seine Arbeitsgruppe und für das lebendige Beispiel, dass Wissenschaft nicht allein darin begründet ist, offensichtliche Wege einzuschlagen. Ich danke Dr. Torsten Siebert für die Einführung in Vier Wellen Mischung und für die Chance meine Stärken beständig weiter zu entwickeln. Ebenso bleibt mir der chronische Optimismus von Prof. Dr. Thorsten Bernhardt in Erinnerung, der notwendig ist, eine Doktorarbeit bis zur Danksagung durchzuhalten.
Since there were so many knobs in the lab, it takes more than two hands to coherently control them. In this sense, I would like to begin with Prof. Dr. Shaohui Li whom I admire for his patience and I am grateful for his proofreading and sharing the Kiwi night in Holland. Eine besondere Unterstützung war Waldemar Unrau während seiner Diplomarbeit für das Weißlicht Projekt, vor allem was die Kontrollierbarkeit mit LabView anbelangt. Daran knüpft die Hilfe von Oli Gause nahtlos an, mit ihm wurden die langwierigen Optimierungen nicht zu langweilig. Dies mag auch Juri Demuth bestätigen, der immer alle Silbercluster eingefangen hat, optimierbare und nicht optimierbare. Darüber hinaus waren die Diskussionen mit Dr. Kamil Stelmaszczyk und Philipp Rohwetter sehr hilfreich, um Licht ins Dunkel des Weißlichts zu bringen.

Da es in dieser Arbeitsgruppe außer dem Arbeiten auch viele Feste zu feiern galt, werde ich mich gern an meine netten Kollegen, Aldo Mirabal, Dr. Andrea Merli, Daniel Lockau und Dr. Stefan Weber erinnern, nicht zu vergessen Fabian Weise, der sein (fast) letztes Hemd für mich gegeben hat sowie Dr. Franziska Sauer, für die Hilfe zum Schluß. Neben all der Technik gab es auch jede Menge menschliche Führsorge und viele bunte Unterschriften, für die sich Inge Siegel und Brigitte Odeh einsetzten.
Herrn Prof. Dr. Nikolaus Schwentner danke ich u.a. für die Erklärung physikalischer Grundgesetze des Propagierens auf Potentialenergieflächen die mit Schnee bedeckt sind. Likewise, I thank Prof. Dr. David Anderson very much for racing, rocking and reading. Furthermore, I greatly appreciate the support form Dr. Daniel J. Kane for providing the basic algorithm used for the spectral phase retrieval. Außerdem war da noch mein (exzellenter) Undercover-Kollege Dr. Maik Eichelbaum, der sich nach unseren Goldgeschäften ins Ausland abgesetzt hat, dem ich dennoch ebensoviel Glück in New York wie Scherben während seiner Doktorarbeit wünsche.

Besonders schön ist es, wenn aus Kollegen Freunde werden, so wie bei Dr. Tobias Gleitsmann, der mich gleich zu Beginn auf den Geschmack von Pumpenöl brachte. Ebenso verhielt es sich mit Tilman Franke, dem ich für die *super* Stimmung bei der Stimulierung neuronaler Aktivität und für die unvergessliche Weihnachtsfeier mehr als danke. Sorry, aber für die Bienen war leider kein Raum mehr!
Meine Dankesliste schließt mit den wichtigsten Menschen, meinen Eltern, denen ich danke für alles was sie mir mit auf den Weg gegeben haben und Heide dafür dass wir diesen Weg gemeinsam gehen, egal in welchem Teil der Erde.

So close, no matter how far...